Reliability Modeling of Microelectronic Interconnections in Long-term Applications

by

Read Al Athamneh

A dissertation submitted to the Graduate Faculty

of Auburn University

in partial fulfillment of the

requirements for the Degree

of Doctor of Philosophy

Auburn, Alabama

December 14, 2019

Keywords: Lead-free solder, Fatigue, Shear, Reliability, Fuzzy, Artificial Neural Networks

Copyright 2019 by Read Al Athamneh

Approved by

Sa'd Hamasha, Chair, Assistant Professor of Industrial and Systems Engineering

John Evans, Charles D. Miller Endowed Chair Professor of Industrial and Systems Engineering

Sean Gallagher, Hal N. and Peggy S. Pennington Associate Professor of Industrial and Systems Engineering

Gregory Harris, Associate Professor of Industrial and Systems Engineering

Abstract

Solder alloy materials are used to form mechanical and electrical connections between printed circuit boards and electronic components. Enhancing the reliability of electronic assemblies is mostly dependent on the reliability of the interconnected solder joints. Therefore, it is crucial to estimate the reliability and fatigue behavior of solder joints under realistic operating conditions. Mechanical and thermal cyclic stresses are the most common factors that lead to failures in solder joints. Aging is another factor that can change the mechanical and fatigue properties of solder joints. One of the most popular solder alloys that are utilized in fabricating solder joints is SAC 305 (96.5 % tin, 3% silver, and 0.5% copper). Adding bismuth (Bi) to SAC-based solder materials could lead to significant evolutions in their fatigue and mechanical properties. Modeling the reliability and the mechanical properties of the SAC-based solder joints under several levels of cycling stress and different aging conditions is the main objective for this dissertation. Instron 5948 Micromechanical Tester is used to perform accelerated shear fatigue and shear tests in order to measure the solder joints performance. Several experimental parameters were utilized in the dissertation, which include: Six levels of stress amplitude (16, 20 and 24MPa ’SAC305’ 22, 26 and 28MPa ’SAC-Q’), four levels of aging time (2, 10, 100 and 1000 hrs), and three levels of aging temperature (50, 100 and 150°C). In the first study, the effcet of different stress amplitudes and aging time conditions on the fatige properties of SAC 305 solder joints with OSP surface finish are investegated. The aging temperature effects on the fatigue and shear properties of SAC 305 solder joints with OSP surface finish are examined in the second study. The effect of aging time on the fatigue and shear properties of SAC305 and SAC-Q (SAC-based with bismuth) solder joint

materials cyled at different stress amplitudes are demonstared in the third study. A Two-parameter Weibull distribution is constructed for each experimental combination to assess the reliability of solder alloys with different conditions. A prediction model is built to assess the fatigue life at different stress amplitudes, aging times, and aging temperatures. The evolutions in the hysteresis loop, plastic strain and the inelastic work at different conditions are determined. Coffin-Manson and Morrow energy models are implemented to estimate the fatigue life as a function of plastic strain and inelastic work per cycle, respectively. Arrhenius model is utilized to describe the effect of aging temperature on the fatigue and shear properties of the solder joints. The artificial neural networks (ANNs) technique is applied to estimate the fatigue life at different experimental combinations. In study four, a new methodology is proposed to determine the optimal process parameters for reliability data by identifying different reliability indices. The fatigue performance of the solder joints under accelerated conditions of the thermal cycling environment is considered as validation case study. Surface finishes, solder paste alloys, and solder sphere materials are the process parameters for this study. Those indices are the scale parameter from the Weibull distribution, the signal to noise ratio, the earlier failure probability and normalized mean-variance. After determining those indices which are considered as the performance response, the multi-response optimization problem is initiated. Fuzzy logic will be then utilized to solve the multi-response problem. The study results indicate that significant reductions in the reliability and shear strength are observed when the loading level, aging time or aging temperature are increased. Fatigue properties (plastic strain and inelastic work) are increased when the stress amplitude or aging levels are increased. Adding Bi into SAC-based solder alloy leads to significantly enhance the solder joints fatigue resistance and decrease the amount of degradation in the solder joints reliability.

Acknowledgments

I would like to express my gratitude to the people who have been vital in the completion of this dissertation. I know it is difficult in few words to thank great people who enlightened your way and led you to success.

First of all, my special thanks is to Dr. Sa'd Hamasha, who without his assistance and support this dissertation will not be completed. He helped in all aspects of the work and revised many drafts. He was patient, supporting and he always responded to my annoying questions and emails. Furthermore, he provided timely and instructive comments and evaluation, to accomplish this work on schedule. I am extremely fortunate to have him as my mentor.

I would like to thank my parents (Qasim and Zainab) and my family. They always support, encourage and help me in pursuing my Ph.D. degree. A special thanks go to my great wife, Dania and my daughters (Ghena and JoAnne) who always provide me with all the support in my life.

Last but not least, I am also grateful to my friends who have supported me along the way.

Table of Content

Abstract ii

Acknowledgments iv

Table of Content v

List of Tables x

List of Figures xii

List of Abbreviations xix

Chapter 1 Introduction 1

1.1 Electronic Manufacturing 1

1.2 Electronic Packaging 2

1.3 Solder Joints 5

1.4 Surface Finish 7

1.5 Fatigue Life Issues for the Interconnection Materials under Harsh Environments 9

1.6 Problem Statement 10

1.7 Research Objectives 13

1.8 Dissertation Organization 14

Chapter 2: General Background 16

2.1 The Reliability 16

2.1.1 Reliability Functions........ 17
2.1.2 Accelerated Reliability Test 19
2.1.3 Failure Analysis........ 24
2.1.4 Statistical Models for Lifetime Data 26
2.1.5 Identifying the Candidate Distribution and Parametric Estimation........ 34
2.1.6 The Reliability of the System 35
2.2 Taguchi Method 38
2.3 Fuzzy Logic........ 39
2.4 Artificial Neural Networks (ANNs) 41
Chapter 3: Literature Review........ 45
3.1 The Reliability Issues in Electronics........ 45
3.2 The Effect of Isothermal Aging on the Reliability and Mechanical Properties of the Solder Joints........ 49
3.3 Reliability Models for the Solder Joints........ 58
3.4 Taguchi Method in Electronics 60
3.5 Applications of Fuzzy Logic on the Reliability 62
3.6 Applications of the Artificial Neural Networks on Reliability 63
Chapter 4: Materials and Methods........ 66
4.1 Introduction 66
4.2 Sample Preparation 66

4.2.1 Testing Board Fabrication 66
4.2.2 Surface Mounting Technology (SMT) Assembly 67
4.3 The Experimental Setup 69
4.4 Proposed Testing Plan 72
4.4.1 Study 1: The Effect of Aging on the Reliability of SAC305 Solder Joints 72
4.4.2 Study 2: The Effect of Aging Temperature on the fatigue behavior and Shear Strength of SAC 305 Solder Joints 74
4.4.3 Study 3: The Reliability Effect for Adding Bismuth on SAC-based Solder alloys at Different Aging Conditions and Stress Amplitudes 76
4.4.4 A New Proposed Methodology of Optimizing the Solder Joint Parameters Using the Fuzzy Logic 77
Chapter 5: Reliability Modeling for the Effect of Aging Time on SAC305 Solder Joints Cycled in Accelerated Shear Fatigue Test 81
5.1 Introduction 81
5.2 Test Matrix 82
5.3 Results and Analysis 83
5.3.1 Weibull Distribution Analysis and Reliability Prediction model 83
5.3.2 The Hysteresis Loop Evaluations 89
5.3.3 The Morrow Energy and the Coffin-Manson Fatigue Models 94
5.4 Summary 99

Chapter 6: Degradation Modeling of the Effect of the Aging Temperature on the Fatigue Behavior of Lead-Free Solder Joints 101

6.1 Introduction 101

6.2 Experimental Layout 102

6.3 Results and Discussion 104

6.3.1 Fatigue Life Modeling Based on the Loading and Aging Conditions 104

6.3.2 Inelastic Work and Plastic Strain 111

6.3.3 Inelastic Work and Plastic Strain Modeling 115

6.3.4 Artificial Neural Networks (ANNs) Model 122

6.3.5 Shear Strength Modeling 125

6.3.6 Microstructure Analysis 129

6.4 Summary 131

Chapter 7: Fatigue Behavior of SAC-Bi and SAC305 Solder Joints with Aging in Actual Setting Conditions 133

7.1 Introduction 133

7.2 Materials and Methods 134

7.3 Test matrix 134

7.4 Results and Discussion 135

7.4.1 Weibull Distribution Analysis 135

7.4.2 Hysteresis Loop Analysis 146

7.4.3 Morrow Energy Model 153

7.4.4 Coffin Manson Model 157

7.4.5 Shear Strength........ 161

7.5 Summary 166

Chapter 8: A New Approach in Assessing the Reliability of the Solder Joints under Thermal Cycling Conditions by Using a New Multi-Criteria Optimization Method 167

8.1 Introduction 167

8.2 Experimental Setup 169

8.3 Results and Analysis 172

8.4 Summary 181

Chapter 9: Overall Summary, Conclusion and Future Works 182

9.1 Overall Summary and Conclusion 182

9.2 Future Works........ 185

References........ 187

Appendices........ 203

Appendix A 204

Two-parameter Weibull probability distribution plots........ 204

Appendix B 211

Artificial neural networks and fuzzy logic Figures........ 211

List of Tables

Table 4.1: The Test Matrix for Studying the Effect of Aging on SAC305 Solder Joint Reliability. 73

Table 4.2: The Test Matrix for Studying the Effect of Aging temperature on SAC305 Solder Joint Reliability 75

Table 4.3: The Test Matrix for Studying the Effect of Aging on SAC305 Solder Joint Shear Strength. 76

Table 4.4: The Test Matrix for Studying the Effect of Aging on SAC-Q Solder Joint Reliability. 77

Table 4.5: The Test Matrix for the Second Validation Case Study. 80

Table 5.1: The Test Matrix for Studying the Effect of Aging time on SAC305 Solder Joint Reliability 83

Table 5.2: Fatigue life of SAC305 solder joints results summary 87

Table 5.3: Inelastic work per cycle empirical model constants 93

Table 5.4: Plastic strain empirical model constants 94

Table 5.5: The fatigue ductility and the fatigue exponent for the Morrow Energy model 95

Table 5.6: Fatigue ductility coefficient and fatigue exponent of the Coffin-Manson model 98

Table 6.1: Test matrix for the accelerated shear fatigue test 103

Table 6.2: Test matrix for the shear test 104

Table 6.3: Stress-life equation constants at different aging conditions 107

Table 6.4: The fatigue results summary 107

Table 6.5: The Morrow energy constants at different aging times and temperatures 117

Table 6.6: The Coffin Manson constants at different aging times and temperatures 121

Table 6.7: The characteristic life at different experimental conditions 124

Table 6.8: The training dataset for the ANNs system 124

Table 6.9: The validation dataset for the ANNs model 124

Table 6.10: The validation and predation data for the ANNs model 125

Table 7.1: The experimental layout for the fatigue test 135

Table 7.2: The experimental layout for the shear test 135

Table 7.3: The power equation constants at different aging time 144

Table 7.4: Morrow energy constants versus aging time for SAC305 and SAC-Q solder alloys 154

Table 7.5: Coffin Manson constants versus aging time for SAC305 and SAC-Q solder alloys 158

Table 7.6: One-way ANOVA for the effect of aging on the shear strength of SAC305 solder . 164

Table 7.7: One-way ANOVA for the effect of aging on the shear strength of SAC-Q solder ... 164

Table 8.1: The experimental combinations of the solder paste, solder sphere, and surface finish 170

Table 8.2: L_{60} testing orthogonal array 170

Table 8.3: The averages of the SNR at each factor level 174

Table 8.4: The responses values at each experimental combination 175

Table 8.5: The optimal factor levels for each response 175

Table 8.6: The Fuzzy rules for the four responses 177

Table 8.7: The COM value at each experimental condition 178

Table 8.8: The average of the COM values at each factor level 178

List of Figures

Figure 2.1: Bathtub Curve 18

Figure 2.2: Serial Configuration 36

Figure 2.3: Parallel Configuration 37

Figure 2.4: The Process Layout with SNR 39

Figure 2.5: Fuzzy Logic System 40

Figure 2.6: General Structure of the RBF Network 43

Figure 4.1: Testing Board Layout 67

Figure 4.2: DEK Galaxy Printing Machine 68

Figure 4.3: 8-zone Pyramax 100N Reflow Oven 69

Figure 4.4: The Reflow Profile 69

Figure 4.5: Instron 5948 Micromechanical Tester and Experimental Setup 70

Figure 4.6: Schematic of the Cylindrical Testing Fixture for an Individual Solder Joint. 71

Figure 4.7: Scanning Electron Microscope (SEM) 72

Figure 4.8: Example of a Complex Comparison Case 78

Figure 5.1: The effect of the thermal cycling process on the solder joints 82

Figure 5.2: Two Parameter Weibull plot for non-aged SAC305 solder joints at different stress amplitudes 84

Figure 5.3: The fatigue life of non-aged SAC305 solder joints versus the cycled stress amplitude 85

Figure 5.4: Typical failures at different stress amplitudes for the surfaces of non-aged SAC305 solder joints 85

Figure 5.5: The effect of different shear stress amplitudes on the characteristic life for the non-aged SAC305 solder joints 86

Figure 5.6: The effect of different shear stress amplitudes on the characteristic life of SAC305 solder joints under different aging conditions 87

Figure 5.7: Prediction model for the power value (C) 88

Figure 5.8: The Full Hysteresis loop for the non-aged SAC305 solder joints cycled at 20 MPa. 89

Figure 5.9: Inelastic work vs. the number of cycles for a non-aged SAC305 solder joints cycled at 16 MPa amplitude until failure 90

Figure 5.10: The effect of different stress amplitudes on the hysteresis loop for non-aged SAC305 solder joints 91

Figure 5.11: The effect of aging on the hysteresis loop for SAC305 solder joints cycled at 16 MPa stress amplitude 91

Figure 5.12: Accumulated work until complete failure vs. aging time at different stress amplitudes 92

Figure 5.13: The relationship between the inelastic work per cycle and the aging time at different stress amplitudes 93

Figure 5.14: The relationship between the plastic strain and the aging time at different stress amplitudes 94

Figure 5.15: Characteristic life vs. inelastic work per cycle for the non-aged SAC305 solder joints 95

Figure 5.16: Characteristic life and inelastic work per cycle for SAC305 solder joints at different aging times in a log-log scale 96

Figure 5.17: Characteristic life vs. plastic strain for non-aged SAC305 solder joints 97

Figure 5.18: Characteristic life vs. plastic strain for SAC305 solder joints at different aging times on a log-log scale 98

Figure 5.19: Coefficient of fatigue ductility (θ) of the Coffin-Manson model vs. aging time 98

Figure 5.20: Fatigue exponent (α) of the Coffin-Manson model vs. aging time 99

Figure 6.1: Weibull probability plot for SAC305 solder joints at different loading scenarios ... 105

Figure 6.2: The relationship between the characteristic life and stress amplitude for non-aged SAC305 solder joints in log-log scale 105

Figure 6.3: Weibull probability plots for SAC305 solder joints at different aging times, 150˚C aging temperature and 16 MPa stress amplitude 108

Figure 6.4: Weibull probability plots for SAC305 solder joints at different aging temperatures, 100 hrs aging time and 16 MPa stress amplitude 108

Figure 6.5: The stress amplitude versus the characteristic life at different aging times and a 150˚C aging temperature 109

Figure 6.6: The stress amplitude versus the characteristic life at different aging temperatures and 100 hrs aging time 109

Figure 6.7: The full hysteresis loop for the non-aged SAC305 solder joints at 24 MPa stress amplitude 113

Figure 6.8: The three main regions in the solder joint fatigue life for the non-aged SAC305 solder joints at 24 MPa stress amplitude 113

Figure 6.9: The evolutions in the hysteresis loop at different stress amplitudes 113

Figure 6.10: The effect of aging time on the hysteresis loop of SAC305 solder joints at 16MPa stress amplitude and 150°C aging temperature 114

Figure 6.11: The effect of aging temperature on the hysteresis loop of SAC305 solder joints at 16 MPa stress amplitude and 100 hrs aging time 114

Figure 6.12: The effect of aging time on the inelastic work and plastic strain of SAC305 solder joints at 150°C aging temperature 114

Figure 6.13: The effect of aging temperature on the inelastic work and plastic strain of SAC305 solder joints at 100 hours of aging time 115

Figure 6.14: The effect of aging temperature and aging time on the inelastic work and plastic strain of SAC305 solder joints at 16 MPa stress amplitude 115

Figure 6.15: The Morrow energy model for the non-aged SAC305 solder joints 116

Figure 6.16: The relationship between the inelastic work per cycle and characteristic life at different aging temperatures 118

Figure 6.17: Arrhenius model for the relationship between the Morrow energy constants and the aging temperature 118

Figure 6.18: The Coffin-Manson model for non-aged SAC305 solder joints 119

Figure 6.19: The relationship between the plastic strain and the characteristic life at different aging time and 100°C aging temperature 121

Figure 6.20: The coffin-Manson constants versus aging conditions 122

Figure 6.21: The stress-strain curve for non-aged SAC305 solder joints 126

Figure 6.22: The effect of aging time on the shear strength of the solder joints 126

Figure 6.23: The effect of aging temperature on the shear strength of the solder joints 127

Figure 6.24: The data summary of the shear strength at different aging conditions 127

Figure 6.25: The main effect plot of the solder joints shear strength with different aging conditions 129

Figure 6.26: The interaction plot of the solder joints shear strength with different aging conditions 129

Figure 6.27: The precipitates coarsening in the Bulk solder of SAC305 solder joints at different aging temperatures 130

Figure 6.28: The precipitates coarsening in the IMC layer solder of SAC305 solder joints at different aging temperatures 131

Figure 6.29: The precipitates coarsening in SAC305 solder joints at different aging times 131

Figure 7.1: Two-parameter Weibull distribution for SAC305 and SAC-Q solder joints at different stress amplitudes 137

Figure 7.2: The relationship between the characteristic life and stress amplitude for SAC-Q and SAC305 solder joints 138

Figure 7.3: Two-Parameter Weibull distribution for SAC305 and SAC-Q solder joints at different aging times and stress amplitudes 139

Figure 7.4: Characteristic life of SAC305 and SAC-Q vs. aging time for different stress amplitudes 140

Figure 7.5: Characteristic life degradation of SAC305 and SAC-Q solder alloys with aging 141

Figure 7.6: The relationship between the characteristic life and stress amplitude for SAC-Q and SAC305 solder joints at different aging time 143

Figure 7.7: *E* value at different aging time for SAC-Q and SAC305 solder alloys 144

Figure 7.8: *c* value at different aging time for SAC-Q and SAC305 solder alloys 144

Figure 7.9: The characteristic life model for SAC305 solder alloy 145

Figure 7.10: The characteristic life model for SAC-Q solder alloy 146

Figure 7.11: Typical hysteresis loop of non-aged SAC305 solder joint cycled at 20MPa stress 147

Figure 7.12: Inelastic work per cycle vs. number of cycles for SAC305 solder join 148

Figure 7.13: The effect of stress amplitude on the hysteresis loop for non-aged SAC305 and SAC-Q solder joints 149

Figure 7.14: The evolution in the hysteresis loop of SAC305 and SAC-Q solder joints cycled at different at 16 MPa and 22 MPa 150

Figure 7.15: SEM images of a typical SAC305 solder joint with aging 152

Figure 7.16: SEM images of a typical SAC-Q solder joint with aging 152

Figure 7.17: The relationship between the characteristic life and inelastic work for the non-aged SAC305 and SAC-Q solder joints 154

Figure 7.18: The relationship between the characteristic life and inelastic work for SAC305 and SAC-Q solder joints at different aging times in log-log scale 156

Figure 7.19: The fatigue exponent constant (Morrow energy model) versus aging time for SAC305 and SAC-Q solder joints 156

Figure 7.20: The fatigue ductility constant (Morrow energy model) versus aging time for SAC305 and SAC-Q solder joints 157

Figure 7.21: The relationship between the characteristic life and plastic strain for the non-aged SAC305 and SAC-Q solder joints 158

Figure 7.22: The fatigue exponent constant (Coffin Manson model) versus aging time for SAC305 and SAC-Q solder joints 159

Figure 7.23: The fatigue ductility coefficient constant (Coffin Manson model) versus aging time for SAC305 and SAC-Q solder joints ... 160

Figure 7.24: Stress-Strain curves for shearing individual non-aged SAC305 and SAC-Q solder joints ... 161

Figure 7.25: A summary of the ultimate shear strength results with aging ... 162

Figure 7.26: The average degradation percentage of fatigue life with aging ... 163

Figure 7.27: The main effect plot of the shear strength for the aging time and solder alloy ... 164

Figure 7.28: the means of the shear strength for each solder alloys ... 165

Figure 7.29: The relationship between the aging time and shear strength for SAC305 and SAC-Q solder joints ... 165

Figure 8.1: Two-parameter Weibull distributions for three products ... 168

Figure 8.2: The test vehicle ... 171

Figure 8.3: The Thermal chamber ... 171

Figure 8.4: Thermal cycling profile ... 171

Figure 8.5: Two-parameter Weibull probability plots for SAC105 and SAC305 solder spheres at different surface finishes for the material 1 solder paste ... 172

Figure 8.6: The Fuzzy logic system ... 176

Figure 8.7: The inputs in the fuzzy system ... 179

Figure 8.8: The MFs for the scale parameter ... 179

Figure 8.9: The five output MFs ... 179

Figure 8.10: The COG method for computing the COM values ... 180

Figure 8.11: The multi-criteria fuzzy logic assessment tool for the reliability data flow chart ... 180

List of Abbreviations

ANNs	Artificial Neural Networks
BGA	Ball Grid Array
BPNN	Backward Propagation Neural Network
COG	Center Of Gravity
COM	Comprehensive Output Measure
ENIG	Electroless Nickle Immersion Gold
ImAg	Immersion Silver
IMCs	Intermetallic Compounds
MF	Membership Function
OSP	Organic Solderability Preservation
PCB	Printed Circuit Board.
RBFNN	Radial Basis Function Neural Network
SAC	Tin-Silver-Copper
SMT	Surface Mount Technology
SNR	Signal to Noise Ratio
THMT	Through-Hole Mount Technology
SAC-Q	Tin-Silver-Copper-Bismuth
B10	Earlier Failure Probability

Chapter 1 Introduction

1.1 Electronic Manufacturing

Electronics manufacturing is a leading manufacturing field in today's world. The electronics industry involves manufacturing, design and development, assembly, servicing of electronic components and equipment. Electronics is one of the most competitive and innovative industries. Companies compete and put much effort and money in the research and development of new, better electronic products. There are thousands of electronic products with a wide variety of applications. The industry of electronics manufacturing can be divided into four major categories which include: government products, industrial products, consumer products and electronic components. Aircraft, military, medical devices, in addition to communication and technology are covered under government products. For the Industrial products, they include a large variety of products such as large-scale computers, radio, and television broadcasting equipment, telecommunications equipment, and electronic office equipment. However, consumer products are the well-known televisions, cell phones, DVD players, smartphones, radios, video game systems, personal computers, electronic ovens, and home intercommunication and alarm systems. The final segment is the manufacturers that produce and sell electron tubes, semiconductors, and passive components. [1] Around $283 billion was the value of the global consumer electronics manufacturing industry according to a 2015 report published by IBISWorld. Because of the huge global market value of the electronics industry and its massive applicability, it is important to invest in better research and development to enhance their quality and extend their service life. [2]

On the other hand, the electronic products are classified into three main classes, where the first class is consumer products which have a low cost of failure and less than five years' service. The second class is industrial, telecom and dedicated products. The service life and cost of failure of this class is more than the service life and cost of failure of the first class. The critical product is the last class for product classifications which includes aerospace and medical device applications. The service life for the third class is more than twenty years, and the failure may lead to a threat on the human life. [3]

1.2 Electronic Packaging

Electronic packaging is one of the electronic manufacturing processes where some electronic components are assembled together; it is a method of creating the interconnection and operating environment to perform the required functions. The Printed Circuit Board (PCB), being used in many electronic devices, is a thin board made of fiberglass, composite epoxy, or other laminate material. This electronic board can form the base for which electronic components are connected. The connections on the PCB can be on one side or both sides. The PCB provides the required mechanical support for other electronic components and provides the required electrical connections between different components. Many active and passive electronic components can be connected to the PCB which include: transistors, resistors, capacitors, and integrated circuits. Conductive pathways are etched or printed onto the board, connecting different components on the PCB. [3] Electronic components can be mounted on the PCB using mainly two different methods which include: Through-Hole Mount Technology (THMT), and Surface Mount Technology (SMT). In the THMT, the connection between the package and PCB is formed by inserting the leads of through-hole components into the board via through-holes. Then, the leads, pads and the solder are connected together. The surface energy and the cooling process is

implemented to form a solid metallic bond. The Wave Soldering is one of the most common methods to perform the mounting in THMT under-which components are soldered simultaneously. In wave soldering components are inserted into or placed on the PCB. Their legs are first cut near the board and slightly bent over to keep the component in place. A wave of liquid flux is then used for which the PCB is moved over it, where the bottom side strikes the flux. The PCB is moved over a wave of melted solder after being heated. The soldering is completed when the solder attaches to the solder pads and component legs. This method of mounting has many drawbacks such as: cracked joints, lifted components, solder skip and poor penetration and a limited number of connections points. [4] In the SMT, Solder joints is another common way for component mounting. In the SMT, the components are mounted by a filler metal "solder". Solder refers to the alloy (a substance composed of two or more metals) that is used to connect the components to the PCB. Thus, the two pieces are joined together in what is called a solder joint**.** Several advantages are obtained when the SMT is utilized over THMT for instance: both sides of PCB can be used for the assembly process, obtaining finer pitch distance, reducing electrical noise and delay and the automating process is easier in SMT. By considering these two types of mounting, there are three types of assembly for the electronic packaging with different process sequences for each type. In the first type, the assembly on both sides of PCB are formed by SMT. For the second type, SMT is used for one side of PCB and the assembly in the second side is done by SMT and THMT. The last type of assembly is performed utilizing SMT for one side and THMT for another side. In the SMT, different alloys can be used for fabricating the solder joints, for instance: SAC solder alloys and leaded solder alloys. [5] The process of melting the solder paste (which is a mixture between solder powder and flux) by controlling the heat of the reflow oven in order to create the robust connections between the substrate and the electronics components is called the reflow soldering.

[6] During the reflow process the intermetallic compounds (IMC) are formed between the solder and the pad where the thickness of IMC depends on the reflow time and temperature. The increase on the IMC layer thickness leads to long term reliability problems where the amount of degradation in the lifetime and electrical performance is a function of the growing IMC layer [7]

There are three main functions of the electronic packaging process. These functions are signal distribution, power distribution, heat dissipation and protection. The first function, signal distribution is related to performing the main function of the electronic devices. The interconnections work as an information carrier between the electronic components where it should cogitate the topological and electromagnetic concerns. Most of the electronic components, especially, for active electronic components need electrical power to be active. This power is mainly provided from a power supply and it holds through these interconnections by considering the electromagnetic materials and structural features. Power distribution is the second function of the electronics packaging where the interconnections transfer the power between the power supply and the electronic components through the PCB and between the electronic components themselves. One of the major problems related to the active components is the generated heat where this significantly has a negative impact on the electronic components function, and the reliability of the solder joints and other interconnections. Therefore, the heat dissipation is very important to protect the electronic components from failing due to heat and it is the third function of the electronics packaging. The structure and the materials of components and interconnection should be considered when the methods of electronics packages are utilized in the cooling system. The electronics packaging is also used to protect the interconnections and components from failures due to mechanical, chemical and electromagnetic aspects and it is the last function of the electronics packaging.

The electronics packaging system is divided into four levels, these levels are level zero, level one, level two and level three. Level zero is gate to gate interconnections in the silicon chip, which is mainly about the fabrication of the silicon die from the single crystal silicon wafer and many solid-state electronic devices, for instance transistors, resistors and capacitors to build a functional electrical circuitry. The connection of the fabricated silicon chip that is formed in level zero to the package is called level one. In this level, the silicon chip is engaged to the lead frame or interposer layer which are connected to the silicon chip by using wire bonding or flip-chip technology. This connection provides a mechanical support, protection for active regions, thermal management and handling for the silicon chip. The second level is the connection between the package and the circuit board. Daughter card to the motherboard is the last level of the electronic packaging system which is basically a connection between two substrates. [5].

The electronic packaging technology is moving forward to use flip-chip technology, where the chip is flipped and bonded into the package or the PCB by utilizing solder bumps and using flux to prevent oxidation. On the other hand, in some applications for instance: biomedical devices, photonic devices and microelectromechanical system, removing the flux residual is hard due to the small gab between the chip and the substrate where the flux residual may influence the reliability of the solder. Therefore, the fluxless flip-chip soldering process is needed to avoid this issue. [8]

1.3 Solder Joints

Solder joints provide the electrical connections between the printed circuit board (PCB) and the electronic components where it provides the mechanical support of the electronic components. The most common material that was used in fabricating the solder joints was eutectic or near eutectic tin/lead (Sn/Pb) solder where it has robust reliability and outstanding solderability. Several

concerns were present because of the health issues that are associated with the leaded solder material and its effect on the environment. Over the last three decades, the electronic industries, and the research centers in the U.S and in the world worked in developing reliable lead-free solder alloys being considered as green products. The most common materials that are used in manufacturing the lead-free solder joints are tin, copper, silver, bismuth, antimony, indium and zinc. With this wide variety in the solder joint materials and because any failure in the interconnections can most likely lead to ruin the overall system, it is vital to investigate which optimal solder alloys can be used in fabricating the solder joints. Several factors should be considered when the solder alloys are to be selected. The mechanical and chemical properties, cost, manufacturability and reliability are some of the major factors that should be considered when discovering the optimal solder alloys. [9-11] Sn-Ag-Cu (SAC) alloys are one of the most common solder alloys that are widely used in different applications in surface mounts packaging technology that starts from daily used products for instance: cell phones, TVs and cameras and ends with heavy duty applications, such as: military, aerospace and aircraft. The ternary eutectic temperature for SAC alloys is 217 ºC which is higher than 183 ºC for Sn-37Pb solder. This leads to some difficulties for SAC alloys in highly refined electronics assembly sequence. This issue is solved by utilizing high/low temperature solder hierarchy pairs of SAC alloys (preassemble) and other lead-free solder alloys to permit effective multi-chip module assembly. [12] The percentage of the silver in the SAC alloys affects the performance of solder joints. For example, if the percentage of the silver on SAC alloys is 3.0% or lower, a better drop shock resistance is obtained with low cost compared to a high silver percentage. On the other hand, a higher percentage of silver in the solder joint leads to an increase in the thermal cycling reliability. [13] The main advantages of the SAC alloys compared to other lead-free alloys are their solderability and superior mechanical strength.

SAC alloys have lower melting temperatures compared to 965Sn-35Ag binary eutectic alloys where this is considered as an advantage for SAC alloys for electronic applications. [14] On the other hand, nonsignificant differences are found between high-Ag and low-Ag in terms of chemistry, thickness and grain size of $(CuNi)_6Sn_5$ and $(NiCu)_3Sn_4$ intermetallic compound layers. [15] SAC solder alloys could have better reliability when they are doped with Mn or Ce. For example, low Ag SAC alloys show a higher drop test and dynamic bending reliability when they are doped to Mn or Ce to form SACM or SACC. [16]

1.4 Surface Finish

The surface finish is applied into the PCB where the main purpose of the surface finish is to prevent the Cu oxidization which in turn will enhance the component soldering. The most common surface finishes are Hot Air Solder Leveling (HASL), Ni/Au Electroless Process, Ni/Au Electroplating Process, Pd or Ni/Pd Electroless Plating, Immersion Silver, Immersion Tin and Organic Solderability Preservative (OSP). All the surface finish types start after curing the solder mask by cleaning the exposed copper. The HASL surface finish is performed by applying the flux and dipping into Sn/Pb solder. The hot air knives are utilized to remove the excess solder away from the pads while the solder is still molten. As a result from this process, a thin layer of solder is formed over the copper. Some issues are associated with the HASL surface finish, for example waves in the plated surface, uniformity in the solder paste, board warp, delamination and damage to the plated holes. [17]

The process of applying the Ni/ Au electroless surface finish is exploited after applying a solder mask into the PCB by implementing the electroless Ni over the exposed copper, and then this is followed by a layer of gold. The immersion Au process is used in this surface finish as well. This process affords a good wettability and flat and uniform surface. Brittle interfacial fracture issues

are addressed for this type of surface finish. [18] The Ni/ Au electroplating surface finish basically contains Ni coating which provides uniform surface and the Au-finish affords a good wettability with high strength. The issue that is associated with this type of surface finish is "black pad" which has effects on the pad site. The black pad is observed after removing the BGA which is basically a fracture in the solder joint leaving an open circuit with dark corroded nickel. [19, 20] Immersion Ag is another type of surface finish, where using this type of surface finish reduces the possibility of forming the embrittling Au-Sn intermetallic compounds (IMCs). The simpler operation of applying, providing a solderable coating and low cost are the main advantages of immersion Ag surface finish. [21] In the immersion tin surface finish, two layers of Cu_3Sn and Cu_6Sn_5 are formed between the Sn and the Cu layer. The growth in the thickness of these layers depends on the temperature and time. Sn/Cu intermetallic compound is formed by consuming the Sn and the wetting of the immersion tin depends on the amount of free tin remaining on the surface and the level of oxidation. Because of immersion tin, a thin layer on the substrate is formed which gives a good solderability feature. In order to prevent the corrosion, the inner surface of copper water tubing is used to apply the immersion tin surface finish. Tin whiskers are formed with increasing the time which results to decrease the reliability. [22, 23] In the OSP surface finish, a temporary layer is used to prevent the copper oxidation by penetrating the organic coating into the exposed copper, where the organic coating is dissolved into the flux and molten solder before wetting onto the copper surface to form the solder joint. The thermal resistance and anti-oxidation of the copper surface are important factors for the thermal processes that are required before attaching the solder ball onto the OSP substrate. There are two methods for applying the OSP surface finish in order to protect the copper surface. The first method uses the resins or active resins for preflux where this method is not considered as the ideal method. The second method utilizes benzotriazoles

imidazole chemistries which is considered to be the best way for applying the OSP surface finish. The OSP surface finish is cheap compared to other surface finish types, has an excellent pads coplanarity, has consistent solderability, and it is easy to find any deteriorated copper visiually. On the other hand, it has limited shelf life, which is usually between 6 to 12 months, and it is too sensitive to any physical contact and can degrade very quickly in high humidity or high temperature environments. [24]

1.5 Fatigue Life Issues for the Interconnection Materials under Harsh Environments

The electronic packaging system fabricated by combining different materials and alloys, may contain metals, ceramics and polymers. Most of the reliability issues came from this diversity on the building materials where each of these materials has its own thermal and mechanical properties. The interconnection materials that connect the substrate with the electronic components and provides mechanical support for the electronic package is the weakest part in the electronic package. Any reduction in the reliability of the interconnection materials leads to reduce the reliability of the overall electronics system. The differences in the Coefficient of Thermal Expansion (CTE) of the electronic packaging materials is one of the major factors that affect the reliability of the interconnection materials. The differences in the expansion of other electronics packaging materials lead to generate shear stress on the interconnection materials. In harsh environments with high thermal cycling on elevated temperatures, the interconnections are exposed to high frequent shear stress on different directions which is called fatigue shear stress. In addition, using the interconnections in elevated temperature environments leads to evolutions of the material properties of the interconnection materials. Because of these issues, a reduction on the reliability of the interconnections is expected when it works in elevated temperature environments. Working in vibrations, mechanical shock and bending stress environments affect the reliability of

the interconnections in different ways which results in making the feebler interconnections. [25, 26]

To predict the reliability of the interconnections under different working conditions, the acceleration life test is utilized where performing the experiment at normal conditions is impossible in most cases. The acceleration life test is performed by increasing the level of stress, the frequency of the cycles, or temperature to achieve failures in a reasonable time and simulate the normal conditions when it is applied for a long time. In order to predict the life at normal conditions, the fatigue life model under the accelerated conditions is constructed, and the accelerated factors or the reliability prediction model is found. [27]

1.6 Problem Statement

Solder joint is an interconnection material that is utilized to provide mechanical and electrical connections between the electronic components through the PCB. Solder joints that are used in harsh environments are usually exposed to thermal and mechanical stresses and strains which might affect its service time. One of the most common stresses that are associated with the solder joints is shear stress. The alternating shear stress on the solder joints leads to fatigue shear stress. The main reason for the fatigue shear stress is the thermal cycling process that is common in temperature changing environments. Due to the cyclic changes in the working temperature from elevated temperatures to low temperatures and the differences in the thermal expansion coefficient of the electronic package system, fatigue shear stress is generated when the solder joints are exposed to the thermal cycling process. Most of the research conducted the fatigue specifications of the solder joints from testing the bulk materials with a rectangular or circular cross-section that is typically in “dumbbell” type. Usually, the tested bulk material is fabricated from rod or tubes. [28] Acquiring the fatigue specifications of the solder joints from a bulk sample is not accurate for

different reasons, for instance: the intermetallic compound (IMC) layer is not presented in the bulk sample, but it is presented in the solder joints, the differences between the bulk sample and actual solder joint in precipitate distributions, crack propagation modes and energy accumulation modes, the variation in the bulk sample size compared to realistic solder joints, [29] and the effect of the surface finish that is used in the electronic packaging on the solder joints reliability. [30] According to the above reasons, the mechanical and the fatigue properties for the bulk sample don't represent precisely these properties of the realistic solder joints and leads to wrong estimations about the service life, the working conditions and the expected performance for solder joints. As a summary, the structure for solder joints is more complicated than the structure of bulk samples and using the thermal and mechanical properties, and fatigue behavior for bulk samples to represent these properties leads to an inappropriate estimation. This can cause a serious problem when it is used in the realistic service conditions and especially for critical applications, for instance, aerospace, airplane and medical devices. Some studies are investigating the fatigue behavior of the solder joints in the real service conditions under different aging conditions by applying the thermal cycling accelerated test on actual solder joints where the tracking of the signals that came from the solder joints are utilized to identify the failures. On the other hand, few studies tested the solder joint in realistic service conditions to find the mechanical properties and the fatigue behavior of the solder joints where these tests are the shear stress, fatigue shear stress, strains and drop test.

The reliability prediction models and degradation models of the solder joint materials at different aging conditions are investigated by using the bulk sample to represent the reliability degradation models for the solder joint. Some studies explored the reliability model for the solder joints in realistic service conditions under different aging conditions by utilizing the thermal cycling test for assessing the reliability. Few studies are working on developing the reliability prediction

models, mechanical properties and degradation models for the actual solder joint under a certain level of aging. However, there is a gap in the research on investigating the reliability prediction models and degradation models and discovering the mechanical properties and fatigue behaviors of different solder joint materials in realistic service conditions under different aging times and aging temperatures.

To find the reliability model for the actual solder joint under certain service conditions, the fatigue data from the accelerated life test should be fitted using a proper distribution. The most common distribution that is utilized to represent the reliability model is the Weibull distribution, two parameters are used to determine the reliability model based on the Weibull distribution. These parameters are θ which is the scale parameter and β which is the shape parameter. Sometimes, a third parameter, the location parameter, is required to construct the reliability model. [31] The optimization process to find the best choice of the electronic packaging parameters, for example, the solder joint material and the surface finish type at certain service condition is vital to achieve a better performance and the lowest cost with consistent results. The most common method that was used in the previous research to assess the reliability of the solder joints among different alternatives is done by comparing the alternatives based on the scale parameter. In this study, a new methodology is proposed to efficiently find the optimal alternative by identifying different process performance responses. Different methods are utilized for optimizing the process performance for a single response problem, for example: mean effect plots and Taguchi method, where those two methods have some difficulties to deal with multi-response problem. On the other hand, the large variability on the shape parameter between the alternatives complicates the slection of the optimal alternative. Different methods can be utilized to compare and assess the reliability of different alternatives, for example mean and variance, scale parameter from Weibull

distribution, signal to noise ratio, value at risk, conditional value at risk and the earlier failure probability. The earlier failure probability is achieved from the Weibull distribution where usually, B10, which is the 10% probability of surviving of the solder joint and it is used to represent the earlier failure probability. [10] There is a limited research for considering all these responses to assess the reliability in general and especially for the solder joints. To deal with this issue, the multi-response optimization problem is represented to obtain the optimal factor levels. There is abundancy in the research that investigated different methods to deal with multi-response problems, for instance: artificial neural networks (ANNs), fuzzy logic, fuzzy Taguchi method, neural fuzzy Taguchi method, genetic algorithm, utility method, goal programming, grey fuzzy method, principal component analysis, fuzzy regression and surface response methodology. On the other hand, there is no efficient method used in the multi-response problem in all cases. [32]

1.7 Research Objectives

This research aims to assess the reliability and determine the mechanical properties for the actual solder joints in real operating conditions. The reliability and the mechanical properties of the solder joints in harsh environmental conditions are determined by different factors, such as surface finish and solder joint materials. To obtain the main objective, several goals should be reached which are represented in the following points.

1- Construct a suitable procedure to test the reliability of individual solder joints in realistic service conditions which include designing the fixture for isothermal shear fatigue test and preparing the testing boards.

2- Determine the fatigue behavior and mechanical properties of solder joint alloys at different stress loads in real-life service conditions.

3- Investigate the effect of different levels of aging time and temperature on the reliability and mechanical properties of the solder joint alloys in real-life service conditions.
4- Develop robust reliability models and degradation models for the solder joint alloys in order to predict the fatigue life of the solder joints at different aging conditions and stress loads.
5- Study the effect of aging at different temperatures, times and stress loads on the plastic strain and the inelastic work per cycle for the solder joint alloys.
6- Utilize a robust methodology to explore the optimal system packaging parameters among different alternatives in order to acquire the required fatigue behavior for the solder joint alloys.

1.8 Dissertation Organization

The dissertation is composed of nine chapters. The first chapter contains a general introduction about the electronics manufacturing and electronics packaging and describes the problem statement and the research objectives. Chapter two contains a general background about the reliability in general, solder joint alloys reliability, artificial neural networks, fuzzy logic, and Taguchi method. Chapter three provides a deep literature review about the most common reliability issues in the electronics, the effect of the isothermal aging on the reliability and mechanical properties for the different solder joint alloys, reliability prediction model for the solder joints and applications of the Taguchi method, fuzzy logic and the artificial neural networks on the reliability. Chapter four covers the experimental procedure, experimental design, preparing the testing boards, the actual experimental studies and the general methodology of data analysis. The effect of isothermal aging on the reliability of SAC 305 solder joints with OSP surface finish under different stress amplitudes and aging times are studied in chapter five. Chapter six addresses

the effect of aging temperature on the fatigue behavior and the ultimate shear stress of SAC 305 solder joints with OSP surface finish under different stress amplitudes and aging times. The effect of adding bismuth to the SAC-based solder alloys (SAC-Q) on their reliability properties at different aging conditions and stress amplitudes are described in Chapter seven. Chapter eight covers a new proposed multi-response optimization methodology for the electronic packaging parameters and a validation case study. The conclusion is summarized in chapter nine.

Chapter 2: General Background

2.1 The Reliability

One of the major concepts that is related to the reliability is failure. The incapability of the item to perform the required function is called failure. Therefore, reliability is the probability that an item or system will execute the predefine functions over a certain period of time when it works under the stated operating conditions. The quality over time and the probability of surviving for a given period of time also are other definitions for reliability. The main purposes of the reliability and maintainability engineering are that of reducing the failure and down time and enhancing the process performance, safety and product life by studying, characterizing, measuring and analyzing the failures. In the last decades, industries in the world started to focus more attention on studying the reliability of the components or system due to several reasons such as: the industrial system became more complex, the increased competition between the industries in terms of product quality, the new regulations and government laws to meet reliability and maintainability specifications and finally, the increased warranty problems due to increasing the cost of failure. There are two main categories of the reliability. The first category is time dependency where the reliability in this category is calculated as a function of time and the time could be continuous or discrete. The second type is cycle dependency where the reliability is determined as a function of cycles. In order to predict the reliability, different methods are utilized to estimate the reliability as a function of time or cycle, for example: the empirical methods, fitted to normal distribution, to exponential distribution, to log-normal distribution, to Gamma distribution and to Weibull

distributions. The least square method and the maximum likelihoods method are mainly applied as a parametric estimation method of the failure data distribution. [33]

2.1.1 Reliability Functions

The reliability function can be constructed from the definition of the reliability which is the probability of surviving under stated operating conditions for a certain period of time. The general reliability equation is expressed in equation 2.1. Where *T* is a continuous random variable for the time to failure, *t* is the predefined time under which the reliability is calculated and *R(t)* is the reliability at time *t*.

$$R(t) = \Pr\{T \geq t\} \qquad (2.1)$$

Where $R(t) \geq 0, R(0) = 1 \; and \; \lim_{t\to\infty} R(t) = 0$

The probability of failure before time *t* (*F(t)*) function is represented in equation 2.2. Where *F(t)* represents the cumulative distribution function (CDF).

$$F(t) = \Pr\{T < t\} = 1 - R(t) \qquad (2.2)$$

Where $F(0) = 0 \; and \; \lim_{t\to\infty} F(t) = 1$

Equation 2.3 can be used to find the probability of failure at time *t* (*f(t)*) which is represented in the probability density function (PDF).

$$f(t) = \frac{dF(t)}{dt} = -\frac{d\,R(t)}{dt} \qquad (2.3)$$

Where $f(t) \geq 0 \; and \; \int_0^\infty f(t)dt = 1$

To find an instantaneous rate of failure at time t, the hazard rate function or failure rate function (*λ(t)*) should be defined by using the conditional probability as shown in equation 2.4.

$$\lambda(t) = \lim_{\Delta t\to\infty} \frac{-[R(t)-R(t+\Delta t)]}{\Delta t} * \frac{1}{R(t)} = \frac{f(t)}{R(t)} \qquad (2.4)$$

The cumulative failure rate over a certain period of time t ($L(t)$) is represented in equation 2.5.

$L(t) = \int_0^t \lambda(t')dt' = -\ln R(t)$ ……………………………………………………………(2.5)

The average failure rate between two times t_1 and t_2 ($AFR(t_1,t_2)$) is calculated by utilizing equation 2.6.

$AFR\ (t_1, t_2) = \frac{L(t_2)-L(t_1)}{t_2-t_1}$……………………………………………………………(2.6)

In general, the failure rate has been characterized into three categories: increasing failure rate (IFR), decreasing failure rate (DFR) and constant failure rate (CFR). The hazard rate with its three categories is represented in the Bathtub curve. The Bathtub curve simulates the failure behavior for any product. As shown in Figure 2.1, the Bathtub curve constructed from three curves: early failure "Infant Mortality" curve, random failures curve and wear out curve. The Bathtub curve is the summation of the three curves which describes the failure behavior of the product. The three categories of the failure rate can be identified from the Bathtub curve.

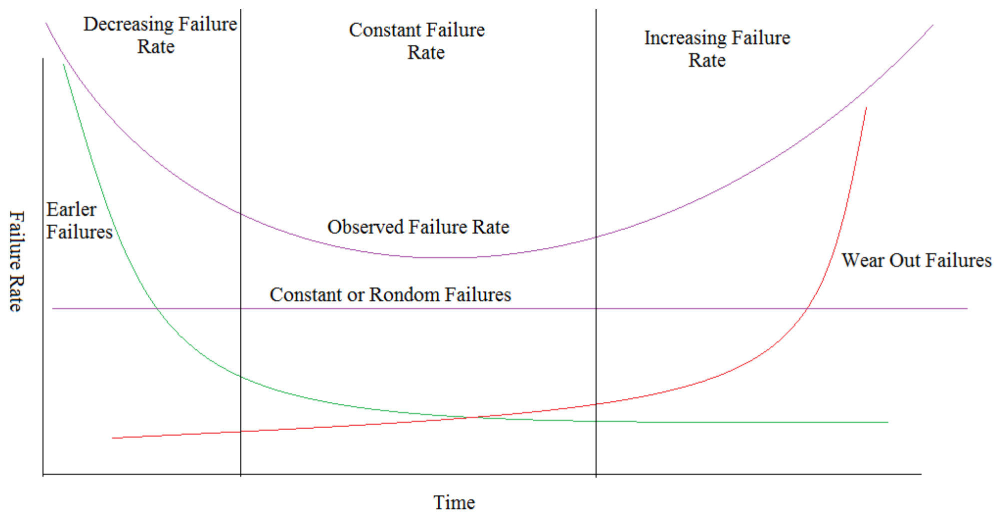

Figure 2.1: Bathtub Curve.

2.1.2 Accelerated Reliability Test

In order to improve and quantify the reliability, obtain the required safety and reliability goals, the reliability life test is implemented to assess the reliability at the stated operating conditions. There are different reliability life tests that are performed for different purposes. Those tests are Burn-in and screen test, acceptance and qualification test, sequential test, accelerated life test and experimental design. In this research, the accelerated life test was performed to assess the reliability in the electronics packaging field. In general, applying the regular reliability life test to assess the reliability takes a long time and in most cases is infeasible. Therefore, the main benefit from the accelerated reliability test is that of performing the reliability test in a shorter time than the regular reliability life test. Seven types of accelerated reliability test data can be obtained to assess the reliability. The first type is complete data which means all samples failed after a certain time or cycle. If the test is stopped after a specific time without achieving complete failure for all samples, the obtained data are classified in the second type which is called type I censor. The type II censor data are found when the accelerated reliability test is finished after obtaining a certain number of failures which is the third data type. The forth data type is close to the second type for which the test is stopped after a predefined time but with a certain number of removed samples where those samples are removed from the test for different purposes, for instance: test the microstructure of the samples after a specific time from the test start point. This data type is called type I k multiply censor. The type II k multiply censor data is similar to the third data type with specific amount of samples that are removed during the test which is the fifth type of the reliability data. The sixth reliability data type is the failure data that are obtained when the reliability test is ended after a certain time and the failed samples are replaced immediately during the test which is called type I replacement. The last type of the reliability data is called type II replacement. In this

data type, the reliability test is completed after a certain number of failures where the failed samples are replaced directly with other new samples during the experiment. In addition, those types of the reliability data are applicable to other types of the reliability test. The accelerated reliability life test is performed in different ways such as: increasing the number of samples, increasing the number of cycles or operating time per sample (frequency) and increasing the stress level that leads to initiate failures. In order to predict the product life at real-life service conditions, the adapted equations should be created with specific multiplier to convert the product life from the accelerated conditions to normal conditions. This multiplier is called accelerated factor (AF). Different research investigated different models to find the accelerated factor. The constant-stress model is one of the models that are utilized to estimate the accelerated factor. In this model, the failure mechanism will have the same behavior when the stress level is increased where the failure mode doesn't change. The linear equation that is applied to transform the product life in the high stress to a product life in normal stress is shown in equation 1 where t_n is the product life at normal stress and t_s is the product life at high stress. [33]

$$t_n = AF * t_s \quad \text{(1)}$$

Arrhenius model is another model applied when the accelerated reliability life test is performed by increasing the environment temperature. The accelerated factor in this model is obtained by using equation 2. [34]

$$AF = \exp[B\left(\frac{1}{T_1} - \frac{1}{T_2}\right)] \quad \text{(2)}$$

Where B is a constant, T_1 is the temperature (Kelvins) at normal conditions and T_2 is the temperature (Kelvins) at accelerated conditions. When the reliability acceleration test is implemented by increasing the working temperature and stress level, Eyring model can be utilized to find the accelerated factor by using equation 3.

$$AF = \left(\frac{T_2}{T_1}\right)^A \exp[B(\frac{1}{T_1} - \frac{1}{T_2})e^{C(S_2 - S_1)} \quad (3)$$

Where A, B and C are constants, T_1 is the temperature (Kelvins) at normal condition, T_2 is the temperature (Kelvins) at accelerated condition, S_1 is the stress level at normal condition and S_2 is the stress level at accelerated condition. [35]

Coffin-Mason model is another degradation model utilized when the accelerated reliability life test is implemented by performing the temperature cycling at different stress levels. The accelerated factor can be calculated by using equation 4.

$$AF = \frac{N_L}{N_H} = \left(\frac{\Delta T_H}{\Delta T_L}\right)^b * (\frac{f_L}{f_H})^{-a} * \exp(\left(\frac{E_A}{K}\right) * \left(\frac{1}{T_{KL}} - \frac{1}{T_{KH}}\right)) \quad (4)$$

Where N_L is the number of cycles that is required to initiate the failure at low stress level temperature cycle, N_H is the number of cycles that is required to initiate failure at high stress level temperature, ΔT_H is the temperature range during temperature cycle at high stress level, ΔT_L is the temperature range during temperature cycles at low stress level, f_L is the number of cycle per day at low stress level, f_H is the number of cycles per day at high stress level, T_{KL} is the maximum absolute temperature at low stress level, T_{KH} is the maximum absolute temperature at high stress level, a is cycling frequency exponent, b is temperature rang exponent, K is Boltzman's constant and E_A is the activation energy. [36]

In all of the previous models, the reliability model is determined as a function of time or cycle only under the stated operating conditions. In many applications, the time is not only the factor that is used to find the reliability model. There are other factors that may have significant impact on the reliability where those factors might include: voltage, temperature, current or other measure of stress or environment. Therefore, the external operation conditions and inherent characteristics of the component should be included in the reliability model. The covariate model was proposed to combine these factors in the failure distribution. In the covariate models, one or more of the

distribution parameters is employed as a function of the explanatory variables where the correlation between the covariates and the parameter value should be detected. Proportional Hazard models are set from model categories of the covariate models where the individual hazard component functions in those models are relational to each other. Location –Scale Models are another family of the covariate models. The location–scale model can be obtained from equations 2.5 and 2.6.

$\mu(\boldsymbol{x}) = \sum_{i=0}^{k} a_i x_i$……………………………………..…………………….…………(2.5)

$Y = \mu(\boldsymbol{x}) + \sigma z$……………………………………..…………………………........(2.6)

Where $\sigma>0$, $\boldsymbol{x}$ is a covariate vector and z has its own distribution without depending on the covariate vector $\boldsymbol{x}$. Static models are a family from the physical model families where the reliability in those models is not a function of time, and the failure is initiated by the instantaneous stress. Four types for the static models were established. The first model type from the static models is random stress and constant strength where the reliability function can be described as shown in equation 2.7.

$R = \int_0^k f_x(x)dx = F_x(k)$………………………………..…………………………………(2.7)

Where k is the system strength which is constant, $f_x(x)$ is the probability density function for the stress. Constant Stress and Random Strength is the second type of the static model where its reliability model can be defined as shown in equation 2.8.

$R = \int_s^\infty f_y(y)dy = 1 - F_y(s)$…………………………………………………………(2.8)

Where s is the constant stress, $f_y(y)$ is the probability density function for the system strength. When the stress and the system strength are random, the reliability becomes the probability of having the stress less than the system strength where the reliability model can be presented as shown in equation 2.9.

$$R = \int_0^\infty R(y) f_y(y) dy \quad (2.9)$$

The last type of the static models is the mixed distributions with analytical solutions. In this case, the system strength and the applied stress are random, but each one of them has different probability distributions. To find the probability model for this case, numerical method and Monte Carlo simulation could be a solution.

Dynamic reliability could be a consequence of the dynamic load where the load is applied on a system repetitively over time. This case describes the Dynamic models. Three types of these models are investigated. When the load is applied in the known interval of time, the dynamic models follow the first type which is called a periodic load. On the other hand in random load, the second case is originated when the time between the applied loads is totally random where the probability distribution of this time can be defined as a Poisson random distribution. In both cases, the distribution of the system strength is assumed to have the same value over time. The third type is the random fixed stress and strength where determining the stress and the strength of the system is completely random for one time and they will be fixed for each cycle.

Physics –Of – Failure models are another family of physics models families. In these models, the failure mechanisms and the root causes of the failures are originated to develop a mathematical or deterministic model in order to predict the reliability of the system. The mathematical model is developed to predict the time of failure based on the material properties, geometry at failure site, environment conditions and operating profile. In general, there are five steps that are defined in order to develop the physics failure models. These steps start with finding the failure mechanisms and sites, then developing a deterministic model, predicting the reliability under certain operating and environmental profile for given components with specific properties, calculating the fatigue life and ends with a design modification to increase the service life. [33]

2.1.3 Failure Analysis

In order to improve the reliability of the product, failure analysis process is the most effective way to achieve the reliability goals which is mainly applied by using failure mode, effect and criticality analysis (FMECA). The FMECA process is a continuous iterative process which starts with identifying the failure modes and finding the corrective action. To apply the FMECA process, five major sectors in engineering should collaborate. Those sectors are reliability engineering, manufacturing engineering, quality engineering, maintainability engineering and product engineering in addition to the facilitator. There are nine steps that should be followed when the FMECA process is implemented.

The first step is Product Definition which is mainly used to identify the product components and its design with the purpose of detecting which components have larger opportunity to fail. The definition includes functional and physical descriptions of the product where the functional analysis offers an initial description regardless to the hardware operation and maintenance process. On the other hand, the physical description contains more details about the product components, subassemblies and their relationships by constructing an indenture diagram. The most important step is identifying the Failure Mode which is the second step. The failure mode can be determined physically (hardware approach) or functionally. Failure mode can be observed or predicted by initiating the reliability tests and analyzing the reliability block diagram. The main purpose from analyzing the failure mode is to predict which component or part will be failed by determining the observable manners of failures in specific operational and environmental conditions. The third step is Determination of Cause. In this step, the root causes should be identified where understanding the failure mechanism is important to identify the corrective action in order to eliminate the critical failures. The key point to implement this step is the differentiating between the secondary causes

and the primary or root causes. The process of exploring the effect of the failure on the product is vital to find the impact of failure on the customers, and it could have a negative impact on the maintenance capability and the safety. The effect can be complete, partial or no impact on the performance of the part, for example; if redundant component fails, the system performance will not be affected but the system reliability will be decreased. Therefore, the Assessment of Effect is the fourth step in the FMECA process where the strong relationship between Assessment of Effect, identification of failure mode and determination of cause is demonstrated.

The fifth step is Estimation of Probability of Occurrence where it relates to detect the failure mode that is more observed compared to other failure modes. The preliminary estimation is based on the existing databases, experiences, reliability specification and comparability with other components and parts that have identified reliability. If the database for specific component is not sufficient to estimate the reliability or the probability of occurrence, the subject ranking with scale from one to ten can be implemented to quantify the reliability of this component. Estimate of Detection is another key step that is applied in FMECA process which is the sixth step. The main purpose of this step is to determine the probability of detecting the failure for current process controls before the product spreads to the last customer. Classification of Severity is a vital step to initiate a severity ranking in order to assess the weightiness of the impact of the failure mode on the customer. The severity of the failure can be classified into four categories. Those categories are, negligible, which is about the minor failures with no effect on the system performance, marginal where in this failure category the performance is partially reduced, critical with complete losing of system performance and catastrophic which it may case major damage, loss of life or injury.

After demonstrating the previous steps the criticality of failure mode should be quantified by the probability of detection, severity of the failure mode and the reliability of the system where those

compensations represent the Computation of Criticality. Several indices are demonstrated to assess the criticality of the failure mode. The risk priority number (RPN) is more popular index which is basically a multiplication of three ranking factors: severity ranking (S), the probability of occurrence ranking (O) and the detection ranking (D). The equation 2.10 is used to find the RPN.

$$RPN = (S) * (O) * (D) \qquad (2.10)$$

The range of the PRN is between 1 and 1000 with a higher number indicating a more critical failure mode. The last step in the FMECA process is Determination of Corrective Action which is also related to the type of the problem. The main purposes of the corrective actions are decreasing the probability of occurrence, increasing the probability of detection, removing the root causes of the failure and reducing the severity of the failure. The purpose of the FMECA process is to improve the reliability of the product during the design stage. On the other hand, there are other purposes for the FMECA process for instance: addressing the system availability, safety, maintainability, and supporting requirements. [33]

2.1.4 Statistical Models for Lifetime Data

Several probabilistic methods were proposed to represent the probability of failure occurrence. This is done to build an estimation reliability model as a function of time or cycle in order to predict the service life of a product or system. Basically, two approaches are demonstrated to deal with the failure data for developing the reliability model. The first approach is constructing a reliability model directly from the failure data by using the empirical reliability function. The other approach is fitting the failure data to a theoretical distribution.

2.1.4.1 The Empirical Method

To apply the empirical method, the failure data should be classified in one of the four failure data categories. These categories are ungrouped complete data, grouped complete data, ungrouped

censored data and grouped censored data. The grouped data means that the failures are counted in time intervals. When all samples are completely failed, the data type is complete data otherwise it is a censored data.

For the ungrouped complete data class, three approaches were proposed to predict the reliability based on the failure data. In the first approach, $t_1, t_2 \ldots\ldots, t_n$ is the time to failure data and n is the number of failures. The reliability function in this case is expressed in equation 2.11.

$$R(t_i) = \frac{n-i}{n} \quad \text{(2.11)}$$

The issue with this approach is that the probability of surviving after t_n is equal to zero and this is not logical in practical applications.

In the second approach which is the most common approach, the reliability function can be described as shown in equation 2.12.

$$R(t_i) = \frac{n+1-i}{n+1} \quad \text{(2.12)}$$

The median position was utilized to formulate the reliability model where the median positions are a function of i and n. this approach is used because the probability of failure is skewed for values i close to zero and n. the reliability model using the third approach is shown in question 2.13

$$R(t_i) = 1 - \frac{i-0.3}{n+0.4} \quad \text{(2.13)}$$

In grouped complete data, the failures are counted in the time interval where $n_1, n_2 \ldots\ldots n_k$ are the number of units that are survived at times $t_1, t_2 \ldots\ldots t_k$ respectively. The reliability function for the group complete data can be expressed as shown in equation 2.14.

$$R(t_i) = \frac{n_i}{n} \quad \text{(2.14)}$$

For the third category, the ungrouped censored data, n is the number of samples that are placed in the test and r is the number of failures where r is always less than n. Different methods are created

to determine the reliability function. The first method is product limit estimator where the equation 2.12 was utilized to formulate the reliability equation as shown in equation 2.15.

$$R(t_i) = \left(\frac{n+1-i}{n+2-i}\right)^{\delta_i} R(t_i - 1) \text{.......................................(2.15)}$$

Where $\delta_i = \begin{cases} 1 & if\ failure\ occurs\ at\ time\ t_i \\ 0 & if\ the\ censoring\ occurs\ at\ time\ t_i \end{cases}$

The Kaplan- Meier form of the product estimator is the second method for estimating the reliability function for ungrouped censored data which is the most popular method that is applied in this case. Where t_j is the ordered failure times and n_j is the is the number of remaining samples without failure before the *jth* failure. The basic assumptions of this method are that there is no coinciding between the failure times and censoring times and the failure times is without any ties. Therefore, the reliability function can be formulated as shown in the equation 2.16. Where *R(t)=1* when the *t is* between zero and t_1.

$$R(t) = \prod_{\{j:t_j \le t\}} (1 - \frac{1}{n_j}) \text{.......................................(2.16)}$$

The last method that is employed to formulate the reliability function for ungrouped censored data is rank adjustment method. The main concept of this method is that the censored samples are affected by the rank of the sequence failures due to the probability of failing before or after the next failure. Equation 2.16 shows the reliability function using the rank adjustment method. Where i_{ti-1} is the rank order of failure time *i-1*, *RI* is the rank increment and *n* is the total number of samples under the risk.

$$R(t_i) = 1 - \frac{i_{t_i} - 0.3}{n + 0.4} \text{.......................................(2.16)}$$

$$i_{t_i} = i_{t_i - 1 + RI}\ , \qquad RI = \frac{(n+1) - i_{t_i - 1}}{1 + number\ of\ unit\ beyond\ present\ censored\ unit}$$

The last category of the reliability data is grouped censored data where the life Table is constructed to find the reliability function when the failures are counted in specific time range without achieving a complete failure for all samples. The life Table is commonly used in the medical research to estimate the probability of surviving of patients when they have a specific illness and they are treated by medical surgery. The reliability function is shown in equation 2.17. Where F_i is the number of failures at *ith* interval, C_i is the number of removal samples at *ith* interval, H_i is the number of remaining samples at t_{i-1}. H_i' adjustable number at risk, P_i is the conditional probability of surviving at the *ith* interval if it survives at t_{i-1} and R_i is the probability of surviving beyond the *ith* interval. [33]

$$R_i = \left[1 - \frac{F_i}{H'_i}\right] * R_{i-1} \qquad (2.17)$$

$$H'_i = H_i - \frac{C_i}{2}, \quad P_i = 1 - \frac{F_i}{H'_i}$$

2.1.4.2 The Random Probability Distributions

The second approach that is used to estimate the reliability is that fitting the failure data to a probabilistic distribution. Several distributions are demonstrated to develop the reliability model. Weibull distribution is the most common distribution that is utilized to describe the reliability for different product sectors. Other distributions could be valid in some cases to represent the failure processes, for instance: exponential, normal, log normal, gamma and log- logistic distributions. First, the exponential distribution or constant failure model is one from the most common distributions to describe the failures that are initiated due to random events. The failure data should be fitted to the exponential probability distribution when the failure rate is constant where it is the simplest failure distribution. To apply the constant failure model, the constant failure rate should

be considered as a basic assumption, $\lambda(t) = \lambda$ where λ is the failure rate value. The reliability function for the constant failure model is shown in equation 2.18.

$$R(t) = 1 - \lambda e^{-\lambda t} \quad (2.18)$$

Equations for the mean time between failure (MTTF) and median t_{med} which is the life time when the reliability equal 0.5 are shown in equation 2.19 and 2.20, respectively. [37]

$$MTTF = \frac{1}{\lambda} \quad (2.19)$$

$$t_{med} = \frac{0.69315}{\lambda} = 0.69315 * MTTF \quad (2.20)$$

The normal distribution is the most popular distribution for demonstrating random data in general where the data quality should have a significant fitting to the normal distribution for applying the majority of quality hypotheses. The normal distribution can be used to describe the failure behavior and wearout phenomena in some cases because of the relationship with the lognormal distribution to analyze lognormal properties. The reliability function when the failure data are fitted to the normal distribution is shown in equation 2.21.

$$R(t) = \int_t^{\infty} \frac{1}{\sqrt{2\pi\sigma}} \exp\left[-\frac{1}{2} * \frac{(t'-\mu)^2}{\sigma^2}\right] dt' \quad (2.21)$$

Where σ is the standard deviation and μ is the mean. Because of the complexity of the integration term in the reliability equation 2.21, the equation was solved numerically, and the data were generated in the Table after converting the data to standard value z which is called the standardized normal distribution Table. In order to simplify, equation 2.21 is converted to the standard form as shown in equation 2.22.

$$R(t) = 1 - \phi\left(\frac{t-\mu}{\sigma}\right) \quad (2.22)$$

Where the median time, MTTF and the mode time t_{mod} is equal to μ, and t_{mod} is the life time that has the largest probability of failure. In this case, the failure rate function is a function of time as shown in equation 2.23 and the density probability function is expressed in equation 2.24. [33]

$$\lambda(t) = \frac{f(t)}{R(t)} = \frac{f(t)}{1-\phi(\frac{t-\mu}{\sigma})} \quad \text{……………………………………………………...……..(2.23)}$$

$$f(t) = \frac{1}{\sqrt{2\pi\sigma}} \exp\left[-\frac{1}{2} * \frac{(t-\mu)^2}{\sigma^2}\right] \qquad -\infty < t < \infty \quad \text{………………………………...…….(2.24)}$$

If the distribution of the logarithmic failure time *T* is normal distribution, then the failure time distribution can be expressed as a lognormal distribution. The probability density function for the lognormal distribution is shown in equation 2.25.

$$f(t) = \frac{1}{\sqrt{2\pi s t}} \exp\left[-\frac{1}{2s^2}\left(ln\frac{t}{t_{med}}\right)^2\right] \qquad t \geq 0 \text{……………………………………………...(2.25)}$$

Where s is the shape parameter and the median time to failure is the location parameter. The MTTF and t_{mode} functions can be expressed in equations 2.26 and 2.67, respectively.

$$MTTF = t_{med} * \exp(\frac{s^2}{2}) \text{…………………………………………………………….....(2.26)}$$

$$t_{mode} = \frac{t_{med}}{\exp(s^2)} \text{………………………………………………………………………....(2.27)}$$

The reliability function for the lognormal distribution is obtained by integrating the probability density function that is shown in equation 2.25. The simplest form for the lognormal reliability function is found in equation 2.28 where the standardized normal distribution is utilized in this formulation to simplify the calculations. [38]

$$R(t) = 1 - \phi\left(\frac{1}{s} ln \frac{t}{t_{med}}\right) \text{………………………………………………………..(2.28)}$$

In the gamma distribution, when the summation of the independent exponential failure time equals the shape parameter, the failure distribution can be represented by the gamma distribution. The probability density function can be expressed as shown in equation 2.29.

$$f(t) = \frac{t^{\gamma-1}e^{-t/\alpha}}{\alpha^{\gamma}\Gamma(\gamma)} \qquad \gamma > 0,\ \alpha > 0 \text{..} (2.29)$$

Where γ is the scale parameter, α is the shape parameter and $\boldsymbol{\Gamma}$ is the gamma function. The reliability function is determined as shown in equation 2.30 by integrating the probability density function in equation 2.29.

$$R(t) = 1 - \frac{I(\frac{t}{\alpha}, \gamma)}{\Gamma(\gamma)} \text{..} (2.30)$$

Where $I(\frac{t}{\alpha}, \gamma)$ is incomplete gamma function and the solution for this term should be obtained numerically. Equations 2.31, 2.32 show the functions for the t_{mode} and *MTTF* respectively, for the failure data that follow the gamma distribution.[37]

$$t_{mode} = \begin{cases} \alpha(\gamma - 1) & \gamma > 1 \\ 0 & otherwise \end{cases} \text{..} (2.31)$$

$$MTTF = \alpha\gamma \text{..} (2.32)$$

The Weibull distribution is a very useful random probability distribution to describe the failure data in the stochastic frame because of the flexibility in the data fitting for the data shape and data scale terms. The Weibull distribution can be used to construct the reliability model for both increasing and decreasing hazard rate functions. Mainly, there are two types of Weibull distribution: two- parameter Weibull distribution and three- parameter Weibull distribution.

For the two- parameter Weibull distribution, the hazard rate function $\lambda(t)$ can be expressed as shown in equation 2.33.

$$\lambda(t) = at^{b} = \frac{\beta}{\theta}\left(\frac{t}{\theta}\right)^{\beta-1} \quad a > 0, b > 0 \text{..} (2.33)$$

Where θ is the scale parameter and β is the shape parameter for the Weibull distribution, where the behavior of the failure process can be demonstrated from the value of β. The probability failure function of the Weibull distribution can be expressed as shown in equation 2.34.

$$f(t) = \frac{\beta}{\theta}\left(\frac{t}{\theta}\right)^{\beta-1} e^{-(t/\theta)^{\beta}} \quad (2.34)$$

From equation 2.34, the reliability function can be formulated as shown in equation 2.35.

$$R(t) = e^{-(t/\theta)^{\beta}} \quad (2.35)$$

According to the reliability function in equation 2.35, the design life for the product at specific reliability *R* can be calculated using equation 2.36

$$t_R = \theta(-\ln R)^{1/\beta} \quad (2.36)$$

The *MTTF*, median (t_{med}), and mode (t_{mode}) can be obtained by utilizing equations 2.37, 2.38 and 2.39 respectively.

$$MTTF = \theta\Gamma\left(1 + \frac{1}{\beta}\right) \quad (2.37)$$

$$t_{med} = t_{0.5} = \theta(-ln0.5)^{1/\beta} \quad (2.38)$$

$$t_{mode} = \begin{cases} \theta\left(1 - 1/\beta\right)^{1/\beta} & for\ \beta > 1 \\ 0 & for\ \beta \leq 1 \end{cases} \quad (2.39)$$

In the three parameters Weibull distribution, t_0 is a minimum life time where the basic assumption is that no failure will occur until t_0. The third parameter is the location parameter t_0. For this type of distribution, the large failure data is recommended to ensure there is no possibility of failing until t_0. Equations 2.40 and 2.41 shows the reliability function of three parameters Weibull distribution and the hazard rate function respectively.

$$R(t) = e^{-(\frac{t-t_0}{\theta})^{\beta}} \quad (2.40)$$

$$\lambda(t) = \frac{\beta}{\theta}\left(\frac{t-t_0}{\theta}\right)^{\beta-1} \quad (2.41)$$

The previous equations for the two parameter Weibull distribution can be used to find the fatigue failure time specifications (*MTTF*, mode time, design life and median time) by adding the value of t_0 to the final answer for the aforementioned fatigue failure time specifications. [33]

2.1.5 Identifying the Candidate Distribution and Parametric Estimation

To find the best distribution to describe the failure data, a knowledge about the theoretical distribution features, statistical analysis and the failure behavior is required. There are six suggested steps that can be used to identify the candidate theoretical distribution. Those steps start with constructing a histogram for the failure data and performing descriptive statistics then, investigating the empirical failure rate, utilizing the existing knowledge about the failure process and it ends with employing the theoretical distribution characteristics and developing a probability plot.

After identifying the candidate distribution, and the parameter estimation, executing a goodness-of-fit test, the next step is to discover the best fit distribution for the failure data. Basically, two methods, the least square method and the maximum likelihood method, are applied to estimate the parameters for the theoretical distribution. On the other hand, the probability plot can be used to develop an initial parameters estimation by implementing the linear regression equation. In the least square approach, a linear plot will be obtained by plotting the x_i in the x-axis and y_i in the y-axis where those variables are calculated from equations 2.42 and 2.43.

$$x_i = \ln t_i \quad \text{(2.42)}$$

$$y_i = lnln\left[\frac{1}{1-F(t_i)}\right] \quad \text{(2.43)}$$

The linear regression mode can be constructed as a result from plotting x_i and y_i. Equation 2.44 shows the general linear model function.

$$y = a + bx \quad \text{(2.44)}$$

Where a and b represent the intersection of the linear plot with the y-axis and its slope. The least square method is applied to estimate constants a and b as shown in equation 2.45 and 2.46 respectively.

$$\hat{b} = \frac{\sum_{i=1}^{n} x_i y_i - \bar{x}\sum_{i=1}^{n} y_i}{\sum_{i=1}^{n} x_i^2 - n\bar{x}^2} \quad (2.45)$$

$$\hat{a} = \bar{y} - b\bar{x} \quad (2.46)$$

The second approach for the parametric estimation is the maximum likelihood method which is the preferable method for estimating the parameters of the candidate distribution because it has the best results in the goodness-of-fit tests. Equation 2.47 shows the likelihood function.

$$f_{x_1 \ldots, x_n(x_1 \ldots, x_n) = p^n (1-p)^{\sum_{i=1}^{n}(x_i - 1)}} \quad (2.47)$$

Where x_i represent the samples, n is the total number of samples and p is the maximum likelihood estimator (MLE). Equation 2.48 shows MLE function.

$$\hat{p} = \frac{n}{\sum_{i=1}^{n} x_i} \quad (2.48)$$

To determine the MLE for the probability distribution. The maximum likelihood function should be demonstrated by implementing equation 2.49. φ_k is unknown parameters where the main objective of this approach is to find the value of its estimators. [33]

$$L(\varphi_1, \ldots, \varphi_k) = \prod_{i=1}^{n} f(t_i | \varphi_1, \ldots, \varphi_k) \quad (2.49)$$

2.1.6 The Reliability of the System

The pervious approaches discuss the reliability estimation for an individual part or component. Several approaches were proposed to determine the reliability of the whole system where demonstrating the system reliability depends on the complexity of the system structure. In order to determine the system reliability, the system structure is classified into four main categories:

serial configuration, parallel configuration, combined serial and parallel systems and complex systems.

For the serial configuration, all of the components or parts in the system are connected in series as shown in Figure 2.2. Where *Ri* is the reliability of component *i*. the reliability function of the system can be expressed as shown in equation 2.50. Where *Rs(t)* is the reliability for the system at time *t*.

$$Rs(t) = R1(t) * R2(t) \dots * Rn(t) = \prod_{i=1}^{n} Ri(t) \qquad (2.50)$$

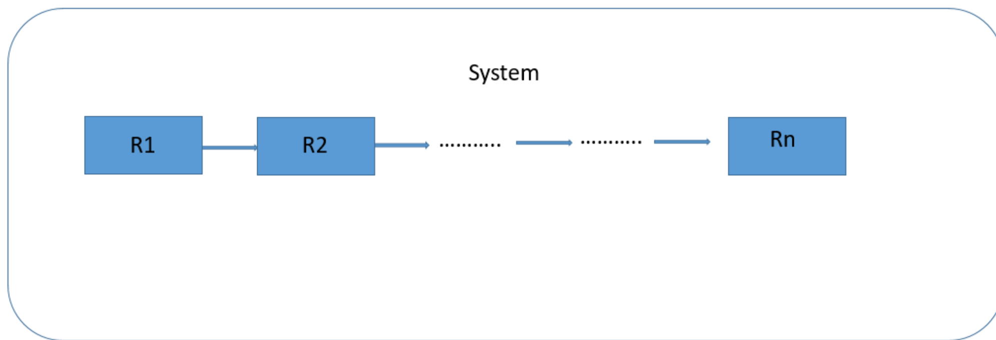

Figure 2.2: Serial Configuration

The second type of the system structure is the parallel configuration where it is basically constructed from two or more components that are connected in parallel as shown in Figure 2.3. The reliability function for the system with parallel structure can be formulated as shown in equation 2.51.

$$Rs(t) = 1 - \prod_{i=1}^{n}(1 - Ri(t)) \qquad (2.51)$$

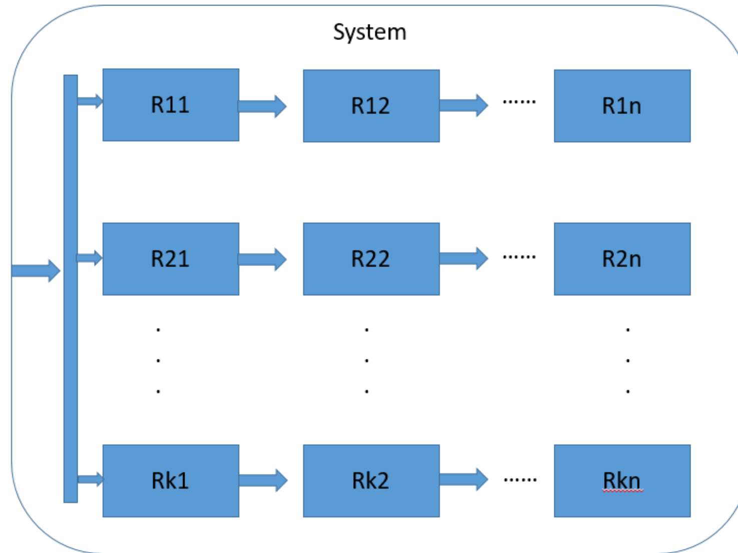

Figure 2.3: Parallel Configuration

For the combined series-parallel system, the same equations that were used in the parallel and series configuration can be implemented into the combined structure to simplify the system and then determine the final reliability function of the system. Comparing the systems in the level of redundancy is vital to demonstrate the best alternative with high reliability. The last category in the system structure categories is the complex configuration. It has the same combination of combined parallel -series structure but the reliability for the system can be calculated by using the previous approaches. Two methods are used to analyze this type of problem. The first method is the decomposition. In this method, a suitable component (key component) in the network should be selected in order to generate other two subnetworks from the original network. This is performed by assuming that the selected component is working to build the first subnetwork and assuming then this component is failed to construct the second network. Equation 2.52 shows the reliability function for the system by using the decomposition method. Where *Rs* is the reliability of the system, *Ra* is the reliability for the first subnetwork, *Rb* is the reliability for the second subnetwork and *Rc* is the reliability of the key component.

$Rs = Rc * Ra + (1 - Rc) * Rb$……………………………………………………………..(2.52)

The second method is the enumeration method where the basic mechanism for this method depends on finding all possible combinations of failing or passing for all components. Then, the probability of occurrence for each combination is found to determine the system reliability by calculating the overall summation of those probabilities.

2.2 Taguchi Method

The Taguchi method was initiated by W.E. Deming's, (1991) in order to produce products with high operation performance with low cost. Genichi Taguchi constructed the Taguchi method statistically to improve the quality of the products. Taguchi method can be used efficiently in single response optimizing problems where the significant reduction in the sensitivity to system variations can be achieved by utilizing this approach. Taguchi method is one of the vital approaches for the design and analysis of experiments because it has several competitive features. [39] The loss function concept is the basic statistical concept that is used to build Taguchi method structure. A special design of fractional factorial designs or orthogonal arrays (OAs) was employed in Taguchi method where it can use a small number of experiments to represent the entire space a permissive reliability. The controllable factors of the system and the factor levels for each are shown in the OA where each row represents different service condition. The Signal to Noise Ratio (SNR) is the measuring index for Taguchi method. The performance response should be converted to SNR to demonstrate the optimal factor levels where SNR determines the deviation of the performance response from the target and represents the magnitude of the mean of a process performance with considering its variations. The performance response should be classified into three classes in order to calculate the SNR where those classes are the Smaller-The-Better (STB), the Larger-The–Better (LTB) and the Nominal-The–Best (NTB). The larger value of SNR means

better performance response Regardless of the quality characteristics category. Equations 2.53, 2.54 and 2.55 represent the SNR function for its three categories: STB, LTB and NTB, respectively. [40]

$$SNR_i = -10\log[1/K\,(\sum_{k=1}^{K} y_{ik}^2)] \quad \forall i \qquad (2.53)$$

$$SNR_i = -10\log\left[1/K\,(\sum_{k=1}^{K} {}^{1}/_{y_{ik}^2})\right] \quad \forall i \qquad (2.54)$$

$$SNR_i = -10\log[\bar{y}_i^2/s_i^2] \quad \forall i \qquad (2.55)$$

Where *k* is the replicate number, *K* is the total number of replicates, s_i is the standard deviation at experiment *i*, *i=1,2,….,n* represents the experiment number and y_{ik} is the process performance value at service condition *i* and replicate k. The optimal factor level setting can be determined by calculating the average SNR at each factor level. The process layout and SNR is shown in Figure 2.4.

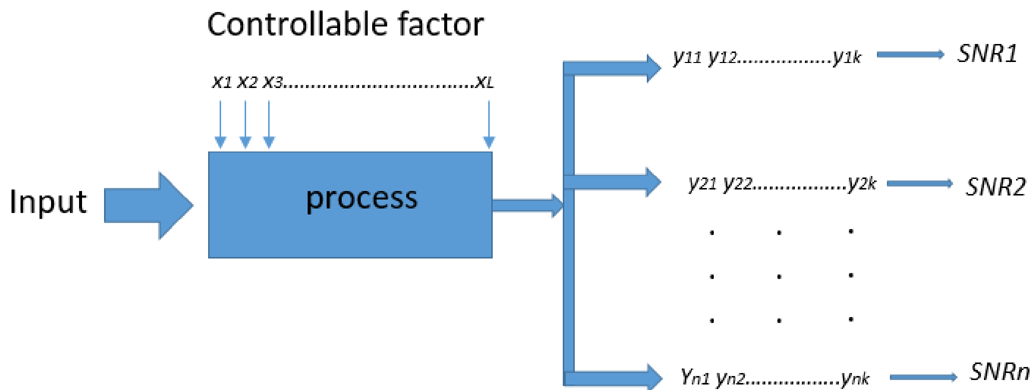

Figure 2.4: The Process Layout with SNR

2.3 Fuzzy Logic

The difficulties in dealing with vague and unsure information by using the traditional methods highlighted the need in the last decades to investigate more about other advanced techniques.

Fuzzy logic is one of the most common methods proposed to deal with this type of information which was introduced by Zadeh in 1965. Takagi-Sugeno (T-S), and Mamdani fuzzy systems are the most popular types of fuzzy logic. All the mathematical expressions in Mamdani approach have a linear function which includes the membership function for the inputs and the output. The Fuzzy structure is shown in Figure 2.5. [41]

To solve a problem by using the fuzzy logic concepts, four major steps are required. The first step is performed by entering the input data to the fuzzifier function which is mainly used to set the Membership Function (MF) for the inputs where different types of MF can be used in the fuzzy logic for example: linear, Gaussian and others. The second step is rule evaluation which contains a fuzzification function to convert the original data to a fuzzy data. The third step consists of defining the output membership function and developing the fuzzy rules. The fourth step includes the defuzzifier function for which the main goal of this function is to convert the fuzzy data into a comprehensive output measure (COM). In this function, the inference system utilized the fuzzy reasoning in the fuzzy rules to get the fuzzy value. [42, 43]

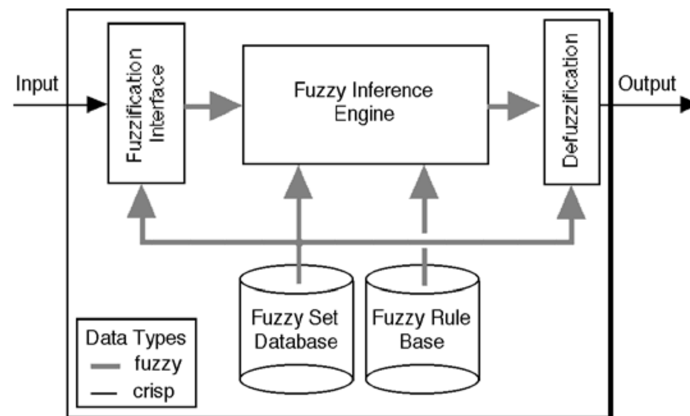

Figure 2.5: Fuzzy Logic System

The previous discussed fuzzy functions can be applied into Mamdani approach which are described in the following steps. In The first step, Input linear Membership Functions for the input variables are developed. In the rule evaluations step, the fuzzification function is used to generate the Fuzzy Input in order to evaluate inferences or rules. The third step is aggregation of the rule outputs. This step is performed by constructing the linear output membership functions. In the last step, the defuzzification function is utilized to determine the Crisp Output value which is called the COM value. For defuzzification functions, there are several methods that are employed. For instance, Center Of Gravity (COG), constraint decision defuzzification, adaptive integration, and extended quality method are common types of the defuzzification function.

2.4 Artificial Neural Networks (ANNs)

The ANN is a soft computing technique which can emulate human behavior by utilizing some complex functions. In general, the ANN structure contains a finite number of layers with different number of neurons at each layer to custom it as the computing elements. The inter-unit connections, strengths, and weights are handled and tuned in the learning process to achieve the required capabilities of the network. [44] ANNs techniques depend on the historical data in the training process which are powerful artificial intelligence techniques due to their adaptability to provide solutions for constructing nonlinear and complex relationships. [45] The most common structure of neural networks contains input, hidden, and output layers. The input and output layers can be described in the neural network by nodes, and the relationship between the input and output layers can be represented by hidden layers. The weights of the nodes are assigned randomly for a particular input pattern and are modified iteratively until obtaining predicted responses that has less susceptibility to errors. [46]

The backward propagation neural network (BPNN) and the radial basis function neural network (RBFNN) are the most common types of ANNs. The BPNN is classified as an overall approximation network where the gradient descent method is implemented in order to adjust the weights that are used in the approximation. The Multilayer perceptron model is one of the most popular models of the BPNN. The main drawbacks in the BPNN are the uncertain decisions, and the over fitting problems that are obtained from considering local minima error rather than global ones. A slow convergence speed is another disadvantage in the BPNN model. To apply BPNN, a fixed number of neurons should be set before using the training data, while large range of inputs can be covered since sigmoid neurons are utilized in the hidden layer. [47] In the radial basis function neural network (RBFNN) or model free estimators, the desired outputs can be approximated without using a mathematical formula to detect the relationship among the outputs and the inputs. The convergence speed in RBFNN is high compared to BPNN because a one hidden layer is only present in the RBFNN. The Architecture of the RBFNN is described in Figure 2.6. Where the inputs and outputs are presented as U_d and y_i respectively and the Gaussian function at hidden layer l are represented by ϕ_l. D is the number of controllable factors, the number of hidden layers are L, n is the number of experiments and the weight is represented by W_{lz}. [48] The Network scale in RBFNN is more than that is used in BPNN where the RBFNN can be used in small area data space. Increasing the number of neurons is one method that is utilized to deal with large area of input space in RBFNN. The main advantage of RBFNN is not having local minima problem. The other advantages that are associated with using RBFNN are high precision, high convergence rate and adaptive structure. RBFNN is commonly implemented for pattern classification and nonlinear functional approximation due to the previous discussed powerful features. [49]

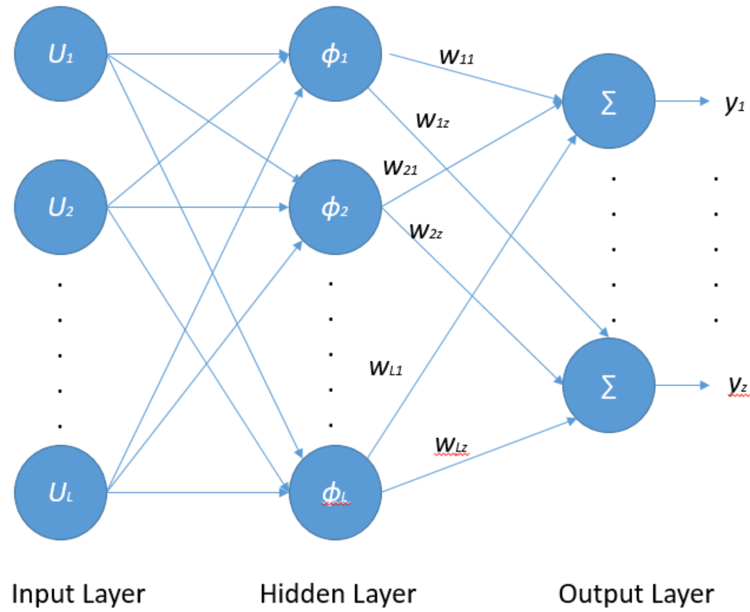

Figure 2.6: General Structure of the RBF Network

In the RBFNN, a linear combination of the outputs from the basis function is used to form the network output vector. The Gaussian function is utilized by the neurons in the hidden layer as an activation function. Equation 2.56 describes the radial basis function when the Gaussian function is utilized.

$$\hat{y}_z(s+1) = \sum_{l=1}^{L} \emptyset_l w_{lz} = \sum_{l=1}^{L} w_{lz} \exp\left(\frac{\|\hat{U}-m_i\|^2}{2\sigma_l^2}\right) \ \forall z = 1,2,\ldots,Z \ldots\ldots\ldots\ldots\ldots\ldots\ldots\ldots(2.56)$$

where U is the input vector, the zth output is $y_z(s+1)$, symbol l represents the hidden neuron, the zth output neurons are connected by utilizing the weight w_{lz}, L represents the number of Gaussian functions which is the same as the number of hidden layer nodes, the Gaussian function is represented by ϕ_l at hidden layer l at the center, the width of the Gaussian function is symbolized by the symbol m_l, and σ_l represents the standard deviation of U_l. [50] The optimal values of w_{lz}, m_l will be found by performing a series of iterations in the training algorithm this is implemented

to the initial RBFNN. Therefore, the initial structure of the network should be identified. The basic functions are calculated by determining the input vectors. Then, the weights that are connected to the output layer will be set by utilizing input and output data. This two-stage training methodology leads to eliminate the problem of local minima, and the RBFNN have high divergence rate. Determining the number of hidden layers is critical in RBFNN since assigning large number of hidden layers provides the prediction model with over-fitting problem. In contrast, allocating small number of hidden layers leads to a low accuracy [49-52].

Chapter 3: Literature Review

3.1 The Reliability Issues in Electronics

Studying the reliability of the electronic components is crucial where the electronic components play the controller role of the system in most of the cases. Any failure on some electronic applications could increase the fixing cost to a higher level because of the subsequences of the damage for the electronic parts on the overall system, such as some electronics devices in the production line and in the internet servers. Moreover, some electronic applications are too critical and if they fail, they can lead to a risk on human life, for instance: electronic parts in medical devices, aerospace and airplanes. In this section, the most common failures that are related to the component reliability in the electronics are investigated to address the root causes of the common problems and to try to eliminate these causes to enhance the electronic performance and reliability. Several factors may have an effect on the reliability of the electronics, for instance the function of the component, working environment conditions, the interconnection materials, the types of the assembly that is used and the heat dissipation system of the electronic component. The following discussion represents some of the most common reliability issues that are related to the electronics. One of the most critical issues that affect the reliability of the electronics is corrosion which can lead to several functional errors. The main reason of the corrosion of electronics is the interaction between the humidity and the internal parts material of the electronic devices. Several approaches investigated the corrosion phenomena in different applications, for example, bridges, pipeline and automobiles. The difference in the corrosion of the electronic components is in a small scale of

electronics, where the small amount of corrosion in the electronic components can lead to functional problems or failure of the electronic device due to changes in the electrical properties. In general, the corrosion behavior can be identified by demonstrating the operating environmental conditions. The main factors that affect of the corrosion behavior are humidity, temperature and electrical potential. Isolation of the electronic components from the working environment is one of the most common solutions that were used in industries to prevent the components from corrosion. Using the passivating or protective films, encapsulating, restrictive packages and protective coatings are the most popular methods of performing the isolation. [53]

Because of the fact that the current technology requires high substrate component densities with smaller dimensions, discovering the material with higher mechanical properties for adapting the packing technology to the new technology requirements is a vital requirement. Delamination and cracking between the dissimilar materials with different thermal expansions is one of the major problems in mechanical reliability. The delamination problem usually occurs after the soldering process and temperature cycling test because of the high internal stress. The main cause of internal stress is the absorbed vaporized water by all plastic packages at high temperature in the soldering process. Because the packaging system usually contains more than one material, the thermal cycling process leads to a thermal expansion mismatching stress. This stress may cause problems with interfacial strength and delamination at the interface between different materials. There are other factors that may increase the possibility of delamination problems, for instance the chip backside contamination, die contamination and the adhesive properties. The cracks and the delamination problems regularly start at the interface, free edges and corners. [54]

The die damage is another problem that may lead to a whole system failure. The die, or the integrated circuit, is the controller of the electronic component where all the functional and logical

activities are performed in the integrated circuit. The failure in the die, which may be a physical crack in the die or open circuits, can result from the mechanical or the thermal mechanical overstress. One of the most common defects that are associated with the integrated circuit failures is the chip insulator defects which is called dielectric pinholes. This type of defect occurs in the dielectric insulator which leads to several types of problems, for example thin and thick silicon oxide and chemical vapor deposited insulators. [55]

Another common fatigue failure in the electronic is the wire bond breaking. The main purpose of the wire bonds is connecting the integrated circuit with its leads. The mechanical stress can create a fracture in the wire bonds because they are thin and fragile. Another possible failure can happen on the intermetallic connection between the wire and the die which is called wire bond liftoff. The main reason of this failure is fabrication issues through the bonding process. [56, 57]

The interconnect level failure is the most common type of reliability or fatigue failures which normally occurs on the solder joints or leads. The environmental conditions have a big role in accelerating the failure in the region and the knowledge about this condition helps to determine the likelihood of the interconnection failures. There are several types of interconnection failures, for example: solder fatigue, solder overstress, lead fracture, board level failures, contamination-induced current leakage, conductive filament failure, plated through hole fatigue and pad cratering and trace fracture. In the following discussion, some of those failures are described.

The root cause of the solder fatigue is the temperature cycling over long period of time where the severity of the problem depends on the differences of the thermal expansion coefficients between the substrate and the component body. There are some factors that may accelerate the fatigue where some of these are associated with the environmental conditions and others are related to the product

itself, for instance increasing the component size, excessive vibration and the component warpage. [58]

Lead fracture is another type of the interconnection failures which usually happens in the lead itself where the solder joint remains tacked with the board and the lead. This type of failure commonly occurs in the gull wing and the leads for the large electrolytic component or capacitors. The driver causes for the lead fracture are frequent shocks and vibrations. [59]

Other types of failures that are associated with overstress events are pad catering and trace fracture. For the pad cratering failure, the fracture has creature shape due to crack structure in the layer below the fractured pad where this type of fracture primarily is presented in the ball grid array (BGA) solder joints. The failure mechanism of the pad cratering starts with a frequent mechanical stress, then the pad begins to rip off the board due to this stress. Usually, the pad cratering failures are followed by trace fracture. In this type of failure, trace fracture, the stress is concentrated between the routing and the fractured pad which leads to break the tin traces. The trace fracture may happen in other places where the stresses are concentrated. [60]

One of the most common failures that appear as a result from the thermal cycling process is plated through hole fatigue. Typically, the cracks are present in two different locations. The first location is called the barrel cracking where the crack appears on the plating of the through hole. The second cracking location is between the plated through hole barrel and its attachment which is called trace cracking. The environmental conditions increase the likelihood of this type of fatigue failure as well. [61]

3.2 The Effect of Isothermal Aging on the Reliability and Mechanical Properties of the Solder Joints

One of the most common factors that affect the reliability of the electronic devices is the fatigue failure of the solder joints. Solder joints provide the electrical connections between the printed circuit board (PCB) and the active electronic components, and it provides a mechanical support of the electronic components. Several studies explicated the changes in the microstructure due to isothermal aging and thermal cycling and its effect on the reliability and mechanical behavior of the solder joints. The most common material that was used for fabricating the solder joint is eutectic or near eutectic tin/lead (Sn/Pb) solder where it has a robust reliability and outstanding solderability. Several concerns were present because of the health issues that are associated with the leaded solder material and its effect on the environment. In the last three decades, the electronic industries, and the research centers in the U.S and worldwide worked in developing reliable lead-free solder alloy which are considered as green products. [62-64]

The Sn-Ag-Cu (SAC) series are the most popular alloys that are utilized in fabricating the solder joints for lead-free applications because of its low cost, manufacturability, reliability and availability. [65] There are several case studies that investigated the reliability and the mechanical behaviors for lead-free solder alloys, specifically, for SAC solder alloys. Those studies assessed the probability of failure for different solder materials under different working conditions of aging and compared their performance with the leaded solder alloys (SnPb). The effect of aging at room temperature on the shear strength of SnPb was studied by Tusi et al. and the degradation model was developed. The study found that the effect of 12 hours aging on the shear strength for SnPb solder ball is nonsignificant. On the other hand, the shear strength drops 10% after aging 3 days at room temperature. [66] Ma et al. demonstrated the effect of 6 months aging at room temperature on the mechanical properties for SAC solder alloys. The large reductions in the stiffness, strain,

ultimate strength and yield stress to failure were found to be approximately 40%. [67] The effect of room temperature annealing or age softening on the shear strength and the hardness of the SnPb and SAC alloys are explored by Coyle et al. The significant decreases in the shear strength and the hardness were determined for SnPb and SAC alloys. The microstructure for both alloys was studied to identify the failure mode and to correlate the evolutions in the microstructure with the shear strength and hardness. [68]

In 1976 Lampe et al. explored the effect of room temperature aging on solder alloys. In this study, the shear stress and the hardness of Sn-Pb and Sn-Pb-Sb solder alloys were studied at 30 days aging time at room temperature. The result showed that their hardness and shear strength were decreased by 20% after the aging process. [69] Another study investigated the effect of aging at room temperature for different aging times of Sn-Pb solder alloy. This research is performed by Medvedev in 1956. The results displayed 30% reduction in the tensile strength when the solder was aged for 450 days at room temperature. On the other hand, the 23% reduction in the tensile strength was achieved at 435 days of aging at room temperature. [70]

Lee et al. studied the effect of aging on long term reliability for BGAs with SAC 305 solder alloy. The thermal cycling test was implemented by cycling the temperature between 0ºC and 100ºC where the aging temperatures were 100ºC and 150ºC. The outcomes from the test showed that 44% reduction on lifetime happened when the aged solders at 150ºC were used. However, aging at 100ºC presented a lower effect on the lifetime with a similar pattern. [71] Smetana et al. inspected the effect of isothermal aging on a variety of electronic components by using thermal cycling fatigue test. The temperatures that were utilized in the thermal cycling test are 0ºC and 100ºC. The results proved that it is not always the aging or preconditioning process that has a negative impact on the lifetime of the electronic components. Where in some cases, the aging process enhances the

reliability for certain components especially when the cycling temperatures range between 20ºC and 80ºC. [72]

Zhang et al. studied the effect of isothermal aging on the mechanical properties of the lead-free solder alloys and leaded Sn-37Pb solder alloy. Creep was one of the mechanical properties that was impacted significantly by the isothermal aging of the lead-free solder alloys. On contrast, Sn-37Pb solder had a lower rate of creep than lead-free solder alloys. This is because the evolutions on the microstructure in lead-free solder alloys were higher than those happened on Sn-37Pb solder. The main reason of shifting in the mechanical behavior was blocking the dislocation movement that leads to a reduction in the strength for lead-free solders which usually happen in high temperatures and harsh environments. [73]

Another study by Li et al. explored the shear strengths for Sn-0.7Cu, Sn-3.8Ag-0.7Cu, Sn-3.5Ag and Sn-Pb eutectics solder bumps. These eutectic solder bumps were aged for 51 days at room temperature. The 5-8% reduction in the shear strength for lead-free solder bumps was reported. [74] Zhang et al. utilized the thermal cycling test to determine the reliability of the Sn-1.0Ag-0.5Cu (SAC105), Sn-3.0Ag-0.5Cu (SAC305) and Sn-37Pb solder ball interconnects under different aging temperatures. The fine-pitch ball grid arrays (BGAs) with three different surface finishes (ImAg, ImSn, SnPb) were used as a testing part and the solder joint aged at 25ºC, 55ºC, 85ºC and 125ºC for 12 months. The results for aged solder alloys were compared with the results for non-aged solder alloys. The degradation model for each experiment combination was constructed. The study showed that the service life of the package was reduced after aging and the amount of reduction in the service time for the package had a negative relationship with the aging temperature. The worst case happened at 125ºC with 58% reduction in the service time compared

to non-aging package. The Sn-37Pb solder ball presented better results in terms of service time of the package compared to the SAC alloys. [75]

In their paper, Zhang et al. implemented an accelerated shear fatigue test to predict the reliability of the solder joint and measure the accumulated work that was consumed to cause failure and the evolutions in the plastic deformation. Hamasha et al. performed fatigue shear experiments on SAC 305 and SAC 105 solder joints to study its reliability at different stresses and to determine the accumulated work and the plastic strain. The power equations predicted the reliability under different conditions and were used to relate the stresses, accumulated work, characteristic life and plastic strain together. The experimental results showed that SAC 305 has more fatigue resistance than SAC 105, where there are nonsignificant differences on the effect of stain rate in both alloys. [76]

Lall et al. explored extensively the impact of the strain rate on the mechanical behavior for SAC 105 and SAC 305 solder alloys. The effect of aging on the mechanical behavior at different aging temperatures and times were investigated. The temperatures that were utilized in the aging process are 25ºC, 50ºC, 75ºC and 100ºC and the durations at each aging temperature are 1 day, 30 days and 60 days. The non-linear Ramberg-Osgood model was used as a fitting model for aged and unaged specimens by using two fitting methods which are statistical regression fit and closed-form model approach. The elastic modulus, the ultimate tensile strength and stress-strain curve have been determined in the strain rate range 1-100sec-1. The experimental results showed that the impact of aging duration at elevated temperature on the ultimate tensile strength is higher than its effect on the elastic modulus. [77] Han et al. have explored the creep behavior and correlated it with the indentation size for SAC 357 lead-free solder. [78]

The influence of aging on lead-free solder joints was investigated by Venkatadri et al. The study was done by utilizing the micro hardness test to implement single idents on the joints. [79] Hasnine et al. determined the influence of different aging conditions for SAC 305 solder joints on the stress-strain and creep behavior. The elastic modulus, yield stress, and hardness were characterized as a function of aging. The creep output was determined as a function of stress level by exploiting nanoindentation techniques. The aging effect on SAC 305 solder joint was correlated with those effects on bulk solder specimens that are tested previously. The results presented that the degradations of the modulus and hardness of both single grain SAC 305 joints and miniature bulk specimens are similar. On the other hand, the degradations of creep response in the solder joints were significantly lower than the degradations of bulk specimens. In the same study, the correlation between crystal orientations of aged specimens and the mechanical properties was found, and the prediction model of the tensile creep strain rate at low stress levels is found by employing the nanoindentation test data that were determined at high compressive stress levels. [80]

The coarsening of the overall microstructure and the size of the precipitate particles was examined in room temperature aging by Chuang et al. where the shifting on the tensile properties for the Sn-9Zn and Sn-9Zn-0.5Al eutectic solder alloys was explored under 30 to 180 days of aging under 30 ºC. The results have demonstrated that that the grain size of tin-rich was increased and recrystallized when the solder alloys were exposed to 35 days of aging at room temperature. [81] The differences in the distribution of precipitate in the bulk sample and solder joint were recognized by Anderson et al. and the effect of the intermetallic layer (IMC) which is formed from the metallurgical reaction between PCB and the solder paste was studied. The results show that a negative relationship was found between the thickness of IMC and the fatigue life. [82]

Another study by Zhang et al. studied the impact of the percentage of silver in the SAC alloys composition on the mechanical behavior under aging conditions. The percentages that were studied are 1%, 2%, 3% and 4% silver with alloys containing 0.5% copper and the aging temperatures were 25ºC, 50ºC, 75ºC, 100ºC and 125ºC. The solder joints were aged for various durations (0-6 months). Several doped SAC solder alloys were tested to examine the effect of using dopants on the drop reliability and to test the ability of dopants to enhance the thermal cycling reliability under aging condition. Analogous tests were applied for 63Sn-37Pb eutectic solder sample to compare it with lead-free solder alloys. The results show that aging at elevated temperature has a significant effect on the stress-strain and creep behavior of the solder joints and that the degradations for the strength and stiffness have a linear relationship with aging time. The creep rates for SAC solder alloys and tin-lead solder alloy have been increased exponentially where SAC solder alloys have higher creep rate at the beginning compared to the tin-lead alloy. The results also showed an increase in the sensitivity of the mechanical behavior with low percentage of silver in the SAC solder alloys when exposed to the aging process. Those changes in the mechanical behavior after aging are due to the evolution in the microstructure. In the first phase of aging when the particles are small and fine precipitations, this leads to prevent the dislocation movements and the grain boundaries sliding which enhances the strength of the material and creep resistance. In contrast, in the second phase, the particle size is increased which reduces their ability to prevent the grain boundary sliding and dislocation movements, thus the resistance to creep deformations and the strength for SAC solder alloys were reduced. [83]

Thirugnanasambandam et al demonstrated the dope effect on the reliability of the ball grid array package with SAC 305 solder joints by using vibration fatigue life. The testing board was fabricated according to JEDEC standards with 208 perimeter solder joints. The solder joints were

placed in the board by utilizing two stencils with different thicknesses and three different reflow profiles. The accelerated life test in this case was performed by exposing the BGA samples to severe random vibration. The ability of the component to withstand under this vibration is the method of measuring the component reliability. Their results showed an increasing in the reliability of the BGAs with doping. The effect of using SAC 105 ball and Innolot solder paste reliability with different combinations with SAC 305 solder ball and paste. The results demonstrated a significant difference between the characteristic life of Innolot and SAC alloys where the failures in all lead-free structure were found within the intermetallic layer. [84] The thermal performance for leaded and leadless packages at different lead-free doped paste alloys are demonstrated by Raj et al. the main objective from this research is to find the better doped solder paste that has the best thermal performance with lower effect on aging process. The effect of solder paste type that was used as dopant for the solder joints, reflow profile, and the doping level on the reliability of the solder joints is also studied. The components that are studied are servile types BGA and 2512 resistors. The accelerated test was accomplished by performing the thermal cycling process where the temperature range is between -40 ºC and 125 ºC with 5 minutes dwell time and 2.5 minutes transition time and the number of testing cycles is 3000 cycles. The testing boards are exposed to an aging process for six months at 125 ºC aging temperature. The capability of the solder joints to withstand under thermal cycling stress was used as a reliability metric. The time to failure was used as a performance response for this experiment and the reflow profile, the solder paste type, the solder sphere material and the stencil thickness were demonstrated as experimental parameters. As a result from this study, all of the previous parameters were significantly having an effect on the time to failure except the reflow profile. [85] To assess the drop impact performance of the solder joints, Sridhar et al. investigated the effect of doped solder paste on the

reliability of the solder joint by implementing the drop impact accelerated test. Two sets of test boards were exploited to perform the accelerated test where the first set is non-aged test board and the second set is aged testing board at 125 ℃ aging temperature for six months. Sixteen BGA packages were utilized for testing. Two solder pastes were selected as a baseline which are SAC solder bumps and SAC 305 and 12 doped levels was used for comparison purposes. The accelerated life test was executed by applying 300 drops for each board where the data was collected for each 20 drops. A comparison between the doped solder pastes was demonstrated and the data was classified into two classes (aging and non-aging data). The results showed that some of the doped solder pastes had better performance in the accelerated life test than the baseline but none of these solder pastes after aging had larger fatigue life than the baseline. [86] Mustafa et al. studied the effect of aging, solder alloy composition, temperature and stress/ strain limits on the behavior of cyclic stress stain for the lead-free solder joints. Four SAC solder alloys with different silver percentages (1%, 2%, 3% and 4%) were employed in the study. Several aging times were implemented in the sample at 125℃ aging temperature. Four environmental temperature (25, 50, 75 and 100 ℃) were utilized to investigate the effect of operating temperature. The cyclic load was applied to Uniaxial SAC solder samples by using stress control method and stain control method. The evolution on the hysteresis loops and creep behavior of the solder joints at different aging times were examined. The results presented a high reduction in the fatigue performance with larger hysteresis loop for solder joints that has lower silver content and for higher operating temperature. The effect of aging on the thermomechanical fatigue life was demonstrated. [87] Ma et al. explored the effect of isothermal aging on the mechanical behavior of the lead-free solder alloys. Two materials lead-free solder alloys (SAC 305, SAC 405) were exploited to assess its mechanical performance. The creep and stress-strain test were utilized to determine the mechanical

behavior of the solder alloys. Leaded solder alloys (63Sn-37Pb) were tested as well for comparison purposes. The samples were aged at different aging times (0-6 months) and at different aging temperatures (80, 100, 125, and 150 ℃). Different mechanical performance responses were investigated for example, the yield stress, ultimate strength, creep compliance and elastic modulus. Different prediction models were constructed as a function of aging time for each of the studied mechanical properties. The results displayed that the mechanical properties were changed exponentially with increasing the aging temperatures compared to room temperature and the changes in the material properties reached to the steady state after 200 aging hours. The mathematical mode was built as a function of aging temperature and aging time to predict the variation on the properties. For the creep performance, the results showed that the creep performance for SAC alloys at room temperature aging is better than the leaded solder alloys. In contrast, the leaded solder alloys have better creep response than SAC alloys at elevated temperature. [88] Mustafa et al. examined the effect of aging of the fatigue and stress strain behaviors for lead-free solder (SAC 105, SAC 305) joints by utilizing stress/strain load on uniaxial specimens where the aging temperature is 125 ℃. The cyclic stress-strain curve was fitted by using the four-parameter hyperbolic tangent empirical model. The accelerated fatigue shear test was studied as well. The fatigue life prediction models at different aging conditions were constructed by utilizing the Coffin-Manson model and Morrow model. [89]

Darveaux et al. exhibited the effect of aging at elevated temperature for five different solder alloys on their deformation behaviors. 63Sn-37-Pb, Sn-3.5Ag, Sn-0.7Cu, SAC 305 and SAC 405 solder alloys were aged for 24 hours at 125 ℃. 10% to 30% reduction in the solder joint strength were recognized for the five solder alloys after the aging process. The results indicated that the ductility of all lead-free solder alloys was decreased when the aging was increased. [90]

Based on the previous literature and study findings, the reliability, the mechanical properties and the microstructure for the lead-free solder alloys can be changed over time when exposed to isothermal aging process. One of the main reasons for studying the effect of isothermal aging is that the electronic products usually spent months or even years under different harsh conditions to be delivered from its manufacturing factory to the final customer, which is known as the aging effect on the hand-held consumer product. [75]

3.3 Reliability Models for the Solder Joints

In this section, the most common applied mechanical models that are used in predicting the solder joint reliability are deliberated at different service conditions and applications.

Pang et al. studied the effect of temperature and the frequency on the low cycle fatigue endurance for lead-free solder alloys. The testing materials are 95.5Sn-3.8Ag-0.7Cu and 99.3Sn-0.7Cu solder. The test was accomplished in two different operating conditions (25ºC, 1 Hz and 125ºC, 0.001Hz). Two main parameters were investigated in order to determine the fatigue behavior for solder alloys where those parameters are plastic strain and inelastic stain energy density. The Coffin-Manson fatigue model was exploited to determine the fatigue life as a function of plastic strain which was obtained from the stress-strain loop. The curve-fitted for Coffin-Manson model constant was constructed. The second model that was employed is the Morrow energy fatigue model where in this model the low cycle fatigue life was predicted as a function of inelastic strain energy. From the fatigue failure analysis, the studied solder lead-free alloys represented larger strength compared to the leaded solder alloys. [91] Shohji et al. examined the fatigue behavior of the 63Sn-37Pb solder joints at different thermal cycling conditions. The modified Coffin-Manson model was implemented to describe the thermal fatigue behavior of the solder alloy where the exponential factors and the activation energy were demonstrated for this model and the

microstructures coarsening was detected for the solder joints. From the microstructure analysis, the modified Coffin-Manson model didn't represent the thermal fatigue behavior, if the solder joints failed without microstructure coarsening. [92] Lau investigated the thermal, vibration and mechanical behavior of the plastic ball grid array and flip-chip. The experiment was performed by using bending and twisting experiments for mechanical response and out of plane vibration experiments for the vibration response to simulate the overload environmental stress and the shipping environmental stress. The thermal response was evaluated by using the fracture mechanics methods, nonlinear finite element and Coffin-Manson model. The leaded solder alloys were used in fabricating the tested solder joints. This research provides different methods to estimate the thermal fatigue life for flip-chip and PBGA solder joints. [93] Darveaux and Banerji developed a method for predicting the fatigue life of the flip-chip bonds under different thermal cycling conditions by utilizing the finite element simulation and Coffin-Manson model. The finite element simulation was used to assess the assembly stiffness for the flip-chip assembly and to simulate the hysteresis loops under different conditions. The Coffin-Manson model was implemented to correlate the creep strain per cycle and the average of the fatigue life. [94] Che ad Pang studied the effect of thermal cycling process on the reliability of the solder joints in plastic ball grid array where the solder alloy was Sn-3.8Ag-0.7Cu solder joint. Quarter model and sub-modeling method were used in finite element analysis to identify the stress strain behavior for the solder alloy. Viscoplastic Anand's model and elastic-plastic-creep model were implemented in finite element analysis as constitutive model for the solder joint material. The energy based and strain based prediction model were employed to estimate the fatigue life. The volume averaged method was implemented as well to extract the parameters for the fatigue life prediction. The thermal shock effect was investigated to demonstrate the effect of the temperature ramp rate on

the fatigue life. Coffin-Manson and Morrow's models were used in energy based and strain based models respectively. The effect of thermal cycling on the fatigue life is smaller than the effect of thermal shock. [95] Sarihan proposed a new methodology for predicting the fatigue life of the solder joints by determining the stable cycle hysteresis energy based. In this method, the damage function was calculated by using nonlinear finite element approach. The relationship between the fatigue life and hysteresis energy based damage function was defined after identifying the stable cycle response. [96] Shi et al. explored the effect of the testing temperature and the applied stress level on the creep behavior of 63Sn-37Pb solder. The new model of creep behavior was proposed by using Gibbs' free-energy and the dislocation controlled creep mechanism. The main goal of this model was to explain the creep flow of the solder and to describe the effect of stress and temperature by employing the activation energy and stress exponent from Arrhenius model. [97] Wang et al. investigate the inelastic deformation behavior for different types of solder alloys by utilizing Anand model. The studied solder alloys were 62Sn36PbAg, 96.5Sn3.5Ag, 97.5Pb2.5Sn and 60Sn40Pb and their material parameters were identified experimentally and from other constitutive relation. As a result from this research, the Anand model successfully represented the inelastic deformation behavior for the solder material at homologous temperature. [98]

3.4 Taguchi Method in Electronics

The Taguchi method is one of the most effective optimization methods that are used in single response problems in the quality control process. The main goal of the Taguchi method is to find the optimal factor levels in order to achieve a good quality with low cost. There are many studies utilizing the Taguchi method to assess the different alternatives by using the fatigue life as a performance response for this method.

Jong et al. utilized the Taguchi method as an optimization method for fatigue life to determine the optimal factor levels of the flip-chip packages. The fatigue test that was performed is the thermal shock where the temperature range is between -55ºC and -125ºC. Four process parameters were studied which are upper diameter, lower diameter, height and width of bumps with three factor levels for each. Analysis of variance was performed to determine the contribution for each parameter on the fatigue response. [99] Wong et al. analyzed the thermo-structure of the gull-wing solder joint assembly by using the Taguchi method for assessing the impact of solder joints assembly factors on the fatigue life solder joints. The main objective of this research is to reduce the number of finite element analysis. Six parameters were considered in the finite element analysis to determine the contribution of each parameter on the fatigue performance response. The results showed that the most factors that have significant impacts of the fatigue life are lead ankle radius, lead thickness and minimum solder thickness. As a conclusion from this study, the fatigue life can be improved by increasing the solder thickness and using thinner lead and large lead ankle radius. [100] The fatigue behavior of the over-molded chip scale package on flex-rape carrier was examined by Mertol. The nonlinear finite element was implemented to simulate the thermal cycling process on the chip scale package. The Taguchi method was used to determine the optimal design and to identify the rules of keeping the package within the acceptable region according to the standards. Eight process parameters were considered in the orthogonal array of the Taguchi method; die size, die thickness, flex-tape thickness, copper trace thickness, solder ball collapsed stand-off height, mold compound thickness, mold compound material and die attached epoxy. The process performance of the model was the fatigue life. The studied temperature range for the thermal cycling process was -40ºC to 125ºC. The results presented that the optimal performance response was achieved at smaller die and thicker over-mold. [101]

3.5 Applications of Fuzzy Logic on the Reliability

The fuzzy logic is one of the artificial intelligence tools that are implemented to analyze the stochastic data. Because the reliability of different components depends on the random (stochastic) events, few studies utilized the fuzzy logic in analyzing the fatigue behavior for different products. The following discussion represents some of these studies.

Zafiropoulos and Dialynas developed a new methodology of predicting the reliability and the failure model effects and criticality analysis by employing the fuzzy logic. Switched mode power supply was used as a validation study of this approach. In order to identify the priority to the criticality of the component, the fuzzy failure mode risk index was determined. The fuzzy rules were constructed by using the knowledge base. Mamdani fuzzy logic type with min-max implication aggregation was implemented to build the fuzzy model. [102] Jarrah et al. explored the fatigue behavior of unidirectional glass fiber/epoxy composites by applying the neuro-fuzzy modeling. Using this method, the relationship between input and output variables of the fatigue behavior were constructed. The performance response was the fatigue life and the process parameters were fiber orientation, maximum stress and stress ratio. The results from this hybrid method were compared with the neural network method results where the most accurate prediction was obtained in the hybrid method. [103] Zalnezhad and Hamdi explored the effect of coating parameters on the coating adhesion strength in magnetron sputtering technique. The fretting fatigue life test was performed for multilayer Cr-CrN coating on AL7075-T6. The process parameters were DC power, nitrogen flow rate and the temperature. The fuzzy logic was developed to enhance the fatigue life of adhesion strength by determining the effect of the input process parameters. [104] Chen et al. explored the fatigue behavior of SAC 305 and 63Sn-37Pb solder joint under rapid thermal cycling test. The fuzzy logic in this case was used as a controller of the

cooling and heating process where the fatigue life was determined under the controlled conditions. [105] Chien et al. utilized the Taguchi method to optimize the moisture gain weight and the adhesion strength in IC packages. The process parameters were the operating temperature, relative humidity, soaking time and solder mask thickness. The signal to noise ratio was calculated for each response where the optimal factor levels were the factor combinations that has the largest signal to noise ratio. In order to find the global optimal solutions for all responses, the fuzzy logic was used to deal with this multi response problem. [106]

3.6 Applications of the Artificial Neural Networks on Reliability

ANNs are effective techniques that are employed to predict the value of one response or more by using the training data set as an input of the ANNs system and setting the ANNs parameters. The accuracy of the ANNs depends on the size of the training data, the range of the data and the ANNs parameters. There are different parameters of ANNs that need to be set in order to achieve accurate results. The number of these parameters depends on the type of ANNs used. The number of hidden layers, the number of iterations and the type of mathematical function that is implemented in the ANNS and the number of neurons on each hidden layer are some of the ANNs parameters. A large body of the research utilized ANNs approach to predict the fatigue life in different applications.

Park and Kang investigated the fatigue life of spot welds under several geometric factors and loading conditions. The fatigue tests that were accomplished to assess the fatigue behavior are combined tension and shear loading and shear- tensile loading. The ANNs were implemented to predict the fatigue life at different loading and geometric dimension conditions where the experimental data was used as a training data set for the ANNs model. The backward propagation method is employed for the ANNs model. [107] Deshpande et al. developed a methodology for predicting the fatigue life of the solder joint as a function of the solder parameters. The structure

of this methodology depends on the design of experiment, regression model and ANNs. The literature data for the plastic ball grid array package was used as a validation study to determine the mechanical behavior of different solder alloys and estimate the fatigue life of those solders under variate levels of stress. The numerical optimization method was implemented to achieve the optimal packaging system. The obtained results were compared with the actual results to identify the accuracy and efficiency of this method. [108] Qasaimeh et al. investigated the microstructure evolution and crack behavior for the lead-free solder joints by implementing the accelerated thermal cycling test. Due to the stochastic nature of the fatigue and the relationship between the microstructure and fatigue behavior of the solder joints, the Sn grain orientation was determined to recognize the fatigue crack growth by applying the ANNs method. As a result from the ANN model, the fatigue life of the solder joints can be estimated with precise accuracy by identifying the correlation between the fatigue life and the microstructure. [109] Subbarayan and Mahajan proposed a new methodology to estimate the reliability of the solder joints by studying the impacts of manufacturing process tolerance and its capability of obtaining the tolerance on the fatigue behavior of the solder joints. The reliability of the solder joints was found by using the finite element method where the process parameters are obtained from the variation on the manufacturing process. Physico-neural approach was developed to utilize the neural network efficacy with the finite element model accuracy. The low computational time with reasonable accuracy was obtained from the Physico-neural approach. The new approach was applied on OMPAC BGA package as a validation study. The studied process tolerances are solder joint volume, height and pad size. The results showed that the height of solder joints have the greatest contribution on the reliability of the solder joints compared with other factors. [110]

As a conclusion of the literature review, a lot of the research investigated the reliability of the electronic components at different conditions. The key of the electronic component's reliability was most likely determined from the reliability of the interconnection material. Good solder joints are a critical part in electronics manufacturing as solder joints that are poor will either cause the equipment not to work once it has been completed, or there is the possibility that the solder joint could fail intermittently or introduce noise into the electronics circuit. Thus, complete and latent failures are both fundamental issues as they may cause the equipment to fail once it is in service. Different studies explored the effect of the thermal and mechanical stress on the fatigue behavior and mechanical properties of the solder joints, but most of those studies explored the fatigue and mechanical behavior of the solder joints by using bulk samples. Several models were utilized to define the relationships between the stress level, the inelastic work, plastic strain, microstructure and aging conditions with the fatigue life. Different accelerated tests were utilized to assess the reliability of the solder joints, for example: thermal cycling, thermal shock, fatigue shear stress, and vibration tests. When in service conditions, the thermal stress is a major issue in solder joints, the thermal stress will be in the form of shear stress and it will cause a plastic strain for the solder joints. This leads to shear fatigue and failure of the solder joint leading to equipment failure. Few studies demonstrated the fatigue behavior using the accelerated fatigue shear test on individual solder joints under different service conditions. The utilization of the accelerated fatigue shear and shear test on individual solder joints to determine the effect of aging and surface finish on fatigue and mechanical behavior of the solder joints had not been discovered before. Few studies utilized the artificial intelligence techniques to assess the fatigue performance of solder joints. Some of the studies used the Taguchi method as a tool for assessing different alternatives of interconnect materials using fatigue performance response.

Chapter 4: Materials and Methods

4.1 Introduction

In this chapter, three main topics are discussed. In the first topic, the testing materials are introduced as actual solder joints on the customized PCB with different surface finishes instead of using the traditional bulk samples. For the experimental setup topic, the design on the experimental setup is demonstrated by designing an adequate fixture for applying fatigue shear and shear test on the Instron micromechanical tester. The last topic is for identifying the testing conditions and the data analysis methodology by constructing the orthogonal array, or the experimental layout, for each study and identifying the mechanical, statistical and artificial intelligence models to predict the fatigue life of the solder joints in the realistic service conditions.

4.2 Sample Preparation

4.2.1 Testing Board Fabrication

A full array PCB, that is fabricated by using FR-4 glass-epoxy substrates, was utilized as a base for the solder joints. The testing sample is a package of nine SAC305 (Sn-3.0%Ag-0.5%Cu) or SAC-Q (Sn-3.41%Ag-0.52%Cu-3.3%Bi) solder joints with 10mm for the package length, 10mm for the package width and 3mm pitch distance between the solder joints. Solder mask defined (SMD) pads and Organic Solderability Preservative (OSP) surface finishes were utilized in the testing board fabrication. The opening diameter of the pads and the solder diameter are 22mil and 30mil respectively. The full testing board and the testing sample layout are shown in Figure 4.1.

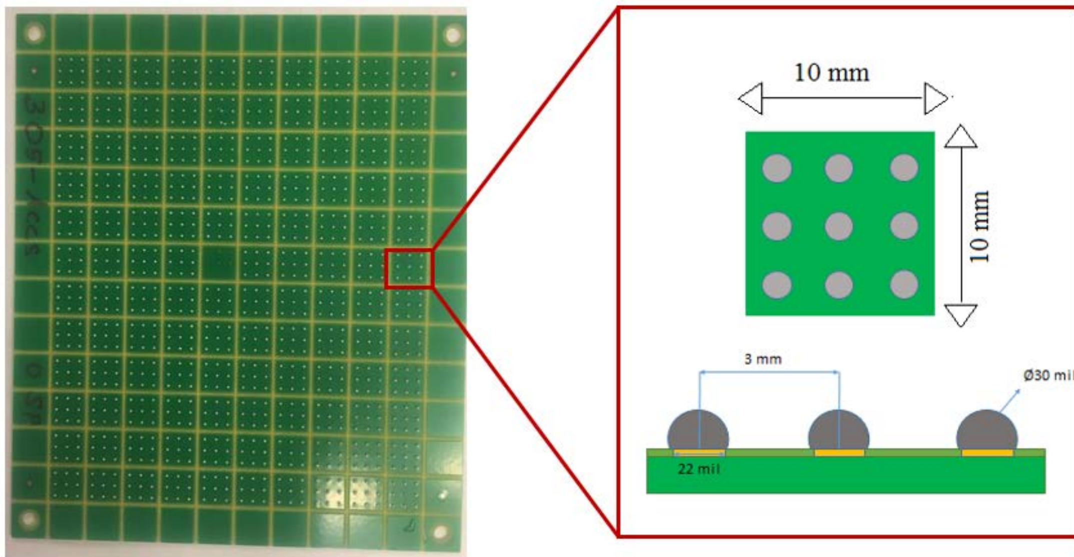

Figure 4.1: Testing Board Layout.

4.2.2 Surface Mounting Technology (SMT) Assembly

The Installation of the solder joints was performed in the electronics packaging lab, and the solder materials supplier is Accurus. Two stencils with different diameters of openings are utilized in the installation process of the solder ball. The first stencil is used to apply the tacky flux by using the DEK Galaxy (Figure 4.2). The second stencil is applied to place the solder sphere on the printed flux. The inspection using a microscope is employed after each step to ensure that the flux and the solder ball are applied in a proper way for all predefined locations.

Figure 4.2: DEK Galaxy Printing Machine

After printing the flux and solder sphere placement processes pass the quality specifications, the next step is the reflow process. Figure 4.3 shows 8 zones Pyramax 100N reflow oven that is used in the reflow process for the testing boards. The reflow process is performed in a nitrogen gas environment. In order to ensure achieving the best wetting for the solder joints without board damage, the thermal reflow profile was monitored during the reflow process. The preheating time for the reflow process and time above the liquids are 200 seconds and 40 seconds respectively, and the cooling rate is around 3.5ºC/ second. The peak and the soaking temperatures are 235ºC and 150ºC. The temperature rate increase is done in increments of 0.75 ºC / second. The detailed reflow profile is shown in Figure 4.4.

Figure 4.3: 8-zone Pyramax 100N Reflow Oven

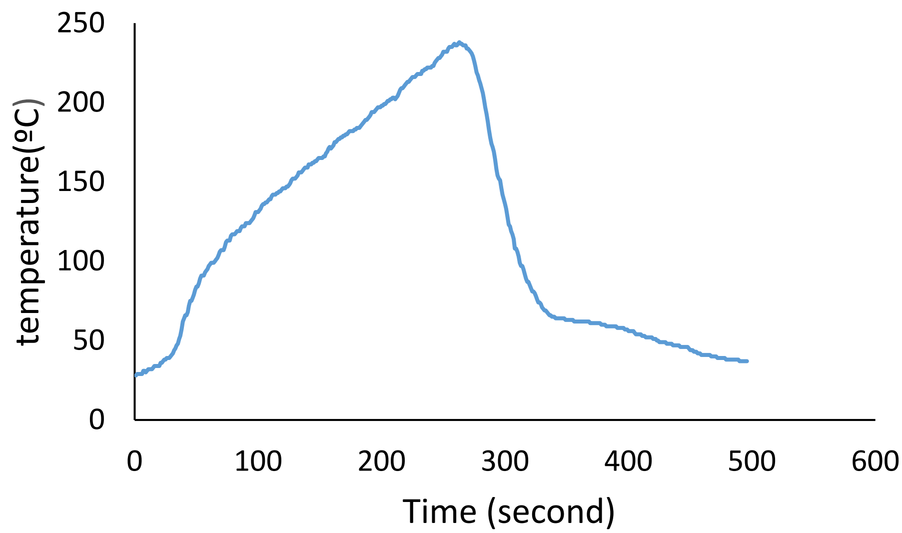

Figure 4.4: The Reflow Profile

4.3 The Experimental Setup

Multifunction Instron 5948 Micromechanical Tester was employed to perform the experiments on the individual solder joint in this research. The Micromechanical Tester has a high precision drive system with 94nm resolution and accurate load cell. The tests that can be executed on this testing

machine are compression, tension, shear and low cycle fatigue tests where it can apply a load with a range of 2mN to 2KN. A screw drive system and an optical encoder were implemented as a driver for the micro-position controller with a 20nm resolution. The 50N load cell was employed to measure the load. In order to find an efficient way to adapt the Micromechanical Tester setup for testing individual solder joints, the fixture and the sample holder were designed and manufactured to work as an adapter between the Micromechanical Tester and the testing sample. The transferred load from the Micromechanical Tester to the specimen through the designed fixture was considered in the fixture design. The sample holder was installed in the top of the adjustable x-y stage. The special glue type was utilized to fix the specimen on the sample holder. The Micromechanical Tester, the installed fixture and the sample holder are shown in Figure 4.5. The fatigue shear test configuration is illustrated in Figure 4.6. To standardize the experiments, a 0.05 mm distance is kept between the ramp and the solder pad where the inner diameter for the ramp is 40 mil. A partial flatting was observed at the beginning cycles.

Figure 4.5: Instron 5948 Micromechanical Tester and Experimental Setup.

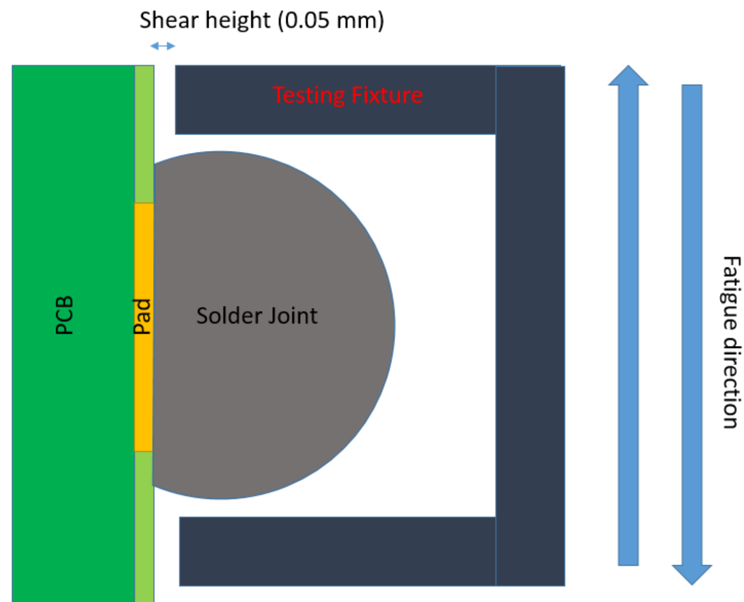

Figure 4.6: Schematic of the Cylindrical Testing Fixture for an Individual Solder Joint.

The microstructure analysis was accomplished, and the evolutions in the IMC layer thickness was identifed for the solder joints at different conditions. The microstructure samples were mounted in epoxy. Four grinding grades and other four polishing grades were utilized to prepare the specimen for microstructure analysis. The microstructure images were captured by using Scanning Electron Microscope (SEM) that is shown in Figure 4.7. The magnification that was implemented in SEM was 5000X. The secondary and back-scattering indenters were used in image capturing.

Figure 4.7: Scanning Electron Microscope (SEM)

4.4 Proposed Testing Plan

In this section, three studies are utilized to assess the reliability of the solder joints under different aging conditions and a new proposed methodology is used for optimizing the solder joint parameters by using a scale parameter, signal to noise ratio, mean-variance and earlier failure probability as performance indices and fuzzy logic as an optimization method. Validation case studies are implemented to verify the approach.

4.4.1 Study 1: The Effect of Aging on the Reliability of SAC305 Solder Joints

In this study, the effect of different aging times on the reliability of SAC 305 solder joints with OSP finish under different levels of cyclic shear stress is addressed. Five aging times (0, 2, 10, 100 and 1000hrs) are used as solder joint conditions before performing the test. The accelerated fatigue shear test is conducted to assess the reliability of the solder joints. In order to investigate the effect of the cyclic stress amplitude on the reliability of the aged solder joints, three levels of cyclic shear stress (16, 20, 24MPa) are employed as test conditions. The changes on the hysteresis loop at different conditions are demonstrated. The total number of combinations that are tested is fifteen

where each has seven solder joint samples. The orthogonal array L_{15} shows the fatigue test plan. Table 4.1 shows the test matrix for this study.

Table 4.1: The Test Matrix for Studying the Effect of Aging on SAC305 Solder Joint Reliability.

Aging time (hrs)	Aging temp (℃)	Stress Amplitude (MPa)		
		16	20	24
0	100	7 samples	7 samples	7 samples
2	100	7 samples	7 samples	7 samples
10	100	7 samples	7 samples	7 samples
100	100	7 samples	7 samples	7 samples
1000	100	7 samples	7 samples	7 samples

For demonstrating the reliability of the solder joints, a Two-parameter Weibull distribution was applied to represent the failure data distribution. From the Weibull distribution, the scale and the shape parameters are determined. To find the hysteresis loop for the solder joint at each cycle of the fatigue life under certain conditions, the deformation and the load are recorded every 0.01 second. The plastic strain and the inelastic work per cycle are determined for each cycle of the fatigue life from the hysteresis loop where the inelastic work equals the area of the hysteresis loop and the plastic strain equals delta strain at zero stress amplitude. MATLAB (Version R 2016) software is employed to calculate the plastic strain and the inelastic work by using the numerical integration. The empirical models are developed to predict the characteristic life as a function of aging time and stress amplitude where the relationship between the characteristic life and the stress amplitude is illustrated in the power equations. The shape parameter is estimated by calculating the mathematical average for the obtained shape parameters if there is a nonsignificant trend for the shape parameters in the obtained failure data. The Coffin-Manson model and Morrow energy model were implemented on the reliability data to predict the characteristic life as a function of the inelastic work per cycle and plastic strain respectively.

4.4.2 Study 2: The Effect of Aging Temperature on the fatigue behavior and Shear Strength of SAC 305 Solder Joints

In this study, the effect of different aging times and temperatures on the reliability and shear strength of the SAC305 solder joints is demonstrated. Three levels of aging temperature (50, 100 and 150°C) were studied. The aging time and stress amplitude conditions and experimental setup that are used in the previous section are applied in this study. The orthogonal array L_{51} that is shown in Table 4.2 was utilized as a test matrix of the effect of aging temperature on the SAC305 solder joints reliability. Seven samples were tested at each experimental condition. Arrhenius model was used to illustrate the effect of aging temperature of the reliability and fatigue properties of the solder joints. A prediction model of the characteristic life as a function of aging time, aging temperature and stress amplitude was constructed. The effects of aging temperature on the hysteresis loop, the Morrow energy and the Coffin-Manson models are demonstrated. The microstructure images are obtained for the solder joints in order to determine the microstructure and IMC layer evolutions at different aging conditions. The precipitates coarsening at different aging conditions was addressed. The microstructure analysis is held by mounting the specimen in plastic epoxy, four grinding stages with different grades of sandpaper, three different polishing stages and capturing the image by the SEM Microscope. The artificial neural networks (ANNs) technique is utilized for predicting the characteristic life at different aging conditions and stress amplitudes by applying the radial basis function type. The ANNs and the empirical models are compared by using a validation data.

Table 4.2: The Test Matrix for Studying the Effect of Aging temperature on SAC305 Solder Joint Reliability

Aging time (hrs)	Aging temp (ºC)	Stress Amplitude (MPa)		
		16	20	24
0	0	7 samples	7 samples	7 samples
2	50	7 samples	7 samples	7 samples
10	50	7 samples	7 samples	7 samples
100	50	7 samples	7 samples	7 samples
1000	50	7 samples	7 samples	7 samples
2	100	7 samples	7 samples	7 samples
10	100	7 samples	7 samples	7 samples
100	100	7 samples	7 samples	7 samples
1000	100	7 samples	7 samples	7 samples
2	150	7 samples	7 samples	7 samples
10	150	7 samples	7 samples	7 samples
100	150	7 samples	7 samples	7 samples
1000	150	7 samples	7 samples	7 samples

In the shear test, thirteen experimental combinations (orthogonal array L_{13}) were utilized to study the shear strength for the solder joint with seven replicates for each. The peak shear value of shear force (ultimate shear strength) is used to represent the shear strength of the solder joints. The Test Matrix for the shear test is shown in Table 4.3. The shear speed is 0.033mm/s (strain rate 0.1 sec^{-1}). Analysis of Variance (ANOVA), the main effect plots, and the interaction plots are implemented to study the contribution for each factor on the shear strength of the solder joints. Arrhenius model was used to predict the effect of aging temperature of the shear strength of the solder joints. The relationship between the aging time, aging temperature and the shear strength is identified by fitting this relation to an empirical model.

Table 4.3: The Test Matrix for Studying the Effect of Aging on SAC305 Solder Joint Shear Strength.

Aging time (hrs)	Aging temp (ºC)		
	50	100	150
0	7 samples		
2	7 samples	7 samples	7 samples
10	7 samples	7 samples	7 samples
100	7 samples	7 samples	7 samples
1000	7 samples	7 samples	7 samples

4.4.3 Study 3: The Reliability Effect for Adding Bismuth on SAC-based Solder alloys at Different Aging Conditions and Stress Amplitudes

Adding bismuth to SAC-based solder materials is one of the factors that lead to enhance the reliability of the solder joints significantly. To demonstrate the evolutions in the fatigue properties of SAC-Q solder joints under different service conditions, three levels of stress amplitude (22 MPa, 26MPa and 29MPa) and four levels of aging time (2, 10, 100, 1000hrs) are used with a 100 ºC aging temperature and OSP surface finish. The non-aged solder joints were tested for comparison purposes. The accelerated shear fatigue test is implemented to determine the solder joint reliability. The fatigue behavior for SAC 305 solder joints at different aging conditions and stress amplitudes is studied as well for comparison purposes. The test matrix for this study is shown in Table 4.4. The reliability model for SAC-Q solder joints is developed at each service condition. The effect of aging time and stress amplitude on the characteristic life are investigated. A general reliability model as a function of aging time and stress amplitude is constructed by using the general empirical models. If there is no trend for the shape parameters, the mathematical average for the obtained shape parameters at different conditions is calculated. The inelastic work per cycle and plastic strain for each sample are numerically found using a MATLAB code. The evolution in the hysteresis loops at different aging conditions and stress amplitudes is determined. The Coffin-

Manson model and the Morrow Energy model are used as prediction models for the fatigue life as a function of plastic and inelastic work per cycle, respectively. The microstructure analysis to determine the evolutions in the IMCs layers and the coarsening of precipitates is performed by using similar experimental procedures to the ones that are used in study 2.

Table 4.4: The Test Matrix for Studying the Effect of Aging on SAC-Q Solder Joint Reliability.

Aging time (hrs)	Aging temp (ºC)	Stress Amplitude (MPa)		
		22	26	29
0		7 samples	7 samples	7 samples
2	100	7 samples	7 samples	7 samples
10	100	7 samples	7 samples	7 samples
100	100	7 samples	7 samples	7 samples
1000	100	7 samples	7 samples	7 samples

4.4.4 A New Proposed Methodology of Optimizing the Solder Joint Parameters Using the Fuzzy Logic

In the majority of the studies, reliability is assessed to find the optimal process parameters by using the characteristic life where this is applied if the Weibull distribution is used as a fitted random distribution for the failure data, the average time between failures or the average time to failure. This is correct in simple cases when the difference between the alternatives is large enough to recognize the gap between them. In contrast, there are more complex cases where the differences between the performance response measures are not significant enough to determine the optimal process parameters or the best alternatives. For example, Figure 4.8 represents the reliability for three different solder alloys by using the Weibull distribution. The reliability of material C is the best according to the characteristic life, but on the other hand, it has the highest earlier failure probability with a large variation on the data. Therefore, finding a robust methodology to find the optimal parameters is crucial hence the small differences between the alternatives has a large

impact on the critical applications and mass production products. In this study, a new methodology for optimizing the solder joint parameters is constructed by applying the following procedure. First, four different indices are defined as performance responses which are signal to noise ratio (SNR), characteristic life, mean-variance and the earlier failure probability. For the SNR, the fatigue life is classified as Larger the Better response, and the SNR is calculated at each solder joint and process parameter by using equation 2.54 in chapter 2 section 2.2.

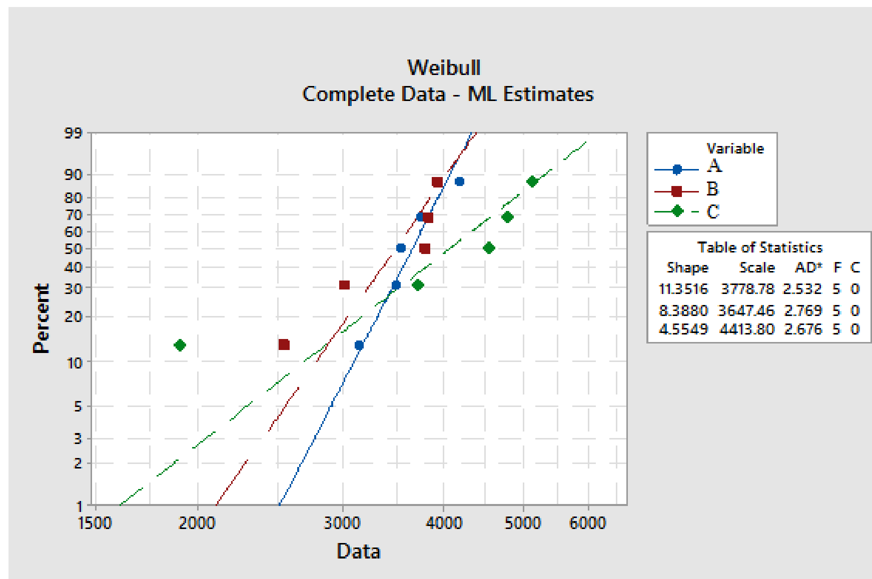

Figure 4.8: Example of a Complex Comparison Case.

The Weibull distribution is constructed at each parameter combination to find the characteristic life value and the earlier failure probability. The mathematical mean and variance are determined for each combination, and then their values are standardized between 0 and 1 by the normalization process. The difference in the normal value of mean and the normal value of variance is calculated as another performance response. After determining the performance indices, the optimization problem is converted into a multi-response optimization problem. The fuzzy logic is implemented to solve the multi-response problem by combining all responses into a single response that is called the comprehensive output measure (COM) by implementing the fuzzy steps that are discussed in

chapter 2 section 2.3. The performance responses that are used as inputs for the fuzzy model and two linear membership functions (Low, High) are defined for each input. After the fuzzification of the inputs, the sixteen rules are set to relate the inputs together. Then, the five linear output membership functions (Lowest, Low, Mid, High, and Highest) are constructed based on the built rules. In order to compute the COM values, the center of gravity method is applied as a defuzzification method. After determining the COM values at each parameter combination, the averages of the COM values are calculated at each parameter level. Because of the large COM value indication of better performance, the parameter levels that have larger COM value are selected to be the optimal parameter levels, where the alternative that has those parameters is the optimal choice. This methodology is applied to a case study to validate the methodology. The case study is about the thermal cycling accelerated test that is performed by another Ph.D. student at Auburn University where his failure data is used as a validation case study. Three solder parameters are studied which are solder sphere materials (two levels), surface finish material (three levels) and the solder paste materials (ten levels). The testing board is cycled between 40ºC to125ºC with 50 minutes ramps time, 3.3ºC per minute ramp rate, 15 minutes dwell time and 115 minutes total cycle time. Table 4.5 represents the test matrix ant the studied factors for the second validation case study.

Table 4.5: The Test Matrix for the Second Validation Case Study.

	Solder sphere			Solder sphere		
	SAC105		SAC305	SAC105		SAC305
solder paste materials	Surface finishes			Surface finishes		
	OSP	ENIG	ImAg	OSP	ENIG	ImAg
M1	5 Samples	5 Samples	5 Samples	5 Samples	5 Samples	5 Samples
M2	5 Samples	5 Samples	5 Samples	5 Samples	5 Samples	5 Samples
M3	5 Samples	5 Samples	5 Samples	5 Samples	5 Samples	5 Samples
M4	5 Samples	5 Samples	5 Samples	5 Samples	5 Samples	5 Samples
M5	5 Samples	5 Samples	5 Samples	5 Samples	5 Samples	5 Samples
M6	5 Samples	5 Samples	5 Samples	5 Samples	5 Samples	5 Samples
M7	5 Samples	5 Samples	5 Samples	5 Samples	5 Samples	5 Samples
M8	5 Samples	5 Samples	5 Samples	5 Samples	5 Samples	5 Samples
M9	5 Samples	5 Samples	5 Samples	5 Samples	5 Samples	5 Samples
M10	5 Samples	5 Samples	5 Samples	5 Samples	5 Samples	5 Samples

Chapter 5: Reliability Modeling for the Effect of Aging Time on SAC305 Solder Joints Cycled in Accelerated Shear Fatigue Test

5.1 Introduction

Solder joints reliability is a determinant factor for the life of the electronic assemblies. The cyclic change in the environmental temperature is one of the most common issues that is associated with the solder joint fatigue life. These changes can create alternating shear stress on the solder joints due to the mismatch in the coefficients of thermal expansion between the substrate and the electronic component materials. Figure 5.1 illustrates the effect of the thermal cycling process on the solder joints. Aging is another factor that may lead to a degradation in the strength and the fatigue properties of the solder joints. Aging changes the microstructure of the solder joints by coarsening the precipitates and increasing the intermetallic compound (IMC) layer thickness.

In this study, the reliability of actual SAC305 solder joints is investigated using accelerated shear fatigue tests. The effect of aging time and stress amplitude are studied. Five levels of aging time at 100 ^{o}C and three levels of stress amplitudes are applied in the experiments. Two-parameters Weibull distribution is used to describe the fatigue life of the solder joints at each test condition. A numerical model for the solder joints reliability is developed as a function of stress amplitude and aging time. The hysteresis loops at different aging times and stress amplitudes are demonstrated. The relationships between the inelastic work, plastic strain, and fatigue life are identified by exploiting the Coffin-Manson and Morrow Energy models. The results indicate a reduction in fatigue life and an increase in inelastic work and plastic strain when the cyclic stress

amplitude is increased. Increasing the aging time has a negative impact on the fatigue life of the solder joint. The Morrow Energy model significantly outperforms the Coffin-Manson model in describing the fatigue behavior of the solder joints regardless of the aging conditions. Finally, a general reliability model as a function of the inelastic work per cycle is introduced.

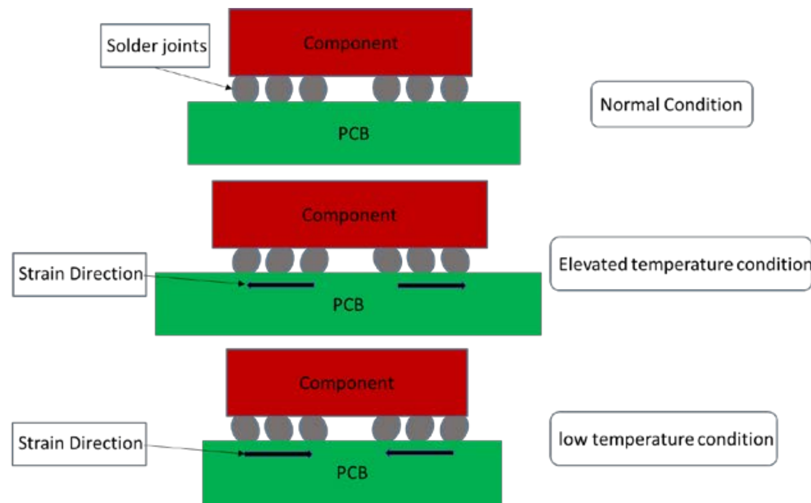

Figure 5.1: The effect of the thermal cycling process on the solder joints.

5.2 Test Matrix

The accelerated shear fatigue test is conducted to assess the reliability of solder joints. The effect of different aging times on the fatigue life of SAC305 solder joints under different levels of cyclic shear stress is investigated. The cyclic shear stress amplitudes were 16, 20, 24MPa. Four different aging times of 2, 10, 100, and 1000hrs at 100ºC are used before performing the tests. The effect of aging time is the main aim for this study; thus, the aging temperature is selected based on the literature to simulate the harsh environmental conditions. Due to the variability from one solder joint to another, 7 solder samples (replicates) were tested at each condition. Table 5.1 shows the test matrix for this study.

Table 5.1: The Test Matrix for Studying the Effect of Aging time on SAC305 Solder Joint Reliability.

Aging Time (hrs)	Aging Temp (°C)	Stress Amplitude (MPa)		
		16	**20**	**24**
0	**100**	7 samples	7 samples	7 samples
2	**100**	7 samples	7 samples	7 samples
10	**100**	7 samples	7 samples	7 samples
100	**100**	7 samples	7 samples	7 samples
1000	**100**	7 samples	7 samples	7 samples

5.3 Results and Analysis

5.3.1 Weibull Distribution Analysis and Reliability Prediction model

To describe the fatigue behavior of the solder joints under different testing conditions, a two-parameter Weibull plot was constructed for each experimental combination. The two-parameter Weibull reliability equation is illustrated in equation 5.1. [111]

$$R(t) = e^{-(\frac{t}{\theta})^{\beta}} \quad (5.1)$$

Where t is the time or the number of cycles, $R(t)$ is the reliability at time t (the probability of surviving), θ is the scale parameter and β is the shape parameter.

Figure 5.2 illustrates the Weibull plots for the non-aged solder joints cycled at different stress amplitudes. A significant reduction in the reliability of the solder joints when the stress amplitude is increased can be noticed. Three censored data points were found in the fatigue life of the non-aged solder joints cycled at 16 MPa because the test was ended at 5000 cycles for all experiments regardless to the failure status of the solder joints.

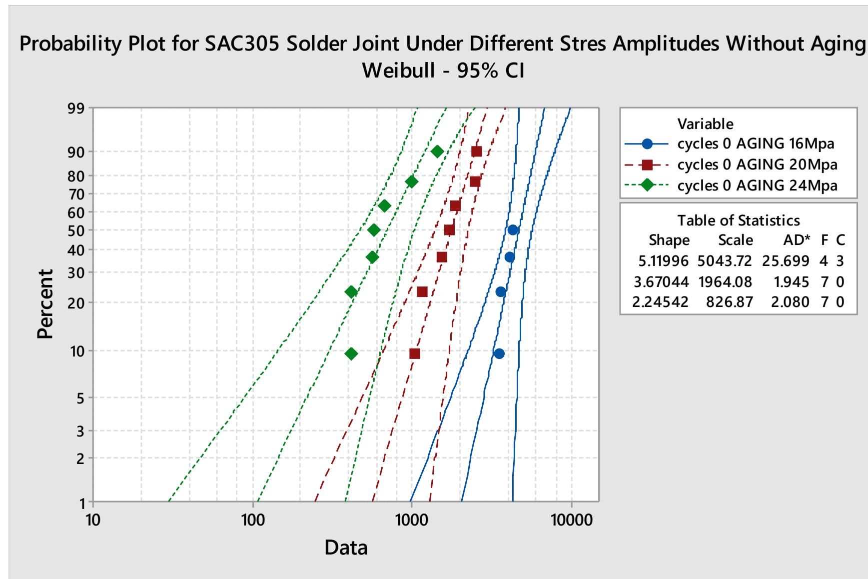

Figure 5.2: Two Parameter Weibull plot for non-aged SAC305 solder joints at different stress amplitudes.

The relationship between the characteristic life and the cyclic stress amplitude is illustrated by utilizing a power equation as shown in equation 5.2. [112]

$$N_{63} = D * P^{-c} \qquad (5.2)$$

Where N_{63} is the characteristic fatigue life of the solder joints, P is the predefined stress amplitude, D and c are constants. The power value c represents the fatigue ductility of the material where a larger value of c means lower ductility.

The fatigue failure data is illustrated in Figure 5.3 for the SAC305 solder joints without aging cycled at different stress amplitudes where seven samples were studied at each condition. Figure 5.3 shows a significant reduction in the fatigue life when the stress amplitude is increased. To identify the fatigue failure mode of the solder joints, the microstructure images were studied for the surfaces of the failed solder joints at different stress amplitudes by using the scanning electron microscope (SEM). Figure 5.4 represents the typical failures that were found for the non-aged SAC305 solder joints at different stress amplitudes.

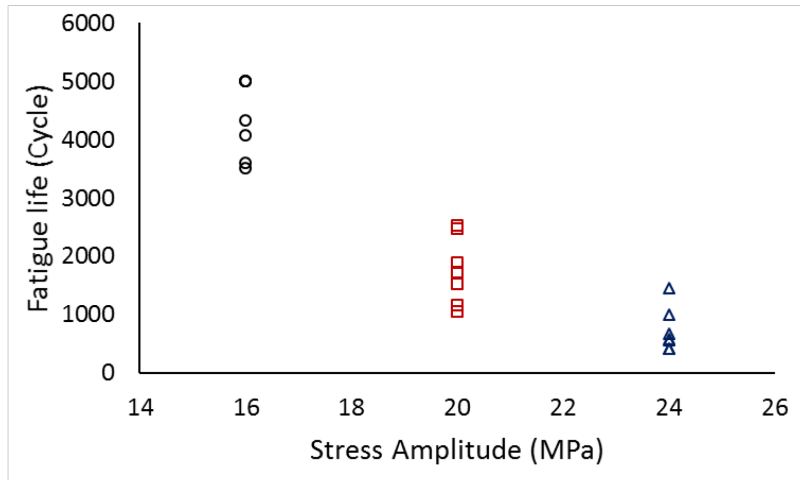

Figure 5.3: The fatigue life of non-aged SAC305 solder joints versus the cycled stress amplitude.

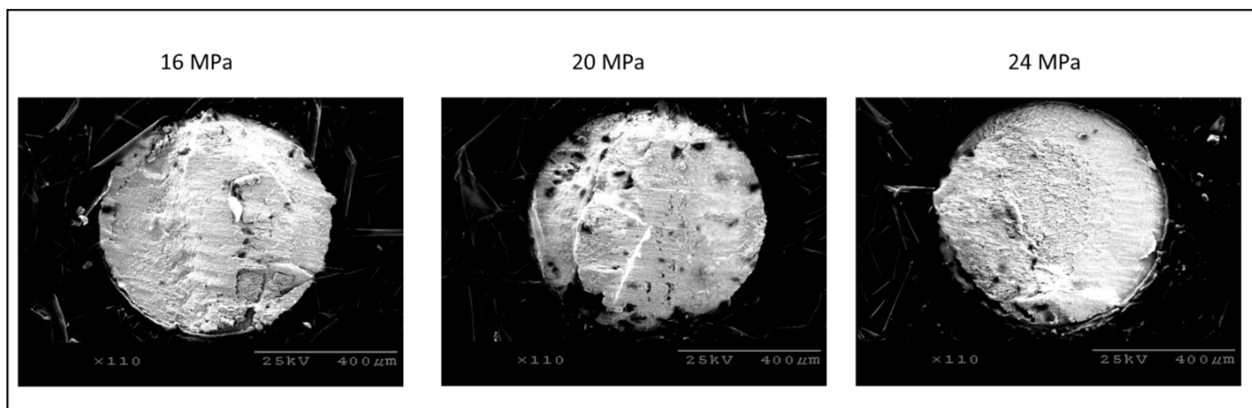

Figure 5.4: Typical failures at different stress amplitudes for the surfaces of non-aged SAC305 solder joints.

In order to describe the effect of increasing the stress amplitude on the solder joints reliability, the characteristic life of the solder joints is used to represent the reliability of the seven solder joints that were tested at each experimental condition. The degradation behavior of the solder joints reliability with the increased stress amplitude is determined as shown in Figure 5.5. Since the characteristic life of the solder joints can be predicted using the power equation that is shown in Figure 5.5, the reliability of the solder joints can be calculated as a function of stress amplitude.

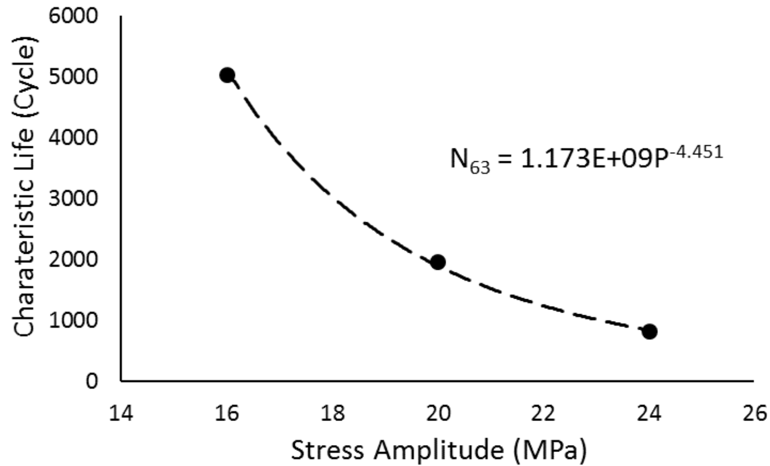

Figure 5.5: The effect of different shear stress amplitudes on the characteristic life for the non-aged SAC305 solder joints.

In order to study the effect of aging on the fatigue behavior of the solder joints at different stress conditions, individual solder joints were tested at amplitudes of 16, 20, and 24 MPa after different aging times of 2, 10, 100, and 1000hrs at 100ºC. The shape and scale parameters of the Weibull distribution were obtained for all combinations. The experimental results for all combinations is summarized in Table 5.2 which includes the characteristic life, shape parameter and the percentage of reduction in the characteristic life at different conditions. The results show a significant decrease in the characteristic fatigue life when the cyclic shear stress amplitude is increased at all aging conditions. Increasing the aging time leads to reductions in the characteristic life at different stress levels but with a lower rate compared with the effect of stress amplitude. From the results summarized in Table 5.2, we can see that the largest drop in the characteristic life was after aging for 1000hrs with around 70% drop. The largest drop in the fatigue life happened during the first 10hrs of aging. There is no observed trend for the shape parameter of the Weibull plot at different aging times and stress amplitudes. The shape parameter values were found between 2 and 7. The two-parameter Weibull distributions at all experimental conditions are shown in the appendix A (Figures A.1 and A.2)

Table 5.2: Fatigue life of SAC305 solder joints results summary.

Stress Amplitude (MPa)	Weibull parameters	Aging time (hrs)				
		0	2	10	100	1000
16	Characteristic Life	5044	4662	3039	2393	2154
	Shape Parameter	5.1	3.8	3.2	3.3	4.9
	Drop in Characteristic Life		8%	40%	53%	57%
20	Characteristic Life	1964	1900	1221	1067	538
	Shape Parameter	3.7	2.3	5.6	3.7	7
	Drop in Characteristic Life		3%	38%	46%	73%
24	Characteristic Life	827	567	450	348	238
	Shape Parameter	2.2	3.1	4.4	3.2	5.7
	Drop in Characteristic Life		31%	46%	58%	71%

Figure 5.6 shows the effect of aging on the relationship between the stress amplitude and the characteristic life. This relationship is expressed in power equations (equation 5.2). From the obtained power equations, an increased trend for the power value (the material ductility index) was observed when the aging time is increased, and there is no observed trend for the constant *D* with aging. The R-squared values for the all fitting lines are between 98% and 99%.

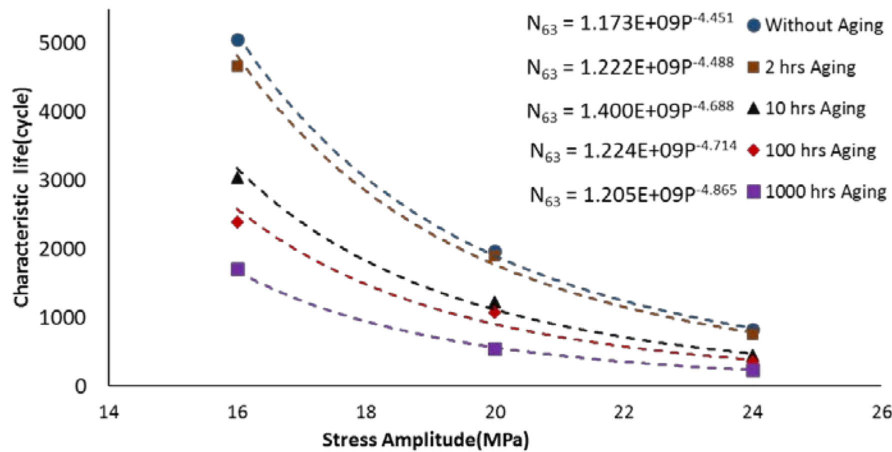

Figure 5.6: The effect of different shear stress amplitudes on the characteristic life of SAC305 solder joints under different aging conditions.

To predict the reliability as a function of aging time and stress amplitude, an empirical model, shown in equation 5.3, was constructed to predict the power value *c* as a function of aging time.

$$c = K_0 + K_1 T - \exp(-K_2 \times T^{K_3}) \ldots\ldots\ldots\ldots\ldots\ldots\ldots\ldots\ldots\ldots\ldots\ldots\ldots\ldots\ldots\ldots\ldots\ldots\ldots\ldots (5.3)$$

Where *c* is the ductility index, *T* is the aging time, and K_0, K_1, K_2, and K_3 are constants. Figure 5.7 shows the fitting values of these constants that was obtained by using a non-linear optimizer. The empirical model of the power value *c* has three terms; the first term is the initial value (K_0) which is related to the power value for the non-aged solder joints (*c* for non-aged solder joints +1). The exponential term ($Exp\ (-K_2 \text{ x } T^{K3})$) represents the behavior of *c* value in the first hours of aging. The linear term ($k_1 * T$) shows the trend of value *c* in long-term aging.

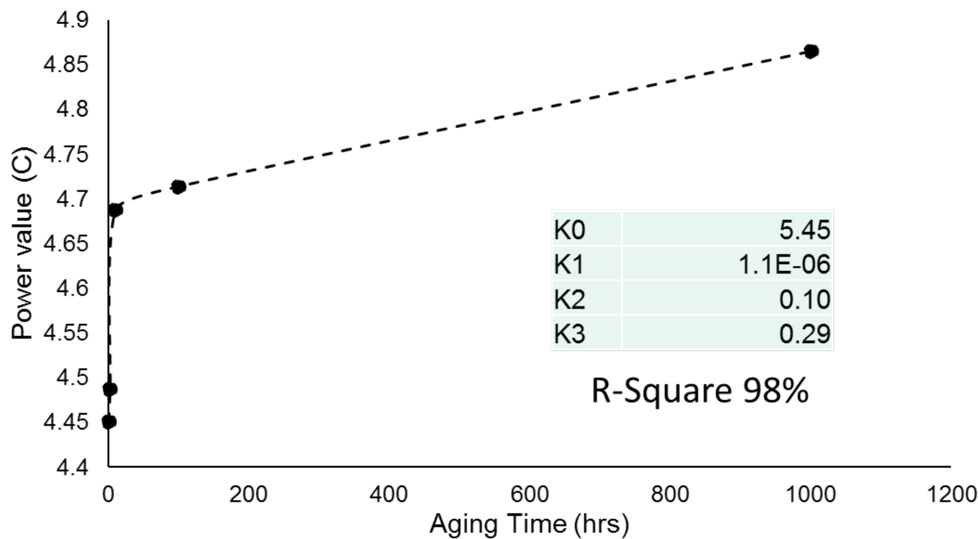

Figure 5.7: Prediction model for the power value (C).

A general prediction model of the characteristic life is established as a function of the stress amplitude and aging time as shown in equation 5.4 by using equations 5.2 and 5.3.

$$N_{63} = \text{Avg}(D) \times P^{-(K_0 + K_1 T - exp(-K_2 \times T^{K_3}))} \ldots\ldots\ldots\ldots\ldots\ldots\ldots\ldots\ldots\ldots\ldots\ldots (5.4)$$

Where N_{63} is the characteristic fatigue life, *Avg* (*D)* is the value for the mathematical average of the *D* values for different aging times, *T* is the aging time and *P* is the stress level. The mathematical average for the shape parameter at different tested conditions was determined which is equal to 3.94. By utilizing the Weibull equation (equation 5.1) and the characteristic life

prediction equation (equation 5.4), a general reliability model for SAC305 solder joints as a function of stress amplitude and aging time was determined as shown in equation 5.5. Where *P* is the predefined stress amplitude, *T* is the aging time, and *t* is the number of cycles.

$$R(t) = e^{-\left(\frac{t}{1.24*10^{9}*P^{-(5.45+1.1*10^{-6}*T-exp(-0.10*T^{0.29}))}}\right)^{3.94}} \quad \ldots\ldots\ldots(5.5)$$

5.3.2 The Hysteresis Loop Evaluations

The evolution in the hysteresis loop (stress-strain diagram) was demonstrated by constructing a hysteresis loop for each cycle through the fatigue life for all samples tested at different conditions. Figure 5.8 shows a typical hysteresis loop for SAC305 solder joint cycled at 20MP without aging. The enclosed area of the hysteresis loop is defined as the inelastic work density per cycle, and the delta strain at stress zero is the plastic strain range. Plastic stain and inelastic work per cycle are commonly used to describe the fatigue properties of solder joints.

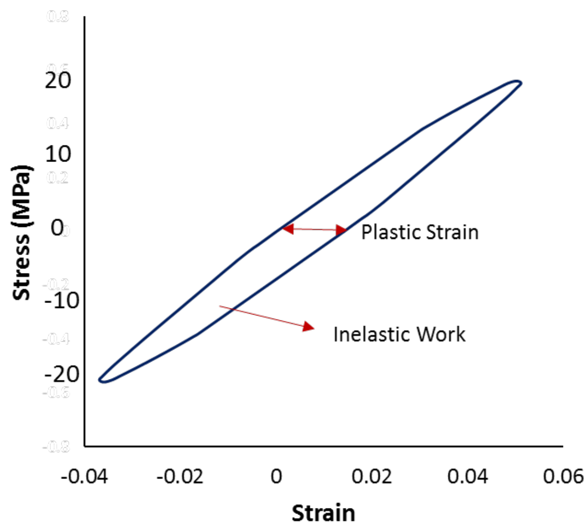

Figure 5.8: The Full Hysteresis loop for the non-aged SAC305 solder joints cycled at 20 MPa.

Figure 5.9 shows the inelastic work per cycle versus the number of cycles for a non-aged SAC305 solder joint cycled at 16 MPa until failure. Three main regions can be identified from Figure 5.9;

strain hardening, steady state, and crack growth regions. Most of the solder joint fatigue life is during the steady-state region where damage keeps accumulating until crack initiation then growth.

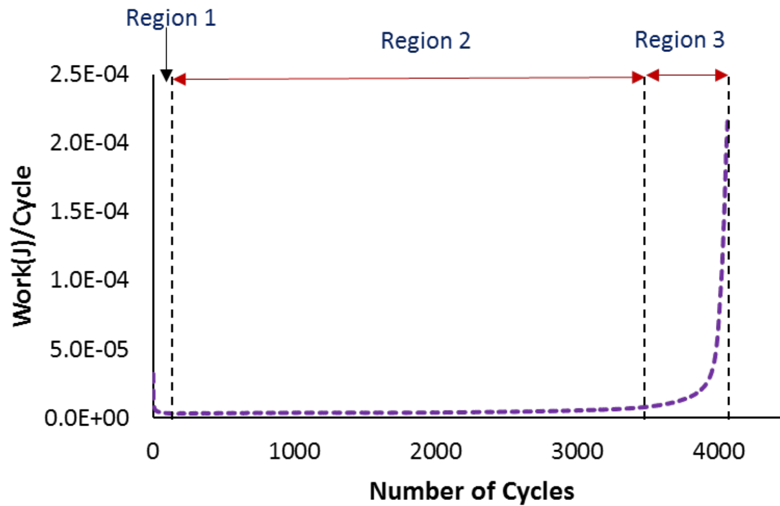

Figure 5.9: Inelastic work vs. the number of cycles for a non-aged SAC305 solder joints cycled at 16 MPa amplitude until failure.

In order to compare the fatigue properties of the solder joints at different testing conditions, the average inelastic work and the average plastic strain were calculated in the steady-state region for each sample. Figure 5.10 shows the effect of different stress amplitudes on the hysteresis loop for the non-aged SAC305 solder joints in steady-state region. Obviously, the area of the hysteresis loop and the strain range are increased when the stress amplitude is increased. Figure 5.11 shows the effect of aging time on the hysteresis loop in the steady-state region for SAC305 solder joints. The hysteresis loop area and the strain range are increased when the aging time is increased. Larger hysteresis loop means more damage per cycle which leads to fewer number of cycles to failure.

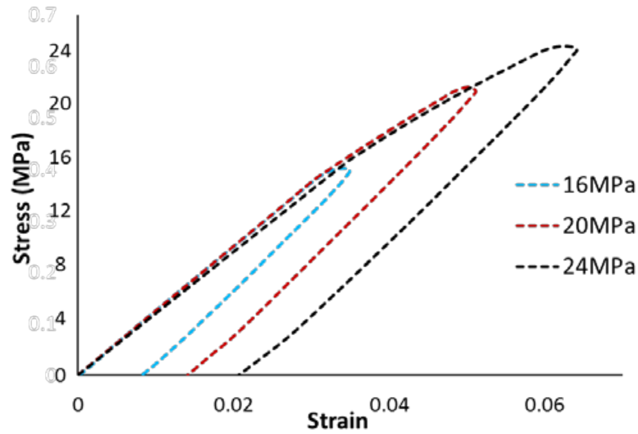

Figure 5.10: The effect of different stress amplitudes on the hysteresis loop for the non-aged SAC305 solder joints.

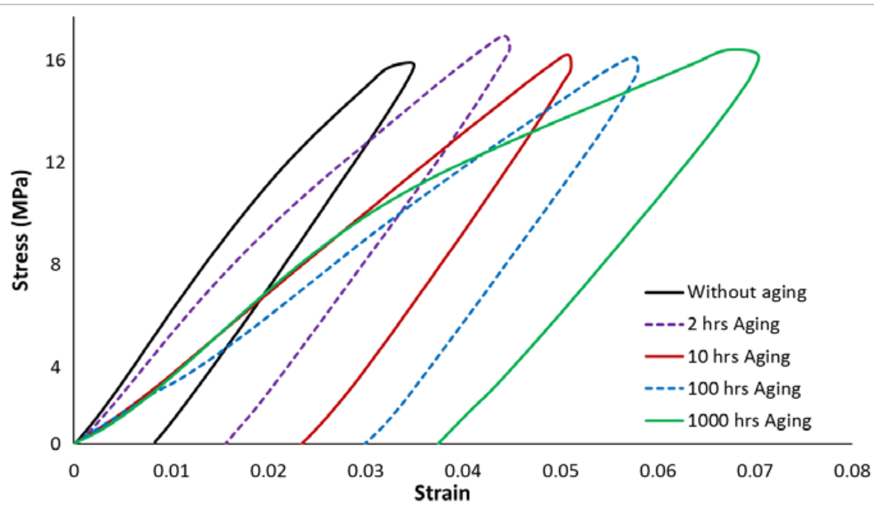

Figure 5.11: The effect of aging on the hysteresis loop for SAC305 solder joints cycled at 16 MPa stress amplitude.

Figure 5.12 shows the average accumulated work until complete failure for SAC305 solder joints as a function of the aging time for different stress amplitudes. It is obvious that increasing the aging time leads to less accumulated work unit complete failure in any cycling stress amplitudes. This indicates that the amount of total fatigue damage to break a solder joint is less when it is aged. It is also clear that cycling with lower stress amplitudes requires more accumulated work to complete failure.

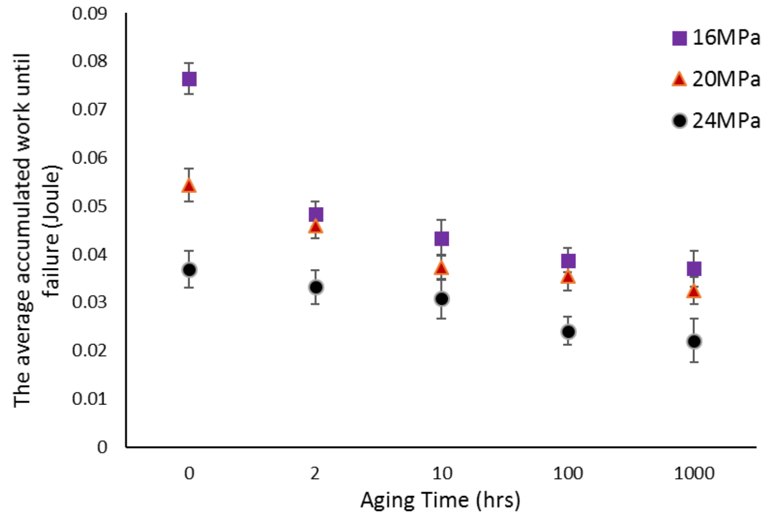

Figure 5.12: Accumulated work until complete failure vs. aging time at different stress amplitudes.

Figure 5.13 shows the effect of aging time on the inelastic work per cycle at different stress amplitudes. To describe the inelastic work per cycle behaviors at different aging times, a general empirical model was utilized as shown in equation 5.6.

$$W = K_0 + 1 + K_1 \times T - \exp(-K_2 \times T^{K_3}) \qquad (5.6)$$

Where W represents the inelastic work per cycle, K_0 to K_3 are model constants and T is the aging time. The constants of equation 5.6 for the tested solder joints at different stress amplitudes are represented in Table 5.3.

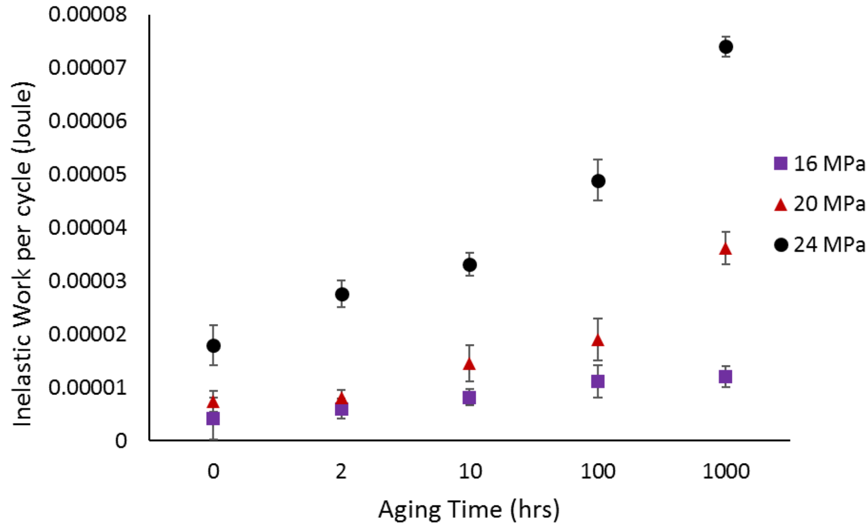

Figure 5.13: The relationship between the inelastic work per cycle and the aging time at different stress amplitudes.

Table 5.3: Inelastic work per cycle empirical model constants.

Stress amplitude (MPa)	K_0	K_1	K_2	K_3
16	4.2E-6	2.5E-11	2.3E-6	0.189
20	7.3E-6	1.85E-08	7.6E-6	0.0470
24	1.8E-5	1.72E-08	1.76E-05	0.099

Figure 5.14 shows the relationship between plastic strain and the aging time at different stress amplitudes. To describe this relationship, an empirical model was used as shown in equation 5.7.

$$PS = 1 + K_0 + K_1 \times T - \exp(-K_2 \times T^{K_3}) \qquad (5.7)$$

Where PS is the plastic strain range, T is the aging time, and K_0 to K_3 are constants. The constants for equation 5.7 for the tested SAC305 solder joints at different stress amplitudes are represented in Table 5.4. Both of the empirical models that describe the relationship between the aging time, the plastic strain and the inelastic work have three terms which are the initial value (K_0), the exponential term for the behavior during the first hours of aging and a linear term for the long aging time effect.

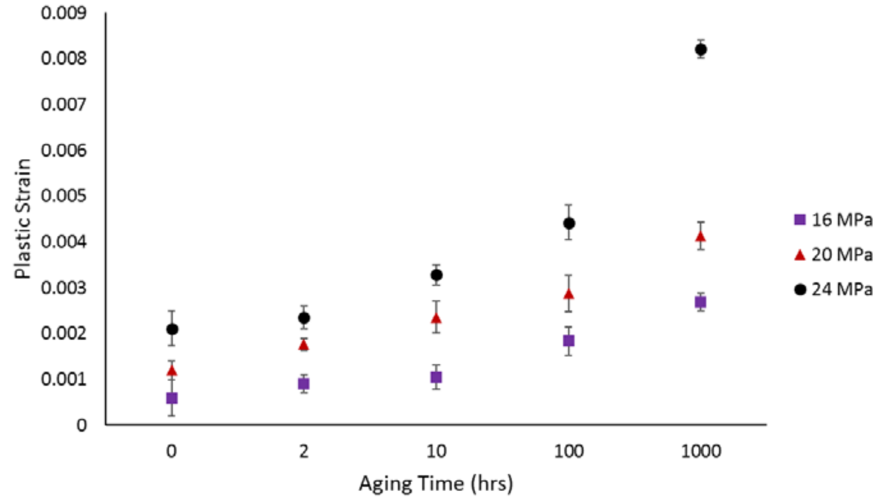

Figure 5.14: The relationship between the plastic strain and the aging time at different stress amplitudes.

Table 5.4: Plastic strain empirical model constants.

Stress amplitude (MPa)	K_0	K_1	K_2	K_3
16	5.95E-4	2.03E-07	4.9E-4	0.200
20	1.2E-3	7.35E-07	8.8E-4	0.119
24	2.11E-2	4.5E-7	8.0E-4	0.093

5.3.3 The Morrow Energy and the Coffin-Manson Fatigue Models

One of the most common models that are used to predict fatigue life as a function of the inelastic work per cycle is the Morrow energy fatigue model. According to the Morrow model, the relationship between fatigue life and inelastic work per cycle can be described by using a power equation. Therefore, the characteristic life can be predicted using equation 5.8. [113]

$$N_{63} = C^{\frac{1}{m}} W^{\frac{-1}{m}} \quad \text{.......... (5.8)}$$

Where W is the inelastic work, C is the fatigue ductility, N_{63} is the characteristic life, and m is the fatigue exponent. By using the Morrow energy fatigue model, the relationship between fatigue life and the average inelastic work per cycle with its fitting equation were illustrated in Figure 5.15. The higher inelastic work per cycle was found when the solder joints have a lower characteristic

fatigue life. Table 5.5 shows the fatigue ductility and the fatigue exponent values at different aging times. There are no clear trends observed for the fatigue ductility and the fatigue exponent at different aging times. Thus, we conclude that aging has no effect on the Morrow Energy model.

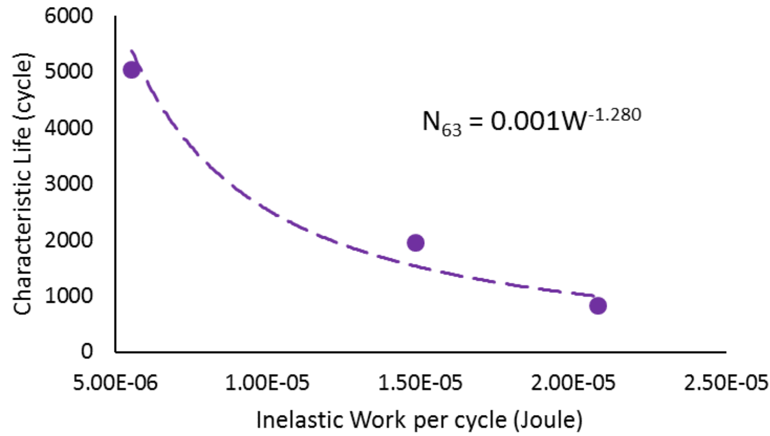

Figure 5.15: Characteristic life vs. inelastic work per cycle for the non-aged SAC305 solder joints.

Table 5.5: The fatigue ductility and the fatigue exponent for the Morrow Energy model.

The Aging time (hrs)	fatigue ductility (C)	The fatigue exponent (m)
0	0.0045	0.781
2	0.0064	0.824
10	0.0049	0.810
100	0.0057	0.810
1000	0.0047	0.788
global	0.0048	0.793

Figure 5.16 shows the characteristic life of SAC305 solder joints as a function of the inelastic work per cycle for different aging times on log-log scale. The data points for all aging conditions have a similar trend (slope). Therefore, all data points were fitted in a one global Marrow energy model using equation 5.8 regardless of the aging time. The fatigue ductility and the fatigue exponent coefficient for the global Morrow model for SAC305 solder joins are 0.0048 and 0.793, respectively.

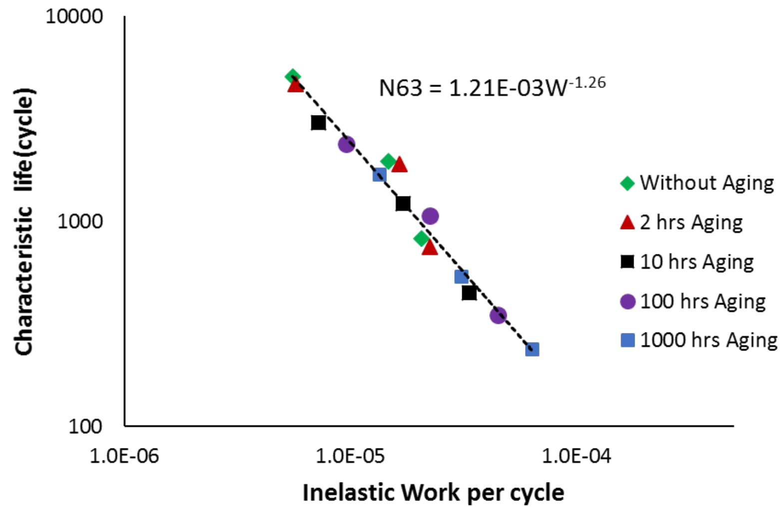

Figure 5.16: Characteristic life and inelastic work per cycle for SAC305 solder joints at different aging times in a log-log scale.

To elucidate the relationship between the characteristic fatigue life and the plastic strain, the Coffin-Manson fatigue model was implemented by using a power equation between the plastic strain and the fatigue life. The Coffin-Manson model is shown in equation 5.9 [114]

$$N_{63} = \gamma^{\frac{1}{\alpha}} S^{\frac{-1}{\alpha}} \quad (5.9)$$

Where N_{63} is the characteristic fatigue life, γ is the fatigue ductility coefficient, S is the plastic strain, and α is the fatigue exponent. Figure 5.17 shows the plot of the plastic strain versus the characteristic fatigue life for the non-aged SAC305 solder joints and its Coffin-Manson model. The results showed that higher plastic strain has a lower characteristic fatigue life.

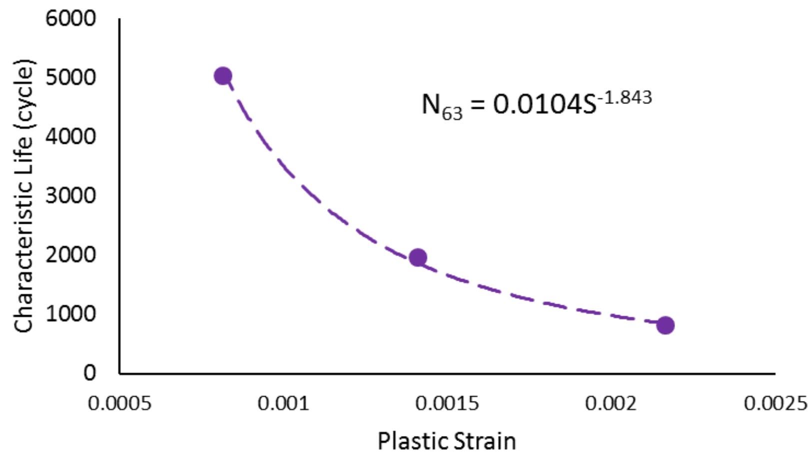

Figure 5.17: Characteristic life vs. plastic strain for non-aged SAC305 solder joints

The Coffin-Manson fatigue equations were found at different aging times by plotting the plastic strain versus the characteristic fatigue life in a log-log scale as shown in Figure 5.18. The fatigue ductility coefficient and the fatigue exponent values at different aging times are summarized in Table 5.6. It is obvious that solder joints didn't follow the same Coffin-Manson behavior when they are aged for different times. There is a significant difference in the fatigue ductility coefficient and the fatigue exponent constants among the different aging times. Figure 5.19 and 5.20 represent the change in the values of the fatigue ductility coefficient and the fatigue exponent, respectively, when increasing the aging times. Therefore, the Coffin-Manson fatigue model was affected by the aging time factor. Thus, the Morrow Energy model represents a robust prediction model for the characteristic fatigue life compared with the Coffin-Manson fatigue model where its constants have not been influenced by the increased aging time.

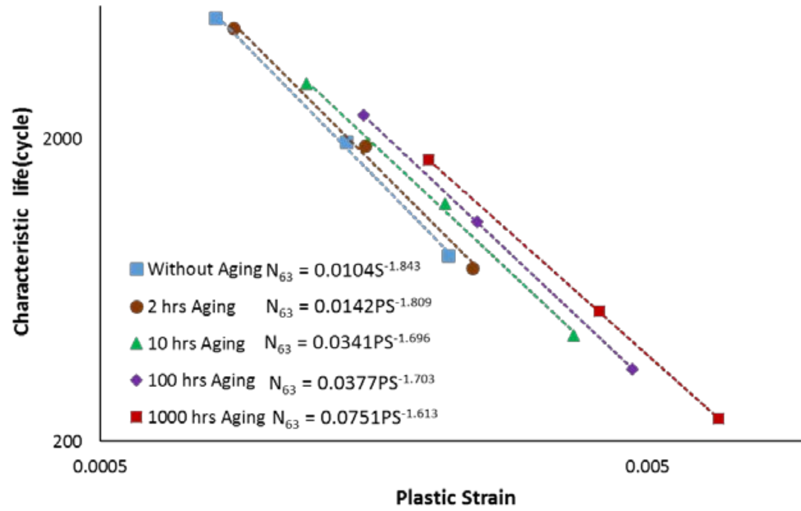

Figure 5.18: Characteristic life vs. plastic strain for SAC305 solder joints at different aging times on a log-log scale.

Table 5.6: Fatigue ductility coefficient and fatigue exponent of the Coffin-Manson model.

Aging time (hrs)	Coefficient of fatigue ductility (γ)	Fatigue exponent (α)
0	0.084	0.543
2	0.095	0.553
10	0.136	0.590
100	0.146	0.587
1000	0.201	0.620

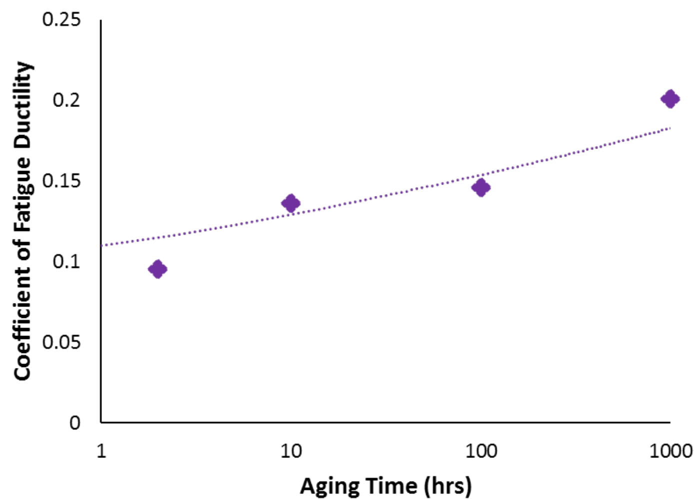

Figure 5.19: Coefficient of fatigue ductility (θ) of the Coffin-Manson model vs. aging time.

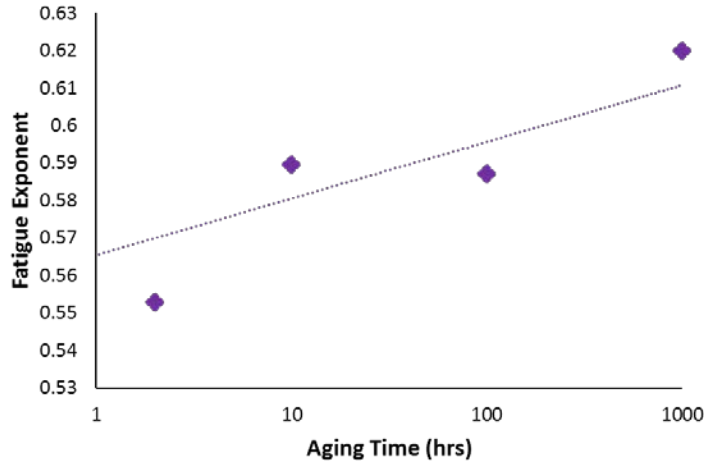

Figure 5.20: Fatigue exponent (α) of the Coffin-Manson model vs. aging time.

Since the characteristic life can be predicted as a function of the inelastic work per cycle by using the Morrow energy model, a general reliability model based on the inelastic work per cycle is developed. The Weibull distribution equation (equation5.1), the Morrow Energy model equation (equation 5.8) and the mathematical average of the shape parameter values are used to build this model as shown in equation 5.10. Where *t* represents the time or cycle, *R(t)* is the reliability at a time or cycle *t* and *W* is the inelastic work. This equation is obtained from 105 experiments that include 7 replicates under 15 different conditions. The mathematical average of the 7 replicates is used to describe the inelastic work per cycle for each condition.

$$R(t) = e^{-\left(\frac{t}{0.0012*W^{-1.261}}\right)^{3.94}} \quad (5.10)$$

5.4 Summary

In this study, different general reliability models were constructed as a function of aging conditions, stress amplitude and inelastic work per cycle by utilizing two-parameter Weibull distribution, stress-life equation and Marrow Energy models. The effect of aging time was assessed by using an empirical model. These models describe the fatigue performance of SAC305 solder

joints under accelerated conditions. Predicting the Weibull distribution parameters (scale and shape) was the basis for those models. Since, there was no clear trend of the shape parameter values with the aging or loading conditions, shape parameter was estimated by determining the mathematical average of the shape parameter values at different experimental conditions. Morrow Energy model showed a robustness in estimating the characteristic life where the Morrow equation constants kept their values at different aging times. Therefore, the reliability distribution of the solder joint can be predicted as a function of the inelastic work regardless of the aging time. Coffin-Manson model had some difficulties to predict the characteristic life as a function of plastic strain at different aging times where its constants are significantly influenced with the aging conditions.

Chapter 6: Degradation Modeling of the Effect of the Aging Temperature on the Fatigue Behavior of Lead-Free Solder Joints

6.1 Introduction

The Performance of the electronic assemblies is extremely reliant on the reliability of the solder joints. Many operation factors may influence the fatigue and mechanical properties of the solder joints with different contributions. The health issues and government regulations associated with the leaded solder joints arise the need for the use of the lead-free solder joints. The fatigue and mechanical behaviors of the lead-free solder joints at actual operating conditions are not well understood. In this study, the fatigue behavior and the shear strength of SAC 305 solder joints with 30mil diameter, SMD and OSP surface finish are studied at different aging conditions. The accelerated shear fatigue test and shear test are used to evaluate the fatigue resistance performance and the shear properties for the individual solder joints in actual operating conditions. Instron 5948 MicroTester machine with a customized fixture is utilized to perform those tests. In this study, three factors are considered in the fatigue test: Cyclic stress amplitude with three levels (16, 20 and 24MPa), aging time with four levels (2, 10, 100 and 1000 hrs) and the aging temperature with three levels (50, 100 and 150°C). Two parameters Weibull distribution is used to describe the reliability of the solder joints. The effects of stress amplitude, aging time and aging temperature on the characteristic life are investigated. A general reliability model as a function of those parameters is constructed by utilizing empirical and Arrhenius models. The evolutions in the

hysteresis loop at different conditions are explored by exploiting the stress-strain diagram at each cycle in the solder joint life. The inelastic work and the plastic strain at the steady-state region are obtained from the hysteresis loop. The relationships between the inelastic work, plastic strain and aging conditions are demonstrated. The Morrow energy and the Coffin-Manson models are used to predict the fatigue life as a function of inelastic work, plastic strain respectively. An artificial neural network model (ANNs) model was constructed to predict the fatigue life as a function of stress amplitude and aging conditions. In the shear test, two factors are studied which are aging time and aging temperature with the same experimental levels that were used in the fatigue test. The ultimate shear strength is used to describe the shear strength of the solder joint. ANOVA analysis is accomplished to identify the contribution of each parameter on the shear strength of the solder joints. A general empirical model is determined to estimate the shear properties of the solder joints as a function of aging conditions. Microstructure analysis is performed at different aging conditions by using SEM. The results revealed a significant reduction in the fatigue life when the stress amplitude or aging level are increased. The increase in the aging level or the stress amplitude leads to an increase in the inelastic work and the plastic strain with different altitudes. The aging time and aging temperature have different contributions in the fatigue results when compared to the shear test results.

6.2 Experimental Layout

FR-4 glass-epoxy printed circuit board (PCB) is used in this experiment with OSP surface finish, solder mask defined (SMD). A full array of 30 SAC305 (Sn-3.0Ag-0.5Cu) solder joints with 30 mil diameter is applied onto the PCB. The copper pad diameter is 22 mil. The PCB is divided into 120 coupons where each coupon has nine solder joints. The pitch distance between the solder balls is 3 mm. The accelerated fatigue shear test was utilized to assess the reliability of SAC305 solder

joints at different loading and aging conditions. Seven samples were exploited to represent the fatigue behavior at each condition. The test matrix of the fatigue test is shown in Table 6.1. A total of 273 solder joints with 39 experimental combinations were used in the test. The shear test was applied to estimate the shear strength of SAC305 solder joints at different aging conditions. The Ultimate Shear Strength (USS) is used to describe the shear strength of the solder joints. All the samples were sheared at a 0.1 S^{-1} strain rate. Seven samples were also used to represent the shear strength performance at each experimental condition. Table 6.2 shows the test matrix of the shear test. Instron 5948 testing machine was used to apply the fatigue and the shear tests on the individual solder joints. According to the experimental layout in Table 2, ninety-one (91) solder joints were used for the shear test at all experimental conditions with 13 different experimental conditions.

Table 6.1: Test matrix for the accelerated shear fatigue test.

Aging Temperature (˚C)	Aging Time (hrs)	Stress Amplitude (MPa)		
		16	20	24
Non-aged	Non-aged	7 Joints	7 Joints	7 Joints
50	2	7 Joints	7 Joints	7 Joints
	10	7 Joints	7 Joints	7 Joints
	100	7 Joints	7 Joints	7 Joints
	1000	7 Joints	7 Joints	7 Joints
100	2	7 Joints	7 Joints	7 Joints
	10	7 Joints	7 Joints	7 Joints
	100	7 Joints	7 Joints	7 Joints
	1000	7 Joints	7 Joints	7 Joints
150	2	7 Joints	7 Joints	7 Joints
	10	7 Joints	7 Joints	7 Joints
	100	7 Joints	7 Joints	7 Joints
	1000	7 Joints	7 Joints	7 Joints

Table 6.2: Test matrix for the shear test.

Aging Temperature (˚C)	Aging Time (hrs)				
	Non-Aged	2	10	100	1000
50	7 Joints	7 Joints	7 Joints	7 Joints	7 Joints
100		7 Joints	7 Joints	7 Joints	7 Joints
150		7 Joints	7 Joints	7 Joints	7 Joints
200		7 Joints	7 Joints	7 Joints	7 Joints

6.3 Results and Discussion

6.3.1 Fatigue Life Modeling Based on the Loading and Aging Conditions

In the accelerated fatigue shear test, the fatigue data for SAC305 solder joints were obtained at different conditions. Two-parameter Weibull distribution was used to describe the fatigue behavior at different loading and aging scenarios. The Weibull distribution equation is shown in equation 6.1. Where β is the shape parameter which mainly represents the variability in the reliability data, *t'* is the time or the cycle number, *R(t)* is the reliability at time *t'* and θ is the scale parameter which is commonly called the characteristic life. [111]

$$R(t) = e^{-(\frac{t'}{\theta})^{\beta}} \quad \text{(6.1)}$$

Figure 6.1 shows the Weibull probability plot for the fatigue life of the non-aged SAC305 solder joints at different stress amplitudes. The effect of the applied stress level on the solder joint fatigue life is observed where increasing the stress level leads to a severe reduction in the solder joint life. Around 84% percent reduction in the solder joint life was found when the stress amplitude is increased to 24 MPa compared to 16 MPa stress amplitude. The characteristic life is commonly implemented to represent the fatigue life value instead of the average of the fatigue life at each experimental condition. The characteristic life represents the 63.2% probability of failure at a

certain condition. The relationship between fatigue life and the cyclic stress amplitude is commonly described by using a power equation (equation 6.2). Where N_{63} is the characteristic life, P is cyclic stress value and E *and* C are the equation constants. The constant C (ductility index) shows the material ductility where a higher C value means lower ductility.[112] To elucidate the relationship between the cyclic stress amplitude and the characteristic life, this relationship is plotted in a log-log scale and fitted to a power equation (equation 6.2) as shown in Figure 6.2.

$$N_{63} = E * P^{-c} \quad \text{...(6.2)}$$

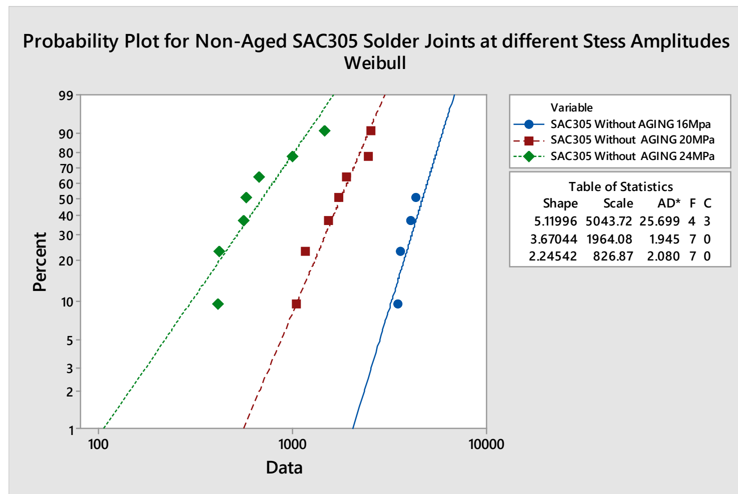

Figure 6.1: Weibull probability plot for SAC305 solder joints at different loading scenarios.

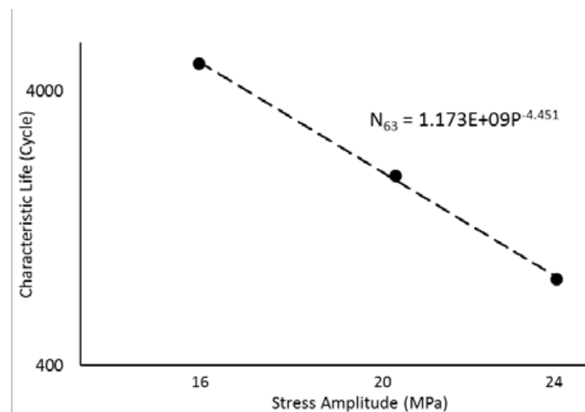

Figure 6.2: The relationship between the characteristic life and stress amplitude for the non-aged SAC305 solder joints in a log-log scale.

The Weibull reliability distribution was conducted to find the reliability function at different aging conditions. Figure 6.3 displays the Weibull probability plots for SAC305 solder joints at different aging times where the cyclic stress was 16 MPa and the aging temperature was 150° C. A significant reduction in the reliability of the solder joint was found with aging where a 79% reduction in the characteristic life was achieved after 1000 hours of aging. The effect of aging temperature on the solder joints reliability that was cycled at 16 MPa and aged for 100 hours is represented in Figure 6.4. The reliability of the solder joint decreased with the increase in aging temperature. Around 77% reduction in the fatigue life was observed when the aging temperature was 150° C, aging time was 100 hours and the cyclic stress amplitude was 16 MPa. A nonsignificant change in the trend of the shape parameter (Weibull distribution) was observed with the change in the aging or loading conditions. The shape parameter values were between 2 and 15 where they display fatigue life variability. To illustrate the effect of aging condition on the relationship between the solder life and the stress, the characteristic life is plotted versus the cyclic stress amplitude in a log-log scale at different aging times and temperatures as shown in Figures 6.5 and 6.6, respectively. Figure 6.5 represents the effect of aging on the stress-life relationship at 150° C. The effect of aging temperature on the stress-life relationship at 100 hours is shown in Figure 6.6. A power fitting equation (equation 6.2) is originated in each aging condition. Table 6.3 shows equation 6.2 constants (*E* and *C*) values at different aging conditions. As a conclusion from Table 6.3, both *E* and *C* constants are changed when the aging condition is different. The Weibull parameters and degradation percentage at different aging and loading scenarios are summarized in Table 6.4. The largest drop (79.2%) in the characteristic life was found for a sample that was aged for 1000 hours at 150° C and cycled at 20 MPa stress amplitude. The two-parameter Weibull distributions at all experimental conditions are shown in appendix A (Figures A.3 and A.7)

Table 6.3: Stress-life equation constants at different aging conditions.

Aging Temperature (˚C)	Aging Time (hrs)	Constants	
		E	*C*
No Aging	No Aging	1.173E+09	4.451
50	2	1.098E+09	4.446
	10	1.590E+09	4.672
	100	1.409E+09	4.728
	1000	2.334E+09	4.979
100	2	1.222E+09	4.488
	10	1.400E+09	4.688
	100	1.224E+09	4.714
	1000	1.205E+09	4.865
150	2	4.126E+08	4.385
	10	1.779E+08	4.212
	100	1.409E+08	4.207
	1000	1.099E+08	4.169

Table 6.4: Summary of the fatigue results.

Aging Temperature (◦C)	Stress Amplitude (MPa)	Weibull Parameters	Aging Time (hrs)				
			0	2	10	100	1000
50	16	Characteristic Life	5044	4736	3705	2601	2269
		Shape parameter	5.1	4.9	5.3	14	4.6
		Drop		6.10%	26.60%	48.40%	55.00%
	20	Characteristic Life	1964	1909	1376	1220	845
		Shape parameter	3.7	4.6	5.2	3.3	2.8
		Drop		2.80%	29.90%	37.90%	57.00%
	24	Characteristic Life	827	776	555	375	299
		Shape parameter	2.2	5.2	3.2	10.2	4.7
		Drop		6.10%	32.90%	47.50%	63.90%
100	16	Characteristic Life	5044	4662	3039	2393	1704
		Shape parameter	5.1	3.8	3.2	3.3	4.9
		Drop		7.60%	39.80%	52.50%	66.20%
	20	Characteristic Life	1964	1900	1221	1067	538
		Shape parameter	3.7	2.3	5.6	3.7	7
		Drop		3.20%	37.80%	45.70%	72.60%
	24	Characteristic Life	827	750	450	348	238
		Shape parameter	2.2	3.1	4.4	3.2	5.7
		Drop		9.30%	45.60%	57.90%	71.20%
150	16	Characteristic Life	5044	2008	1501	1186	1057
		Shape parameter	5.1	9.9	4.6	10	15.6

		Drop		54.80%	74.20%	76.50%	77.70%
	20	Characteristic Life	1964	960	596	498	409
		Shape parameter	3.7	2.6	3.3	8.7	10.03
		Drop		51.10%	69.60%	74.60%	79.20%
	24	Characteristic Life	827	334	272	214	195
		Shape parameter	2.2	4.6	3	6.2	5.27
		Drop		59.70%	67.10%	74.10%	76.40%

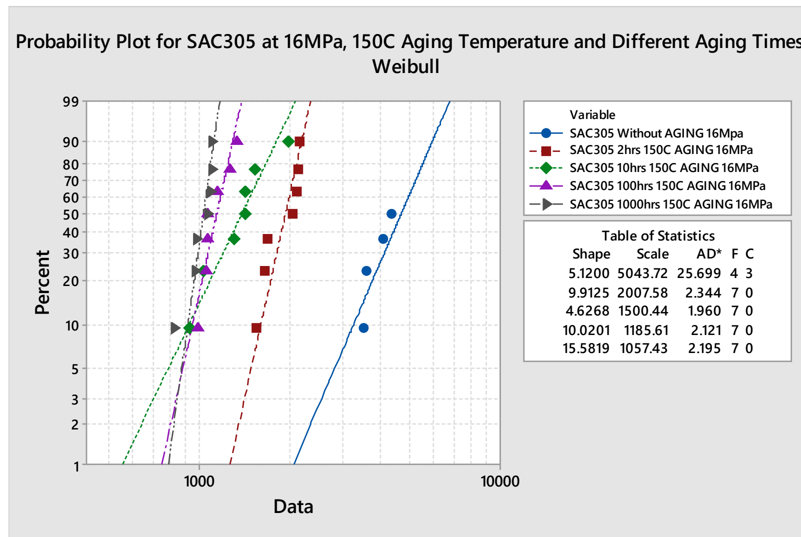

Figure 6.3: Weibull probability plots for SAC305 solder joints at different aging times, 150°C aging temperature and 16 MPa stress amplitude.

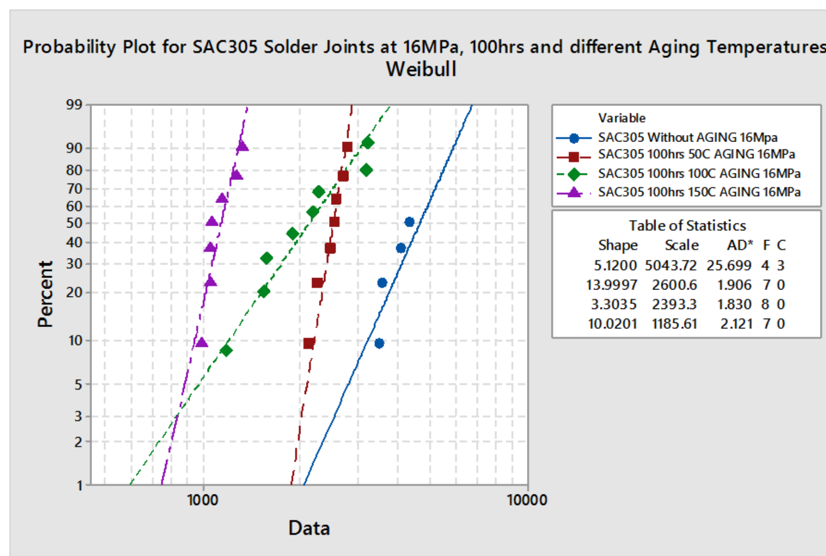

Figure 6.4: Weibull probability plots for SAC305 solder joints at different aging temperatures, 100 hrs aging time and 16 MPa stress amplitude.

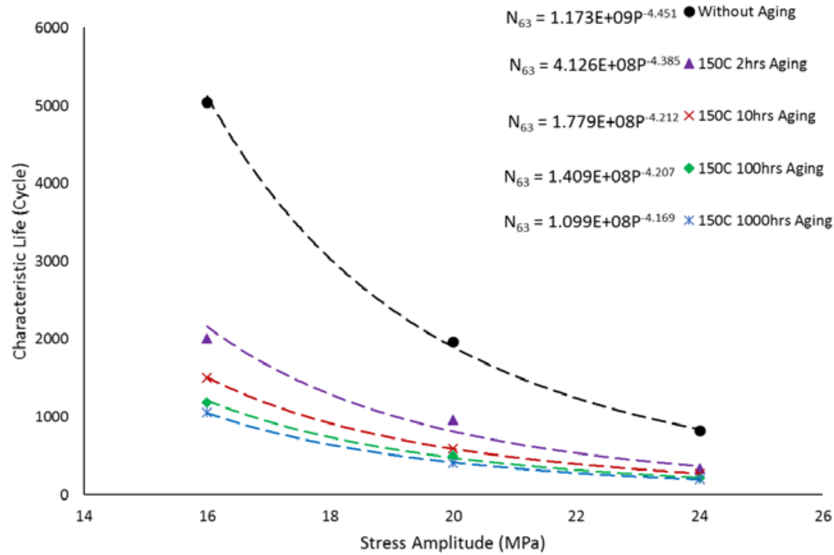

Figure 6.5: The stress amplitude versus the characteristic life at different aging times and a 150°C aging temperature.

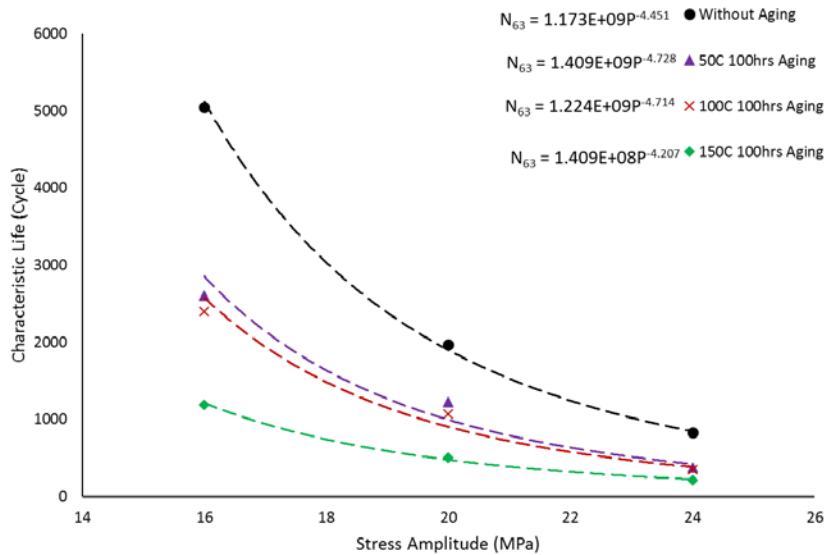

Figure 6.6: The stress amplitude versus the characteristic life at different aging temperatures and 100 hrs aging time.

Arrhenius model is one of the most common models that is used to describe the effect of the temperature on the fatigue life. Equation 6.3 represents the Arrhenius equation. Where *T* is the aging temperature, *r* is the process rate and *A*, *B* are constants. [115]

$$r = A * e^{-\frac{B}{T}} \qquad (6.3)$$

Since the stress- life equation constants (equation 6.2) are influenced by the aging conditions, a general prediction model as a function of stress amplitude, aging time and aging temperature can be constructed to estimate the characteristic life by using a general empirical equation. This model was built based on the stress-life equation where the constants *E* and *C* are predicted as a function of aging temperature and aging time. The Arrhenius model (equation 6.3) was utilized to describe the effect of aging temperature. The exponential and linear terms shown in equation 6.4 are used to define the effect of aging time, where *t* is the aging time, U_1 to U_3 are the equation constants and *H* is the stress-life equation constant (*E* or *C*).

$$H = U_1 * e^{t*U_2} + t * U_3 \qquad (6.4)$$

In the aging time term, the exponential function is applied for the first hours of aging and the linear function is employed for the long-term aging. The general prediction equation is shown in equation 6.5. Where N_{63} is the characteristic life, *t* is the aging time, *T* is the aging temperature and K_1-K_{10} are the equation constants.

$$N_{63} = \overbrace{\left(\overbrace{\underbrace{K_1 * e^{\frac{-K_2}{T}}}_{\text{Arrhenius term}} + \underbrace{K_3 * e^{t*K_4} + t * K_5}_{Aging\ time\ term}}^{E}\right) * P^{\wedge} - \left(\overbrace{\underbrace{K_6 * e^{\frac{-K_7}{T}}}_{\text{Arrhenius term}} + \underbrace{K_8 * e^{t*K_9} + t * K_{10}}_{Aging\ time\ term}}^{C}\right)}^{Stress\ Amplitude\ term} \qquad (6.5)$$

A nonlinear optimizer was used to find the equation constant values, where an objective function was used to maximize the R-squared. The final empirical model is shown in equation 6.6. The R-squared value for this model is 97%.

$$N_{63} = \left(4.66 * e^{\frac{0.019}{T}} + 22693.9 * e^{-t*2.6} + t * 6468215.6\right) * P\wedge\left(-3.89 * e^{\frac{-0.12}{T}} - 4.38 * e^{-t*13.63} - t * 0.0065\right) \quad (6.6)$$

In order to build a general reliability model, equation 6.6 is substituted in equation 6.1 instead of the characteristic life. The shape parameter value is determined by calculating its mathematical average (5.22) since there is a nonsignificant change in the trend of the shape parameter with aging and loading conditions. The general reliability model as a function of aging time, aging temperature and stress amplitude is shown in equation 6.7.

$$R(t) = e^{-\left(\frac{t\prime}{\left(4.66*e^{\frac{0.019}{T}}+22693.9*e^{-t*2.6}+t*6468215.6\right)*P\wedge\left(-3.89*e^{\frac{-0.12}{T}}-4.38*e^{-t*13.63}-t*0.0065\right)}\right)^{5.22}} \quad (6.7)$$

6.3.2 Inelastic Work and Plastic Strain

To identify the effect of different loading and aging scenarios on the fatigue properties (inelastic work and plastic strain), changes in the hysteresis loop at different experimental conditions were investigated. First, the inelastic work and plastic strain are determined by computing the area of the hysteresis loop and the delta strain at stress zero, respectively as shown in Figure 6.7. The inelastic work and plastic strain were numerically computed using a MATLAB code (Version R 2016). The inelastic work per cycle and plastic strain should be computed at the steady-state region, thus the steady-state region was identified by plotting the inelastic work versus the life. From this plot, three regions in the solder joint life are demonstrated which are strain hardening, steady-state and crack growth. Figure 6.8 shows the inelastic work per cycle evolutions along with the solder joint life and the three main regions in the solder joint life for the non-aged SAC305

cycled at 24MPa. Figure 6.9 illustrates the effect of cyclic stress amplitude on the hysteresis loop for the non-aged SAC305 solder joints. An increase in the area and a shift of the strain at a zero-stress value were observed. This indicates that the inelastic work and plastic strain are increased when the cyclic stress is amplified. The effect of aging conditions on the fatigue properties was determined by finding the evolutions in the hysteresis loop at different aging times and temperatures. Figure 6.10 represents the effect of aging time on the hysteresis loop for the solder joints that were cycled at 16 MPa stress amplitude and 150° C aging temperature. Figure 6.11 shows the hysteresis loop for the solder joint at different aging temperatures, 16 MPa cyclic stress and 100 hours of aging time. A significant increase in the inelastic work and plastic strain are found when the aging time or aging temperatures are increased. To describe the behavior of the inelastic work and plastic strain with aging, Figure 6.12 displays the averages of the inelastic work per cycle and plastic strain versus aging time at 150° C and 16 MPa cyclic stress amplitude. Figure 6.13 shows the relationship between the averages of the inelastic work per cycle, plastic strain and the aging temperature at 100 hours of aging and 16 MPa stress amplitude. Each point in those graphs displays the average of the inelastic work per cycle or plastic strain for seven samples at a certain experimental condition. The amount of increase in the inelastic work and plastic strain with aging time decreased exponentially. The largest growth on these properties was observed in the first hours of aging. When the aging temperature was increased, the largest evolution in the inelastic work and plastic strain was found between the non-aged solder joint and 50°C aging temperature. Figure 6.14 represents the evolutions in the inelastic work per cycle and plastic strain at different aging conditions for SAC305 solder joints that were cycled at 16 MPa. It is observed that the contribution of the aging time on the inelastic work and plastic strain is higher than the contribution of the aging temperature for the studied experimental conditions.

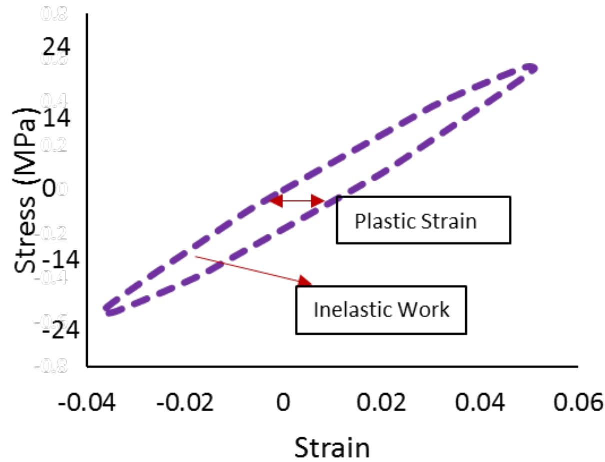

Figure 6.7: The full hysteresis loop for the non-aged SAC305 solder joints at 24 MPa stress amplitude.

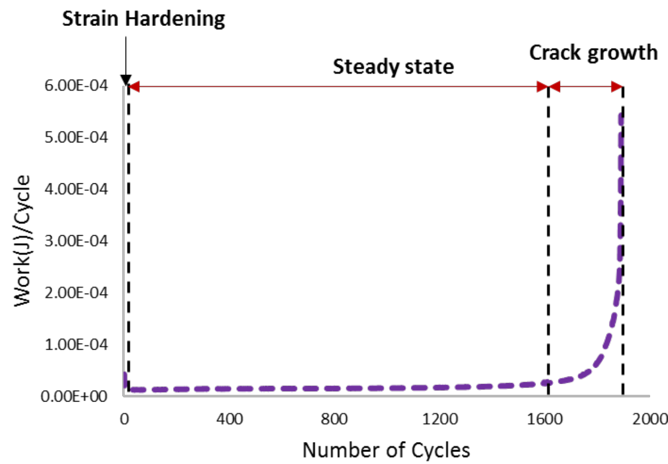

Figure 6.8: The three main regions in the solder joint fatigue life for the non-aged SAC305 solder joints at 24 MPa stress amplitude.

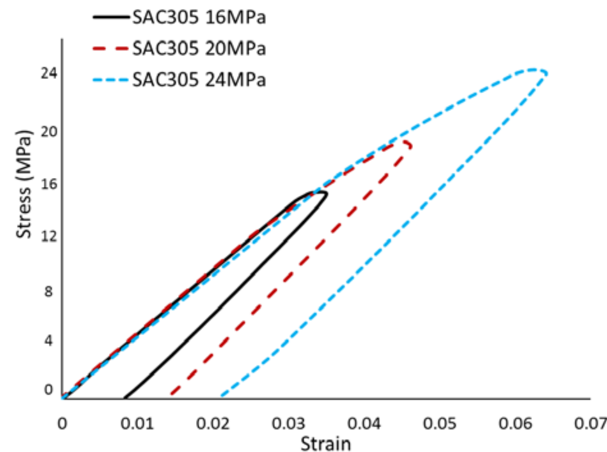

Figure 6.9: The evolutions in the hysteresis loop at different stress amplitudes.

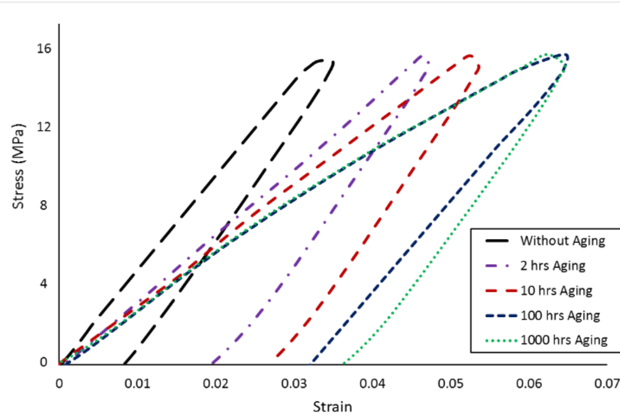

Figure 6.10: The effect of aging time on the hysteresis loop of SAC305 solder joints at 16MPa stress amplitude and 150°C aging temperature.

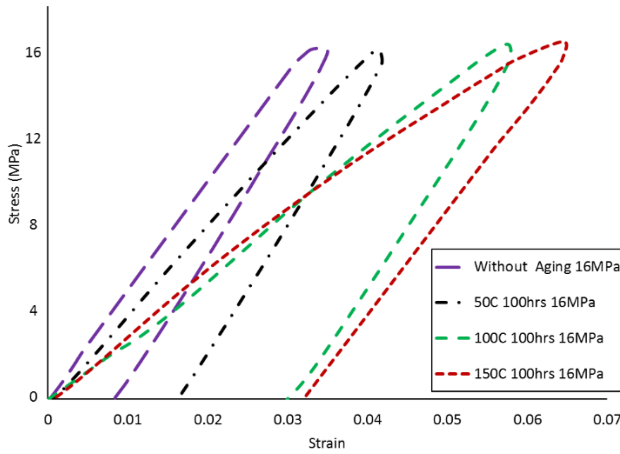

Figure 6.11: The effect of aging temperature on the hysteresis loop of SAC305 solder joints at 16 MPa stress amplitude and 100 hrs aging time.

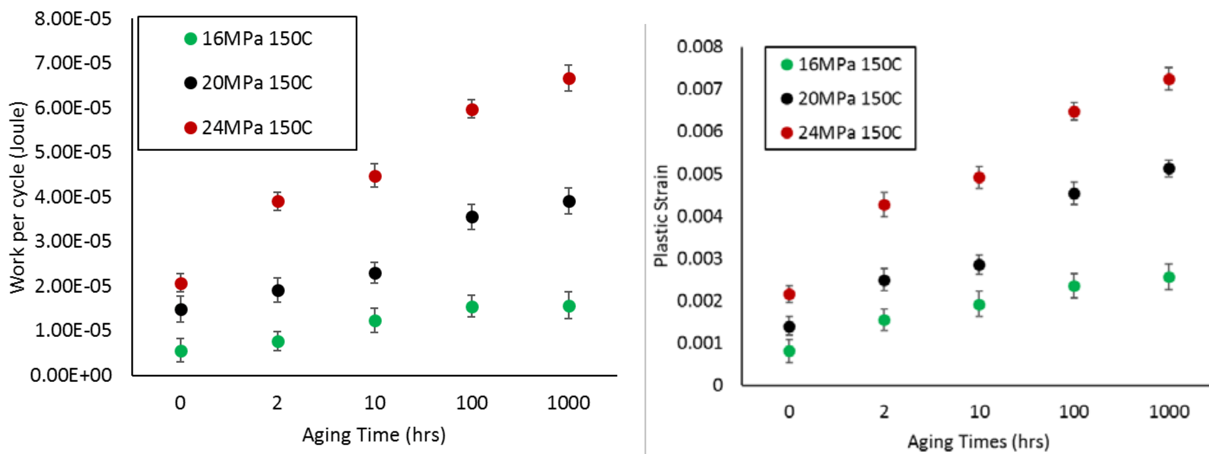

Figure 6.12: The effect of aging time on the inelastic work and plastic strain of SAC305 solder joints at 150°C aging temperature.

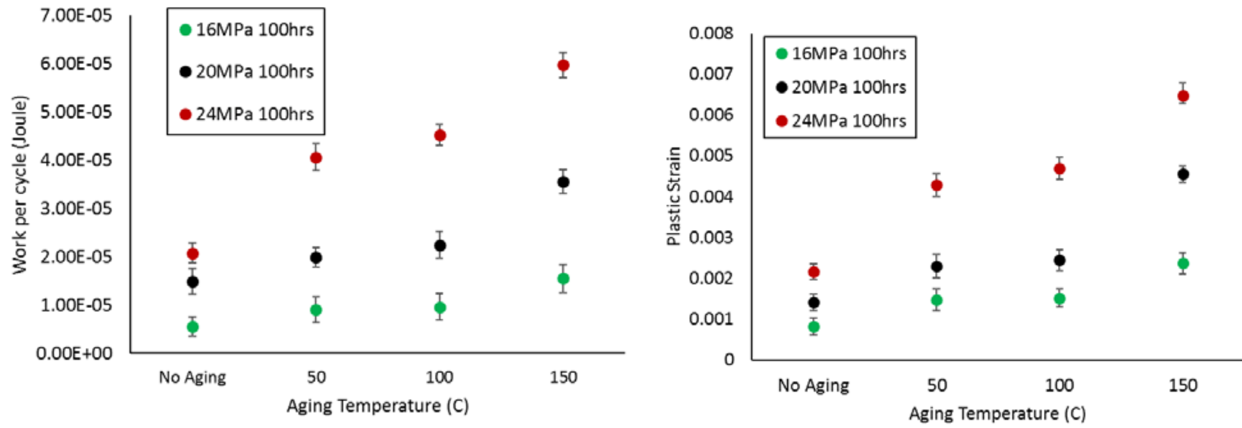

Figure 6.13: The effect of aging temperature on the inelastic work and plastic strain of SAC305 solder joints at 100 hours of aging time.

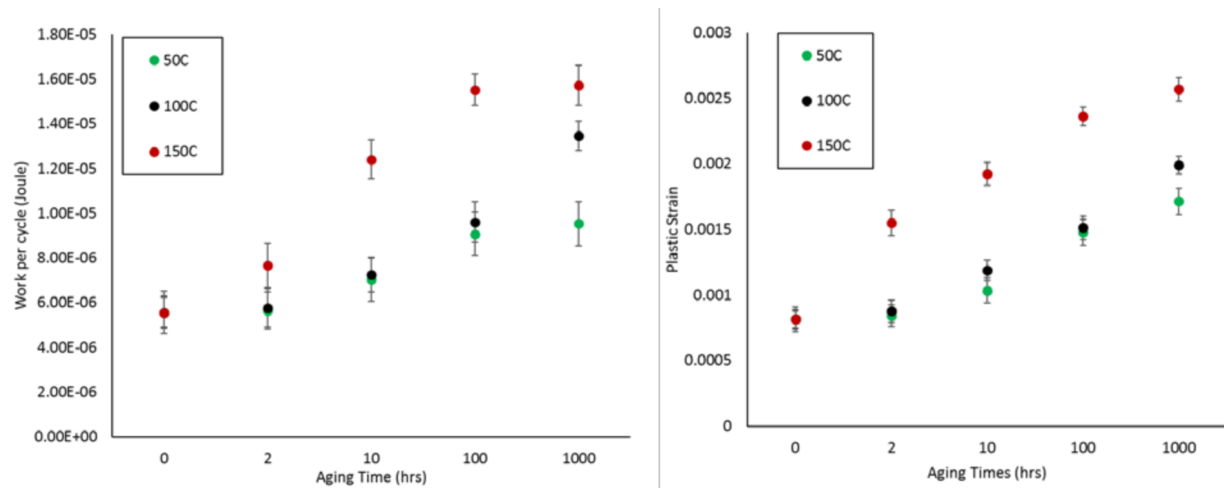

Figure 6.14: The effect of aging temperature and aging time on the inelastic work and plastic strain of SAC305 solder joints at 16 MPa stress amplitude.

6.3.3 Inelastic Work and Plastic Strain Modeling

After computing, the averages of the inelastic work per cycle and plastic strain at the steady-state region, the Morrow Energy and Coffin-Manson models were utilized to predict the characteristic life as a function of the inelastic work and plastic strain, respectively. The Morrow model equation is shown in equation 6.8, where W is the inelastic work, C is the fatigue ductility, m is the fatigue exponent, and N_{63} is the characteristic life. [113] Figure 6.15 represents the relationship between the characteristic life and the inelastic work per cycle for the non-aged SAC305 solder joints and

the fitted power equation (Morrow equation) to describe this relationship. Each point in this Figure shows the average of the inelastic work for seven samples at a stress amplitude.

$$N_{63} = C^{\frac{1}{m}} W^{\frac{-1}{m}} \quad (6.8)$$

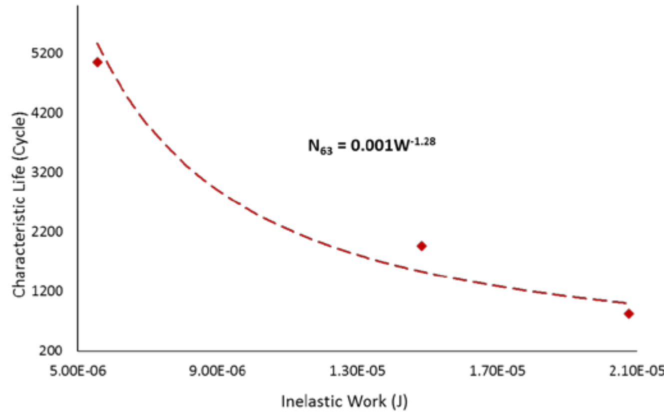

Figure 6.15: The Morrow energy model for the non-aged SAC305 solder joints.

To investigate the effect of aging on the Morrow model, the Morrow equation constants (the fatigue exponent and the fatigue ductility) were determined at different aging conditions as shown in Table 6.5. No specific trend was found for the equation constants with changing the aging time. Therefore, one global Morrow model can be found to define the relationship between the characteristic life and the inelastic work at each aging temperature. As a result, three general Morrow equations were determined at different aging temperatures to predict life as a function of the inelastic work per cycle regardless of the aging time as shown in Figure 6.16. To find a general prediction model of the characteristic life as a function of aging temperature and inelastic work, the relationships between the Morrow constants for the three global models and the aging temperature are defined by using the Arrhenius model (equation 6.3) as shown in Figure 6.17. The final prediction model of the characteristic life based on the Morrow and Arrhenius models was determined by substituting the Morrow constants equations from Figure 6.17 to the general

Morrow model equation (equation 6.8) as shown in equation 6.9, where T is the aging temperature, W is the inelastic work and N_{63} is the characteristic life. The R-squared for the general model is 99%.

$$N_{63} = 0.0024 * e^{\frac{-68.86}{T}} * W^{1.2*e^{4.77/T}} \quad \text{(6.9)}$$

The general reliability model as a function of the aging temperature and inelastic work was found as shown in equation 6.10. This is achieved by substituting the prediction equation of the characteristic life (equation 6.9) in equation 6.1 and the shape parameter value was estimated by calculating its mathematical average at different conditions.

$$R(t) = e^{-\left(\frac{t}{0.0024*e^{\frac{-68.86}{T}}*W^{1.2*e^{4.77/T}}}\right)^{5.22}} \quad \text{(6.10)}$$

Table 6.5: The Morrow energy constants at different aging times and temperatures.

Aging Temperature (˚C)	Aging Time (hrs)	The fatigue exponent (m)	The fatigue ductility (c)
No Aging	No Aging	0.781	0.00453
50	2	0.683	0.00186
	10	0.688	0.00177
	100	0.777	0.00431
	1000	0.777	0.00392
	Global Model	**0.757**	**0.00364**
100	2	0.824	0.00644
	10	0.810	0.00488
	100	0.810	0.00570
	1000	0.788	0.00466
	Global Model	**0.793**	**0.00483**
150	2	0.900	0.00788
	10	0.753	0.00277
	100	0.801	0.00458
	1000	0.866	0.00670
	Global Model	**0.807**	**0.00526**

A-50°C

B-100°C

C-150°C

Figure 6.16: The relationship between the inelastic work per cycle and characteristic life at different aging temperatures.

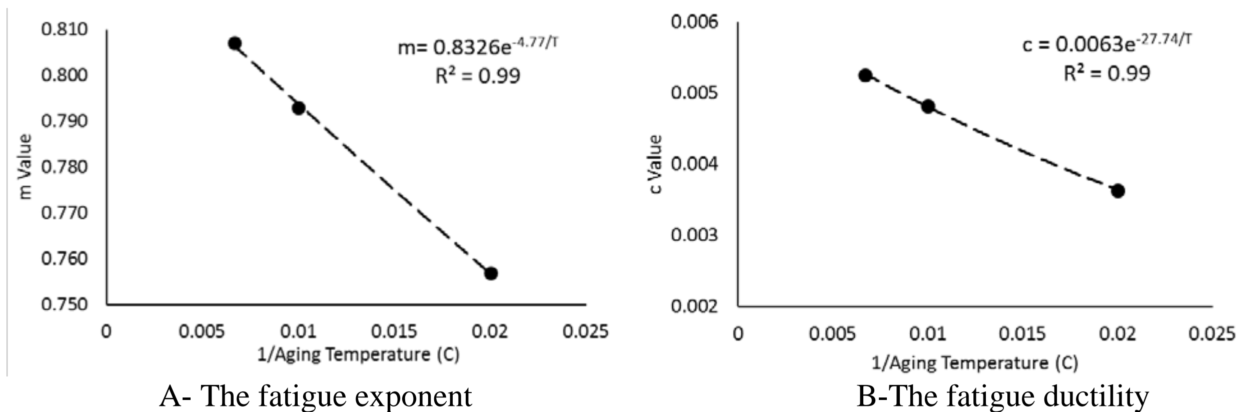

A- The fatigue exponent

B-The fatigue ductility

Figure 6.17: Arrhenius model for the relationship between the Morrow energy constants and the aging temperature.

To find the prediction model of the fatigue life as a function of plastic strain, the Coffin-Manson model is exploited to elucidate the relationship as shown in equation 6.11. Where γ is the fatigue ductility coefficient, α is the fatigue exponent. N_{63} is the characteristic fatigue life, and S is the plastic strain. The characteristic fatigue life was used to represent the fatigue life on the solder joints. [114] In Figure 6.18, the plastic strain is plotted versus the characteristic life and the Coffin-Manson equation is utilized as a fitting equation for this relationship.

$$N_{63} = \gamma^{\frac{1}{\alpha}} S^{\frac{-1}{\alpha}} \quad (6.11)$$

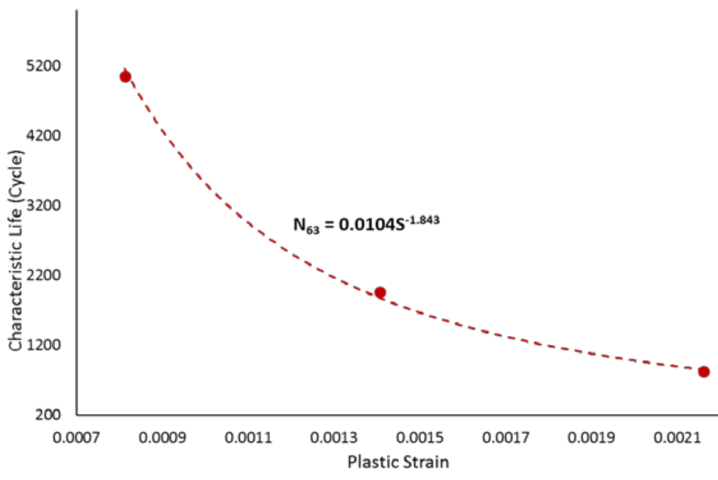

Figure 6.18: The Coffin-Manson model for non-aged SAC305 solder joints

The effect of aging conditions on the Coffin-Manson model is determined by finding the Coffin-Manson equation at each aging condition. Figure 6.19 represents the effect of aging time on the Coffin-Manson relationship at different conditions in a log-log scale. Table 6.6 shows the Coffin-Manson equation constants at different aging conditions. As a result of Figure 6.19 and Table 6.6, the Coffin-Manson equations constants are changed with aging where a significant trend was observed at different aging conditions for those constants. Therefore, a global model as a function of plastic strain can't be constructed regardless of the aging conditions. Figure 6.20 shows the trend of the Coffin-Manson equation constants with aging time and temperature. A general

empirical equation (equation 6.12) is used as a fitted equation to predict the life as a function of plastic strain, aging temperature and aging time. Where N_{63} is the characteristic fatigue life, S is the plastic strain, t is the aging time, T is the aging temperature and k_1 *to* k_8 are equation constants. The general structure of equation 6.12 is constructed based on the Coffin-Manson model (equation 6.11). The equation constants are determined based on the Arrhenius model (equation 6.3) for the effect of aging temperature and an empirical model for the effect of aging time. The nonlinear optimizer was used to find the equation constants and the final prediction model of the characteristic life is shown in equation 6.13. The R-squared for this model is 99%. The reliability model of SAC305 solder joints as a function of the plastic strain, aging time and the aging temperature is obtained by substituting equation 6.13 in equation 6.1 as shown in equation 6.14. The shape parameter is found by calculating its mathematical averages at different experimental conditions.

$$N_{63} = \overbrace{\left(\overbrace{\underbrace{K_1 * e^{\frac{-K_2}{T}}}_{\text{Arrhenius term}} + \underbrace{K_3 * e^{t*K_4}}_{\textit{Aging time term}}}^{\gamma^{\frac{1}{\alpha}}} \right) * S\text{^} \left(\overbrace{\underbrace{K_5 * e^{\frac{-K_6}{T}}}_{\text{Arrhenius term}} + \underbrace{K_7 * e^{t*K_8}}_{\textit{Aging time term}}}^{\frac{-1}{\alpha}} \right)}^{\text{Coffin-Manson } term} \quad \text{.........(6.12)}$$

$$N_{63} = \left(815.4 * e^{\frac{-1.175}{T}} + 12577.5 * e^{-t*1501}\right) * S\text{^}\left(0.112 * e^{\frac{-0.0271}{T}} - 0.0539 * e^{t*322.9}\right) \text{.(6.13)}$$

$$R(t') = e^{-\left(\frac{t"}{\left(815.4*e^{\frac{-1.175}{T}}+12577.5*e^{-t*1501}\right)*S\text{^}\left(0.112*e^{\frac{-0.0271}{T}}-0.0539*e^{t*322.9}\right)}\right)^{5.22}} \quad \text{........................(6.14)}$$

Table 6.6: The Coffin Manson constants at different aging times and temperatures.

Aging Temperature (°C)	Aging Time (hrs)	Coefficient of fatigue ductility (γ)	Fatigue exponent (α)
No Aging	No Aging	0.084	0.543
50	2	0.090	0.550
	10	0.194	0.639
	100	0.112	0.549
	1000	0.127	0.551
100	2	0.095	0.553
	10	0.136	0.590
	100	0.146	0.587
	1000	0.201	0.620
150	2	0.107	0.552
	10	0.109	0.558
	100	0.179	0.607
	1000	0.209	0.629

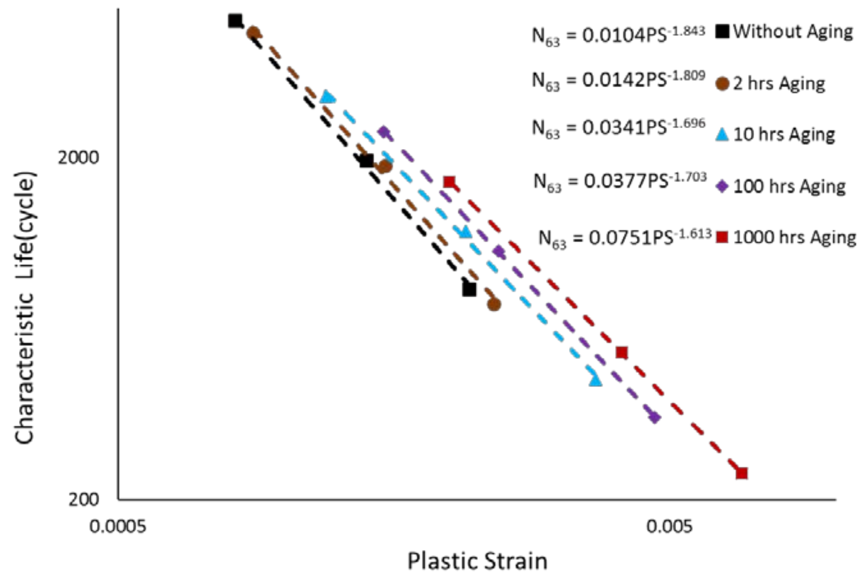

Figure 6.19: The relationship between the plastic strain and the characteristic life at different aging time and 100°C aging temperature.

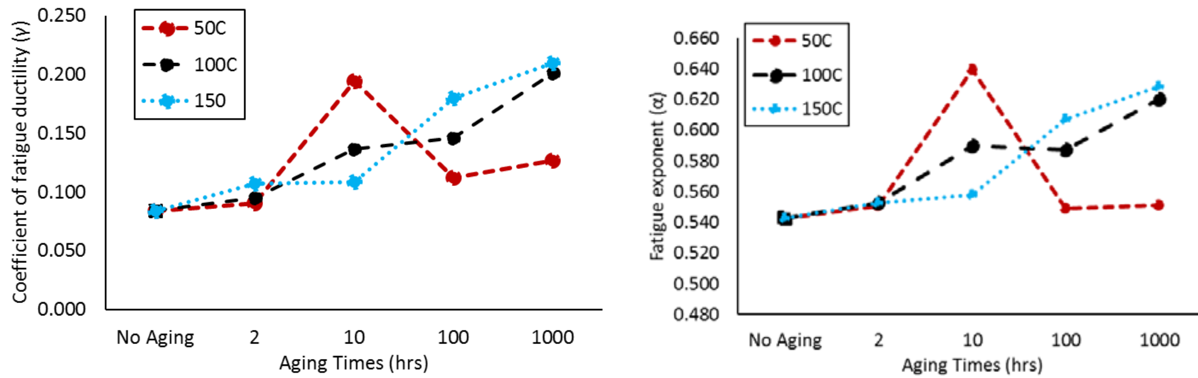

Figure 6.20: The coffin-Manson constants versus aging conditions.

6.3.4 Artificial Neural Networks (ANNs) Model

In this section, a prediction model of the characteristic life for SAC305 solder joints as a function of stress amplitude, aging temperature and aging time was constructed using the artificial neural networks (ANNs). Radial Bases Function Neural Networks (RBFNN) was utilized in this prediction model. The input layer was the studied operating factors and the output layer was the fatigue life. Two hidden layers were defined where the first layer has a Gaussian function which is used as an activation function and second layer is a linear function. The number of neurons in each hidden layer was three which is equal to the number of inputs in the ANNs system. The function type that was used in RBFNN was newrbe, in which the spread constant (smoothing factor) was one. The experiments were performed on the individual solder joints at the actual setting conditions. Three levels of the stress amplitude (16, 20, and 24MPa) four levels of aging time (2, 10, 100, and 1000 hrs), and three level of aging time (50, 100 and 150°C) were utilized. The non-aged solder joints were tested as well for comparison purposes. The obtained reliability data were fitted to a Two-parameter Weibull distribution and the characteristic life at each experimental condition was determined as shown in Table 6.7. This data for the non-aged solder joint and other two levels of aging time (10 and 1000 hrs) were used as a training data which is displayed in Table 6.8. The data that were found at 2 and 100 hours aging time were considered

as a validation data to verify the model accuracy. Table 6.9 shows the second set of the data (validation data). The RBFNN code was written in MATLAB software (Version R 2016). Table 6.10 shows the predicted values and actual values of the characteristic life based on the ANNs model. The R-squared for the ANNs model was calculated which is 91.7%. The R-squared for the empirical model that was discussed in the previous section (97%) is larger than the ANNs model R-squared. The empirical model was dependent on different proved theoretical models such Coffin-Manson, Morrow Energy, and Arrhenius model. Therefore, the empirical model has more accuracy compared to the ANNs model. The ANNs model is more efficient when the size of training dataset is increased. With Small size of training dataset, it is expected to obtain low accuracy models. The ANNs model has better performance than other models when the number of process parameters increase significantly where constructing the empirical model in this case will be so complicated. The relationship between some of the process parameters and characteristic life is theoretically known to demonstrate a decrease in the characteristic life. Thus, the possibility to create an accurate empirical model is increased. On the other hand, when the relationship between the process factors and the response is changed when the level of any factor is changed (multiple peaks and valleys) or different directions of the relationship are found, the ANNs model will be more accurate than any empirical model. Another ANNs method was used to predict the fatigue life which is called the Backward Propagations Neural Networks (BPNN) method. The results of RBFNN represent more accuracy in predicting the fatigue life of the solder joint when compared to the BPNN. The model parameters of BPNN method are shown in appendix B (Figures B.12-B.15).

Table 6.7: The characteristic life at different experimental conditions.

Aging Temperature (${}^{\circ}C$)	Aging Time (hrs)	Stress Amplitude (MPa)		
		16	20	24
Non-aged	Non-aged	5043.7	1964.1	826.9
50	2	4736.1	1908.6	776.1
	10	3704.5	1375.9	555.2
	100	2600.6	1220.2	374.5
	1000	2268.7	845.1	298.7
100	2	4662	1900.4	750
	10	3038.7	1221.2	449.8
	100	2393.3	1067.4	348
	1000	1704.4	538.3	238.2
150	2	2077.7	960.4	333.6
	10	1500.6	596.4	271.7
	100	1185.6	497.9	214.3
	1000	1057.2	408.9	195.3

Table 6.8: The training dataset for the ANNs system.

Aging Temperature (${}^{\circ}C$)	Aging Time (hrs)	Stress Amplitude (MPa)		
		16	20	24
Non-aged	Non-aged	5043.7	1964.1	826.9
50	10	3704.5	1375.9	555.2
	1000	2268.7	845.1	298.7
100	10	3038.7	1221.2	449.8
	1000	1704.4	538.3	238.2
150	10	1500.6	596.4	271.7
	1000	1057.2	408.9	195.3

Table 6.9: The validation dataset for the ANNs model.

Aging Temperature (${}^{\circ}C$)	Aging Time (hrs)	Stress Amplitude (MPa)		
		16	20	24
50	2	4736.1	1908.6	776.1
	100	2600.6	1220.2	374.5
100	2	4662	1900.4	750
	100	2393.3	1067.4	348
150	2	2077.7	960.4	333.6
	100	1185.6	497.9	214.3

Table 6.10: The validation and prediction data for the ANNs model.

Aging Temperature (˚C)	Aging Time (hrs)	Stress Amplitude (MPa)	Actual value	Predicted value
50	2	16	4736.1	3646.5
50	100	16	2600.6	2848.4
100	2	16	4661.96	3819
100	100	16	2393.34	2895.8
150	2	16	2077.7	2051.1
150	100	16	1185.6	1236.7
50	2	20	1908.6	1784.7
50	100	20	1220.2	1382.5
100	2	20	1900.44	1547.6
100	100	20	1067.43	937
150	2	20	960.4	625.9
150	100	20	497.9	679.5
50	2	24	776.1	685
50	100	24	374.5	500.9
100	2	24	750	683.4
100	100	24	348.02	416
150	2	24	333.6	367.9
150	100	24	214.3	289.7

6.3.5 Shear Strength Modeling

Studying the effect of aging on the shear strength of SAC305 solder joints and constructing the prediction model of the shear strength are the main aims of this test. The test matrix of the shear test is represented in Table 6.2. The strain rate that was utilized is 0.1^{-1}S. The stress-strain curve for SAC305 solder joints without aging is shown in Figure 6.21. The ultimate shear strength of the solder joints is used to display its shear strength. The effects of aging time and temperature on the shear strength of the solder joints are demonstrated in Figures 6.22 and 6.23, respectively. The shear strength is decreased with increasing the aging temperature or the aging time. The amount of reduction in the shear strength is exponentially decreased with aging time. Figure 6.24

represents a summary of the shear test results. The largest reduction in the shear strength was found in the solder joint that was aged for 1000 hours at 150˚C aging temperature.

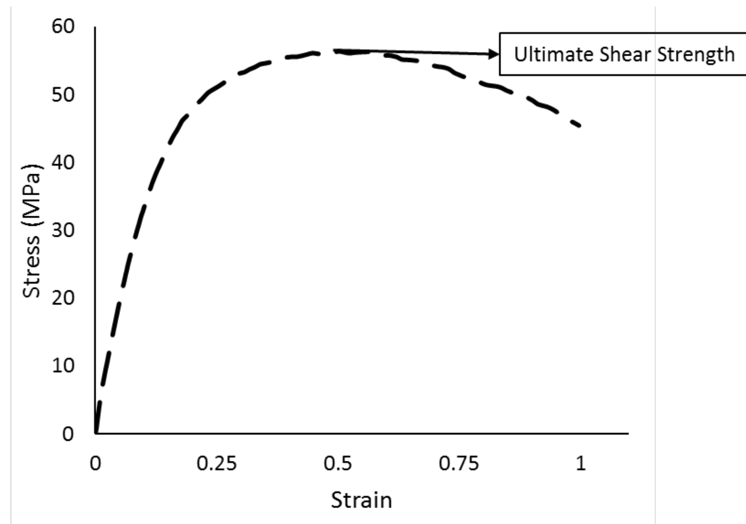

Figure 6.21: The stress-strain curve for the non-aged SAC305 solder joints.

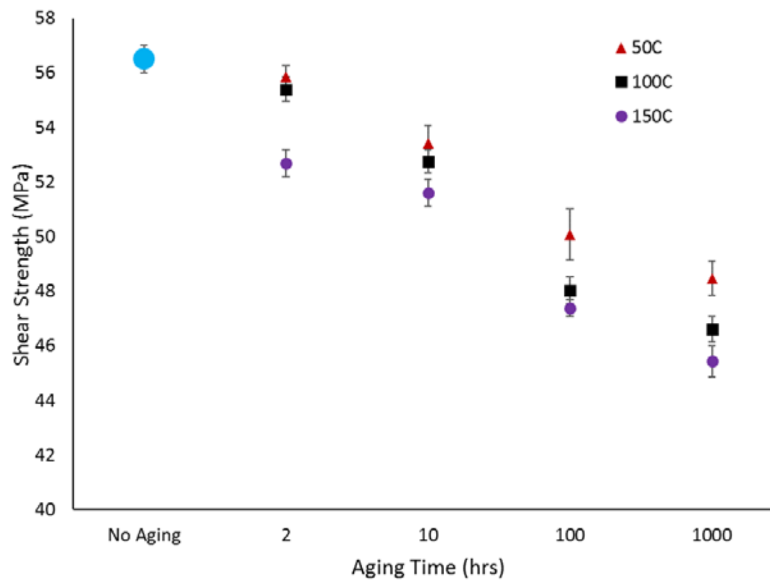

Figure 6.22: The effect of aging time on the shear strength of the solder joints.

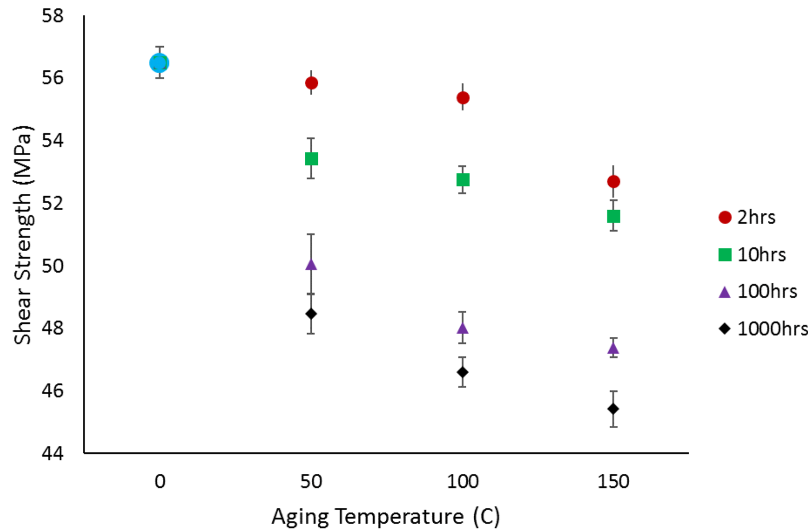

Figure 6.23: The effect of aging temperature on the shear strength of the solder joints.

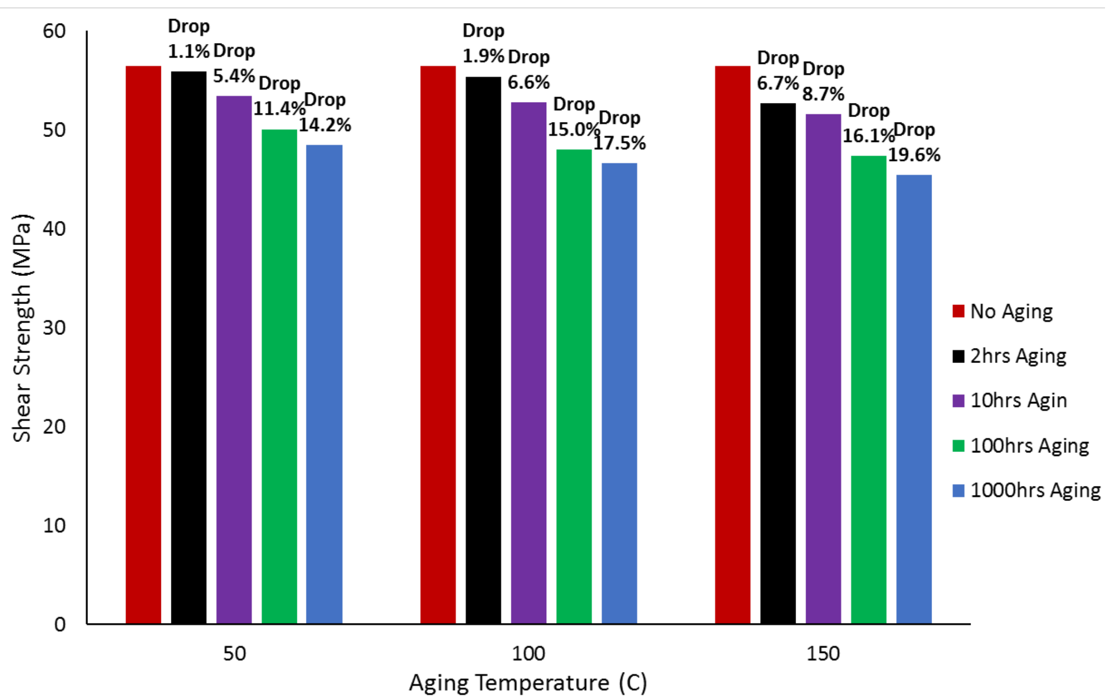

Figure 6.24: Summary of the data for the shear strength at different aging conditions.

To construct a prediction model of the shear strength as a function of aging conditions, a general empirical equation (equation 6.15) was utilized as a fitted equation of the relationship between the aging conditions and the shear strength. Where *SS* is the shear strength of the solder joints, *t* is the aging time, *T* is the aging temperature and k_1-k_6 are equation constants. An exponential term is

applied to represent the effect of aging time in the first hours and another linear term is employed to describe the long-term aging. The Arrhenius model (equation 6.3) is used to illustrate the aging temperature effect. The final shear model is determined by using a non-linear optimizer which is shown in equation 6.16. The R-squared for the obtained model is 98%.

$$SS = \underbrace{K_1 + K_2 * e^{t*k_3} + t * k_4}_{Aging\ time\ term} + \underbrace{K_5 * e^{\frac{-K_6}{T}}}_{\text{Arrhenius term}} \quad \ldots\ldots(6.15)$$

$$SS = 56.5 + 0.0021 * e^{t*0.01} - t * 7.14 - 97.88 * e^{\frac{-0.056}{T}} \quad \ldots\ldots(6.16)$$

The Analysis of Variance (ANOVA) was performed to find the contribution of the aging conditions on the shear strength and determine the level of significance of each aging factor, the results are shown in Table 6.11. The main effect and the interaction plots for the effect of aging time and temperature on the shear strength are shown in Figures 6.25 and 6.26. Results from the ANOVA analysis indicated that both aging time and temperature have a significant effect on the shear strength of the solder joints. The aging time has a larger contribution on the shear strength (53.5%) compared to the aging temperature contribution (16.6%). The interaction effect between aging time and temperature on the shear strength of the solder joints was nonsignificant which can be observed from the ANOVA and interaction plots (Figure 6.26).

Table 6.11: ANOVA analysis for the effects of aging time and temperature on the solder joints shear strength.

Source	DF	Contributions	Adj SS	Adj MS	F-value	P-value
Regression	7	70.1%	1362.6	194.7	27.7	<0.0001
Aging Time	4	53.5%	1040.7	260.2	37.1	<0.0001
Aging Temperature	3	16.6%	321.9	107.3	15.3	<0.0001
Error	83		582.6	7.0		
Total	90		1945.2			

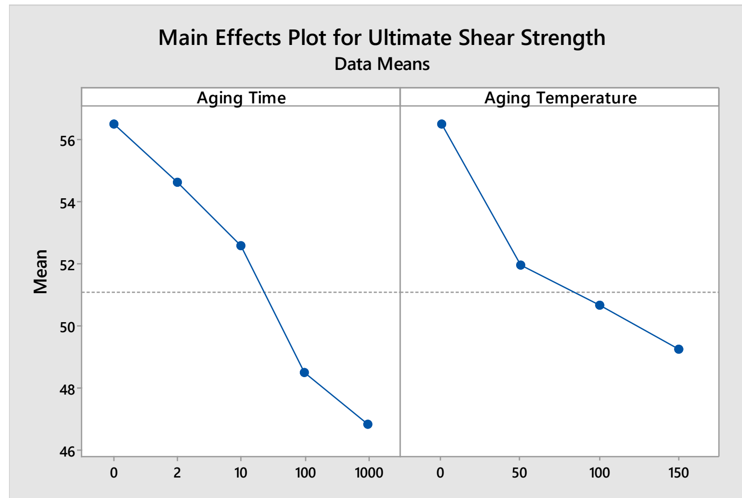

Figure 6.25: The main effect plot of the solder joints shear strength with different aging conditions.

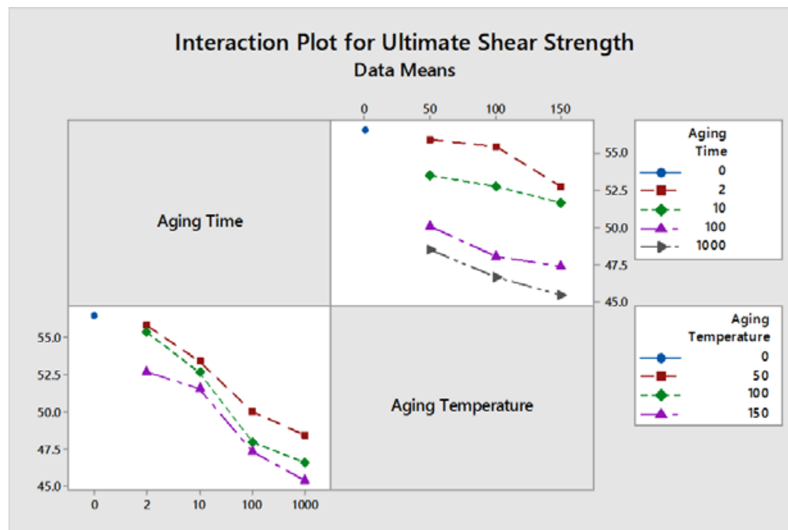

Figure 6.26: The interaction plot of the solder joints shear strength with different aging conditions.

6.3.6 Microstructure Analysis

A Microstructure analysis was performed to investigate the different causes behind the reduction of the fatigue life and shear strength of SAC305 solder joints with aging. The Scanning Electron Microscope (SEM), shown in Figure 4.7 was utilized for capturing the microstructure images. The magnification level that was applied using SEM was 5000K. Four stages of grinding and four stages of polishing were exploited for SAC305 solder joints that were mounted in epoxy. Solder

joints aged for 1000 hours at different aging temperatures were studied. The results showed that aging leads to an increase in the IMC layer and precipitates coarsening. Figure 6.27 represents the effect of aging temperature on the precipitates coarsening in the bulk solder. An increase in the precipitates coarsening was observed when the aging temperature is increased. The growth in the IMC layer with aging and the precipitates coarsening near to the IMC layer are illustrated in Figure 6.28. The IMC layer thickness was increased when the aging temperature is increased. The precipitates size at the IMC layer is larger than the precipitates in the bulk solder. Figure 6.29 shows an increase in the precipitates coarsening and IMC layer thickness when the solder joints are aged for more time at 100˚C aging temperature. The reduction in the fatigue life is influenced with the increase in the precipitates coarsening. The uniform distribution of the precipitates leads to block the dislocation process that is associated with crack propagation. Therefore, the precipitates coarsening leads to change the precipitates distribution to be less uniform. On the other hand, the increase in IMC layer thickness with aging leads to an increase in the brittleness and it also decreases the strength of the solder joints. Because of these phenomena, fatigue life and shear strength are decreased with aging.

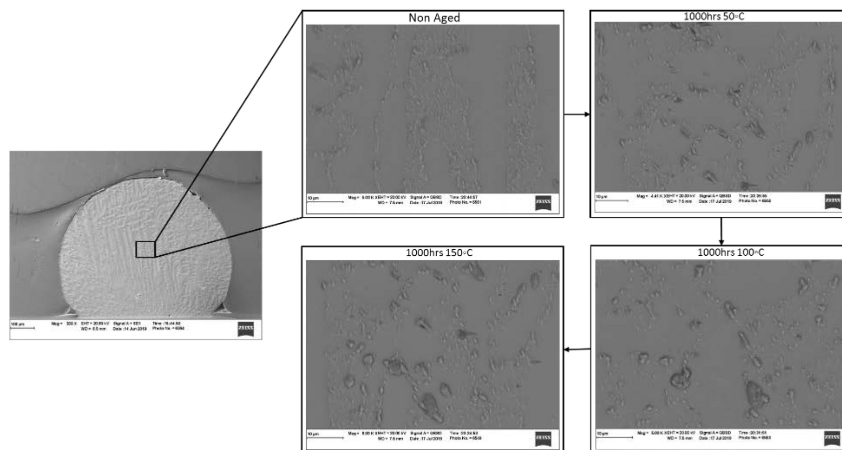

Figure 6.27: The precipitates coarsening in the Bulk solder of SAC305 solder joints at different aging temperatures.

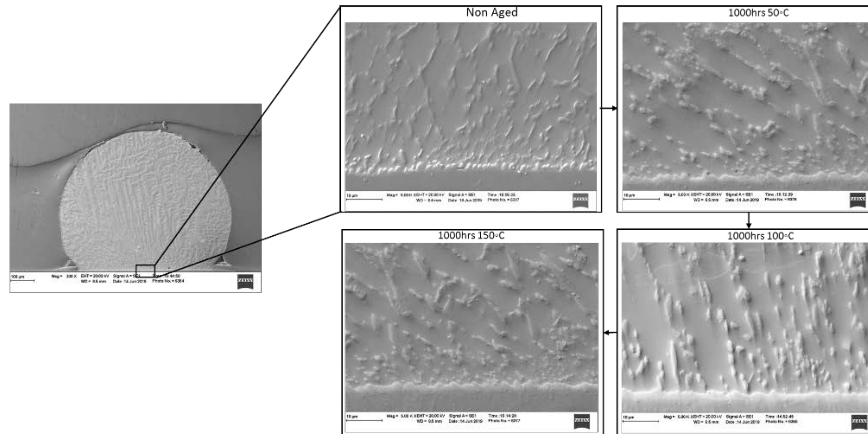

Figure 6.28: The precipitates coarsening in the IMC layer solder of SAC305 solder joints at different aging temperatures.

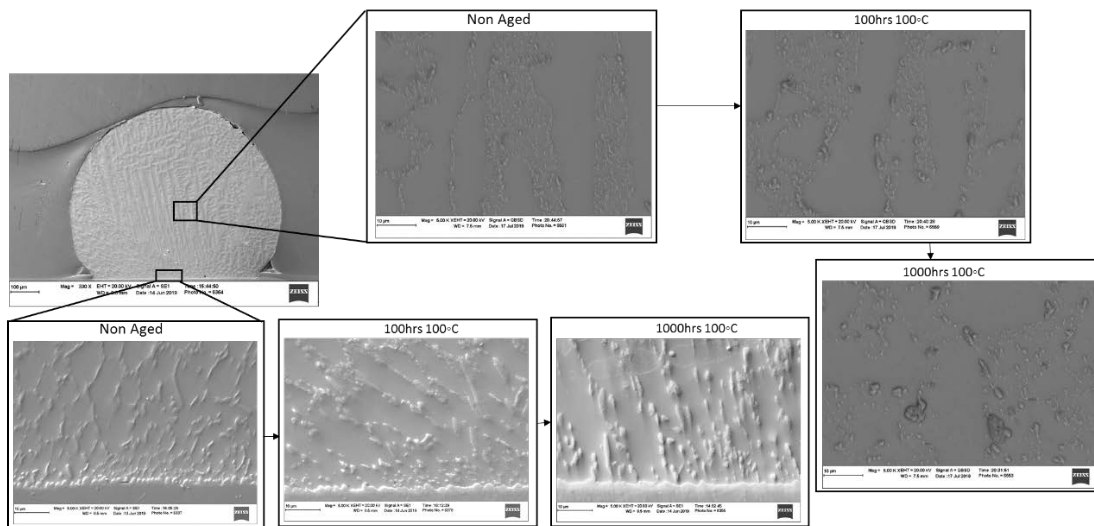

Figure 6.29: The precipitates coarsening in SAC305 solder joints at different aging times.

6.4 Summary

In this study, degradations on the reliability and shear strength of SAC305 solder joints with changing the aging temperature were modeled by exploiting the Arrhenius model. Different stress amplitudes and aging times were used at each level of aging temperature for the fatigue test. The prediction model of the characteristic life was built based on the Stress-life power equation. An empirical equation was implemented to describe the degradation of the fatigue life at different

aging times. Morrow Energy and Coffin-Manson models were employed to construct other reliability models based on the values of the inelastic work and plastic strain. The relationships between the constants of those models and the aging conditions was identified and modeled using the Arrhenius model. Three reliability Models were defined based on a two-parameter Weibull distribution. The contributions of aging time and temperature on the shear strength of the solder joints were found by performing ANOVA analysis. Shear strength prediction model was found by using a general empirical equation. This equation was built based on the Arrhenius model for the effect of aging temperature, and linear and exponential equations for the effect of short and long terms of the aging time. Coarsening of the precipitates and the increase in the IMC layer with aging were investigated in the microstructure analysis using SEM microscope. Another method for predicting the fatigue life using the artificial neural networks was proposed. A comparison between the empirical model and the ANNs model was accomplished by using the R-squared value as a quality response. The empirical model shows more accuracy compared with the ANNs model. This is because of the theoretical methods that were used to construct the empirical model.

Chapter 7: Fatigue Behavior of SAC-Bi and SAC305 Solder Joints with Aging in Actual Setting Conditions

7.1 Introduction

Fatigue performance of the microelectronic assemblies is highly reliant upon solder joints reliability. In the last decades, the electronics industry began moving forward towards using lead-free solder joints due to the health and environmental concerns that are associated with the use of lead. The fatigue behavior of the lead-free solder joints under mutable loading and aging conditions is not clearly understood. The main aim of this study is to investigate the effect of adding bismuth on the mechanical reliability of SAC-based solder alloys at different loading and aging conditions. The fatigue behavior and the shear strength of SAC305 (Sn-3.0Ag-0.5Cu) and SAC-Q (Sn-3.4Ag-0.5Cu-3.3Bi) solder alloys are examined and compared. Instron 5948 micro tester machine with a unique fixture is used to perform the fatigue and shear tests on individual solder joints at different experimental conditions. Five levels of aging time (0, 2, 10, 100, and 1000 hrs) at 100 °C are considered for SAC305 and SAC-Q solder joints. For the fatigue test, each solder alloy is subjected to three levels of cyclic stress amplitude; 16, 20 and 24MPa for SAC305 and 22, 26, and 28MPa for SAC-Q. Two-parameter Weibull distribution is utilized to analyze the failure life of the solder joints. The microstructure evaluations are investigated using SEM for both solder alloys to recognize the precipitates coarsening with aging. The impacts of aging and stress amplitude on the fatigue properties are measured by constructing the hysteresis loop for each sample at each condition. The Coffin-Manson and the Morrow energy models are developed for both solder alloys

at different aging conditions. Different reliability models are constructed for each solder alloy as a function of aging condition, stress amplitude, inelastic work and plastic strain. A general prediction model is built for each solder to estimate the shear strength of the solder joints as a function of aging time.

7.2 Materials and Methods

The printed circuit board (PCB) that is used in this study is made of two layers of FR-4 epoxy glass material. Solder mask define (SMD) with copper pad opening diameter of 0.55 mm is used with Organic Solderability Preservative (OSP) surface finish. Solder spheres with 0.76 mm diameter are assembled in a convection reflow oven. The reflow profile includes a peak temperature of 250°C and 60 seconds above liquidus. Two different solder alloys were assembled for testing, including SAC305 (Sn-3.0Ag-0.5Cu) and SAC-Q (Sn-3.41Ag-0.51Cu-3.3Bi).

7.3 Test matrix

Accelerated fatigue shear tests are conducted using an Instron 5948 Micro-Mechanical Tester. A unique fixture with a cylindrical tip was designed and used to apply cyclic stresses on individual solder joints. Individual Solder joints were aged at 100°C for five different levels of aging time (0, 2, 10, 100, and 1000 hrs) and then tested in the shear fatigue experiment. The individual solder joints were cycled with three different levels of stress amplitudes at each aging condition until complete failure. The stress levels for SAC305 joints were 16, 20, and 24MPa, while for SAC-Q joints were 22, 26, and 28MPa. Seven samples (replicates) at each experimental condition for both solder alloys were considered. Table 7.1 shows the L_{30} experimental orthogonal array (the test matrix), where the total number of the experimental combinations is equal to 30. The Fatigue test is ended after 5000 cycles, where the solder joints that didn’t fail are considered censored data.

Table 7.1: The experimental layout for the fatigue test.

Alloy	Stress Amplitude (MPa)	Aging Time (hrs)				
		0	2	10	100	1000
SAC-Q	22	7 samples	7 samples	7 samples	7 samples	7 samples
	26	7 samples	7 samples	7 samples	7 samples	7 samples
	28	7 samples	7 samples	7 samples	7 samples	7 samples
SAC305	16	7 samples	7 samples	7 samples	7 samples	7 samples
	20	7 samples	7 samples	7 samples	7 samples	7 samples
	24	7 samples	7 samples	7 samples	7 samples	7 samples

The same experimental setup was used to execute a shear test on individual solder joints. The primary purpose of this test is to determine the effect of adding Bi to the SAC solder alloy on the shear strength considering aging. Seven samples were tested at each aging condition. The shear strain rate was constant at 0.1 s^{-1} for all tests. Table 7.2 shows the shear test matrix.

Table 7.2: The experimental layout for the shear test.

Alloy	Aging Time (hrs)				
	0	2	10	100	1000
SAC-Q	7 samples	7 samples	7 samples	7 samples	7 samples
SAC305	7 samples	7 samples	7 samples	7 samples	7 samples

7.4 Results and Discussion

7.4.1 Weibull Distribution Analysis

After performing the accelerated shear fatigue test for SAC305 and SAC-Q solder joints, the fatigue data at each experimental condition was analyzed using a two-parameter Weibull distribution. Equation 7.1 represents the modeling formula for the two-parameter Weibull distribution, where θ is the scale parameter or characteristic life, and β is the shape parameter

[111]. Figure 7.1 represents the probability plot for the Weibull distribution for the non-aged SAC305 and SAC-Q solder joints at different stress amplitudes. SAC-Q solder joints exhibited more robust reliability when compared to SAC305 solder joints. For example, the fatigue life of the non-aged SAC-Q solder joints that are cycled at 22MPa is higher than the fatigue life of the non-aged SAC305 solder joints that are cycled at 16MPa. A significant reduction in the reliability of the solder joints with increasing the stress amplitude is observed for both solder alloys. There is no observed relationship between the shape parameter values and the stress amplitude values.

$$R(t) = e^{-(\frac{t}{\theta})^{\beta}} \quad (7.1)$$

The degradation of the reliability of the solder joints can be described by plotting the obtained characteristic life versus the stress amplitude for each solder alloy, as shown in Figure 7.2. This relationship is illustrated by fitting the fatigue data to a power equation (equation 7.2) [112].

$$N_{63} = E * P^{-c} \quad (7.2)$$

Where E and c are condition constants, P is the stress amplitude, and N_{63} is the characteristic life. The constant c represents the solder joint ductility where an increase in the c value means that the ductility is decreased. From Figure 7.2, more brittle behavior is observed for SAC-Q solder joints with 9.24 (c value) compared to 4.45 for SAC305 solder joints.

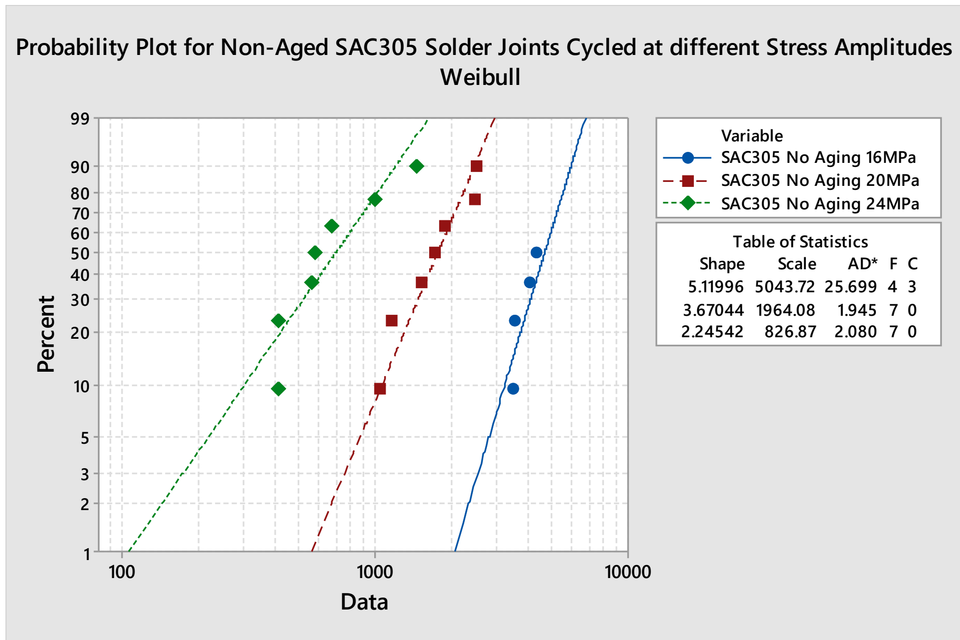

(a). SAC305

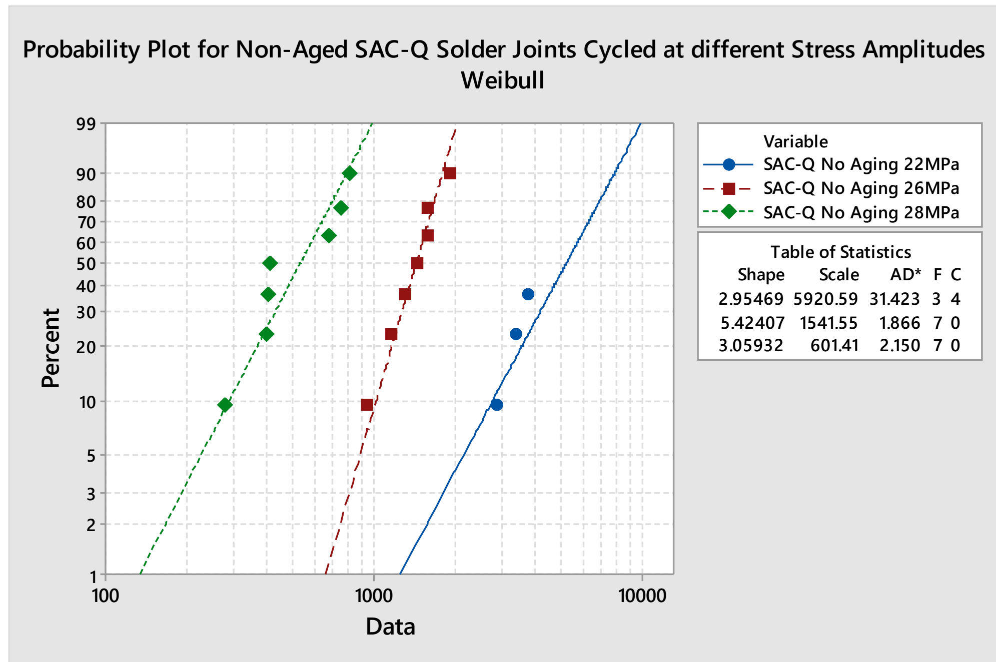

(b). SAC-Q

Figure 7. 1:Two-parameter Weibull distribution for SAC305 and SAC-Q solder joints at different stress amplitudes.

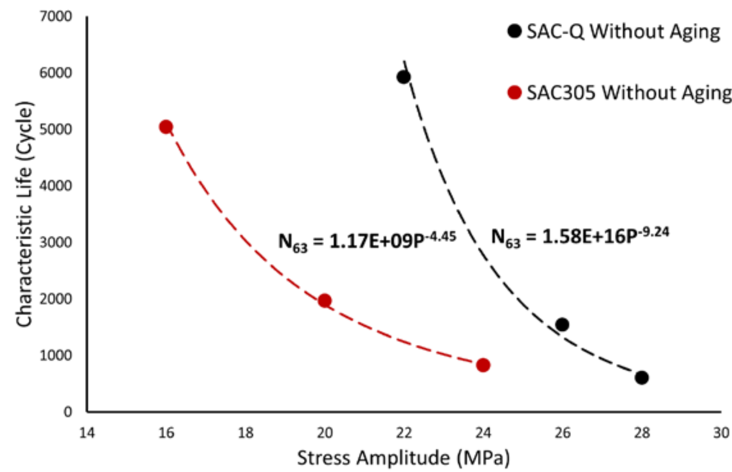

Figure 7. 2:The relationship between the characteristic life and stress amplitude for SAC-Q and SAC305 solder joints.

In order to investigate the effect of aging on the fatigue life of SAC305 and SAC-Q solder joints, a two-parameter Weibull distribution analysis was implemented. Figure 7.3 shows the two-parameter Weibull distribution at different aging times for SAC-Q and SAC305 solder joints that are cycled at 22MPa and 16MPa stress amplitudes, respectively. Then the characteristic life was calculated and plotted versus the aging time for different stress amplitudes, as shown in Figure 7.4. It is obvious that the characteristic life is decreased with increasing the aging time for both solder alloys. However, SAC-Q solder alloy has a lower life degradation rate with aging when compared to SAC305.

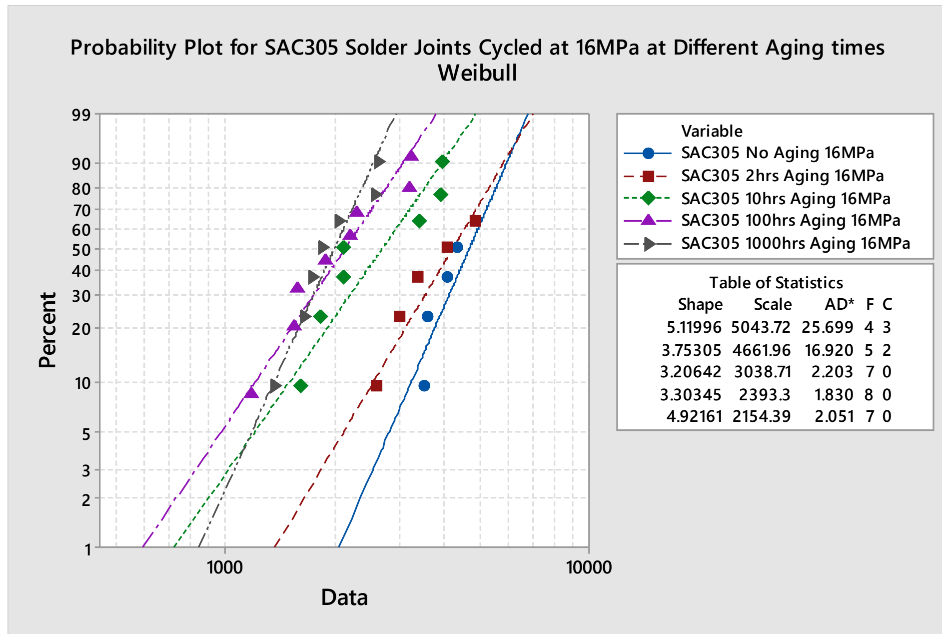

(a). SAC305

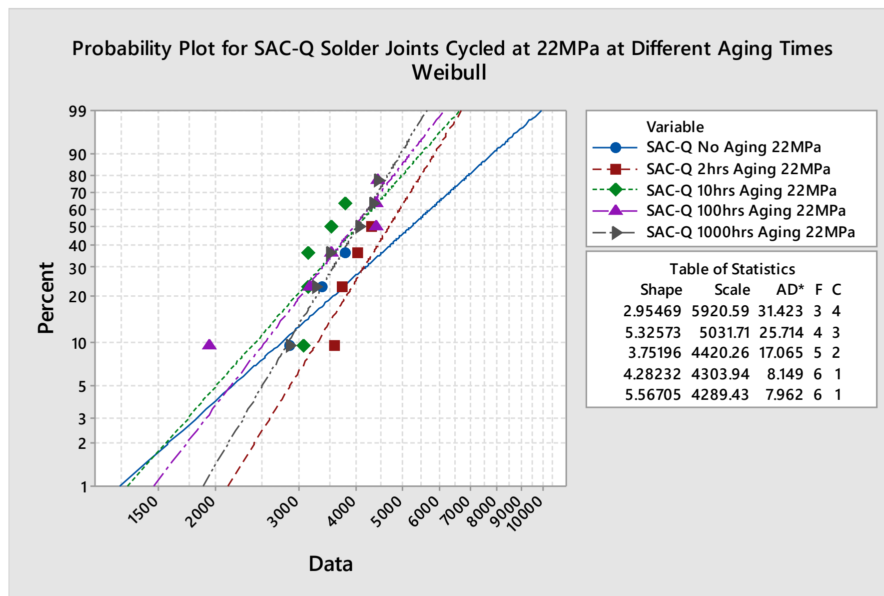

(b). SAC-Q

Figure 7.3: Two-Parameter Weibull distribution for SAC305 and SAC-Q solder joints at different aging times and stress amplitudes.

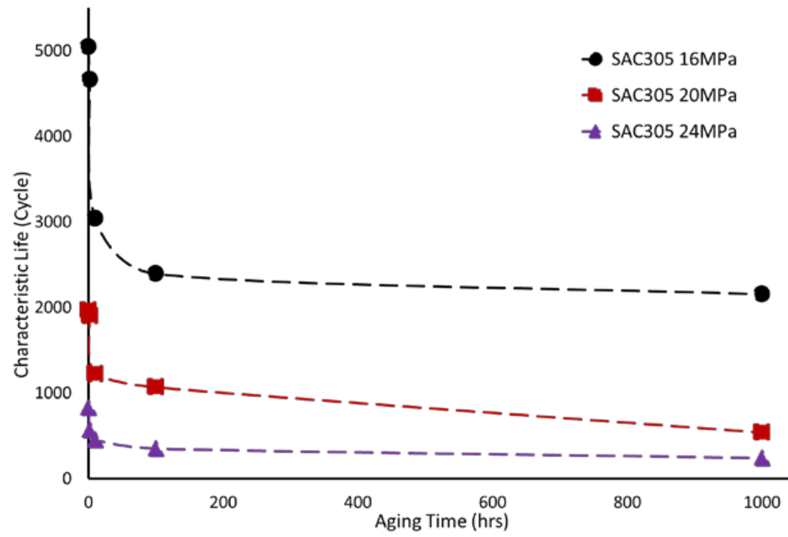

(a). SAC305

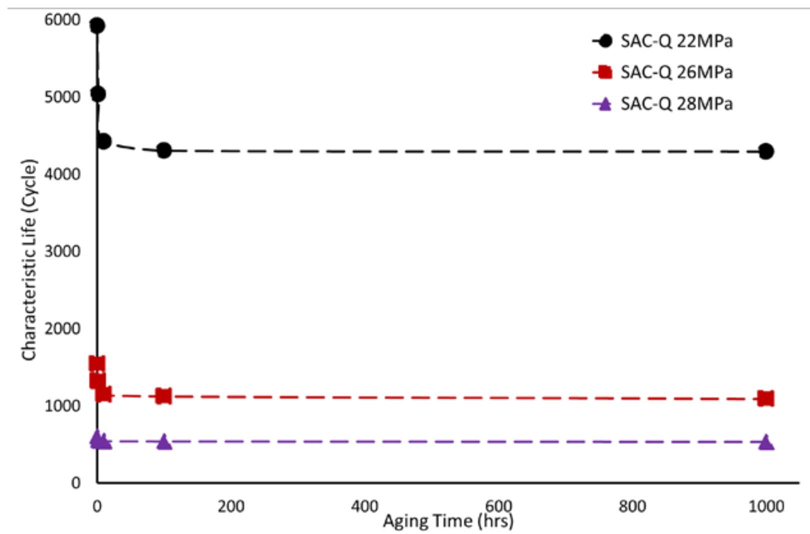

(b). SAC-Q

Figure 7.4: Characteristic life of SAC305 and SAC-Q vs. aging time for different stress amplitudes.

The characteristic life percentage and the degradation with aging at different stress amplitudes for SAC305 and SAC-Q solder alloys are summarized using bar-charts, as shown in Figure 7.5. A 100% value represents a fatigue life without aging at each stress amplitude. The largest degradation value in the characteristic life for SAC-Q solder was observed after two hours of aging. On the

contrary, the largest degradation in the characteristic life for SAC305 solder was observed between two and ten hours of aging.

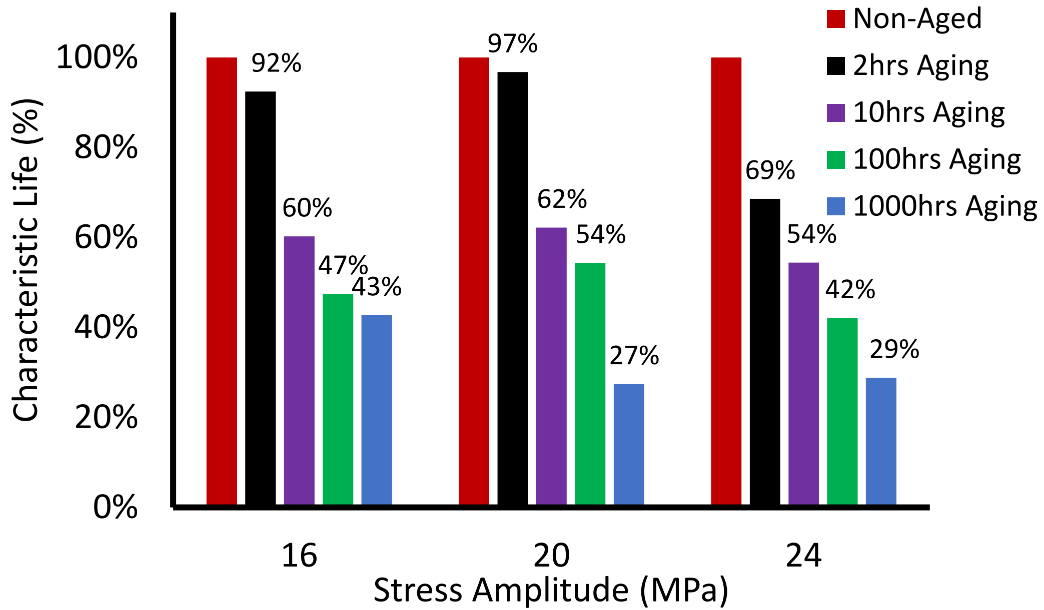

(a). SAC305

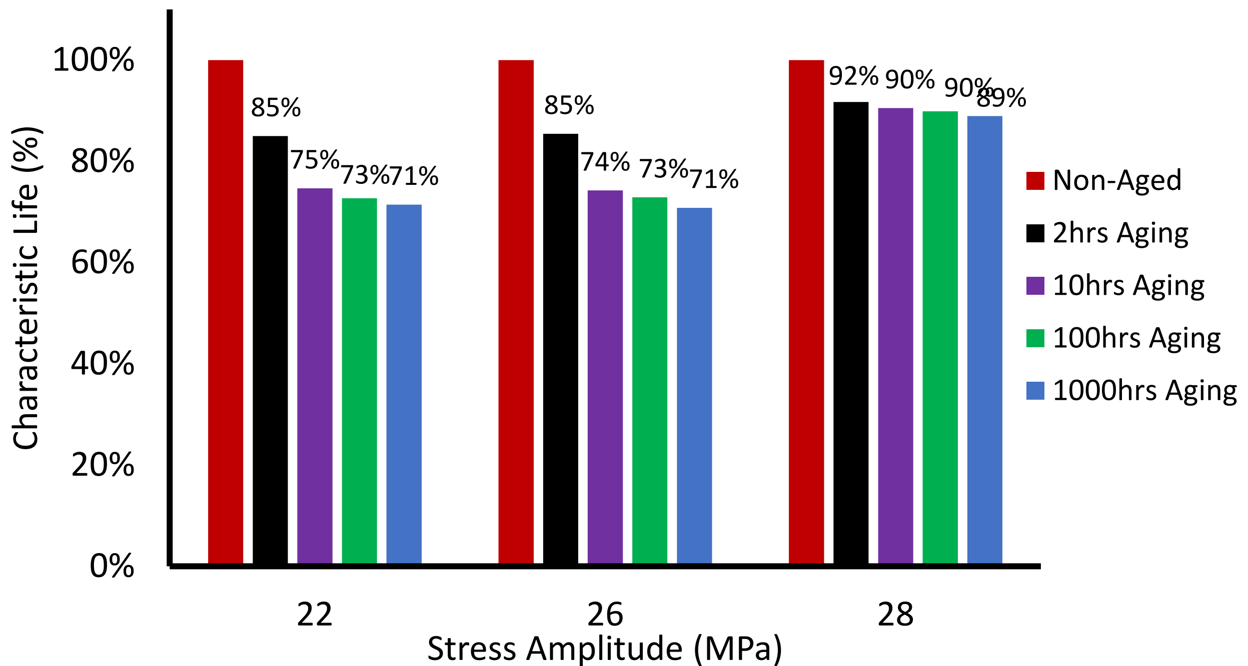

(b). SAC-Q

Figure 7.5: Characteristic life degradation of SAC305 and SAC-Q solder alloys with aging.

To illustrate the effect of the aging on the relationship between the stress amplitude and the characteristic life, the characteristic life is plotted as a function of stress amplitude at different aging conditions for both solder alloys as shown in Figure 7.6. The same conclusion can be drawn from Figure 7.6 where the characteristic life is decreased significantly when the aging time or the stress amplitude are increased for both solder alloys. The effect of the stress amplitude has more contribution on the characteristic life than aging time. The SAC305 solder has a higher degradation rate in the characteristic life with aging compared to SAC-Q solder. It can be highly noted from Figure 7.6 that both constants value (*E* and *c*) for power equation (equation 7.2) of SAC-Q solder are changed when the solder joints were aged for more time. In SAC305 solder, the *E* constant is almost fixed with a small fluctuation in its value and the *c* constant has a clear trend with aging time. Table 7.3 represents the values of power equation constants at different aging conditions for both solder alloys. In order to build a prediction model for the characteristic life as a function of aging time and stress amplitude, the *E* and *c* constants for SAC-Q solder and *c* constant for SAC305 solder are plotted versus the aging time and the power equation is used as a fitted equation for this relationship as presented in Figures 7.7 and 7.8. The obtained equations are then substituted in equation 7.2 to acquire the final equations for predicting the characteristic life. To estimate the *E* value in SAC305 equation, the mathematical average for the *E* values at different aging conditions are calculated. The final prediction models of the characteristic life for SAC305 and SAC-Q solder alloys are shown in equations 7.3 and 7.4 respectively. Where N_{63} is the characteristic life, *T* is the aging time and *P* is the stress amplitude.

$$N_{63} = 1.24 * 10^{9} * P^{-4.5679 * T^{0.0078}} \quad (7.3)$$

$$N_{63} = 5 * 10^{15} * T^{-0.256} * P^{-8.8955 * T^{-0.008}} \quad (7.4)$$

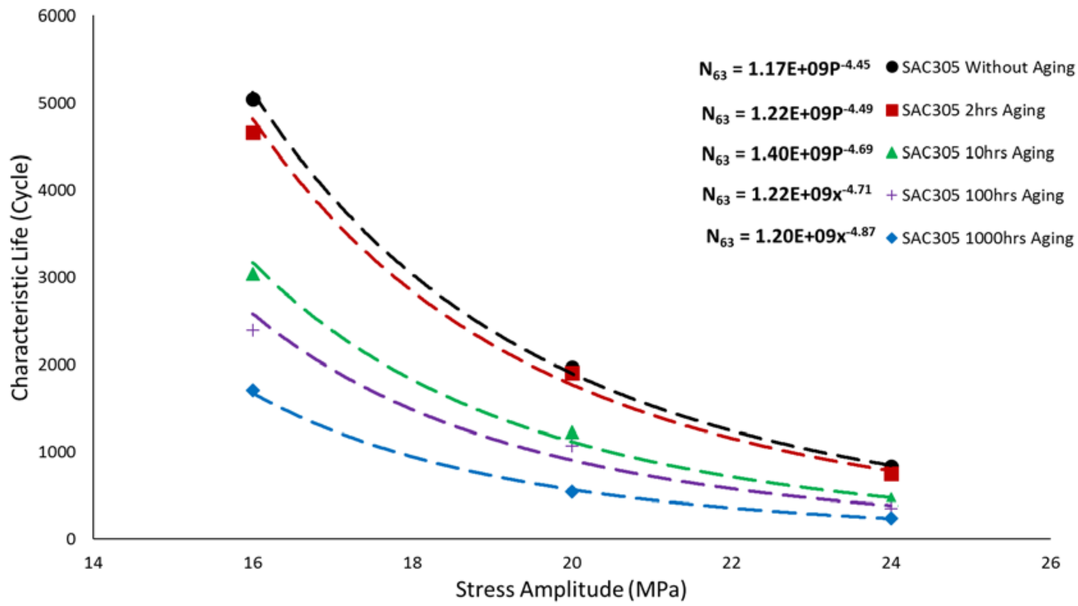

(a). SAC305

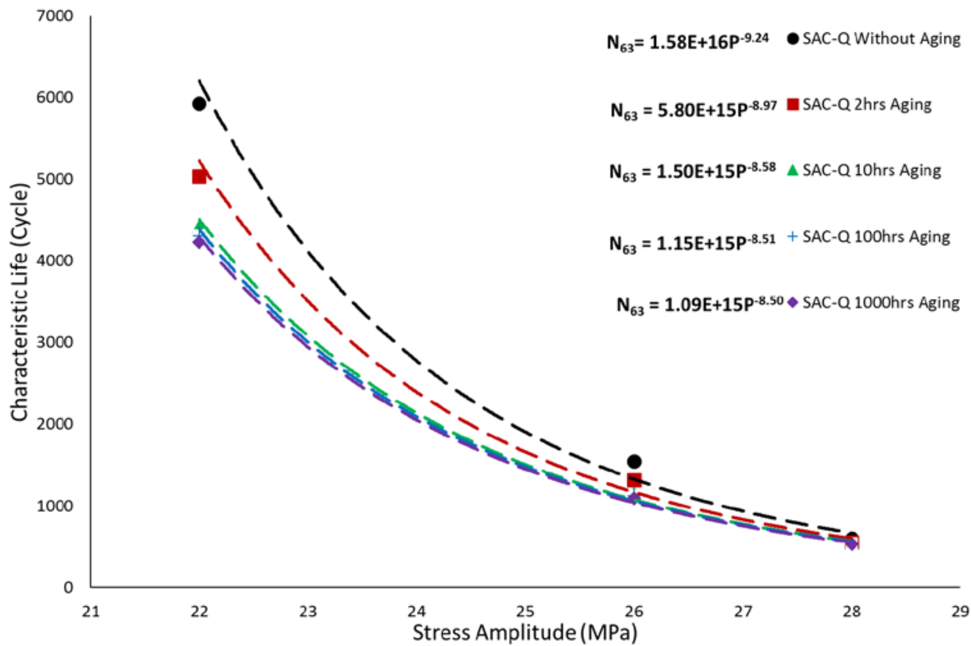

(b). SAC-Q

Figure 7.6: The relationship between the characteristic life and stress amplitude for SAC-Q and SAC305 solder joints at different aging times.

Table 7.3: The power equation constants at different aging times.

Aging Time (hrs)	*E* constant (SAC-Q)	*c* constant (SAC-Q)	*E* constant (SAC305)	*c* constant (SAC305)
0	1.58*10^(16)	9.24	1.17*10^(9)	4.45
2	5.80*10^(15)	8.97	1.22*10^(9)	4.49
10	1.50*10^(15)	8.58	1.40*10^(9)	4.69
100	1.15*10^(15)	8.51	1.22*10^(9)	4.71
1000	1.09*10^(15)	8.50	1.20*10^(9)	4.87

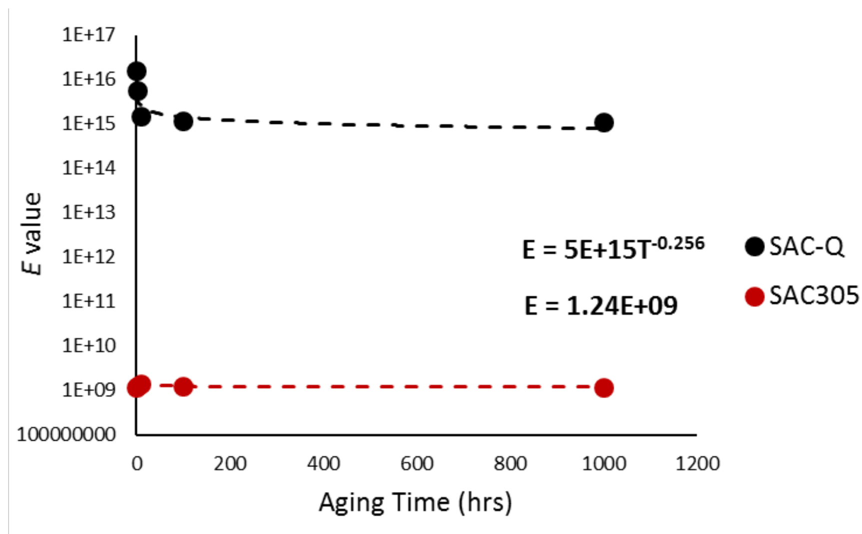

Figure 7.7: Constant *E* value at different aging times for SAC-Q and SAC305 solder alloys.

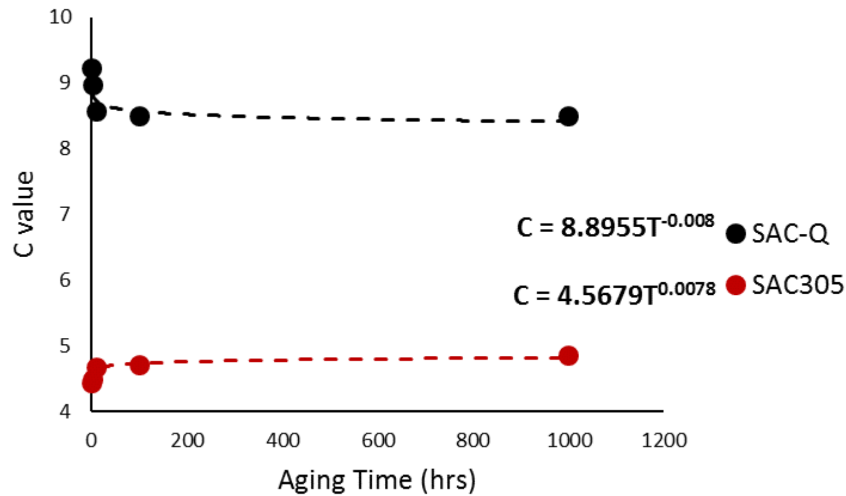

Figure 7.8: Constant *c* value at different aging times for SAC-Q and SAC305 solder alloys.

Figures 7.9 and 7.10 show the prediction models for the characteristic life of SAC305 and SAC-Q solders in three dimensions. From those Figures, the behavior of fatigue life is clearly observed at different experimental conditions. To construct a general reliability model for both solders, equations 7.3 and 7.4 are substituted on equation 7.1 instead of the scale parameter for both solders. For the shape parameter value, the relationship between β and the experimental conditions was nonsignificant. Therefore, the shape parameters for the general reliability models are estimated by calculating the mathematical average of the shape parameter at different experimental conditions for each solder alloy. Equations 7.5 and 7.6 represent the final reliability models as a function of aging time and stress amplitude for SAC305 and SAC-Q solder alloys, respectively.

$$R(t) = e^{-\left(\frac{t}{1.24*10^{9}*P^{-4.5679*T^{0.0078}}}\right)^{3.94}} \quad \text{(7.5)}$$

$$R(t) = e^{-\left(\frac{t}{5*10^{15}*T^{-0.256}*P^{-8.8955*T^{-0.008}}}\right)^{3.87}} \quad \text{(7.6)}$$

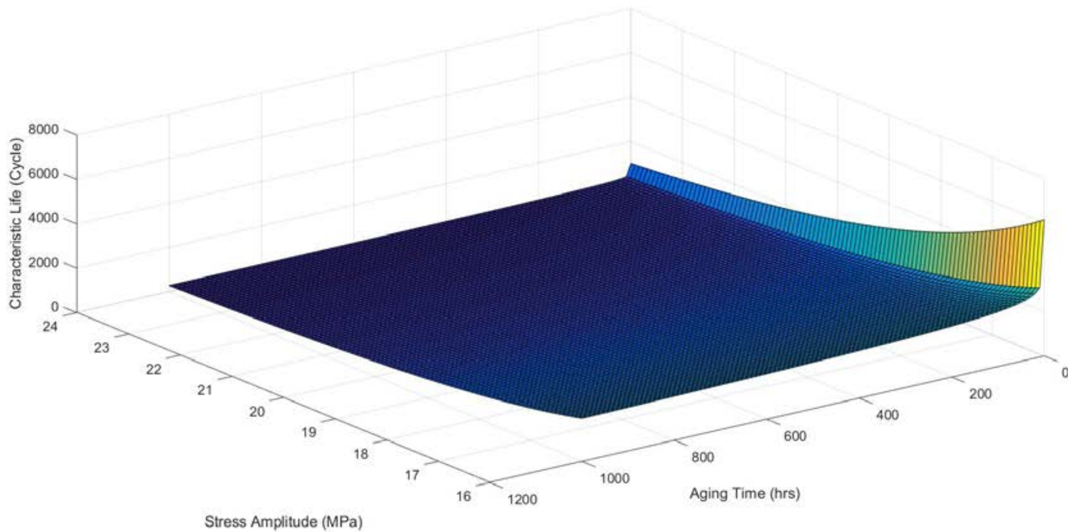

Figure 7.9: The characteristic life model for SAC305 solder alloy.

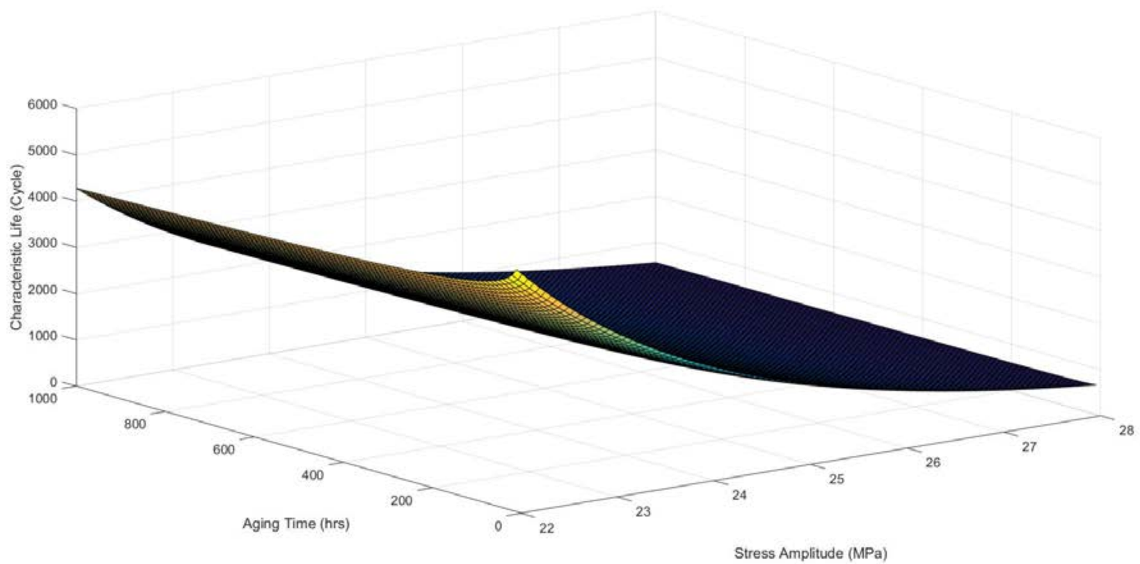

Figure 7.10: The characteristic life model for SAC-Q solder alloy.

7.4.2 Hysteresis Loop Analysis

To investigate the effect of adding Bi on SAC-based fatigue properties (inelastic work and plastic strain) at variant stress amplitudes and aging times, a hysteresis loop (stress-strain loop) is constructed for each cycle of SAC305 and SAC-Q. A typical hysteresis loop for the non-aged SAC305 solder joint cycled at 20MPa stress amplitude is shown in Figure 7.11. The plastic strain range is obtained by calculating the delta strain at stress zero, and the inelastic work per cycle is obtained by calculating the hysteresis loop area using numerical integration.

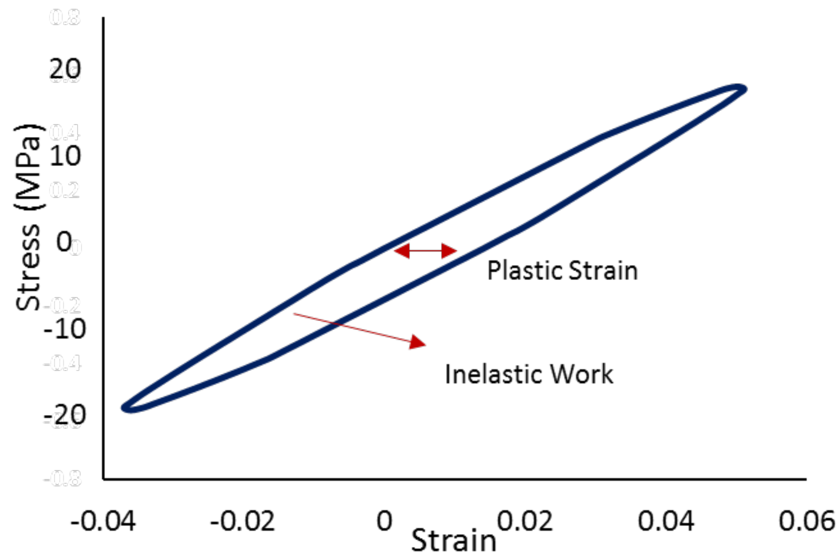

Figure 7.11: Typical hysteresis loop of the non-aged SAC305 solder joint cycled at 20MPa stress.

Figure 7.12 shows the work per cycle of a SAC305 solder joint cycled at 20 MPa as a function of the number of cycles until complete failure. It is obvious that there are three distinct regions; strain hardening, steady-state, and crack growth. The strain-hardening stage is associated with a decrease in the work per cycle due to the limited strain hardening that happened during the first few cycles. Then the steady-state region is associated with almost a constant work per cycle for around 80% for the fatigue life. The third region represents the major crack initiation and propagation, which is associated with an exponential increase in the work per cycle until complete failure. This behavior is typical for both alloys at different stress levels and aging times.

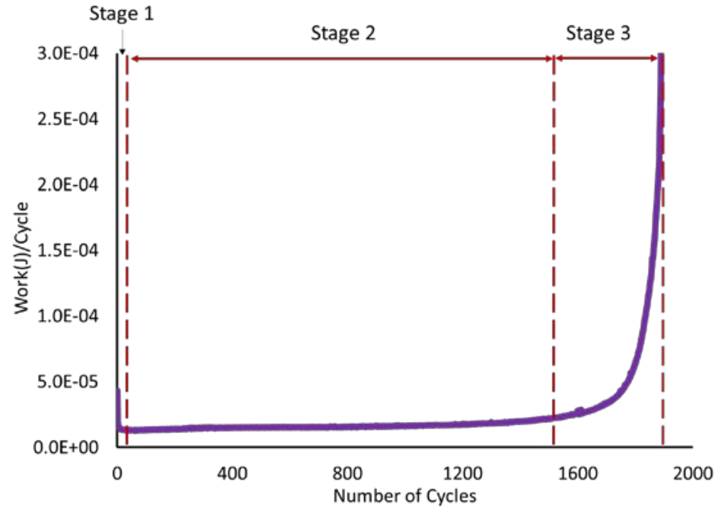

Figure 7.12: Inelastic work per cycle vs. number of cycles for SAC305 solder join.

Figure 7.13 represents the effect of stress amplitude on the hysteresis loop for both solder alloys. Higher stress amplitude cycles lead to a larger hysteresis loop (higher plastic strain range and higher work per cycle). This trend is true for both alloys. However, the effect is more evident for SAC305 since the hysteresis loops of SAC-Q are much smaller. SAC-Q has 3.3% Bi content, which leads to a solid solution hardening that decreases the solder plastic deformation and work dissipation per cycle, and thus increases the fatigue resistant.

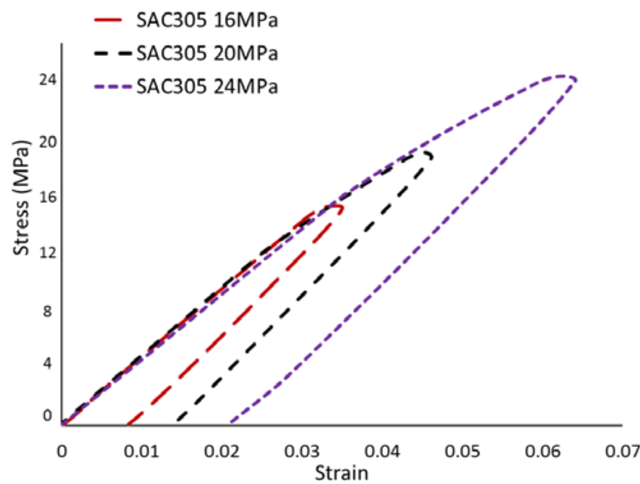

(a). SAC305

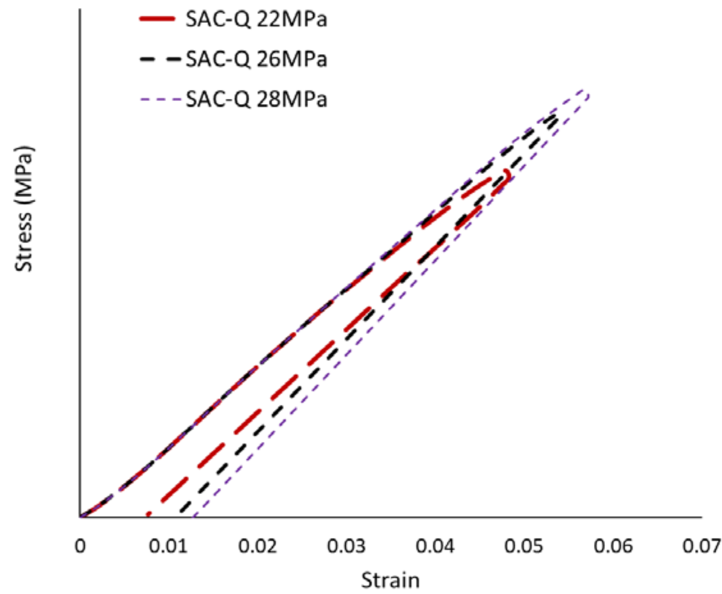

(b). SAC-Q

Figure 7.13: The effect of stress amplitude on the hysteresis loop for the non-aged SAC305 and SAC-Q solder joints.

Figure 7.14 shows the effect of aging time on the hysteresis loop for both solder alloys. The aging time has a significant impact on the inelastic work per cycle and plastic strain range for SAC305 compared to SAC-Q. For SAC305, the plastic strain range and the inelastic work per cycle are increased significantly when the solder joint is aged (Figure 7.14.a). In contrast, a small contribution of the aging time is observed on the plastic strain range and inelastic work per cycle for SAC-Q solder joints (Figure 7.14.b). Aging SAC305 solder joints leads to coarsening of the Ag and Cu precipitates and thus makes the solder joint softer and less fatigue resistant. However, adding Bi to the SAC system prevents or slows down the coarsening of the precipitates, which creates a relatively stable solder structure with aging.

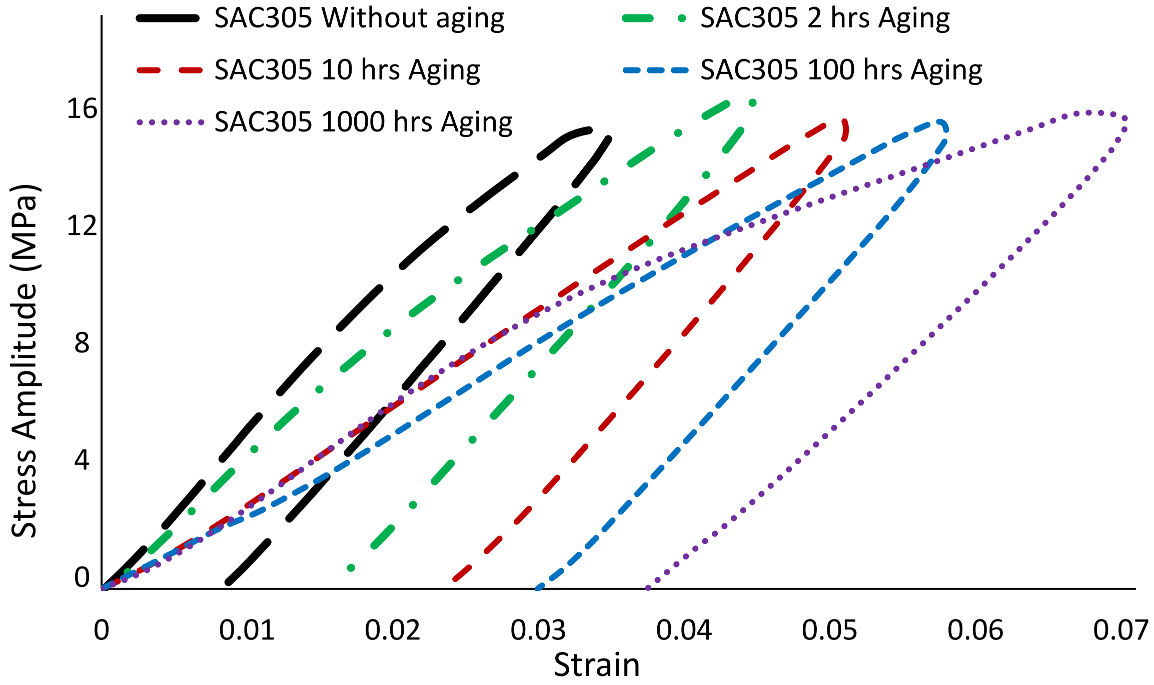

(a). SAC305

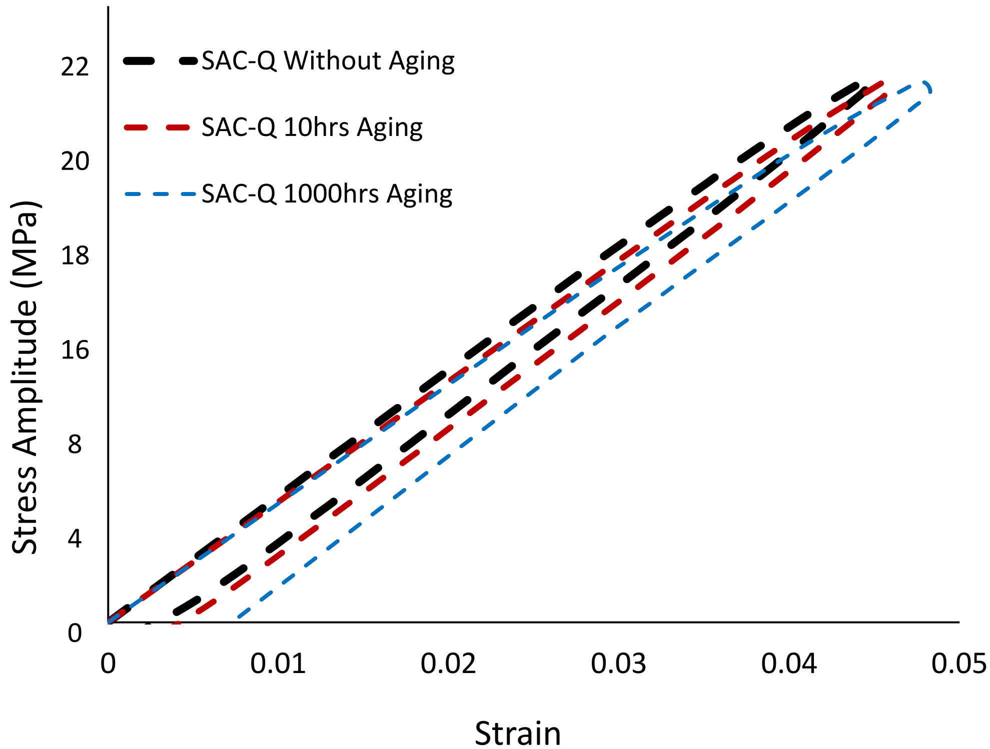

(b). SAC-Q

Figure 7.14: The evolution in the hysteresis loop of SAC305 and SAC-Q solder joints cycled at different aging time at 16 MPa and 22 MPa stress amplitudes.

Microstructure analysis was performed by capturing images using a Scanning Electron Microscope (SEM) for SAC305 and SAC-Q after aging. Figure 7.15 shows the typical distribution of the precipitates before and after aging at the middle of the joint and at a region closer to the IMC layer for a SAC305 solder joint. The precipitates coarsening is obvious after 1000 hours of aging. The distance between the precipitates and their size were increased significantly with aging. Also, the size of the precipitates in the IMC region is larger than that in the middle of the joint at any aging condition.

Figure 7.16 shows the evolutions in the microstructures of a typical SAC-Q solder joint with aging in the middle of the joint and next to the IMC layer. Slight precipitates coarsening can be observed for SAC-Q solder joint after 1000 hours of aging compared to the SAC305. Adding Bi to the SAC solder leads to slowing down the precipitates coarsening with aging, and this is clear in the SEM images. The Bi-rich phase is found at different locations for different aging times. The solubility of Bi in Sn is increased with increasing the temperature. The solubility of Bi in Sn at room temperature is 1.8%; thus, it is expected to observe the Bi-rich phase under the SEM since the SAC-Q has 3.3% of Bi and the SEM images were taken at room temperature. More Bi particles are dissolved in the Sn solid solution when the temperature is increased for aging, but when it returns to the room temperature, some of the Bi is diffused out of the solid solution to form a separate phase.

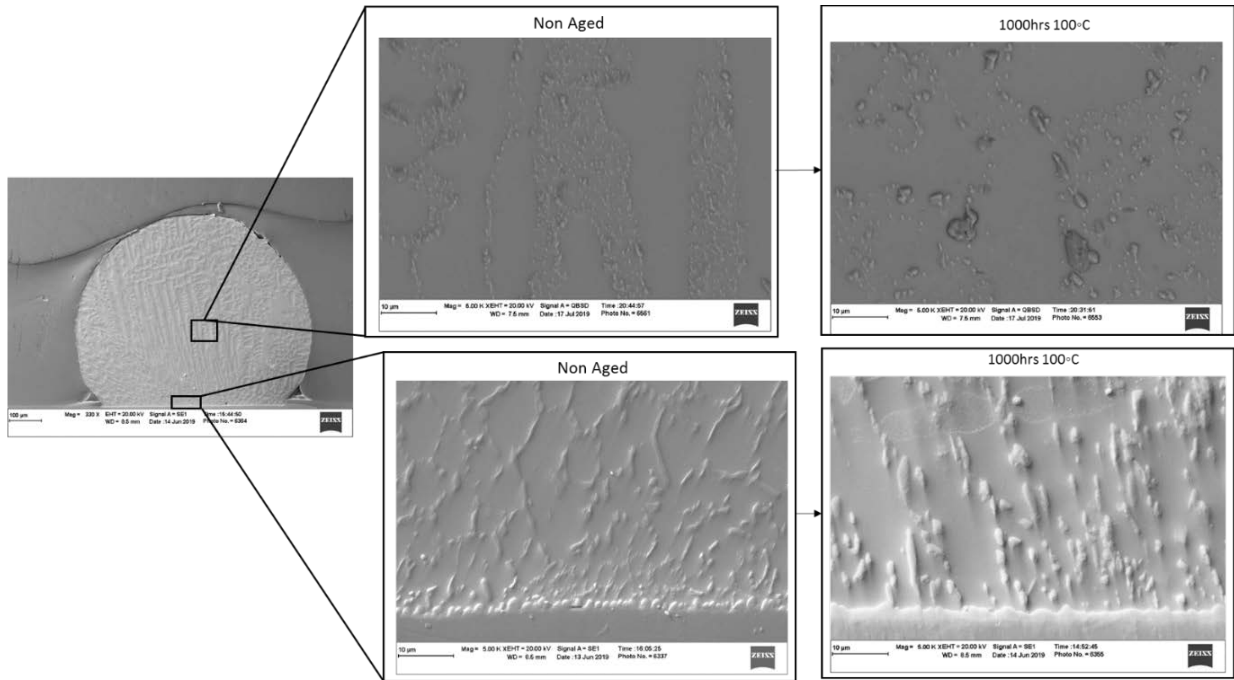

Figure 7.15: SEM images of a typical SAC305 solder joint with aging.

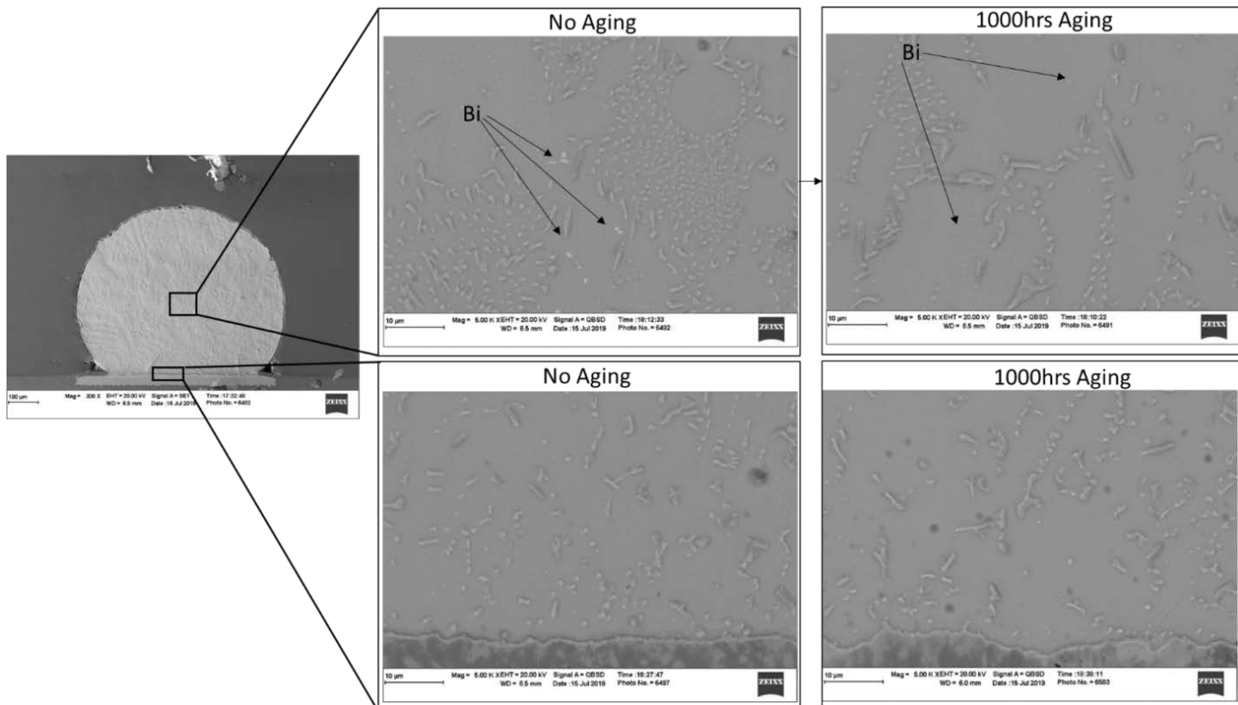

Figure 7.16: SEM images of a typical SAC-Q solder joint with aging.

7.4.3 Morrow Energy Model

The Morrow energy model is used to describe the relationship between the inelastic work per cycle and the characteristic life for different aging times. Therefore, the characteristic life can be predicted as a function of the inelastic work per cycle by using a power equation (Morrow energy equation), equation 7.7.[113]

$$N_{63} = C^{\frac{1}{m}} W^{\frac{-1}{m}} \qquad (7.7)$$

Where N_{63} is the characteristic life, C is the fatigue ductility, W is the inelastic work per cycle, and m is the fatigue exponent. Figure 7.17 shows the average inelastic work per cycle versus the average characteristic life for the non-aged SAC305 and SAC-Q solder alloys. The fitted power equation (Morrow energy equation) is used to describe this relationship. In order to investigate the effect of aging on this relationship, the fatigue ductility (C) and the fatigue exponent (m) are determined at each aging time, as shown in Table 7.4. According to the results, aging time has almost no impact on the Morrow energy constants for SAC305 solder, but a trend can be noticed for the constants of SAC-Q solder.

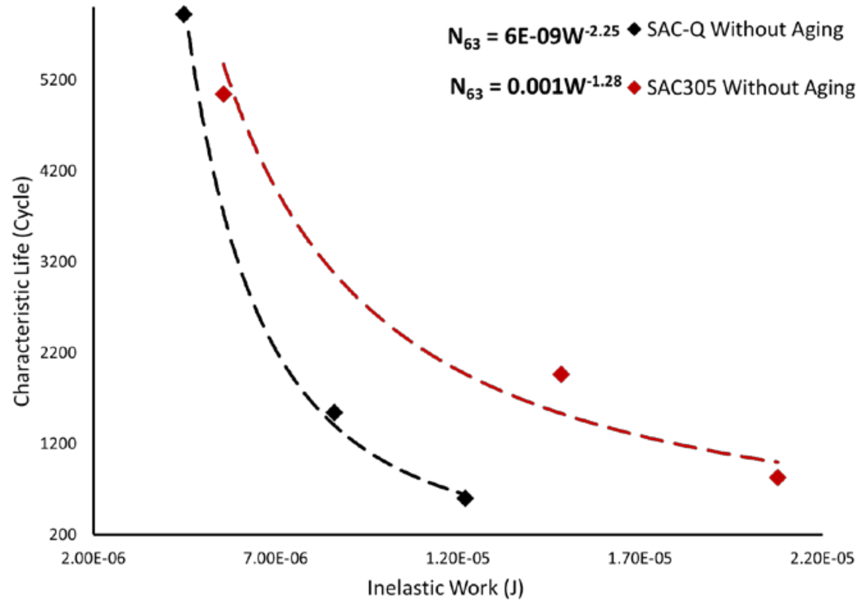

Figure 7.17: The relationship between the characteristic life and inelastic work for the non-aged SAC305 and SAC-Q solder joints.

Table 7.4: Morrow energy constants versus aging time for SAC305 and SAC-Q solder alloys.

Alloy	Aging time (hr)	Fatigue exponent (m)	Fatigue ductility (C)
SAC305	0	0.781	0.0045
SAC305	2	0.824	0.0064
SAC305	10	0.809	0.0048
SAC305	100	0.810	0.0057
SAC305	1000	0.788	0.0047
SAC-Q	0	0.444	0.00021
SAC-Q	2	0.483	0.00033
SAC-Q	10	0.532	0.00034
SAC-Q	100	0.565	0.00049
SAC-Q	1000	0.588	0.00053

According to the results, the aging time doesn't have a significant impact on the Morrow energy constants for SAC305 solder. Therefore, a general prediction equation can be constructed by fitting all the SAC305 solder data points into a general fitting power equation (equation 7.8) as shown in Figure 7.18.

$$N_{63} = 0.0012W^{-1.261} \text{..........} (7.8)$$

On other hand, the Morrow energy constants have a clear trend with aging time for SAC-Q solder. To build a general prediction model for the characteristic life as a function of inelastic work and aging time, the relationship between the fatigue ductility (*C*) and the fatigue exponent (*m*) constants and aging time is identified by using a power equation as shown in Figures 7.19 and 7.20. The R-squared values for the obtained prediction models were between 97% and 99%. Equation 7.9 shows the prediction model for the characteristic life as a function of the inelastic work and aging time of SAC-Q solder joints. As a summary of Morrow energy model, the characteristic life for SAC305 can be determined by using the general prediction equation as a function of the inelastic work regardless to the aging time. For SAC-Q. The Morrow energy constants are influenced by the aging time, so the general Marrow prediction equation for the characteristic life is defined as a function of inelastic work and aging time. To construct the general reliability model, equation 7.8 and 7.9 are substituted in equation 7.1 instead of the scale parameters (θ) for SAC305 and SAC-Q solder alloys, respectively. The shape parameter for each solder is estimated by calculating its mathematical average for each solder. Equations 7.10 and 7.11 represent the general reliability models that are obtained from the Morrow energy model for SAC305 and SAC-Q solder alloys, respectively.

$$N_{63} = (0.0003 * T^{0.0807})^{\frac{1}{0.494*T^{0.0257}}} * W^{-\frac{1}{0.494*T^{0.0257}}} \text{..........} (7.9)$$

$$R(t) = e^{-\left(\frac{t}{0.0012W^{-1.261}}\right)^{3.94}} \text{..........} (7.10)$$

$$R(t) = e^{-\left(\frac{t}{(0.0003*T^{0.0807})^{\frac{1}{0.494*T^{0.0257}}}*W^{-\frac{1}{0.494*T^{0.0257}}}}\right)^{3.87}} \quad \text{...(7.11)}$$

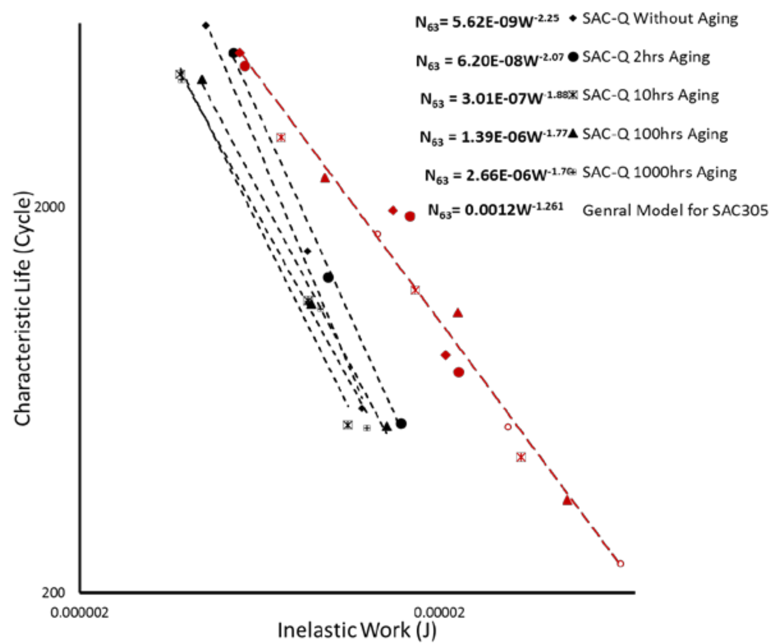

Figure 7.18: The relationship between the characteristic life and inelastic work for SAC305 and SAC-Q solder joints at different aging times in a log-log scale.

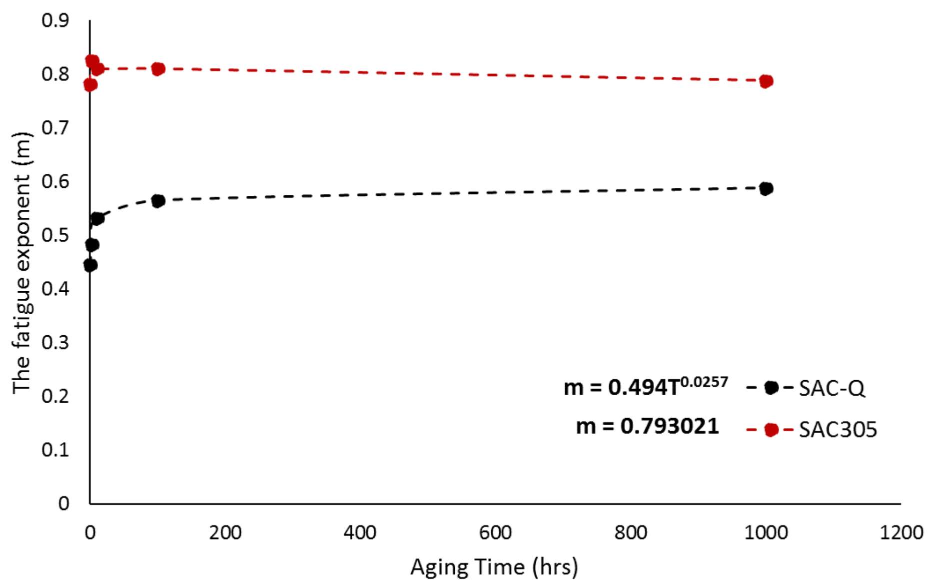

Figure 7.19: The fatigue exponent constant (Morrow energy model) versus aging time for SAC305 and SAC-Q solder joints.

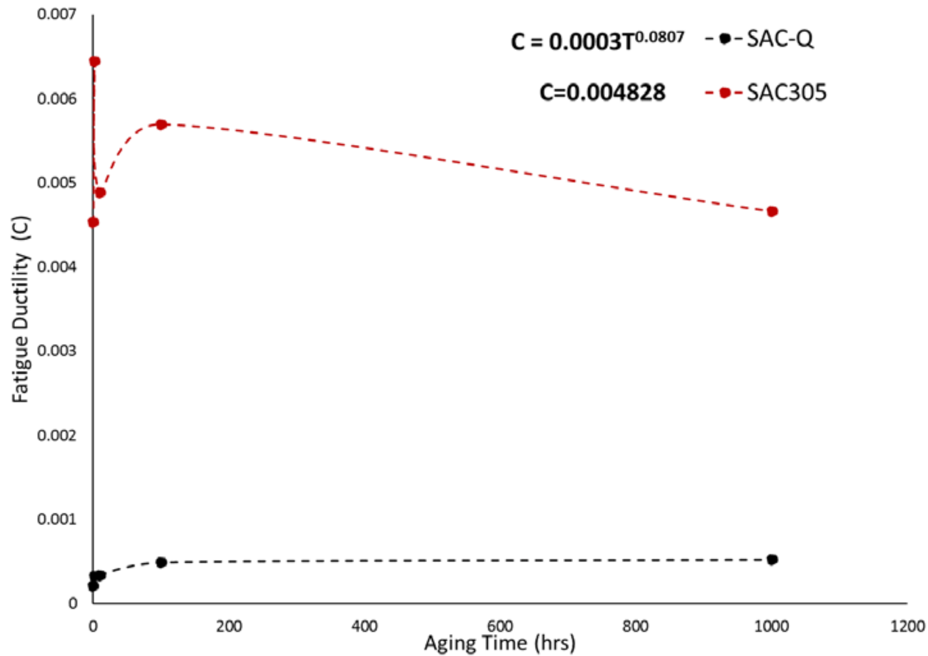

Figure 7.20: The fatigue ductility constant (Morrow energy model) versus aging time for SAC305 and SAC-Q solder joints.

7.4.4 Coffin Manson Model

The Coffin Manson model (equation 7.12) is commonly used to construct a prediction model for fatigue life as a function of the plastic strain [114]

$$N_{63} = \gamma^{\frac{1}{\alpha}} S^{\frac{-1}{\alpha}} \qquad (7.12)$$

Where N_{63} is the characteristic fatigue life, S is the plastic strain range, γ is the fatigue ductility coefficient, and α is the fatigue exponent. Figure 7.21 shows the relationship between the plastic strain and the characteristic life for both solder alloys, where a power equation (Coffin Manson equation) is fitted for each curve. A negative relationship is observed between the characteristic life and the plastic strain for both solder alloys with different rates. In order to investigate the effect of aging on the Coffin Manson model, the values of the constants at different aging times for

SAC305 and SAC-Q solder alloys are determined, as shown in Table 7.5. A significant increase in the Coffin Manson constants (fatigue ductility coefficient and fatigue exponent) is observed for both solder alloys with aging time.

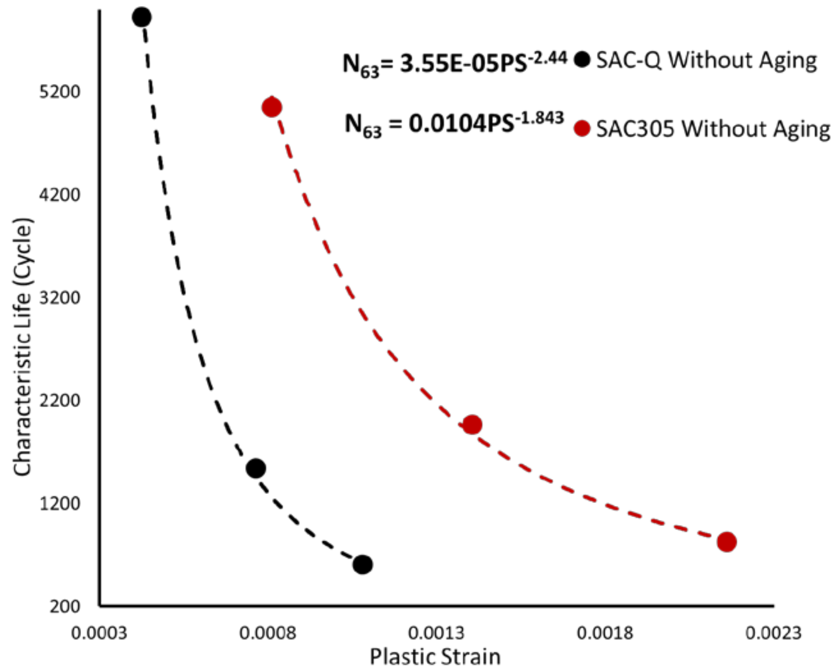

Figure 7.21: The relationship between the characteristic life and plastic strain for the non-aged SAC305 and SAC-Q solder joints.

Table 7.5: Coffin Manson constants versus aging time for SAC305 and SAC-Q solder alloys.

Alloy	Aging time (hr)	Fatigue exponent (α)	Fatigue ductility coefficient (γ)
SAC305	0	0.543	0.084
SAC305	2	0.553	0.095
SAC305	10	0.590	0.136
SAC305	100	0.587	0.146
SAC305	1000	0.620	0.201
SAC-Q	0.01	0.410	0.015
SAC-Q	2	0.476	0.031
SAC-Q	10	0.524	0.027
SAC-Q	100	0.526	0.035
SAC-Q	1000	0.543	0.036

To construct a general prediction model for each solder alloy as a function of plastic strain and aging time, the relationships between the fatigue ductility coefficient, the fatigue exponent constants and the aging time are identified as shown in Figure 7.22 and 7.23 and the fitted power equation is used to describe these relationships. The R-squared values for the prediction models were between 95% and 99%. The fitted power equations that are obtained from Figure 7.22 and 7.23 are substituted in equation 7.12 for solder alloy. The final general equations that are achieved to predict the characteristic life using Coffin Manson Model for SAC305 and SAC-Q solder alloys are shown in equation 7.13 and 7.14, respectively.

$$N_{63} = (0.1087 * T^{0.0753})^{\frac{1}{0.5649*T^{0.0114}}} * S^{\frac{-1}{0.5649*T^{0.0114}}} \quad (7.13)$$

$$N_{63} = (0.0237 * T^{0.075})^{\frac{1}{0.4692*T^{0.0253}}} * S^{\frac{-1}{0.4692*T^{0.0253}}} \quad (7.14)$$

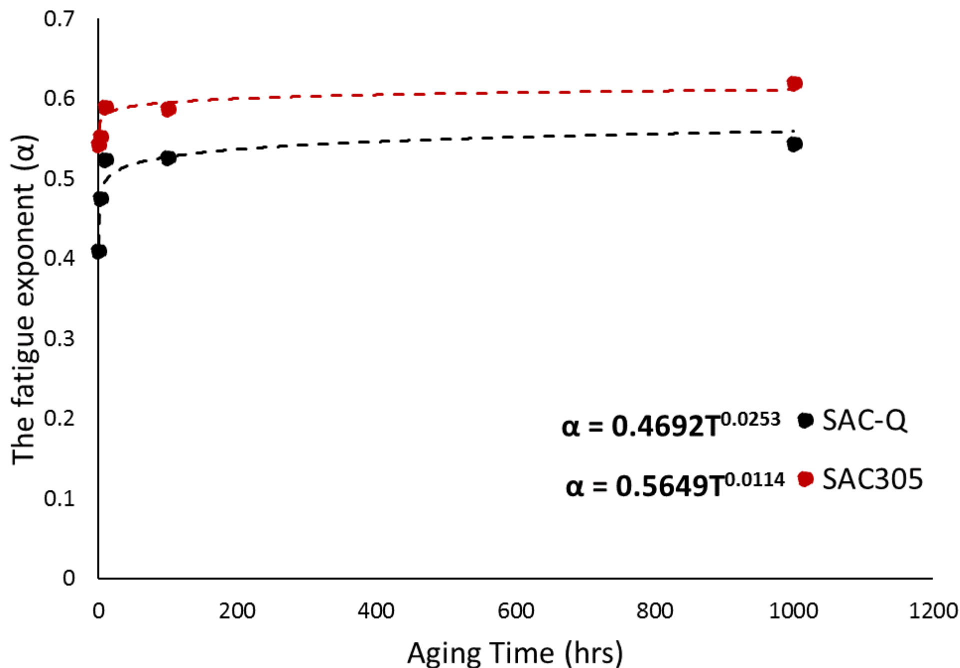

Figure 7.22: The fatigue exponent constant (Coffin Manson model) versus aging time for SAC305 and SAC-Q solder joints.

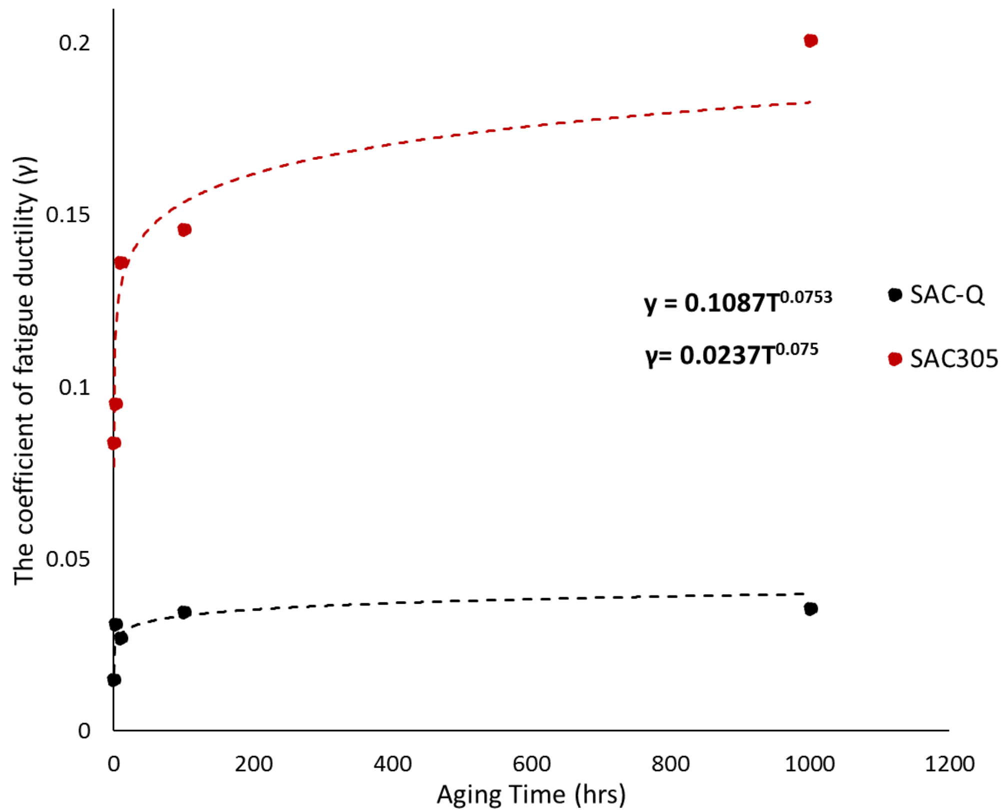

Figure 7.23: The fatigue ductility coefficient constant (Coffin Manson model) versus aging time for SAC305 and SAC-Q solder joints.

As a conclusion, the increase in the aging time or the cyclic stress leads to increase the plastic strain for SAC305 and SAC-Q solder alloys with different levels. The Coffin Manson constants have a clear trend with the aging time for both solder alloys. The characteristic life can be predicted using the plastic strain and aging time as predictors where the Coffin Manson model and a power empirical equation are used to build a general prediction equation. By substituting the prediction equations for the characteristic life, equation 7.13 (SAC305) and equation 7.14 (SAC-Q), in the general reliability equation (equation 7.1), general reliability models are constructed as a function of aging time and plastic strain for SAC305 and SAC-Q solder alloys as shown in equation 7.15 and 7.16 respectively.

$$R(t) = e^{-\left(\frac{t}{(0.1087*T^{0.0753})^{\frac{1}{0.5649*T^{0.0114}}}*S^{\frac{-1}{0.5649*T^{0.0114}}}}\right)^{3.94}} \quad \ldots\ldots\ldots\ldots\ldots\ldots\ldots\ldots\ldots\ldots\ldots\ldots\ldots\ldots(7.15)$$

$$R(t) = e^{-\left(\frac{t}{(0.0237*T^{0.075})^{\frac{1}{0.4692*T^{0.0253}}}*S^{\frac{-1}{0.4692*T^{0.0253}}}}\right)^{3.87}} \quad \ldots\ldots\ldots\ldots\ldots\ldots\ldots\ldots\ldots\ldots\ldots\ldots(7.16)$$

7.4.5 Shear Strength

In the shear test, the effect of aging time on the ultimate shear strength for both solder alloys after aging at 100°C was investigated. The test matrix for the shear experiment is represented in Table 2. Seven replicates are tested at each combination. The shear rate was fixed at 0.1 s^{-1} for all experiments. Figure 7.24 shows typical stress-strain curves for shearing individual non-aged SAC305 and SAC-Q solder joints. The shear strength of the SAC-Q solder joints is significantly higher than the shear strength of the SAC305. The total strain to fracture is lower for SAC-Q compared to SAC305, which indicates a lower ductility. As discussed previously, adding Bi to the SAC system leads to solid solution hardening, which leads to higher strength and less ductility.

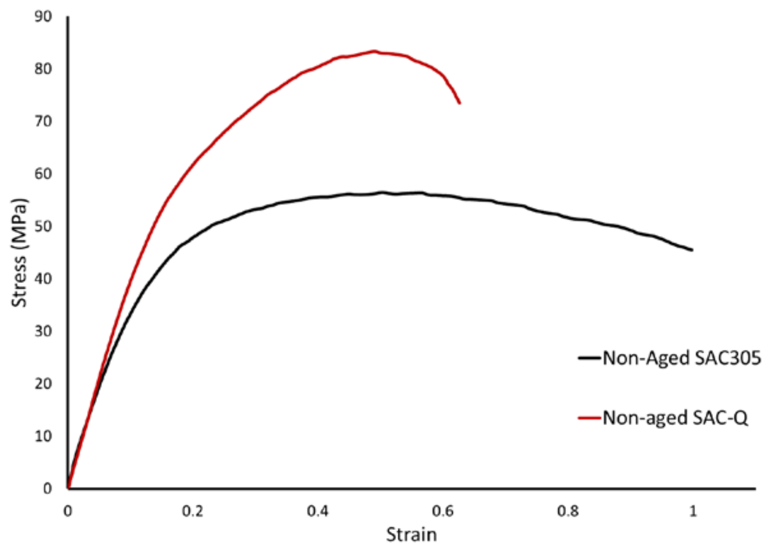

Figure 7.24: Stress-Strain curves for shearing individual non-aged SAC305 and SAC-Q solder joints.

The average shear strength and its degradation with aging for both solder alloys are summarized in Figure 7.25. Figure 7.26 shows the average degradation percentage of the fatigue life for both

alloys at different aging conditions. The amount of shear strength reduction with aging for SAC305 is larger than that for SAC-Q. The amount of fatigue life reduction with aging for SAC305 is also larger than that for SAC-Q. For SAC305 solder joints, the reduction in the shear strength and fatigue life is significant in the first hours of aging, then the rate of reduction is decreased with increasing the aging time. For SAC-Q solder joints, a smaller reduction in the shear strength and fatigue life is found in the first hours of aging (10 hours of aging), the rate of reduction is then decreased to a negligible value. The effect of aging time has a larger impact on the fatigue life of the solder joint compared to the impact on the shear strength.

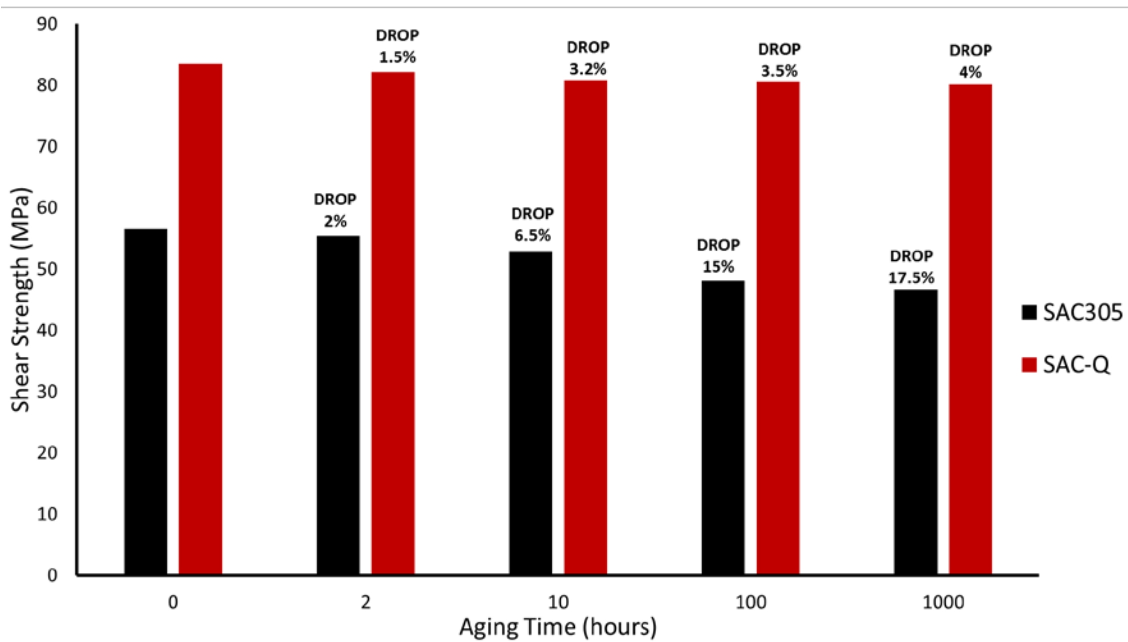

Figure 7.25: A summary of the ultimate shear strength results with aging.

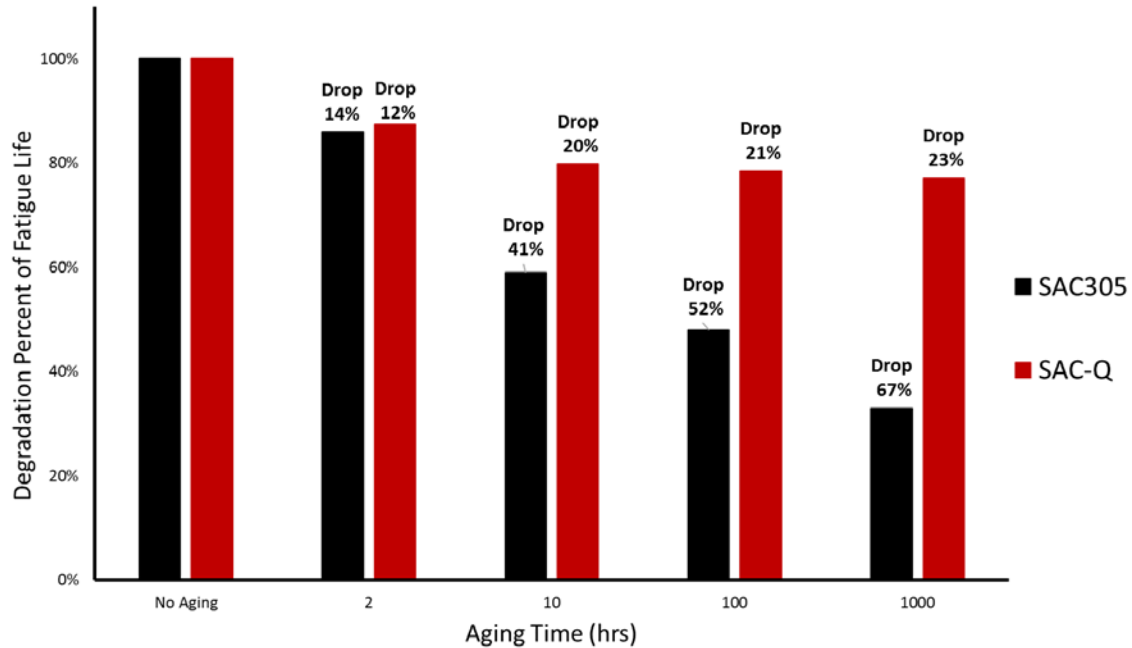

Figure 7.26: The average degradation percentage of fatigue life with aging.

The main effect plot is constructed for both solder alloys as shown in Figure 7.27. One- way ANOVA analysis is executed to find the contribution of the aging time factor on the shear strength for each solder alloy which is represented in Tables 7.6 and 7.7. The results indicated that, the aging time has a significant effect on SAC305 solder alloy with a p-value less than 0.0001. In contrast, the effect of aging time is nonsignificant for SAC-Q solder alloy where its P-value is 0.35. Figure 7.28 shows the means of the shear strength and the variability on the shear strength data for both solders with aging. According to the shear strength results, the amount of reduction on the shear strength of SAC305 solder joints with aging is larger than the amount of reduction on the shear strength of SAC-Q solder joints with aging. For SAC305 solder joints, a significant reduction in the shear strength is observed in the first hours of aging and the amount of reduction is decreased exponentially with increasing the aging time. On the other hand, for SAC-Q solder joints, a small reduction in the shear strength is found in the first hours of aging where the shear

strength reached to the steady state region after 10 hours of aging which means that the long term aging has a nonsignificant effect on the SAC-Q solder joints shear strength.

Table 7.6: One-way ANOVA for the effect of aging on the shear strength of SAC305 solder.

Source	DF	Adj SS	Adj MS	F-Value	P-Value
Aging Time	4	539.4	134.861	21	<0.0001
Error	30	192.7	6.422		
Total	34	732.1			

Table 7.7: One-way ANOVA for the effect of aging on the shear strength of SAC-Q solder.

Source	DF	Adj SS	Adj MS	F-Value	P-Value
Aging Time	4	53.61	13.4	1.15	0.35
Error	30	348.22	11.61		
Total	34	401.83			

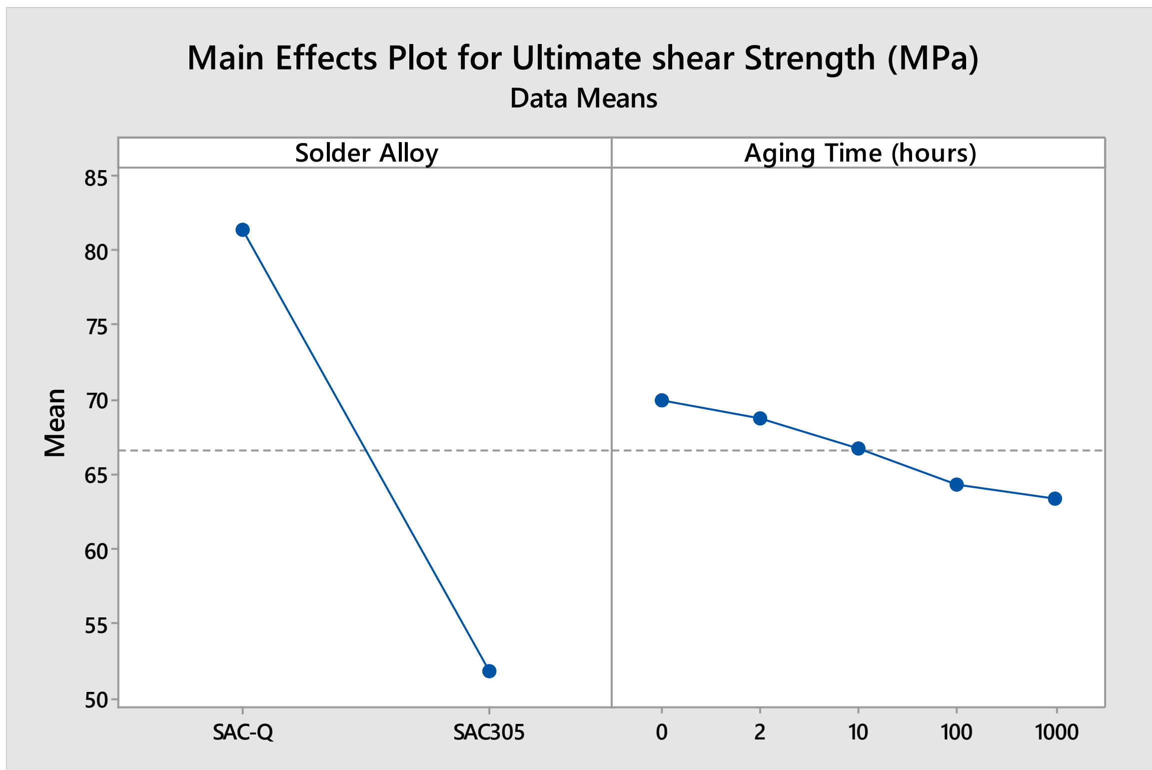

Figure 7.27: The main effect plot of the shear strength for the aging time and solder alloy.

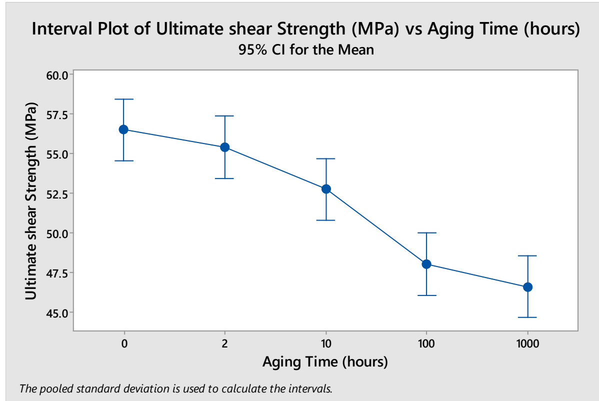

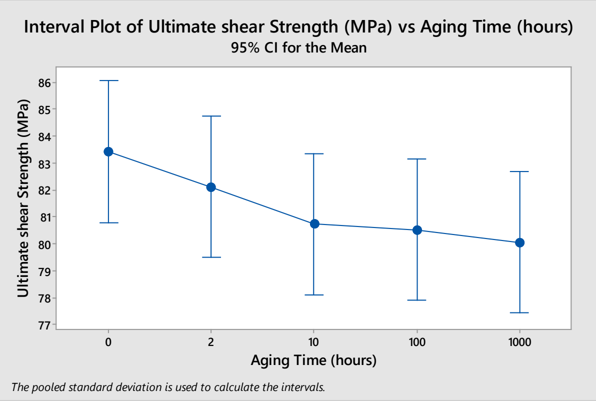

a) SAC305 shear strength b) SAC-Q shear strength

Figure 7.28: The means of the shear strength for each solder alloys.

In order to predict the degradation of the shear strength for both solder alloys at different aging times, the averages of the shear strength are plotted versus the aging time for each solder as shown in Figure 7.29. A general empirical equation, equation 7.17, is used to identify the relationship between aging time and shear strength for each alloy. Where *SS* is the shear strength and *T* is the aging time and *U* and *F* are equation constants. The final empirical prediction models that can be used to predict the shear strength as a function of aging time for each solder alloy at 0.1 S^{-1} strain rate are represented in Figure 7.29.

$$SS = U * \ln(T) + F \quad (7.17)$$

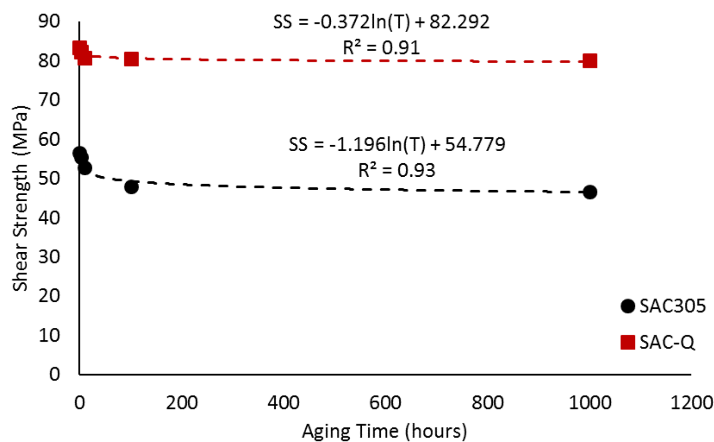

Figure 7.29: The relationship between the aging time and shear strength for SAC305 and SAC-Q solder joints.

7.5 Summary

The degradation of the fatigue and shear properties with aging were examined when the Bi is added to SAC-based solder alloy (SAC-Q). Different stress amplitudes were used in the fatigue test. These tests were performed on individual solder joints at actual stetting conditions. The reliability and shear strength of SAC305 solder joints were determined for comparison purposes. A reliability model as a function of aging time and stress amplitude was developed for both solders. The Morrow Energy and Coffin-Manson models were utilized to construct other reliability models as a function of inelastic work, plastic strain and aging conditions. A prediction model for the shear strength of the solder joints as a function of aging time was built for each solder alloy. One-way ANOVA analysis was executed for the effect of aging time on the shear strength for both solder alloys. Results from the ANOVA analysis revealed that the effect of aging time on the shear strength of the solder joint was significant for SAC305 and nonsignificant for SAC-Q. The evolutions in the microstructure were specified for each solder where the coarsening of the precipitates and the IMC layer thickness were monitored at different aging conditions. A significant increase in the IMC layer thickness and a higher level of precipitates coarsening were observed for SAC305 solder joints. In contrast, there are small observations for the evolutions in the IMC layer thickness and the precipitates size for SAC-Q solder joints. As a summary, Adding Bi for SAC-based solder alloy leads to enhance the fatigue and shear properties of the solder joints and decreases the amount of degradation on its reliability and strength with aging. This can be explained by the solid solution phenomena of the Bi in the Sn rich solder.

Chapter 8: A New Approach in Assessing the Reliability of the Solder Joints under Thermal Cycling Conditions by Using a New Multi-Criteria Optimization Method

8.1 Introduction

Assessing the reliability of a product is one of the methods used to maintain the product quality within an acceptable region along its lifetime. Different distributions are used to describe the fatigue performance of a product such as exponential, normal and log-normal. Two-parameter Weibull distribution is commonly used as a fitted distribution for the reliability data. Scale and shape parameters are the Weibull distribution parameters. A location parameter is used when the three-parameter Weibull distribution is applied to the reliability data. Using the scale parameter (characteristic life) to compare between alternatives may cause improper selection of the optimal choice. The scale parameter-based selection neither considers the data variability nor is the chance of earlier failure. For example, Figure 8.1 represents the Weibull reliability distributions for three products (A, B and C). If the selection is based on the characteristic life, product C is more reliable than products A and B. On the other hand, product A has a lower probability of earlier failure compared to products A and C. Therefore, using different responses that consider these criteria is an efficient way to find the global optimal operating factor levels. To solve this problem, a suitable multi-response technique should be utilized. Different techniques were implemented to optimize the process performance for multi-response problems, for example, Fuzzy logic, artificial neural networks (ANN), grey fuzzy, fuzzy regression utility, data envelopment analysis, fuzzy regression, principal component analysis, and goal programming. In this study, a new approach for process

parameters selection is proposed to find the optimal parameter values that better improve the fatigue resistance. The reliability of microelectronic connections in thermal cycling operating conditions is used as a validation case study for this approach. The validation case study illustrates the reliability of solder joints. Solder joints are one of the most popular methods that provide both mechanical and electrical connections between the electronic package and the Printed Circuit Board (PCB). Since most common failure modes that are associated with the electronic assemblies are found in the interconnection materials, it is vital to study the reliability behavior of the solder joints under harsh environmental conditions. In the validation case study, the optimal process parameters will be found for CABGA208 that is aged for 12 months at 125˚C. Two levels (2) of the solder sphere material, three levels (3) of the surface finish type and ten levels (10) of the solder paste alloy are studied as process parameters. In this approach, four quality responses are employed to assess the reliability data which are the scale parameter, the B10 (10% of the probability of surviving ’earlier failure’), mean- standard deviation response and the signal to noise ratio (SNR). The fuzzy logic will be applied to solve the multi-response problem. An optimal process parameter setting that considers different quality characteristics was found for the validation case study.

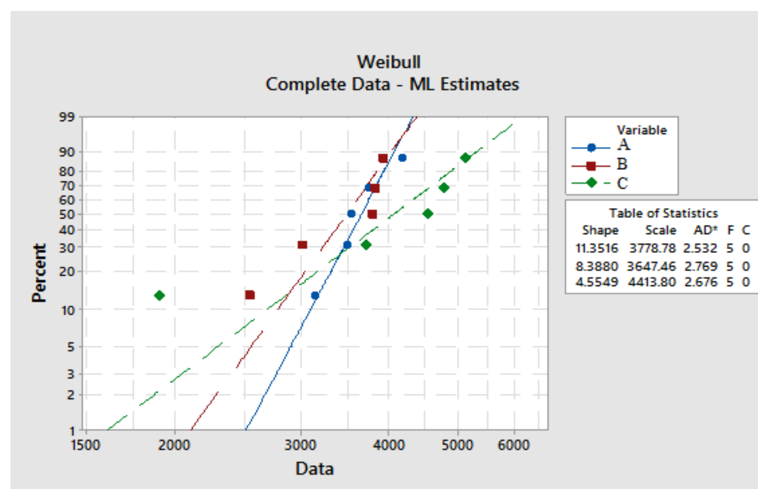

Figure 8.1: Two-parameter Weibull distributions for three products.

8.2 Experimental Setup

The test vehicle for the validation study is shown in Figure 8.2. FR-4 glass epoxy was used to fabricate the printed circuit board (PCB) with a non-solder mask defined copper pads. The test vehicle contains different electronic components (QFNs, SMRs, and CABGAs). The reliability CABGA208 at 12 months of aging time and 125˚C aging temperature was investigated by implementing the thermal cycling test. The thermal cycling test was performed using a highly controlled thermal chamber (Figure 8.3). The thermal cycling temperature was between 125˚C and -40˚C. The detailed thermal profile is shown in Figure 8.4. The dwell time was 15 minutes, the ramp time was 50 minutes, and the total cycle time was 115 minutes. The test vehicles were cycled for 5000 cycles and any component that didn't fail was considered as a censored data point. Ten (10) solder paste materials were studied with three different surface finishes for SAC105 and SAC305 solder spheres. All testing boards were aged using the same aging parameters. Five (5) samples were utilized at each experimental combination. Table 8.1 shows the solder pastes, solder spheres and the surface finishes that were used in this test. The L60 experimental orthogonal array that was used in this test is shown in Table 8.2.

Table 8.1: The experimental combinations of the solder paste, solder sphere, and surface finish.

Aging for 12 months CABGA208					
solder paste materials	level	surface finish	level	solder sphere	level
Material 1 (95.5Sn-3.8Ag-0.7Cu-0.02Ni-1.5Sb-3Bi)	1	OSP	1	SAC 105 (98.5Sn-1.0Ag-0.5Cu)	1
Material 2 (95.5Sn-3.8Ag-0.7Cu-0.02Ni-1.5Sb-3Bi)	2	ENIG	2	SAC 305 (96.5Sn-3.0Ag-0.5Cu)	2
Material 3 (92.77Sn-3.41Ag-0.52Cu-3.3Bi)	3	ImAg	3		
Material 4 (96.62Sn-0.92Cu-2.46Bi)	4				
Material 5 (Sn-3.5Ag-0.7Cu-0.125Ni-1.5Sb-3Bi)	5				
Material 6 (Sn-3.0Ag-3Bi-0.8Cu-Ni)	6				
Material 7 (Sn-3.4Ag-0.7Cu-3.2Bi-3.0Sb-Ni-Co)	7				
Material 8 (98.47Sn-0.5Ag-1.0Cu-0.03Mn)	8				
Material 9 (SAC+Sb)	9				
Material 10 (Sn-3.8Ag-0.8Cu-Bi-X)	10				

Table 8.2: L_{60} testing orthogonal array.

Exp (i)	solder past	surface finish	solder sphere
1	1	1	1
2	1	1	2
3	1	2	1
4	1	2	2
5	1	3	1
6	1	3	2
.	.	.	.
.	.	.	.
.	.	.	.
56	10	1	2
57	10	2	1
58	10	2	2
59	10	3	1
60	10	3	2

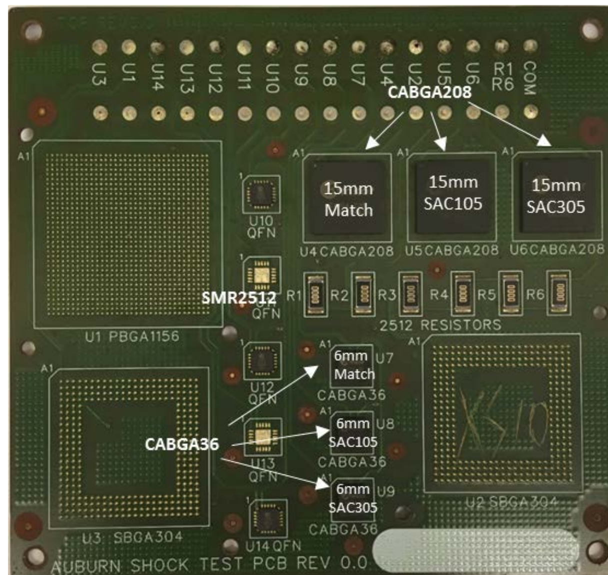

Figure 8.2: The test vehicle.

Figure 8.3: The Thermal chamber.

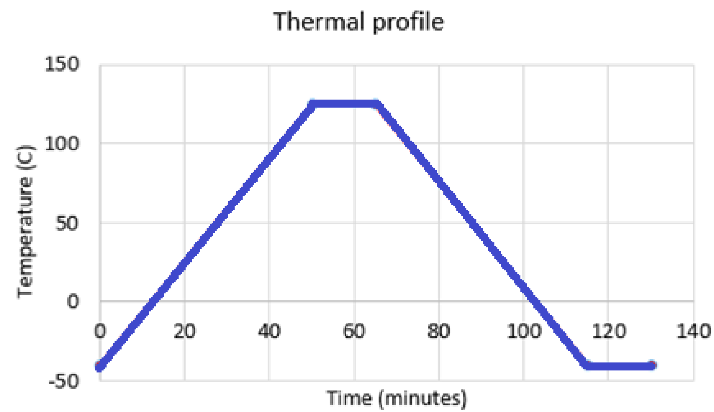

Figure 8. 4: Thermal cycling profile.

8.3 Results and Analysis

Two-parameter Weibull analysis was performed to illustrate the fatigue behavior of the solder joints under thermal cycling conditions for each experimental combination. Figure 8.5 represents the Weibull probability plots for the SAC105 and SAC305 solder spheres at different surface finishes for material 1 solder paste. The maximum likelihood method was used to estimate the Weibull distribution parameters. Equation 8.1 represents the Weibull distribution equation. Where θ is the scale parameter, β is the shape parameter, t is the number of cycles. The Weibull distribution was applied at each experimental combination and their scale and shape parameters were determined. B10 was computed as well at each combination by using equation 8.2 which describes the earlier failure opportunity at a 10% probability of surviving. The characteristic life and B10 were considered as two different responses. [111]

$$R(t) = e^{-(\frac{t}{\theta})^{\beta}} \text{ ....(8.1)}$$

$$B10 = (-1 * \ln 0.9)^{\frac{1}{\beta}} * \theta \text{ ....(8.2)}$$

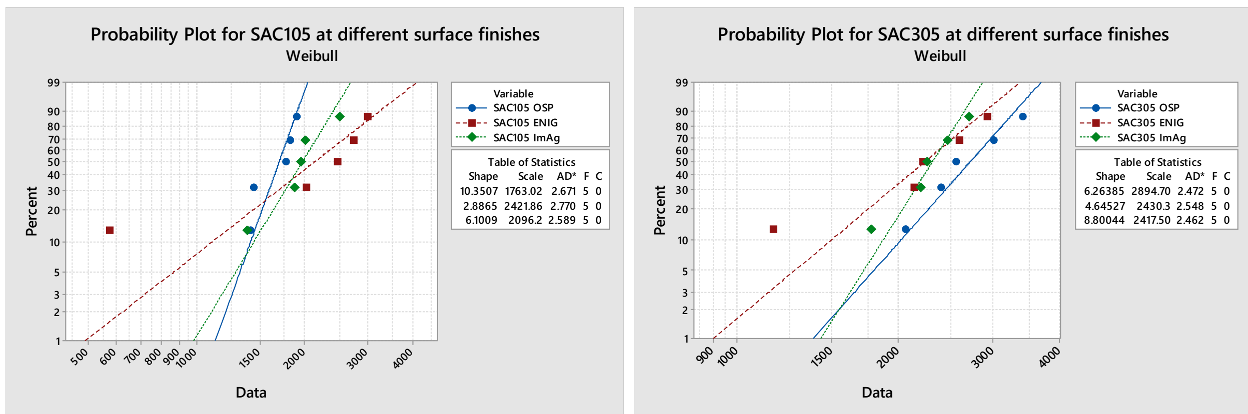

Figure 8.5: Two-parameter Weibull probability plots for SAC105 and SAC305 solder spheres at different surface finishes for material 1 solder paste.

Another way to analyze the fatigue data is by calculating the mathematical averages of the fatigue life and its standard deviation at each experimental combination. To combine the mean and standard deviation in one response which is called mean-SD response, first, the averages and the standard deviations were normalized to keep the contribution of each one equal by using equations 8.3 and 8.4. Where M_i and SD_i are the fatigue life average and standard deviation at experiment *i,* respectively. *M* max and *SD* max are the maximum averages and standard deviation among all combinations, and *M min* and *SD* min are the minimum averages and standard deviation at all experimental conditions, respectively.

$$mean_normal(i) = \frac{(M\,max - M_i)}{(M\,max - M\,\min)} \quad (8.3)$$

$$SD_normal\,(i) = \frac{(SD\,max - SD_i)}{(SD\,max - SD\,\min)} \quad (8.4)$$

The increase in the average means a better performance and the decrease in the standard deviation leads to increase the consistency in the fatigue life date. Thus, the Mean-SD response was determined by subtracting the normal value of the average from the normal value of standard deviation as shown in equation 8.5.

$$mean - SD(i) = mean_normal(i) - SD_normal\,(i) \quad (8.5)$$

The last type of analysis that is discussed in this study is the Signal to Noise Ratio (SNR). SNR is commonly used in the Taguchi method for optimizing the process performance when the process has one quality response which is used for optimizing the mean and variance of the quality response at the same time. To compute the SNR, the class of the quality response should be identified. There are three mean classes for the quality response which are larger-the-better (LTB), nominal-the-best (NTB) and smaller-the-better (STB). The fatigue life always follows the LTB

class. The SNR is determined at each experiment by using equation 8.6, where K is the number of replicates at each experiment, $SNR\ (i)$ is the signal to noise ratio at experiment i, y_{ik} is the fatigue life of the solder joints at replicate k and experiment i. [116] The optimal operating process parameters were found by computing the average of SNR at each factor level as shown in Table 8.3. Table 8.3 represents the averages of the COM values for the validation study. The optimal factor levels based on the SNR were identified by selecting the factor levels that have the largest value of the SNR average from Table 8.3. The optimal operating factor levels were level 6 for factor 1, level 2 for factor 2 and level 2 for factor 3.

$$SNR(i) = -10 \log \left[(1/K) \sum_{k=1}^{K} \frac{1}{y_{Ik}^2} \right] \ldots\ldots\ldots\ldots\ldots\ldots\ldots\ldots\ldots\ldots\ldots (8.6)$$

Table 8.3: The averages of the SNR at each factor level.

SNR			
Level	Factor		
	1	2	3
1	65.25546	65.56628	64.83559
2	67.70102	**65.82471**	**66.42449**
3	65.72393	65.49913	
4	65.21995		
5	64.70572		
6	**68.45623**		
7	68.16235		
8	58.24817		
9	65.7266		
10	67.10096		

After computing the four quality responses (characteristic life, B10, mean-SD, and SNR) as shown in Table 8.4, the problem became a multi-response problem and finding the optimal experimental combination will be more complicated. The optimal factor levels of the characteristic life, B10, and the mean-SD responses were determined by choosing the factor levels that have the highest

values of those responses. The optimal factor levels for all quality responses are shown in Table 8.5. Four different process parameters settings were obtained from four different responses. Therefore, it is vital to find a robust method to determine the global optimal factor levels.

Table 8.4: The responses values at each experimental combination.

Exp (i)	solder paste	surface finish	solder sphere	SNR	mean-SD	scale parameter	B10
1	1	1	1	64.3	0.203	1763	1702.5
2	1	1	2	68.2	0.275	2894.7	2761.8
3	1	2	1	61.3	-0.198	2421.8	2345.7
4	1	2	2	65.5	0.036	2430.3	2328.6
5	1	3	1	65.3	0.156	2096.2	2010.2
6	1	3	2	66.9	0.292	2417.5	2340.8
.	.	.	.	.	.	.	.
.	.	.	.	.	.	.	.
.	.	.	.	.	.	.	.
56	10	1	2	68	0.212	2922.9	2795.8
57	10	2	1	66.6	0.056	2685.7	2542.4
58	10	2	2	69.8	0.473	3339.2	3214.7
59	10	3	1	65.6	0.055	2675.7	2532.4
60	10	3	2	67.4	0.079	3024.9	2897.389

Table 8.5: The optimal factor levels for each response.

optimal factor levels			
Quality Response	Factor		
	solder paste	surface finish	solder sphere
Characteristic Life	7	2	2
B10	2	3	2
mean-SD	2	1	2
SNR	6	2	2

To convert the multi-response problem into a single response problem, the Mamdani fuzzy inference method was employed to find the Comprehensive Output Measure (COM). The fuzzy system includes different functions which are fuzzification (defining the inputs membership

functions 'MFs'), rule evaluation, output membership functions, and defuzzification method. The detailed fuzzy structure is presented in Figure 8.6. [117,118]

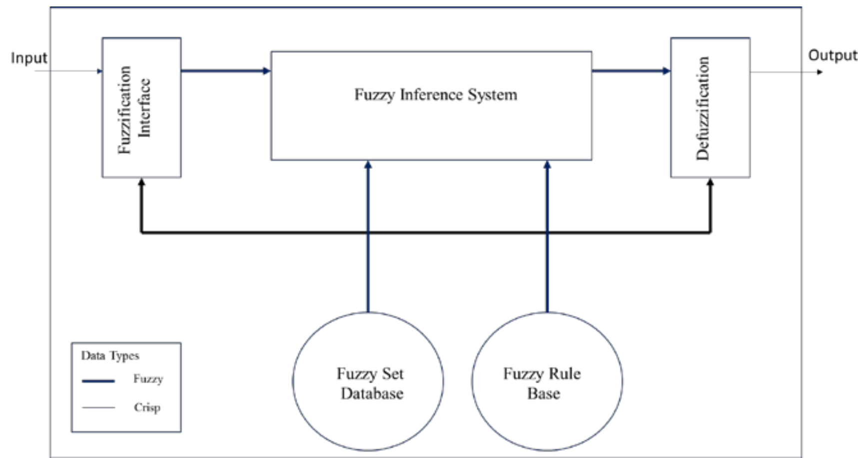

Figure 8.6: The Fuzzy logic system

The four responses obtained were used as inputs for the fuzzy system as shown in Figure 8.7. The first step in the fuzzy logic is the fuzzification of the input by identifying two MFs for each response (Low, High). Figure 8.8 represents the MFs for the scale parameter. The other input MFs are displayed in appendix B (Figures B.1-B.3). Then, the rules of the fuzzy system were established based on the number of fuzzy inputs as shown in Table 8.6. The output MFs were defined based on the rule aggregation as shown in Figure 8.9. Five MFs (Lowest, Low, Mid, High, and Highest) were utilized in the fuzzy system. The last step is the defuzzification method which is used to convert the fuzzy values into COM values. The center of gravity (COG) was used in this study as a defuzzification method. Figure 8.10 displays an example of how the COM value calculated from three output MFs. The COM values were determined by calculating the average of the values that were achieved from the COG method for the 16 rules. This was performed using a MATLAB (version R 2016) code. Table 8.7 shows the COM value at each experimental combination. After determining the COM value at each experimental combination, the average of the COM values at each factor level was determined as shown in Table 8.8. The optimal factor

levels were chosen by selecting the level that has the highest average COM value for each factor, which are level 6 for factor 1 (Material 6), level 2 for factor 2 (ENIG surface finish) and level 2 for factor 3 (SAC305 solder sphere). Figure 8.11 shows the flow chart for the proposed fuzzy methodology to assess the reliability of the solder joints by using the multi criteria-based decision method. The new methodology provides a higher fatigue life, acceptable variability, and low earlier failure opportunity compared to the use of the characteristic life for comparison. Other detailed procedures for fuzzy system are represented in appendix B (Figures B.6-B.11). The response surface graphs for all fuzzy parameters are shown in appendix B (Figures B.4-B.5).

Table 8.6: The Fuzzy rules for the four responses.

SNR	mean-SD	Scale Parameter	B10	OUTPUT
LOW	LOW	LOW	LOW	LOWEST
LOW	LOW	LOW	HIGH	LOW
LOW	LOW	HIGH	LOW	LOW
LOW	LOW	HIGH	HIGH	MID
LOW	HIGH	LOW	LOW	LOW
LOW	HIGH	LOW	HIGH	MID
LOW	HIGH	HIGH	LOW	MID
LOW	HIGH	HIGH	HIGH	HIGH
HIGH	LOW	LOW	LOW	LOW
HIGH	LOW	LOW	HIGH	MID
HIGH	LOW	HIGH	LOW	MID
HIGH	LOW	HIGH	HIGH	HIGH
HIGH	HIGH	LOW	LOW	MID
HIGH	HIGH	LOW	HIGH	HIGH
HIGH	HIGH	HIGH	LOW	HIGH
HIGH	HIGH	HIGH	HIGH	HIGHEST

Table 8.7: The COM value at each experimental condition.

Exp (i)	solder paste	surface finish	solder sphere	COM value
1	1	1	1	0.4657
2	1	1	2	0.5511
3	1	2	1	0.4568
4	1	2	2	0.4985
.	.	.	.	.
.	.	.	.	.
.	.	.	.	.
58	10	2	2	0.622
59	10	3	1	0.5232
60	10	3	2	0.5519

Table 8.8: The average of the COM values at each factor level.

Average COM			
Level	Factor		
	1	2	3
1	0.5001333	0.505015	0.4854433
2	0.5728	**0.5267**	**0.5414167**
3	0.5087	0.508575	
4	0.4962333		
5	0.49555		
6	**0.5887**		
7	0.5854333		
8	0.3214667		
9	0.5179		
10	0.5373833		

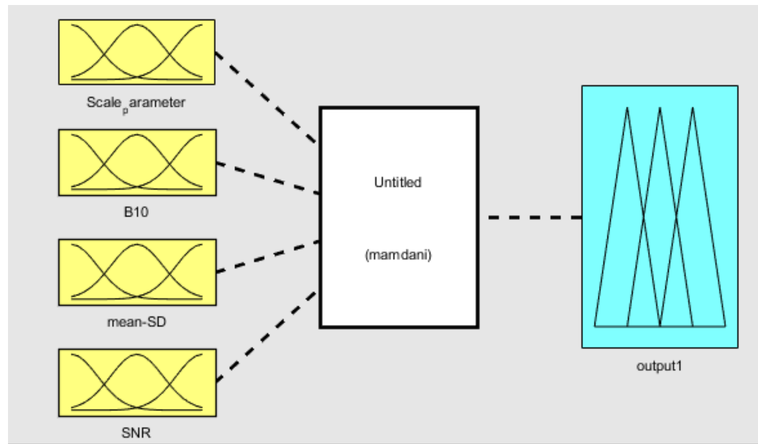

Figure 8.7: The inputs in the fuzzy system.

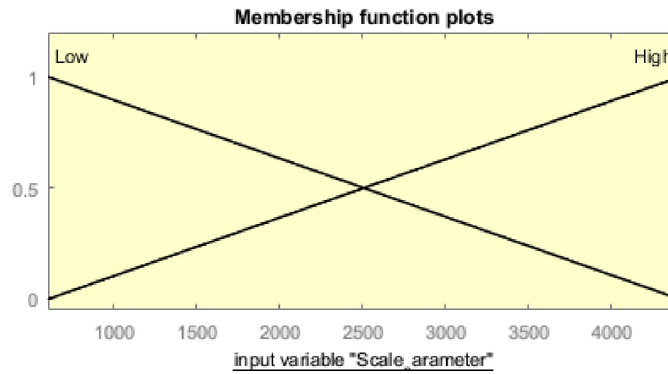

Figure 8.8: The MFs for the scale parameter.

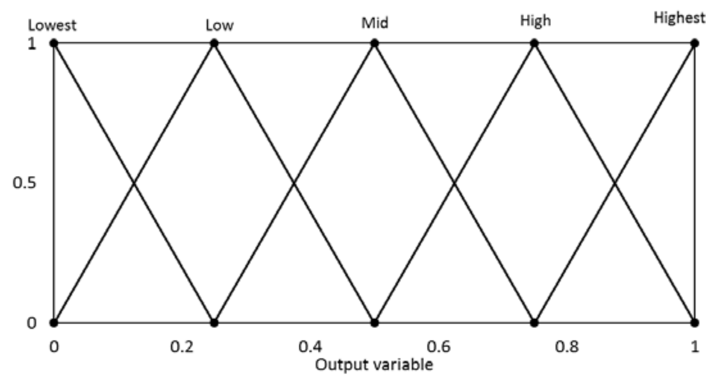

Figure 8.9: The five output MFs.

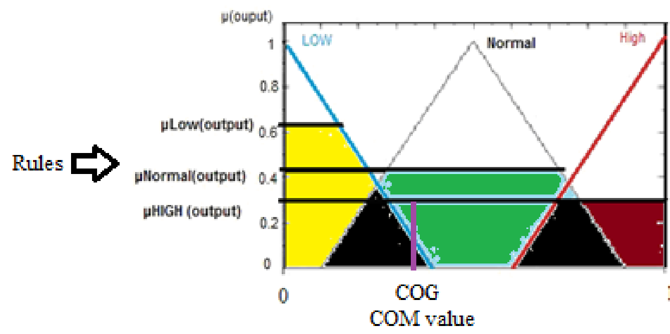

Figure 8.10: The COG method for computing the COM values.

The proposed approach

Failure data

2-paramenter Weibull (characteristic life, shape parameter) $R(t) = e^{-\left(\frac{t}{\theta}\right)^{\beta}}$

characteristic life

Mean and Standard Deviation

Normalization for the Mean and the Standard Deviation

Result of: the Mean normal value –Standard Deviation normal value

Conditional Value at Risk (CVAR)

The optimization model for calculating the CVAR at alpha 0.1

Signal to Noise Ratio (SNR)

$SNR_i = -10 \log \left[1/K \left(\sum_{k=1}^{K} 1/y_{ik}^2 \right) \right]$

Multi Response Problem

Inputs to the Fuzzy Model

Fuzzy Model

Fuzzfification

Defining the membership functions for the inputs (Low, High)

Aggregation of the rule & Rule evaluations

Defining the membership functions for the output

Set the rules

Defuzzfification

Calculating the COM value by using the central of gravity method (COG)

Figure 8.11: A flow chart for the multi-criteria fuzzy logic assessment methodology for the reliability data.

8.4 Summary

A new approach for dealing with reliability data was proposed where four responses were extracted from the data. The first two responses which are the characteristic life and earlier failure probability (B10) were obtained from fitting the data to a two-parameter Weibull distribution. The third response was the result of subtracting the normal values of average and standard deviation. SNRs was the last response which was calculated from the SNR larger-the-better equation. The fuzzy logic was employed to convert the problem from a multi-criteria decision-based problem into a single response problem by determining the COM value at each experimental combination. The average COM values at each factor level was found. The optimal factor levels were identified based on the level that has the highest average COM value for each factor. This approach was also validated against a reliability data for aged solder joints to choose the optimal solder sphere material, surface finish and solder paste alloy under harsh environmental conditions.

Chapter 9: Overall Summary, Conclusion and Future Works

9.1 Overall Summary and Conclusion

In study one, the fatigue life of individual SAC305 solder joints was examined in shear fatigue experiments. Two factors were considered in this study which are the aging time with five levels (0, 2, 10, 100 and 1000 hrs) and the cyclic shear stress amplitude with three levels (16, 20 and 24MPa). A Two-Parameter Weibull distribution was used to describe the fatigue behavior of the solder joints. The results indicated a reduction in the characteristic fatigue life when the aging time or the stress amplitude were increased. A general prediction model for the reliability of the solder joints was developed by relating the characteristic life to the stress amplitude and aging time. The evolutions in the hysteresis loop were determined at different aging times and stress amplitudes. The inelastic work per cycle and the plastic strain were calculated as well from the hysteresis loop. Empirical models were found to identify the relationships between the inelastic work per cycle, the plastic strain and aging time. Increasing the stress amplitude leads to an increase in the inelastic work per cycle and the plastic strain. Aging also leads to an increase in the inelastic work per cycle and the plastic strain. The Morrow Energy model and the Coffin-Manson model were used to predict the characteristic life as a function of the inelastic work per cycle and the plastic strain, respectively. The Morrow Energy model exhibited more robustness in predicting the characteristic life compared to the Coffin-Manson model.

The fatigue resistance and the shear properties of SAC305 solder joints were assessed by utilizing the accelerated shear fatigue test and shear test at different aging times and temperatures in the second study. A customized experimental setup was designed and manufactured to apply the experimental tests on the individual solder joints at actual operating conditions. The effects of the cyclic stress amplitude, aging time and aging temperature on the fatigue life of SAC305 solder joints were investigated. The evolutions on the inelastic work per cycle and plastic strain at different experimental conditions were found by determining the hysteresis loops at the steady state for the studied experimental conditions. An empirical model and Arrhenius model were used to build the reliability degradation model as a function of aging time, aging temperature and stress amplitude. The Morrow Energy and Coffin-Manson models were applied to construct a general reliability model as a function of the inelastic work and plastic strain respectively. An empirical model was used to describe the effect of aging time in the Coffin-Manson model. The Arrhenius model was used to illustrate the effect of aging temperature. The aging time contribution on the Morrow energy model was nonsignificant for all the levels of aging temperature. In the shear test, the relationship between shear strength and different aging conditions was identified. The shear strength model was found as a function of aging conditions by using the Arrhenius model and the general empirical model. The results revealed a significant reduction in the fatigue life and shear strength of the solder joints with aging. The amount of reduction in fatigue life and the shear strength exponentially decreased with aging time. Aging at 150° C had the highest degradation on fatigue life and shear strength for all aging time levels. The inelastic work per cycle and plastic strain at the steady-state region are significantly increased with increasing the aging level or the applied stress amplitude. The microstructure analysis was executed by using the SEM microscope to evaluate the evolutions in the solder joint microstructure. The precipitates coarsening and

increasing in the IMC layer thickness were observed when the aging level was increased. ANOVA analysis was accomplished for the shear test data of SAC305 solder joints where the results indicated that both aging conditions have significant effects on the shear strength of the solder joints. The aging time has larger contributions on the degradation of the solder joints shear strength compared to the aging temperature effect. The aging time has the highest effect on the inelastic work and plastic strain compared to the aging temperature.

In study three, the effect of aging on the fatigue life and the shear strength of SAC305 and SAC-Q solder joints is investigated. The results indicated that the fatigue life is decreased significantly with increasing the cyclic stress amplitude for both solder alloys. SAC-Q solder joints have a higher fatigue resistance and shear strength than SAC305. Aging has a negative impact on the fatigue life and shear strength for both alloys. The effect of aging on SAC-Q solder joints is less than that for SAC305. The reduction in the shear strength and fatigue life of SAC-Q solder joints is observed in the first hours of aging, and then they tend to be stable in long-term aging. However, SAC305 tends to age continually, but the rate is decreased with aging time. In addition, increasing the cyclic stress amplitude leads to an increase in work per cycle and plastic strain for both alloys. The correlations between the fatigue life, inelastic work per cycle, and plastic strain are defined by using the Morrow Energy model and Coffin Manson model, respectively. Neither model can predict the life considering the effect of aging; aging affects the constants of both models. Moreover, the microstructure analysis shows a more substantial amount of precipitates coarsening with aging for SAC305 compared to SAC-Q.

In last study, a new methodology to analyze the reliability data is proposed. This methodology is designed to find the best operating factor levels to obtain the global optimal experimental operating settings. Dealing with a multi-response problem by extracting multiple outputs from the reliability data is the basis for this approach. To implement this methodology, a sequence of steps should be followed. The first step is fitting the reliability data to a Weibull distribution. From Weibull distribution, the characteristic life and B10 are obtained, which are the first two responses. The results of subtracting the normal value of the average and the normal value of the standard deviation are the third output in this approach. The SNR for the fatigue life is the last output which is determined at each experimental combination. Different optimal factor levels may be obtained for each response. To define the global optimal solution in a multi-response problem, the Mamdani fuzzy inference method is implemented to transform those responses into a single response which is called COM output. Calculating the average COM values at each factor level is the last step in this approach. The optimal factor levels are identified by determining the level that has the largest COM value at each factor. The reliability of the aged solder joints under thermal cycling conditions is considered as a validation case study. Three experimental factors are studied which are solder paste materials with ten levels, surface finish with three levels and solder sphere alloys with two levels. The reliability data are obtained and the values of the four responses are calculated. The fuzzy logic is applied to achieve the COM value at each factor level. Finally, the optimal factor levels found for this study are material 6 solder paste, ENIG surface finish, and SAC305 solder sphere.

9.2 Future Works

This work will be extended by studying more levels of stress amplitude, aging temperature and aging time. Investigating the effect of different surface finishes on the fatigue behavior and

mechanical properties of SAC305 solder joints at different aging levels in actual setting condition is another extension of this research. Another topic that could be added to this research is to examine the reliability of different solder joint alloys in actual setting conditions at different levels of aging.

Demonstrating the effect of creep due to dwelling in the thermal cycling environment by studying different levels of dwell time using the same experimental setup is another way to improve this research. Using strain control instead of stress control at different levels of aging might be added to this study in the future. The reliability of the solder joints under varying stress amplitudes, and strain rate could be studied to achieve full understanding of the mechanical failure phenomena. Comparing the obtained data from the mechanical reliability tests with the reliability data from other tests such as thermal cycling, creep, vibration and drop tests. Utilizing other artificial intelligence techniques to build a more robust and accurate prediction models such as genetic algorithms, clustering and backward propagation artificial neural networks. Improving the proposed approach for optimizing the process parameters of the reliability data by considering other responses such as: cost, manufacturability, creep resistance and drop failure resistance. Using other techniques to optimize the process performance of the multi-responses problem such as: utility method, principal component analysis, grey fuzzy and goal programming and then compare the results of those methods.

References

[1] Mason, S. J., Cole, M. H., Ulrey, B. T., & Yan, L. (2002). Improving electronics manufacturing supply chain agility through outsourcing. *International Journal of Physical Distribution & Logistics Management*, *32*(7), 610-620.

[2] Lv, S., Kim, H., Zheng, B., & Jin, H. (2018). A Review of Data Mining with Big Data towards Its Applications in the Electronics Industry. *Applied Sciences*, *8*(4), 582.

[3] J. H. Lau, "Electronics manufacturing with lead-free," *Halogen-free & Conductive-adhesive materials,* vol. 17, 2003.

[4] Kang, S. K., & Sarkhel, A. K. (1994). Lead (Pb)-free solders for electronic packaging. *Journal of Electronic Materials*, *23*(8), 701-707.

[5] Prasad, R. (2013). *Surface mount technology: principles and practice*. Springer Science & Business Media.

[6] Lin, R., Blackshear, E., & Serisky, P. (1988, April). Moisture induced package cracking in plastic encapsulated surface mount components during solder reflow process. In *Reliability Physics Symposium 1988. 26th Annual Proceedings., International* (pp. 83-89). IEEE.

[7] Tu, P. L., Chan, Y. C., & Lai, J. K. L. (1997). Effect of intermetallic compounds on the thermal fatigue of surface mount solder joints. *IEEE Transactions on Components, Packaging, and Manufacturing Technology: Part B*, *20*(1), 87-93.

[8] Kim, J., Kim, D., & Lee, C. C. (2006). Fluxless flip-chip solder joint fabrication using electroplated Sn-Rich Sn–Au Structures. *IEEE transactions on advanced packaging*, *29*(3), 473-482.

[9] Frear, D. R., Jang, J. W., Lin, J. K., & Zhang, C. (2001). Pb-free solders for flip-chip interconnects. *Jom*, *53*(6), 28-33.

[10] Xu, T. H., Zhao, M. Q., & Liu, X. H. (2004). Study on the optimal free-lead solder alloy of Sn-Ag-Cu system. *Electronic components and materials*, *23*(8), 14-16.

[11] Pietriková, A., Livovsky, L. U., Urbancik, J., & Bucko, R. (2006, May). Optimisation of lead free solders reflow profile. In *2006 29th International Spring Seminar on Electronics Technology* (pp. 459-464). IEEE.

[12] Anderson, I. E. (2006). Development of Sn-Ag-Cu and Sn-Ag-Cu-X alloys for Pb-free electronic solder applications. In *Lead-Free Electronic Solders* (pp. 55-76). Springer, Boston, MA.

[13] Pandher, R., & Healey, R. (2008, May). Reliability of Pb-free solder alloys in demanding BGA and CSP applications. In *Electronic Components and Technology Conference, 2008. ECTC 2008. 58th* (pp. 2018-2023). IEEE.

[14] Cai, Z., Zhang, Y., Suhling, J. C., Lall, P., Johnson, R. W., & Bozack, M. J. (2010, June). Reduction of lead-free solder aging effects using doped SAC alloys. In *Electronic Components and Technology Conference (ECTC), 2010 Proceedings 60th* (pp. 1493-1511). IEEE.

[15] Suh, D., Kim, D. W., Liu, P., Kim, H., Weninger, J. A., Kumar, C. M., ... & Tejada, H. B. (2007). Effects of Ag content on fracture resistance of Sn–Ag–Cu lead-free solders under high-strain rate conditions. *Materials Science and Engineering: A*, *460*, 595-603.

[16] Liu, W., Lee, N. C., Porras, A., Ding, M., Gallagher, A., Huang, A., ... & Lee, J. C. (2009, May). Achieving high reliability low cost lead-free SAC solder joints via Mn or Ce doping. In *Electronic Components and Technology Conference, 2009. ECTC 2009. 59th* (pp. 994-1007). IEEE.

[17] Bradley, E., & Banerji, K. (1996). Effect of PCB finish on the reliability and wettability of ball grid array packages. *IEEE Transactions on Components, Packaging, and Manufacturing Technology: Part B*, *19*(2), 320-330.

[18] Mei, Z., Kaufmann, M., Eslambolchi, A., & Johnson, P. (1998, May). Brittle interfacial fracture of PBGA packages soldered on electroless nickel/immersion gold. In *Electronic Components & Technology Conference, 1998. 48th IEEE* (pp. 952-961). IEEE.

[19] Snugovsky, P., Arrowsmith, P., & Romansky, M. (2001). Electroless Ni/immersion Au interconnects: investigation of black pad in wire bonds and solder joints. *Journal of electronic materials*, *30*(9), 1262-1270.

[20] Zeng, K., Vuorinen, V., & Kivilahti, J. K. (2002). Interfacial reactions between lead-free SnAgCu solder and Ni (P) surface finish on printed circuit boards. *IEEE Transactions on Electronics Packaging Manufacturing*, *25*(3), 162-167.

[21] Yoon, Jeong-Won, and Seung-Boo Jung. "Effect of immersion Ag surface finish on interfacial reaction and mechanical reliability of Sn–3.5 Ag–0.7 Cu solder joint." *Journal of Alloys and Compounds* 458.1-2 (2008): 200-207.

[22] Arra, M., Shangguan, D., Xie, D., Sundelin, J., Lepistö, T., & Ristolainen, E. (2004). Study of immersion silver and tin printed-circuit-board surface finishes in lead-free solder applications. *Journal of electronic materials*, *33*(9), 977-990.

[23] Chen, Y. H., Wang, Y. Y., & Wan, C. C. (2007). Microstructural characteristics of immersion tin coatings on copper circuitries in circuit boards. *Surface and Coatings Technology*, *202*(3), 417-424.

[24] Chang, D., Bai, F., Wang, Y. P., & Hsiao, C. S. (2004, December). The study of OSP as reliable surface finish of BGA substrate. In *Electronics Packaging Technology Conference, 2004. EPTC 2004. Proceedings of 6th* (pp. 149-153). IEEE.

[25] Clech, J. P., Langerman, F. M., & Augis, J. A. (1990, May). Local CTE mismatch in SM leaded packages: a potential reliability concern. In *Electronic Components and Technology Conference, 1990.., 40th* (pp. 368-376). IEEE.

[26] Dai, X., Brillhart, M. V., & Ho, P. S. (2000). Adhesion measurement for electronic packaging applications using double cantilever beam method. *IEEE Transactions on Components and Packaging Technologies*, *23*(1), 101-116.

[27] Bhattacharyya, G. K., & Soejoeti, Z. (1989). A tampered failure rate model for step-stress accelerated life test. *Communications in Statistics-Theory and Methods*, *18*(5), 1627-1643.

[28] Wickham, M., Nottay, J., & Hunt, C. (2001). *A review of mechanical test method standards for lead-free solders*. National Physical Laboratory.

[29] Hui, I. K., & Law, H. W. (2000). An alternative approach for the analysis of intermetallic compounds in SMT solder joints. *Soldering & Surface Mount Technology*, *12*(1), 23-31.

[30] Jaradat, Y., Qasaimeh, A., Obaidat, M., & Borgesen, P. (2014). Assessment of solder joint fatigue life under realisticistic service conditions. *Journal of electronic materials*, *43*(12), 4472-4484.

[31] Kapur, K. C., & Lamberson, L. R. (1977). Reliability in engineering design. *New York, John Wiley and Sons, Inc., 1977. 605 p.*

[32] Al-Refaie, A., Chen, T., Al-Athamneh, R., & Wu, H. C. (2016). Fuzzy neural network approach to optimizing process performance by using multiple responses. *Journal of Ambient Intelligence and Humanized Computing*, *7*(6), 801-816.

[33] Ebeling, C. E. (2004). *An introduction to reliability and maintainability engineering*. Tata McGraw-Hill Education.

[34] Escobar, L. A., & Meeker, W. Q. (2006). A review of accelerated test models. *Statistical science*, 552-577.

[35] Caruso, H., & Dasgupta, A. (1998). A fundamental overview of accelerated testing analytical models. *Journal of the IEST*, *41*(1), 16-20.

[36] Cui, H. (2005, January). Accelerated temperature cycle test and Coffin-Manson model for electronic packaging. In *Reliability and Maintainability Symposium, 2005. Proceedings. Annual* (pp. 556-560). IEEE.

[37] Lawless, J. F. (2011). *Statistical models and methods for lifetime data* (Vol. 362). John Wiley & Sons.

[38] Jordan, A. S. (1978). A comprehensive review of the lognormal failure distribution with application to LED reliability. *Microelectronics Reliability*, *18*(3), 267-279.

[39] Fratila, D., & Caizar, C. (2011). Application of Taguchi method to selection of optimal lubrication and cutting conditions in face milling of AlMg3. *Journal of Cleaner Production*, *19*(6-7), 640-645.

[40] Al-Refaie, A., Wu, T. H., & Li, M. H. (2009). Data envelopment analysis approaches for solving the multiresponse problem in the Taguchi method. *AI EDAM*, *23*(2), 159-173.

[41] Lilly, J. H. (2011). *Fuzzy control and identification*. John Wiley & Sons.

[42] Pontes, F. J., de Paiva, A. P., Balestrassi, P. P., Ferreira, J. R., & da Silva, M. B. (2012). Optimization of Radial Basis Function neural network employed for prediction of surface roughness in hard turning process using Taguchi's orthogonal arrays. *Expert Systems with Applications*, *39*(9), 7776-7787.

[43] Zuniga, K. V., Castilla, I., & Aguilar, R. M. (2014). Using fuzzy logic to model the behavior of residential electrical utility customers. *Applied Energy*, *115*, 384-393.

[44] Asiltürk, I., & Çunkaş, M. (2011). Modeling and prediction of surface roughness in turning operations using artificial neural network and multiple regression method. *Expert systems with applications*, *38*(5), 5826-5832.

[45] Moosavi, M., & Soltani, N. (2013). Prediction of the specific volume of polymeric systems using the artificial neural network-group contribution method. *Fluid Phase Equilibria*, *356*, 176-184.

[46] Almonacid, F., Rus, C., Pérez-Higueras, P., & Hontoria, L. (2011). Calculation of the energy provided by a PV generator. Comparative study: conventional methods vs. artificial neural networks. *Energy*, *36*(1), 375-384.

[47] Xia, C. Wang, J. McMenemy, K. (2010), Short, medium and long term load forecasting model and virtual load forecaster based on radial basis function neural networks. Electrical Power and Energy Systems, 32(7), 743–750.

[48] Peng, X., Li, Q., & Wang, K. (2014). Core axial power shape reconstruction based on radial basis function neural network. *Annals of Nuclear Energy*, *73*, 339-344.

[49] Javan, D. S., Mashhadi, H. R., & Rouhani, M. (2013). A fast static security assessment method based on radial basis function neural networks using enhanced clustering. *International Journal of Electrical Power & Energy Systems*, *44*(1), 988-996.

[50] Ko, C. N., & Lee, C. M. (2013). Short-term load forecasting using SVR (support vector regression)-based radial basis function neural network with dual extended Kalman filter. *Energy*, *49*, 413-422.

[51] Tsai, T. N. (2011). Improving the fine-pitch stencil printing capability using the Taguchi method and Taguchi fuzzy-based model. *Robotics and Computer-Integrated Manufacturing*, *27*(4), 808-817.

[52] Krokhmal, P., Palmquist, J., & Uryasev, S. (2002). Portfolio optimization with conditional value-at-risk objective and constraints. *Journal of risk*, *4*, 43-68.

[53] Comizzoli, R. B., Frankenthal, R. P., Milner, P. C., & Sinclair, J. D. (1986). Corrosion of electronic materials and devices. *Science*, *234*(4774), 340-345.

[54] Amagai, M. (2002). Mechanical reliability in electronic packaging. *Microelectronics Reliability*, *42*(4-5), 607-627.

[55] Stapper, C. H. (1983). Modeling of integrated circuit defect sensitivities. *IBM Journal of Research and Development*, *27*(6), 549-557.

[56] McLeish, J., & Schueller, R. (2015, October). Ensuring Suitability of Cu Wire Bonded ICs for Automotive Applications. In *International Symposium on Microelectronics* (Vol. 2015, No. 1, pp. 000751-000756). International Microelectronics Assembly and Packaging Society.

[57] Schueller, R., & Solutions, D. (2012). Copper wire bond failure mechanisms. *DfR Solutions*.

[58] Sharon, G., & Tulkoff, C. (2014, September). Temperature Cycling and Fatigue in Electronics. In *Surface Mount Technology Association International Conference*.

[59] Ham, S. J., & Lee, S. B. (1996). Experimental study for reliability of electronic packaging under vibration. *Experimental Mechanics*, *36*(4), 339-344.

[60] Lu, L. N., Huang, H. Z., Su, X. X., Wu, B. Y., & Cai, M. (2009, August). Investigation on PCB related failures in high-density electronic assemblies. In *Electronic Packaging Technology & High Density Packaging, 2009. ICEPT-HDP'09. International Conference on* (pp. 128-132). IEEE.

[61] Fu, C., Ume, I. C., & McDowell, D. L. (1998). Thermal stress and fatigue analysis of plated-through holes using an internal state variable constitutive model. *Finite Elements in Analysis and Design*, *30*(1-2), 1-17.

[62] Ma, H., Suhling, J. C., Lall, P., & Bozack, M. J. (2006, May). Reliability of the aging lead-free solder joint. In *Electronic Components and Technology Conference, 2006. Proceedings. 56th* (pp. 16-pp). IEEE.

[63] Su, S., Fu, N., & Akkara, F. J. (2018). Effect of Long-Term Room Temperature Aging on the Fatigue Properties of SnAgCu Solder Joint. *Journal of Electronic Packaging*.

[64] Borgesen, P., Hamasha, S., Wentlent, L., Watson, D., & Greene, C. (2016, January). Interpreting accelerated test results for lead-free solder joints. In *Pan Pacific Microelectronics Symposium (Pan Pacific), 2016* (pp. 1-9). IEEE.

[65] McCormack, M., & Jin, S. (1994). New, lead-free solders. *Journal of Electronic Materials*, *23*(7), 635-640.

[66] Tsui, Y. K., Lee, S. R., & Huang, X. (2002, December). Experimental investigation on the degradation of BGA solder ball shear strength due to room temperature aging. In *Electronic Materials and Packaging, 2002. Proceedings of the 4th International Symposium on* (pp. 478-481). IEEE.

[67] Ma, H., & Suhling, J. C. (2009). A review of mechanical properties of lead-free solders for electronic packaging. *Journal of materials science*, *44*(5), 1141-1158.

[68] Coyle, R. J., Solan, P. P., Serafino, A. J., & Gahr, S. A. (2000). The influence of room temperature aging on ball shear strength and microstructure of area array solder balls. In *Electronic Components & Technology Conference, 2000. 2000 Proceedings. 50th* (pp. 160-169). IEEE.

[69] Lampe, B. T. (1976). Room temperature aging properties of some solder alloys. *Welding Journal*, *55*(10), 330.

[70] Medvedev, A. S. (1956). Aging of tin-lead solders and joints soldered by them. *Metallovedenie i Obrabotka Metallov*, (7), 16-23.

[71] Lee, T. K., Ma, H., Liu, K. C., & Xue, J. (2010). Impact of isothermal aging on long-term reliability of fine-pitch ball grid array packages with Sn-Ag-Cu solder interconnects: Surface finish effects. *Journal of Electronic Materials*, *39*(12), 2564-2573.

[72] Smetana, J., Coyle, R., Read, P., Popowich, R., Fleming, D., & Sack, T. (2011, October). Variations in thermal cycling response of Pb-free solder due to isothermal preconditioning. In *Proceedings of the 2011 SMTAI Conference* (pp. 641-654).

[73] Zhang, Y., Cai, Z., Suhling, J. C., Lall, P., & Bozack, M. J. (2008, May). The effects of aging temperature on SAC solder joint material behavior and reliability. In *Electronic Components and Technology Conference, 2008. ECTC 2008. 58th* (pp. 99-112). IEEE.

[74] Li, L., Jang, J. W., & Allmen, B. (2001). Shear property and microstructure evaluation of Pb-free solder bumps under room temperature and multiple reflow/high temperature aging. In *Advanced Packaging Materials: Processes, Properties and Interfaces, 2001. Proceedings. International Symposium on* (pp. 347-353). IEEE.

[75] Zhang, J., Hai, Z., Thirugnanasambandam, S., Evans, J. L., Bozack, M. J., Zhang, Y., & Suhling, J. C. (2013). Thermal aging effects on the thermal cycling reliability of lead-free fine pitch packages. *IEEE transactions on components, packaging and manufacturing technology*, *3*(8), 1348-1357.

[76] Su, S., Akkara, F., Dawahdeh, A., Borgesen, P., & Qasaimeh, A. (2017, May). Solder joint reliability in isothermal varying load cycling. In *Thermal and Thermomechanical Phenomena in Electronic Systems (ITherm), 2017 16th IEEE Intersociety Conference on* (pp. 1331-1336). IEEE.

[77] Lall, P., Shantaram, S., Suhling, J., & Locker, D. (2013, May). Effect of aging on the high strain rate mechanical properties of SAC105 and SAC305 leadfree alloys. In *Electronic Components and Technology Conference (ECTC), 2013 IEEE 63rd* (pp. 1277-1293). IEEE.

[78] Han, Y. D., Jing, H. Y., Nai, S. M. L., Xu, L. Y., Tan, C. M., & Wei, J. (2010). Temperature dependence of creep and hardness of Sn-Ag-Cu lead-free solder. *Journal of Electronic Materials*, *39*(2), 223-229.

[79] Venkatadri, V., Yin, L., Xing, Y., Cotts, E., Srihari, K., & Borgesen, P. (2009, May). Accelerating the effects of aging on the reliability of lead-free solder joints in a quantitative fashion. In *Electronic Components and Technology Conference, 2009. ECTC 2009. 59th* (pp. 398-405). IEEE.

[80] Hasnine, M., Mustafa, M., Suhling, J. C., Prorok, B. C., Bozack, M. J., & Lall, P. (2013, May). Characterization of aging effects in lead-free solder joints using nanoindentation. In *Electronic Components and Technology Conference (ECTC), 2013 IEEE 63rd* (pp. 166-178). IEEE.

[81] Chuang, C. M., Lui, T. S., & Chen, L. H. (2002). Effect of aluminum addition on tensile properties of naturally aged Sn-9Zn eutectic solder. *Journal of Materials Science*, *37*(1), 191-195.

[82] Andersson, C., Lai, Z., Liu, J., Jiang, H., & Yu, Y. (2005). Comparison of isothermal mechanical fatigue properties of lead-free solder joints and bulk solders. *Materials Science and Engineering: A*, *394*(1-2), 20-27.

[83] Zhang, Y., Cai, Z., Suhling, J. C., Lall, P., & Bozack, M. J. (2009, May). The effects of SAC alloy composition on aging resistance and reliability. In *Electronic Components and Technology Conference, 2009. ECTC 2009. 59th* (pp. 370-389). IEEE.

[84] Thirugnanasambandam, S., Sanders, T., Raj, A., Stone, D., Evans, J., Flowers, G., & Suhling, J. (2014, May). The study of vibrational performance on different doped low creep lead-free solder paste and solder ball grid array packages. In *Thermal and Thermomechanical Phenomena in Electronic Systems (ITherm), 2014 IEEE Intersociety Conference on* (pp. 920-923). IEEE.

[85] Raj, A., Thirugnanasambandam, S., Sanders, T., Sridhar, S., Gordon, S., Evans, J., ... & Carpenter, M. (2016, May). Proportional Hazard Model of doped low creep lead-free solder paste under thermal shock. In *Thermal and Thermomechanical Phenomena in Electronic Systems (ITherm), 2016 15th IEEE Intersociety Conference on* (pp. 1191-1201). IEEE.

[86] Sridhar, S., Raj, A., Gordon, S., Thirugnanasambandam, S., Evans, J. L., & Johnson, W. (2016, May). Drop impact reliability testing of isothermally aged doped low creep lead-free solder paste alloys. In *Thermal and Thermomechanical Phenomena in Electronic Systems (ITherm), 2016 15th IEEE Intersociety Conference on* (pp. 501-506). IEEE.

[87] Mustafa, M., Cai, Z., Suhling, J. C., & Lall, P. (2011, May). The effects of aging on the cyclic stress-strain behavior and hysteresis loop evolution of lead-free solders. In *Proceedings of the 61st Electronic Components and Technology Conference* (pp. 927-939).

[88] Ma, H., Suhling, J. C., Zhang, Y., Lall, P., & Bozack, M. J. (2007, May). The influence of elevated temperature aging on reliability of lead-free solder joints. In *Electronic Components and Technology Conference, 2007. ECTC'07. Proceedings. 57th* (pp. 653-668). IEEE.

[89] Mustafa, M., Roberts, J. C., Suhling, J. C., & Lall, P. (2014, May). The effects of aging on the fatigue life of lead-free solders. In *Electronic Components and Technology Conference (ECTC), 2014 IEEE 64th* (pp. 666-683). IEEE.

[90] Darveaux, R. (2005, May). Shear deformation of lead-free solder joints. In *Electronic Components and Technology Conference, 2005. Proceedings. 55th* (pp. 882-893). IEEE.

[91] Pang, J. H., Xiong, B. S., & Low, T. H. (2004). Low cycle fatigue models for lead-free solders. *Thin solid films*, *462*, 408-412.

[92] Shohji, I., Mori, H., & Orii, Y. (2004). Solder joint reliability evaluation of chip scale package using a modified Coffin–Manson equation. *Microelectronics Reliability*, *44*(2), 269-274.

[93] Lau, J. H. (1996). Solder joint reliability of flip-chip and plastic ball grid array assemblies under thermal, mechanical, and vibrational conditions. *IEEE Transactions on Components, Packaging, and Manufacturing Technology: Part B*, *19*(4), 728-735.

[94] Darveaux, R., & Banerji, K. (1991, May). Fatigue analysis of flip-chip assemblies using thermal stress simulations and a Coffin-Manson relation. In *Electronic Components and Technology Conference, 1991. Proceedings., 41st* (pp. 797-805). IEEE.

[95] Che, F. X., & Pang, J. H. (2004, December). Thermal fatigue reliability analysis for PBGA with Sn-3.8 Ag-0.7 Cu solder joints. In *Electronics Packaging Technology Conference, 2004. EPTC 2004. Proceedings of 6th* (pp. 787-792). IEEE.

[96] Sarihan, V. (1993, June). Energy based methodology for damage and life prediction of solder joints under thermal cycling. In *Electronic Components and Technology Conference, 1993. Proceedings., 43rd* (pp. 32-38). IEEE.

[97] Shi, X. Q., Wang, Z. P., Zhou, W., Pang, H. L. J., & Yang, Q. J. (2002). A new creep constitutive model for eutectic solder alloy. *Journal of Electronic Packaging*, *124*(2), 85-90.

[98] Wang, G. Z., Cheng, Z. N., Becker, K., & Wilde, J. (2001). Applying Anand model to represent the viscoplastic deformation behavior of solder alloys. *Journal of electronic packaging*, *123*(3), 247-253.

[99] Jong, W. R., Chen, S. C., Tsai, H. C., Chiu, C. C., & Chang, H. T. (2006). The geometrical effects of bumps on the fatigue life of flip-chip packages by Taguchi method. *Journal of reinforced plastics and composites*, *25*(1), 99-114.

[100] Wong, T. E., Kachatorian, L. A., & Tierney, B. D. (1997). Gull-wing solder joint fatigue life sensitivity evaluation. *Journal of Electronic Packaging*, *119*(3), 171-176.

[101] Mertol, A. (2000). Application of the Taguchi method to chip scale package (CSP) design. *IEEE transactions on advanced packaging*, *23*(2), 266-276.

[102] Zafiropoulos, E. P., & Dialynas, E. N. (2005). Reliability prediction and failure mode effects and criticality analysis (FMECA) of electronic devices using fuzzy logic. *International Journal of Quality & Reliability Management*, *22*(2), 183-200.

[103] Jarrah, M. A., Al-Assaf, Y., & Kadi, H. E. (2002). Neuro-fuzzy modeling of fatigue life prediction of unidirectional glass fiber/epoxy composite laminates. *Journal of composite materials*, *36*(6), 685-700.

[104] Zalnezhad, E., Sarhan, A. A., & Hamdi, M. (2013). Adhesion strength predicting of Cr/CrN coated Al7075 using fuzzy logic system for fretting fatigue life enhancement. In *Proceedings of the world congress on engineering and computer science* (Vol. 1, pp. 2-8).

[105] Chen, J., Yin, Y., Ye, J., & Wu, Y. (2015). Investigation on fatigue behavior of single SnAgCu/SnPb solder joint by rapid thermal cycling. *Soldering & Surface Mount Technology*, *27*(2), 76-83.

[106] Chien, Chi-Hui, Thaiping Chen, Wei-Bang Lin, Chi-Chang Hsieh, Yii-Der Wu, and Cheng-Hsiu Yeh. "Experimental and statistical study in adhesion features of bonded interfaces of IC packages." *Microelectronics Reliability* 48, no. 1 (2008): 140-148.

[107] Park, J. M., & Kang, H. T. (2007). Prediction of fatigue life for spot welds using back-propagation neural networks. *Materials & design*, *28*(10), 2577-2584.

[108] Deshpande, A. M., Subbarayan, G., & Mahajan, R. L. (1997). Maximizing solder joint reliability through optimal shape design. *Journal of Electronic Packaging*, *119*(3), 149-155.

[109] Qasaimeh, A., Lu, S., & Borgesen, P. (2011, May). Crack evolution and rapid life assessment for lead-free solder joints. In *Electronic Components and Technology Conference (ECTC), 2011 IEEE 61st* (pp. 1283-1290). IEEE.

[110] Subbarayan, G., Li, Y., & Mahajan, R. L. (1996). Reliability simulations for solder joints using stochastic finite element and artificial neural network models. *Journal of Electronic Packaging*, *118*(3), 148-156.

[111] Al Athamneh, R., Abueed, M., Hani, D. B., Su, S., Suhling, J., & Lall, P. (2019, May). Effect of Aging on the Fatigue Life and Shear Strength of SAC305 Solder Joints in Actual Setting Conditions. In *2019*

18th IEEE Intersociety Conference on Thermal and Thermomechanical Phenomena in Electronic Systems (ITherm) (pp. 1146-1154). IEEE.

[112] Chilton, A. C., Whitmore, M. A., & Hampshire, W. B. (1989). Fatigue Failure in a Model SMD Joint. *Soldering & Surface Mount Technology, 1(3), 21-24.*

[113] Morrow, J. (1965). Cyclic plastic strain energy and fatigue of metals. In *Internal friction, damping, and cyclic plasticity*. ASTM International.

[114] Coffin Jr, L. F. (1954). A study of the effects of cyclic thermal stresses on a ductile metal. *Transactions of the American Society of Mechanical Engineers, New York, 76,* 931-950.

[115] Suhir, E., Ghaffarian, R., & Yi, S. (2017). Solder material experiencing low temperature inelastic stress and random vibration loading: predicted remaining useful lifetime. *Journal of Materials Science: Materials in Electronics*, *28*(4), 3585-3597.

[116] Al-Refaie, A. (2015). A proposed weighted additive model to optimize multiple quality responses in the Taguchi method with applications. *Proceedings of the Institution of Mechanical Engineers, Part E: Journal of Process Mechanical Engineering*, *229*(3), 168-178.

[117] Berkan, R. C., & Trubatch, S. (1997). Fuzzy system design principles. Wiley-IEEE Press.

[118] Sun, J. H., & Hsueh, B. R. (2011). Optical design and multi-objective optimization with fuzzy method for miniature zoom optics. Optics and Lasers in Engineering, 49(7), 962-971.

Appendices

Appendix A
Two-parameter Weibull probability distribution plots

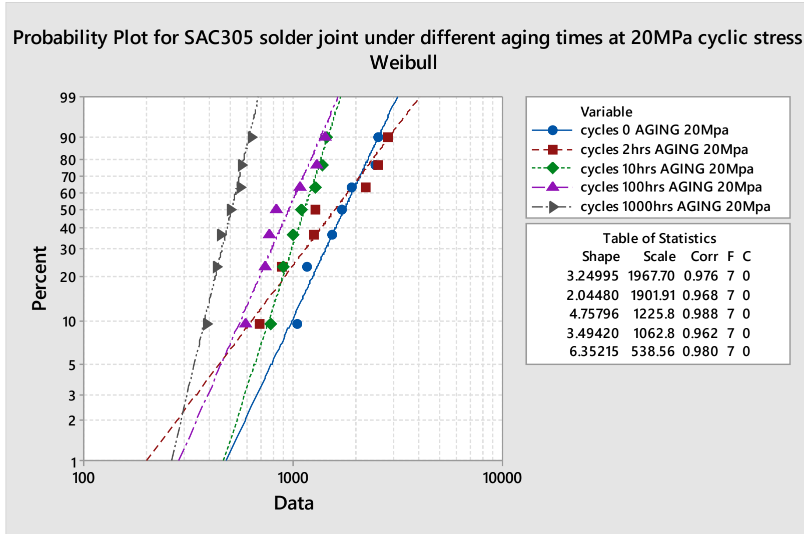

Figure A. 1: Two-parameter Weibull distribution for SAC305 solder joints under 20MPa cyclic stress amplitude at different aging times and 100°C aging temperature.

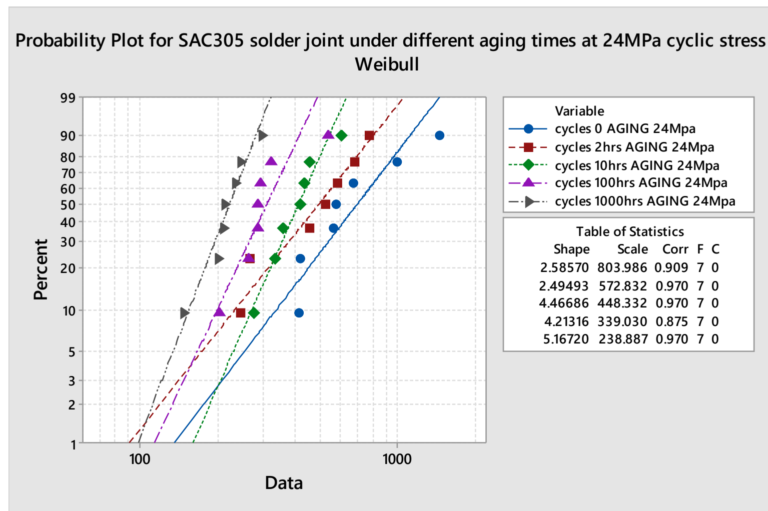

Figure A. 2: Two-parameter Weibull distribution for SAC305 solder joints under 24MPa cyclic stress amplitude at different aging times and 100°C aging temperature.

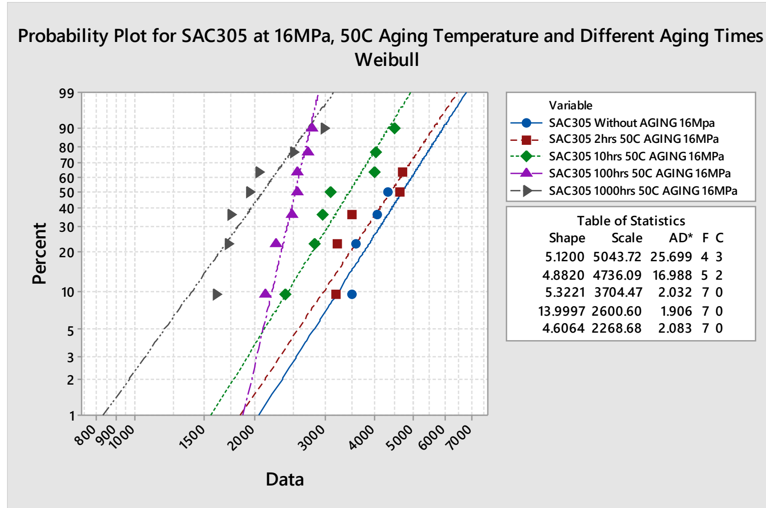

Figure A. 3: Two-parameter Weibull distribution for SAC305 solder joints under 16MPa cyclic stress amplitude at different aging times and 50˚C aging temperature.

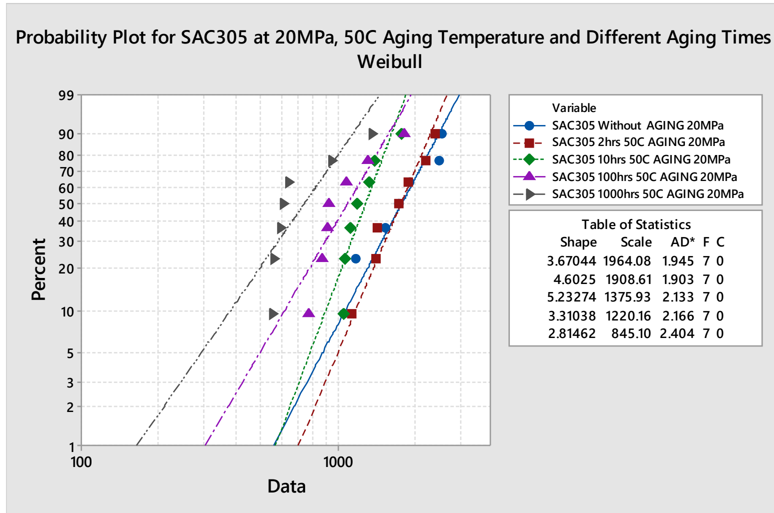

Figure A. 4: Two-parameter Weibull distribution for SAC305 solder joints under 20MPa cyclic stress amplitude at different aging times and 50˚C aging temperature.

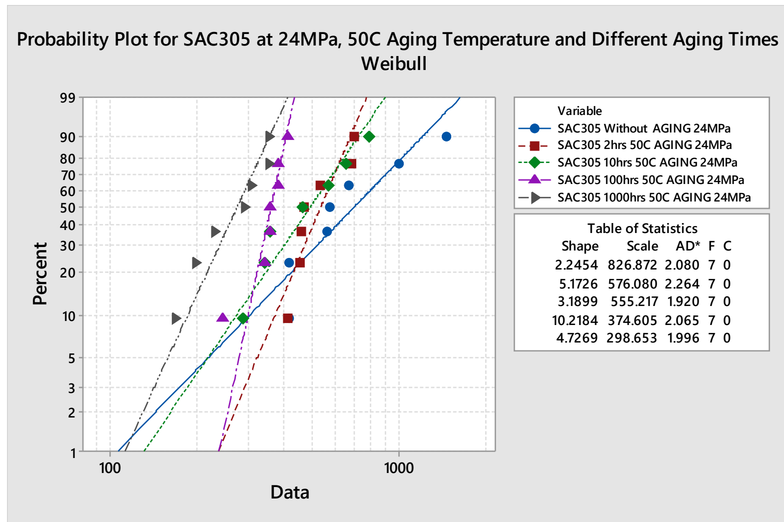

Figure A. 5: Two-parameter Weibull distribution for SAC305 solder joints under 24MPa cyclic stress amplitude at different aging times and 50˚C aging temperature.

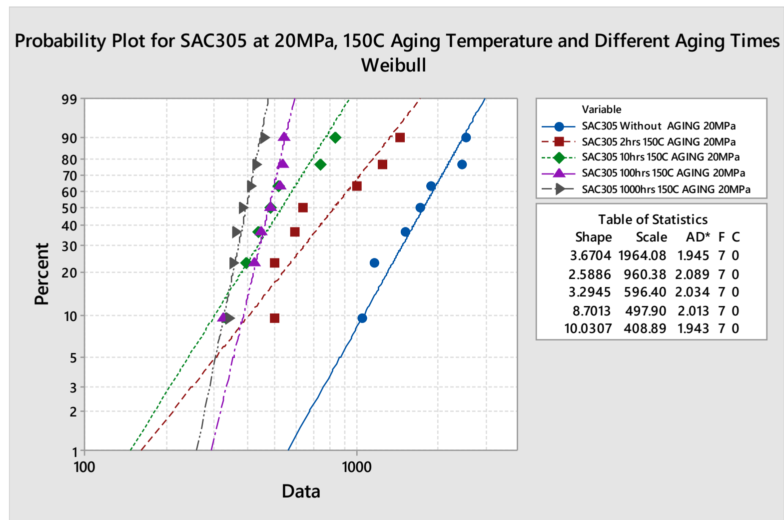

Figure A. 6: Two-parameter Weibull distribution for SAC305 solder joints under 20MPa cyclic stress amplitude at different aging times and 150˚C aging temperature.

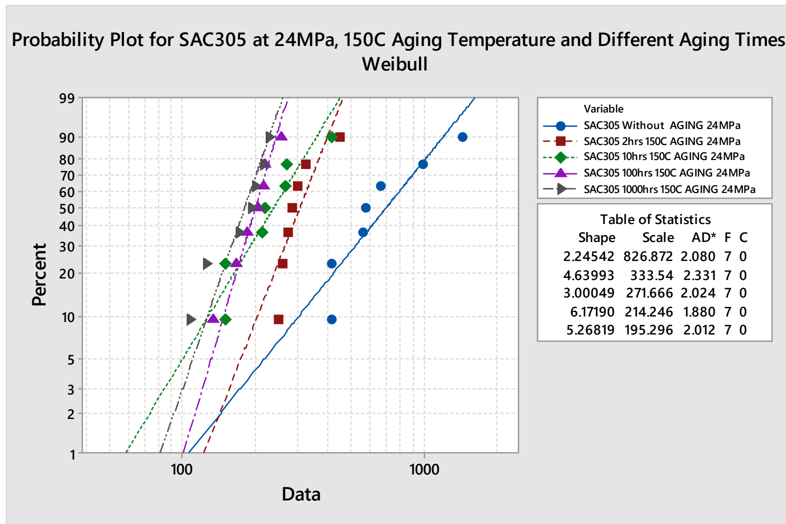

Figure A. 7: Two-parameter Weibull distribution for SAC305 solder joints under 24MPa cyclic stress amplitude at different aging times and 150°C aging temperature.

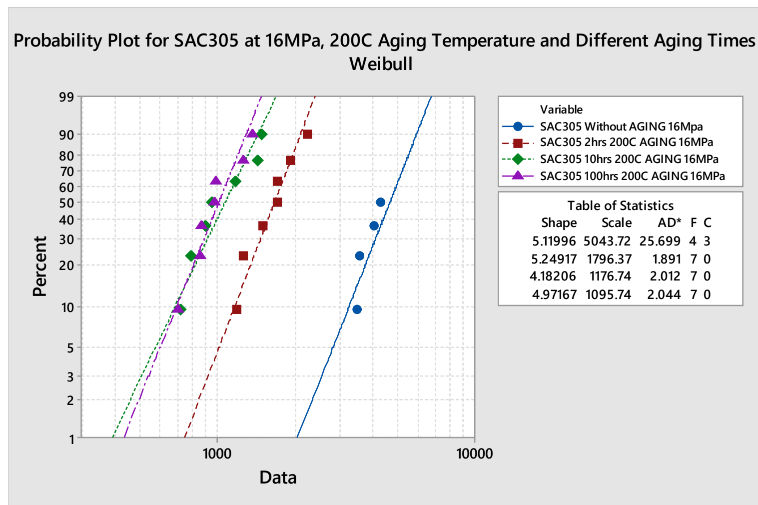

Figure A. 8: Two-parameter Weibull distribution for SAC305 solder joints under 16MPa cyclic stress amplitude at different aging times and 200°C aging temperature.

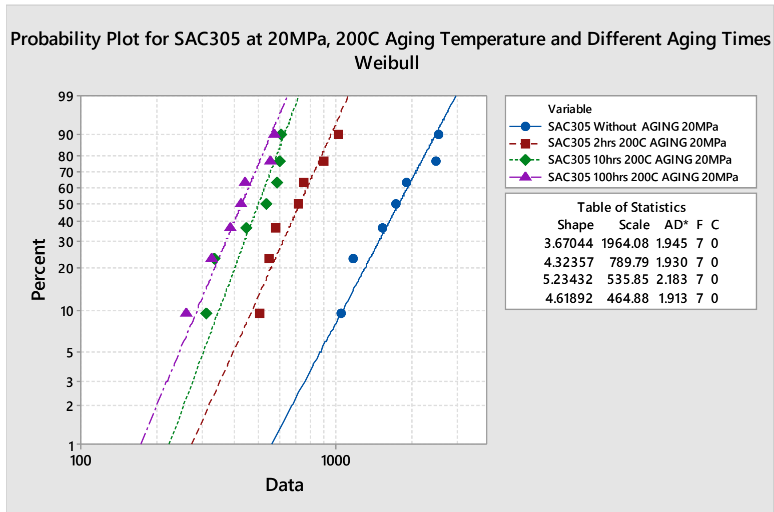

Figure A. 9: Two-parameter Weibull distribution for SAC305 solder joints under 20MPa cyclic stress amplitude at different aging times and 200°C aging temperature.

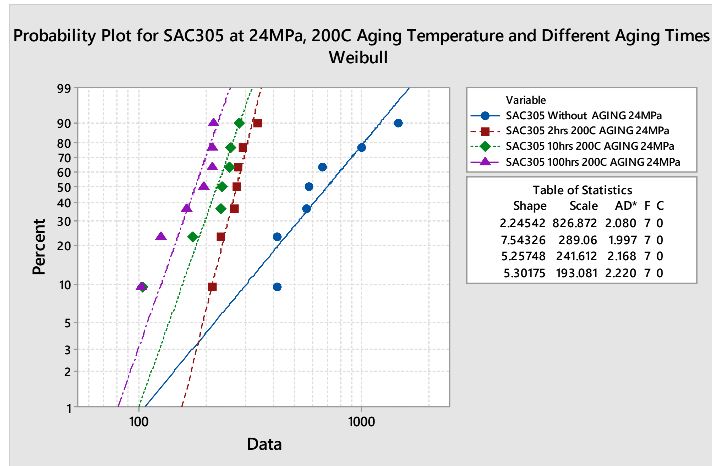

Figure A. 10: Two-parameter Weibull distribution for SAC305 solder joints under 24MPa cyclic stress amplitude at different aging times and 200°C aging temperature.

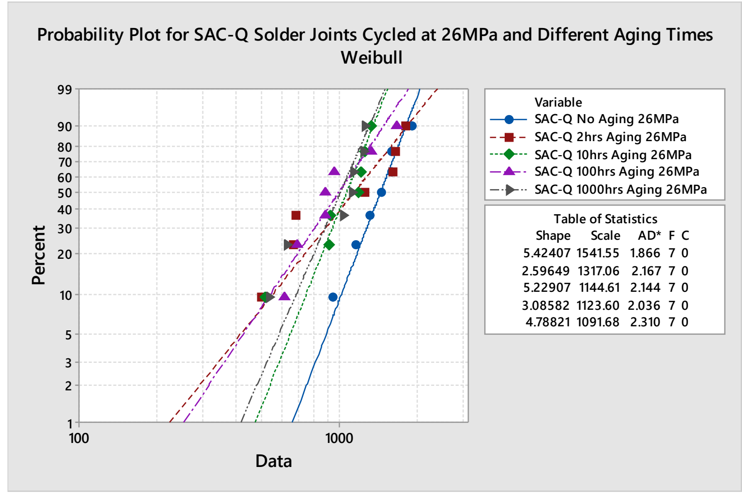

Figure A. 11: Two-parameter Weibull distribution for SAC-Q solder joints under 26MPa cyclic stress amplitude at different aging times and 100˚C aging temperature.

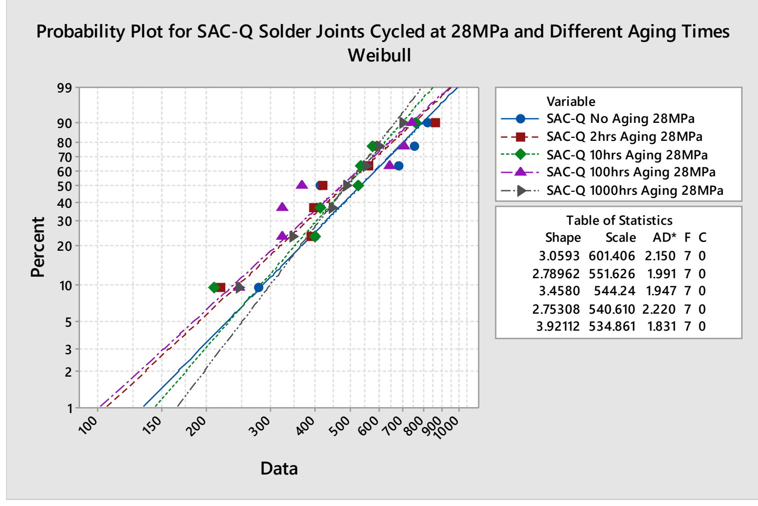

Figure A. 12: Two-parameter Weibull distribution for SAC-Q solder joints under 28MPa cyclic stress amplitude at different aging times and 100˚C aging temperature.

Appendix B
Artificial neural networks and fuzzy logic Figures

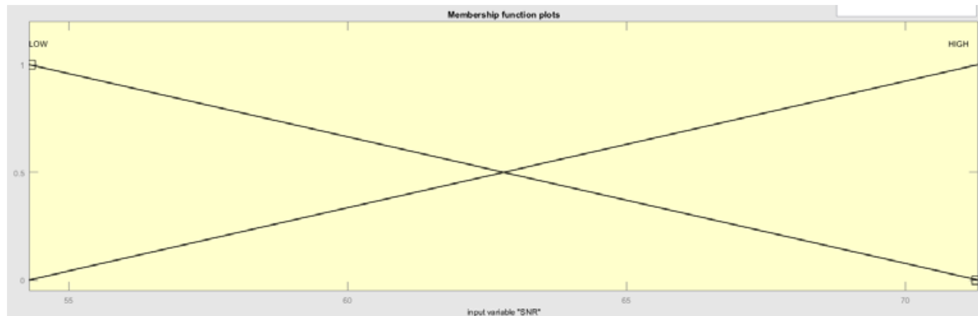

Figure B. 1: The input MFs for the SNR quality response in fuzzy system.

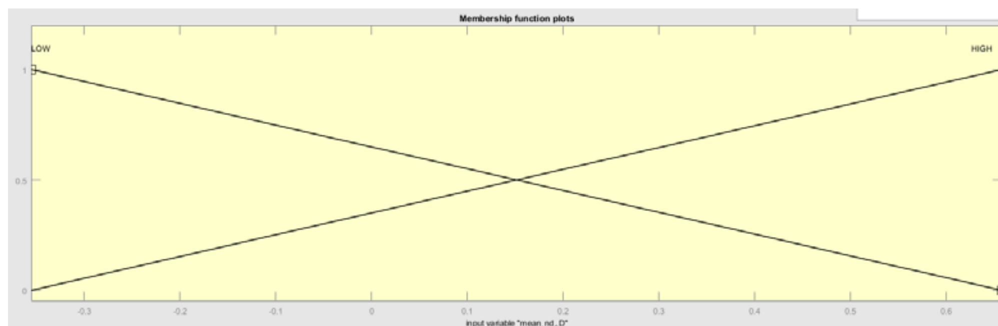

Figure B. 2: The input MFs for the mean-standard deviation quality response in fuzzy system.

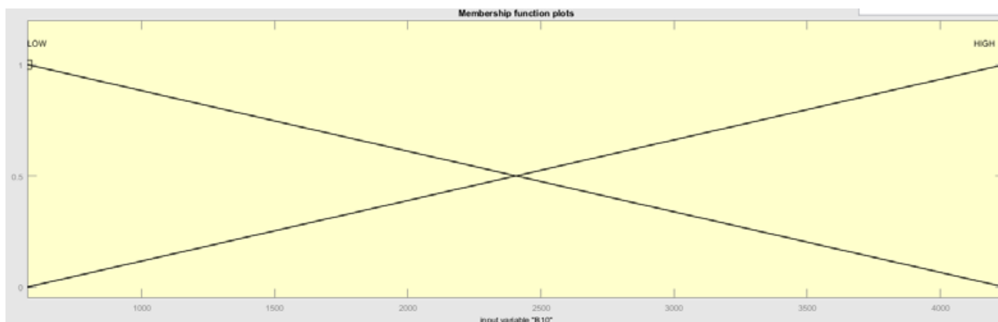

Figure B. 3: The input MFs for the B10 quality response in fuzzy system.

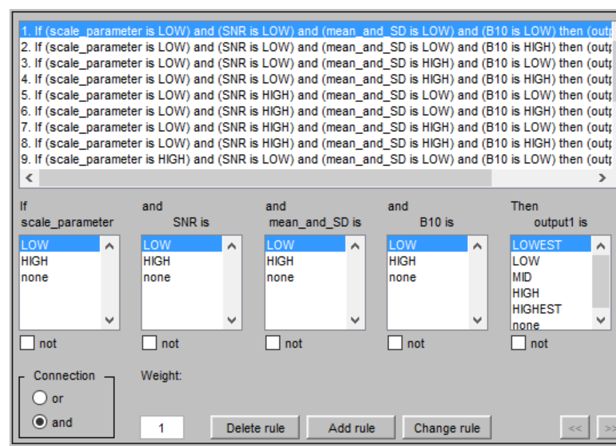

Figure B. 4: Setting the rules in fuzzy system.

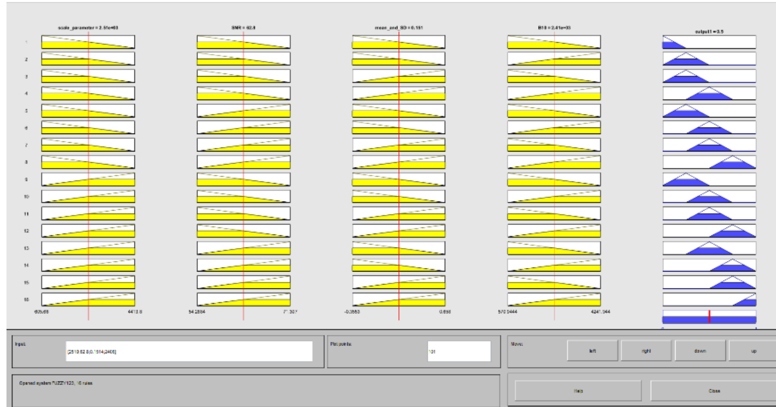

Figure B. 5: Rules aggregations in fuzzy system in fuzzy system.

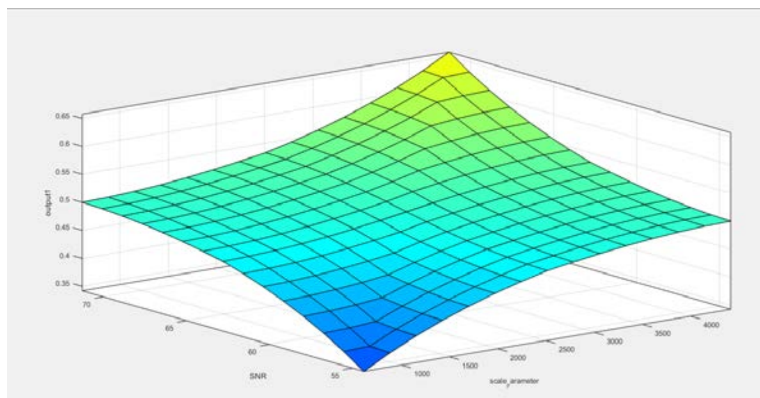

Figure B. 6: Surface response for the scale and SNR parameters in fuzzy system.

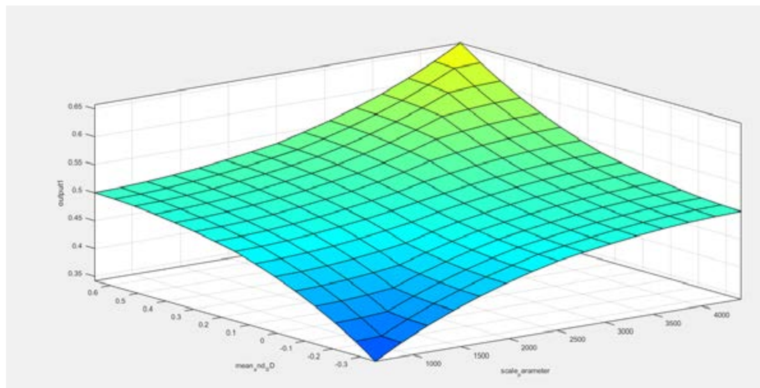

Figure B. 7: Surface response for the scale and mean-standard deviation parameters in fuzzy system.

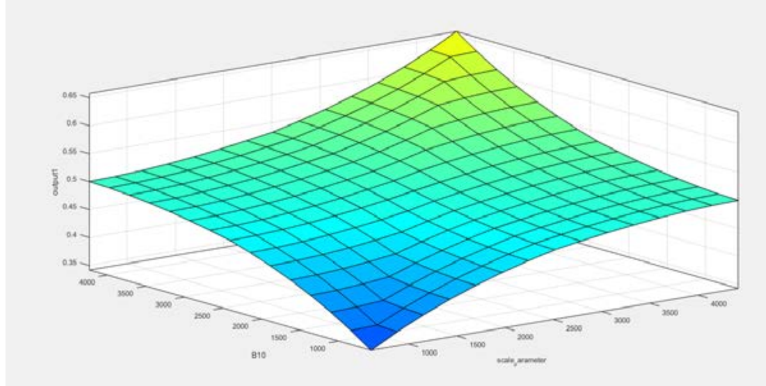

Figure B. 8: Surface response for the scale and B10 parameters in fuzzy system.

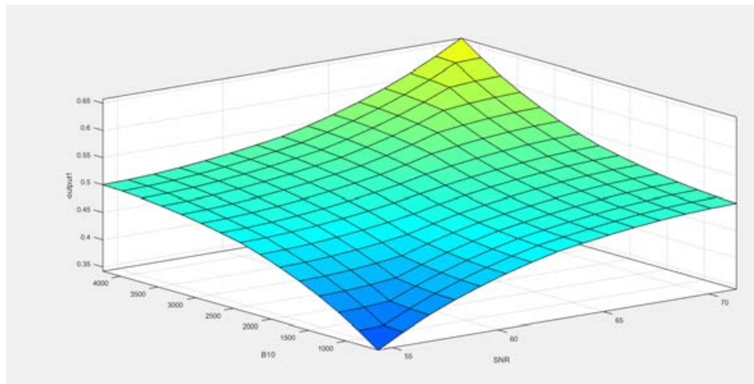

Figure B. 9: Surface response for the SNR and B10 parameters in fuzzy system.

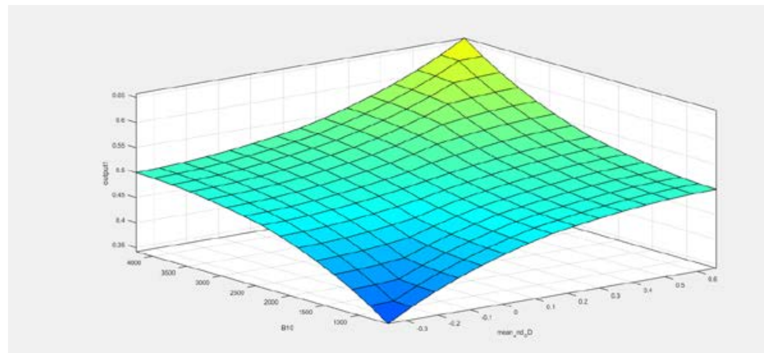

Figure B. 10: Surface response for the mean-standard deviation and B10 parameters in fuzzy system.

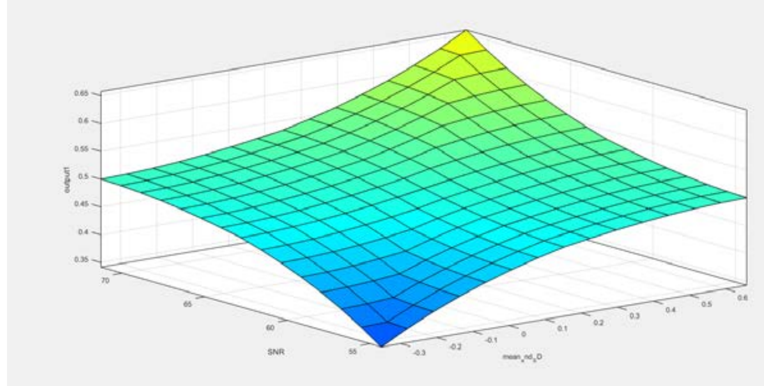

Figure B. 11: Surface response for the mean-standard deviation and SNR parameters in fuzzy system.

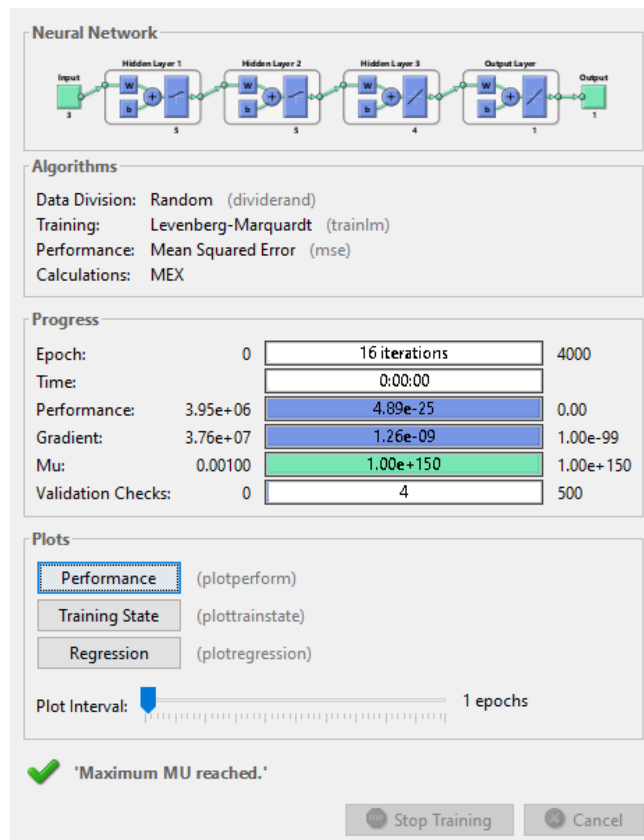

Figure B. 12: Backward propagation ANNs predication parameters.

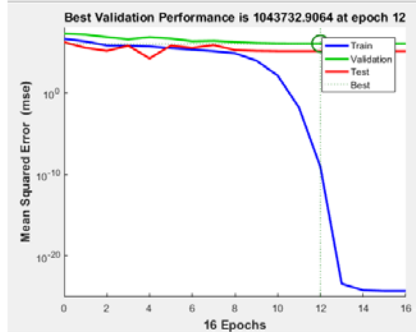

Figure B. 13: Performance for ANNs model.

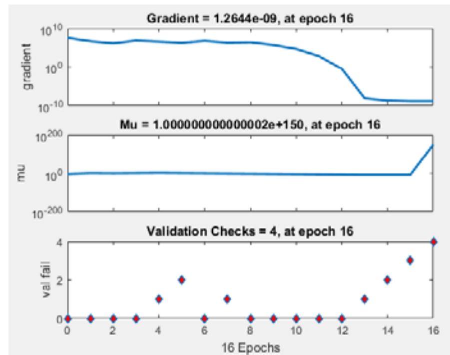

Figure B. 14: Training state for ANNs model.

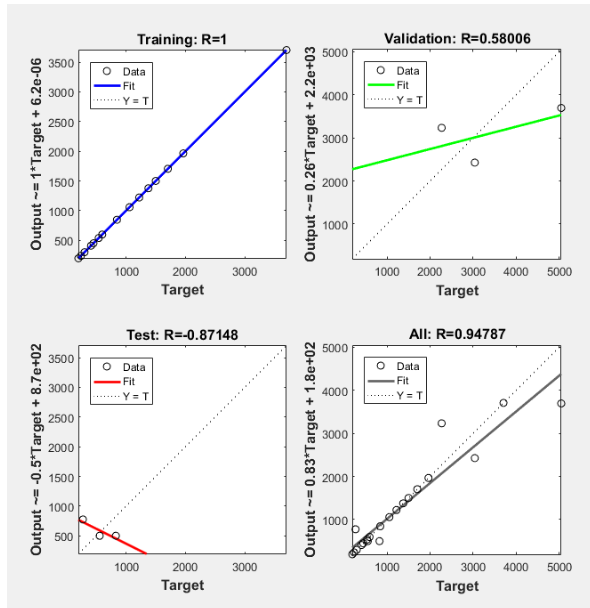

Figure B. 15: Regression for ANNs model.